

On the Discrimination and Interaction of Droplets and Ice in Mixed-Phase Clouds

(Phasendiskriminierung und Interaktion von
Wassertropfen und Eispartikeln in
Mischphasenwolken)

Zur Erlangung des akademischen Grades eines
DOKTORS DER NATURWISSENSCHAFTEN
(Dr. rer. nat.)

von der KIT-Fakultät für Physik
des Karlsruher Institut für Technologie (KIT)

genehmigte
DISSERTATION

von

Fritz Waitz, M. Sc.

Referent:	Prof. Dr. T. Leisner
Korreferent:	Prof. Dr. C. Hoose
Datum der mündlichen Prüfung:	19. November 2021

*I've come to realize; With every little glimpse you fade
I was told that I could fly; When least expected
Cloud Connected*

– A. Fridén, In Flames, 2002

Abstract

Mixed-phase clouds, consisting of both supercooled liquid droplets and ice particles, play a major role in the life cycle of clouds and the radiative balance of the Earth. However, mixed-phase cloud processes are still rather poorly understood and represent a great source of uncertainty for climate predictions. The main reason for this is the insufficient understanding of the microphysical properties of mixed-phase cloud particles. The biggest challenge is the correct discrimination of droplets and ice particles. In this work, the Particle Habit Imaging and Polar Scattering (PHIPS) probe, an airborne in situ cloud instrument, is used to investigate the composition and microphysical properties of mixed-phase clouds. It combines optical microscopy with polar nephelometry to simultaneously measure the angular scattering behaviour while acquiring stereo-microscopic images of single cloud particles. Based on PHIPS data, a novel method to determine the phase of individual cloud particles based on their angular light scattering behaviour is presented. Comparisons with manually classified in situ data show that the algorithm is able to confidently discriminate spherical droplets and aspherical ice particles with a 98% accuracy. Furthermore, a sizing method based on single particle scattering data is presented. Combined, this allows the determination of phase discriminated particle size distributions in a size range of $50 \leq D \leq 700 \mu\text{m}$ and $20 \leq D \leq 700 \mu\text{m}$ for droplets and ice, respectively. This fills the gap between the commonly used forward scattering instruments and optical array probes. The PHIPS probe was deployed during three in situ aircraft field campaigns in the Southern Ocean, the Arctic and the US east coast. In over 250 flight hours, an extensive data set of single particle microphysical data over a wide range of ambient cloud conditions was acquired. Using the aforementioned newly developed methods, the phase composition of the sampled clouds is analysed and the difference between clouds in high latitudes of the northern and southern hemisphere is discussed. Furthermore, riming, the accretion of droplets by ice particles, is investigated based on manual classification of PHIPS' stereo-micrographs. Riming is observed on over 30% of the investigated ice particles in a size range from $20 \leq D \leq 700 \mu\text{m}$ in clouds between $-10^\circ\text{C} \leq T \leq 0^\circ\text{C}$. The meteorological conditions of riming are investigated and the correlation of ambient parameters with riming state and riming degree are discussed. It is shown that riming increases the light scattering in the angular range from $\theta = 42^\circ$ and 170° by up to 135% compared to unrimed particles. Further, particles with faceted, crystalline build-up which is aligned to the lattice structure of the underlying particle are described. For these particles, which are believed to be the result of vapor deposition during the ageing process of rimed particles, the term "epitaxial riming" is proposed.

Zusammenfassung

Mischphasenwolken bestehend aus unterkühlten Wassertröpfchen und Eispartikeln spielen eine bedeutende Rolle für den Lebenskreislauf von Wolken und beeinflussen das Strahlungsgleichgewicht der Erde. Die exakten Wolkenprozesse in Mischphasenwolken sind bisher noch recht schlecht verstanden und stellen so einen signifikanten Unsicherheitsfaktor für Klimavorhersagemodelle dar. Die größte Herausforderung ist dabei die korrekte Unterscheidung von Eispartikeln und Wassertröpfchen. In dieser Arbeit werden die Zusammensetzung und mikrophysikalischen Eigenschaften von Mischphasenwolken mithilfe des Particle Habit Imaging and Polar Scattering (PHIPS) Messgeräts untersucht. PHIPS ist ein flugzeuggetragenes Messinstrument welches optische Mikroskopie mit Polarnephelometrie verbindet und so gleichzeitig mikroskopische Stereo-Bildaufnahmen von individuellen Wolkenpartikeln aufnimmt und simultan deren Streueigenschaften misst. Basierend auf PHIPS Daten wird eine neu entwickelte Methode präsentiert, mit der die Phase von individuellen Wolkenpartikeln auf Basis ihrer Streueigenschaften bestimmt werden kann. Der Vergleich mit händisch klassifizierten in situ Daten zeigt, dass der Algorithmus in der Lage ist, verlässlich sphärische Tröpfchen und aspherische Eispartikel zu unterscheiden. Die Diskriminierungsgenauigkeit übersteigt 98%. Weiterhin wird eine Methode vorgestellt, mit welcher die Größe von diesen individuellen Partikeln basierend auf der Intensität des gestreuten Lichts bestimmt werden kann. Kombiniert können damit phasendiskriminierte Größenverteilungen von Tröpfchen und Eispartikeln im Größenbereich $50 \leq D \leq 700 \mu\text{m}$ und $20 \leq D \leq 700 \mu\text{m}$ errechnet werden. Das füllt die Lücke zwischen den gemeinhin genutzten Messinstrumenten welche die Vorwärtstreueigenschaften von Wolkenpartikeln messen oder deren Schattenbilder detektieren. PHIPS wurde bei drei in situ Flugzeugmesskampagnen über dem Südlichen Ozean, der Arktis und der Ostküste der USA eingesetzt. In über 250 Flugstunden wurde ein ausgiebiger Datensatz von individuellen Wolkenpartikeln mit verschiedenen mikrophysikalischen Eigenschaften in unterschiedlichen meteorologischen Umgebungsbedingungen aufgenommen. Mithilfe der vorgestellten neuen Methoden wurden damit die Phasenzusammensetzung der gebroten Wolken untersucht und die Unterschiede zwischen Mischphasenwolken in der nördlichen und südlichen Hemisphäre diskutiert. Weiterhin wurde das Bereifen von Eispartikeln durch kleine Wassertröpfchen untersucht. Basierend auf den von PHIPS aufgenommenen Stereomikrographen wurden die aufgenommenen Partikel bezüglich ihres Bereifungsgrads klassifiziert. Im Temperaturbereich zwischen $10^\circ\text{C} \leq T \leq 0^\circ\text{C}$ weisen über 30% aller untersuchten Eispartikel Anzeichen von Bereifung auf. Die meteorologischen Umgebungsbedingungen von Bereifung werden in dieser Arbeit untersucht und die Korrelation von Bereifungsgrad mit verschiedenen Parametern werden diskutiert. Es wird gezeigt, dass die Lichtstreuung im Winkelbereich von $\theta = 42^\circ$ bis 170° von bereiften Eispartikeln im Vergleich zu unbereiften Partikeln um bis zu 135% verstärkt ist. Außerdem werden Partikel beschrieben, welche kristalline Aufbauten mit klar definierten Kanten aufweisen, die parallel zu der Kristallstruktur des zugrundeliegenden Partikels ausgerichtet sind. Für dieses Phänomen, das durch das Altern von bereiften Partikeln entsteht, wird der Terminus "epitaxiale Bereifung" vorgeschlagen.

Erklärung zur Selbstständigkeit

Ich versichere, dass ich diese Arbeit selbstständig verfasst habe und keine anderen als die angegebenen Quellen und Hilfsmittel benutzt habe, die wörtlich oder inhaltlich übernommenen Stellen als solche kenntlich gemacht und die Satzung des KIT zur Sicherung guter wissenschaftlicher Praxis in der aktuellen Fassung beachtet habe.

Karlsruhe, den 15.09.2021, _____
Fritz Waitz

Contents

Abstract	v
Zusammenfassung	vii
Ehrenwörtliche Erklärung	xi
1. Introduction	1
1.1. Motivation	1
1.2. Outline of this Thesis	2
2. Theoretical Background	5
2.1. Water and Ice in Nature	5
2.1.1. Hydrological Cycle	5
2.1.2. Chemical and Physical Properties of Water and Ice	6
2.2. Optical Properties of Droplets and Ice Particles	8
2.2.1. Light as an Electro-Magnetic Wave	9
2.2.2. Refraction	12
2.2.3. Mie Theory for Spherical Particles	15
2.2.4. Scattering Phase Function	19
2.3. Life Cycle of Mixed-Phase Cloud Particles	22
2.3.1. Definition Mixed-Phase Clouds	22
2.3.2. Implications for the Climate	23
2.3.3. Particle Formation	25
2.3.4. Growth of Ice Particles and Wegener-Bergeron-Findeisen Process	28
2.4. Microphysical Properties of MPC Ice Particles	28
2.4.1. Ice Particle Habit	28
2.4.2. Crystal Complexity	30
2.4.3. Riming	32
2.5. In situ Measurement of Cloud Particles	33
2.5.1. Particle Sizing	33
2.5.2. Phase Discrimination	34
2.5.3. Particle Size Distributions	36
2.5.4. Condensed Water Content	36
2.5.5. In situ Aircraft Cloud-Particle Measurement Instruments	37
3. Experimental Setup	41
3.1. The Particle Habit Imaging and Polar Scattering Probe (PHIPS)	41
3.1.1. Scattering Measurement	43
3.1.2. Image Acquisition	45
3.1.3. Trigger Sensor and Sensitive Area	47
3.2. Image Processing	48
3.2.1. Image Analysis	48
3.2.2. Image Post-processing	50

3.2.3.	Manual Habit Classification	53
3.2.4.	Manual Riming Classification	54
3.3.	Field Campaigns	55
3.3.1.	ACLOUD	56
3.3.2.	SOCRATES	57
3.3.3.	IMPACTS	58
3.3.4.	Overview of the Experimental Data Set	59
4.	Phase Discrimination of Individual Cloud Particles based on their Angular Scattering	63
4.1.	Discrimination Features	64
4.1.1.	f_1 : Comparison with Mie Scattering	64
4.1.2.	$f_2 + f_3$: Down and Up-Slope	66
4.1.3.	f_4 : Ratio around the 90° Minimum	66
4.1.4.	Unused Discrimination Features	67
4.2.	Simulation of the Feature Parameters	68
4.3.	Calibration	69
4.3.1.	Determination of the Optimum Weight	71
4.4.	Discrimination Accuracy	72
4.4.1.	Cross-correlation of the Feature Parameters	72
4.4.2.	Validation of the Discrimination Algorithm	73
4.5.	Special Cases, Limitations and Misclassified Particles	74
4.6.	Machine Learning	76
4.7.	Summary	78
5.	Derivation of Particle Size Distributions based on Single Particle Polar Nephelometer Data	79
5.1.	Particle Sizing based on Angular Scattering Function	79
5.2.	Identification of Shattering Artefacts	81
5.2.1.	Interarrival Time Analysis	82
5.2.2.	Shattering Flag based on the Presence of Large Particles	83
5.3.	Statistical Significance of Particle Size Distributions	84
5.4.	Case Studies: Verification of Phase Discrimination and Particle Sizing Methods	85
5.4.1.	Case Study 1 — Pure Liquid Cloud	85
5.4.2.	Case Study 2 — Heterogeneous Mixed-Phase Cloud	86
5.4.3.	Case Study 3 — Ice dominated Mixed-Phase Cloud	87
5.5.	Summary	88
6.	Phase Composition of MPC in High Latitudes	91
6.1.	Approach and Experimental Data-Basis	91
6.1.1.	Cloud Probe Data during SOCRATES	92
6.1.2.	Cloud Probe Data during ACLOUD	92
6.2.	Temperature Dependency of the Cloud Phase Composition	94
6.3.	Discussion	95
6.3.1.	Comparison with Previous Studies	95
6.3.2.	Sensitivity Analysis: Impact of PHIPS Measurements	98
6.3.3.	Concentration-based Phase-Composition Coefficient	99
6.4.	Summary	99
7.	Observations of Riming in High Latitude Mixed-Phase Clouds	101
7.1.	Statistical Analysis and Correlation with Ambient Conditions	101
7.2.	Riming Degree	104

7.3. Epitaxial Rimming	105
7.3.1. Case Study — Epitaxial Rimming on Columns	107
7.4. Angular Light Scattering of Rimed Particles	109
7.5. Summary	111
8. Conclusion	113
8.1. Summary	113
8.2. Outlook	115
A. Appendix	117
A.1. Crosstalk	117
A.2. Averaging the Background Intensity of an Empty Image	117
A.3. Proof Sigmoid function	118
A.4. Fit Parameters Phase Discrimination Algorithm	119
A.5. Correlation Histograms Rimming	120
List of Figures	130
List of Tables	131
Publications	133
Bibliography	135
Acknowledgements	151

1. Introduction

1.1. Motivation

Climate change and global warming are some of the biggest problems of the 21st century. In recent years, people all over the world have suffered from the increasing frequency of extreme weather events which are just one of many repercussions of climate change [Stott, 2016]. In the first half of the year 2021 alone, hundreds of people died and thousands lost their homes due to wildfires (Greece, Italy, Russia, Africa, USA, Australia), floods (Germany, Britain, Belgium, China), cyclones (Indonesia, Fiji) and heavy snow fall (Spain, US) [NOAA, 2021]. Just recently, the Sixth Assessment Report of The Intergovernmental Panel on Climate Change (IPCC) has alerted that increase of Earth's global mean temperature will reach +1.5 °C compared to pre-industrial levels already sooner than expected before the year 2030 [IPCC, 2021].

As clouds are a key factor in Earth's hydrological cycle and radiative budget, they play a vital role not only towards our everyday life, whether we should bring wellington boots or sun screen for a walk in the park, but are also elementary for understanding climate change and its implications. Hence, accurate implementation of clouds into climate prediction and radiative transfer models is crucial.

In clouds, water can exist in all three aggregate states — as liquid droplets, solid ice crystals as well as gaseous vapor. This results in three main types of clouds: single phase ice and liquid clouds as well as mixed-phase clouds that consist of a mixture of droplets and ice particles at the same time. To estimate properties such as lifetime and radiative effects of clouds, it is necessary to know the phase composition of clouds as well as the microphysical properties of the cloud particles.

Mixed-phase clouds occur all over the world in various meteorological conditions. They represent one of the major uncertainties towards models and more experimental data are needed to improve our knowledge of mixed-phase cloud processes. One important way to derive the properties of cloud particles are in situ measurements using airborne cloud probes that date back to 1940's when the first mixed-phase cloud observations were made and found that droplets and ice particles coexist at cloud temperatures as low as -40 °C [Peppler, 1940; Findeisen, 1942]. Whereas in recent years, much progress has been made in terms of measuring total cloud water content as well as the size of cloud hydrometeors, the determination of the phase of cloud particles is still afflicted with high uncertainties.

Due to the *Wegener-Bergeron-Findeisen* process, ice particles in a mixed-phase cloud grow on the expense of evaporating droplets. Thus, mixed-phase clouds typically consist of many small droplets and a few ice particles. Therefore, it is crucial that those few ice particles are correctly detected and discriminated from liquid droplets.

Currently, phase discrimination of cloud hydrometeors is mainly based on either sphericity analysis of captured images of individual cloud particles acquired when passing through a

cloud or via remote sensing methods such as radar and lidar measurements. However, the limited optical resolution of the shadow imagers leads to uncertainties in discrimination accuracy for small, quasi spherical particles, especially for "fogged" or out of focus images. Remote sensing methods have the disadvantage that the coarse spatial resolution cannot resolve small pockets of e.g. ice in a mixed-phase cloud. Further, small concentrations of ice particles cannot be resolved in dense liquid clouds where the radar reflectivity is saturated.

Additionally, surface complexity features such as riming, the accretion of droplets on ice particles, significantly affect the microphysical properties of cloud particles. Such small scale phenomena cannot be resolved in detail by the limited optical resolution of shadow imagers or remote sensing methods and are thus not well studied and often overlooked in climate models.

Motivated by these challenges, the following three key questions are investigated in this work:

1. How can we accurately discriminate water and ice in clouds?
2. What is the relative occurrence of droplets and ice particles in high latitude (mixed-phase) clouds?
3. Under which conditions can we observe riming?

In this work, a new method is presented to discriminate the phase of individual cloud particles based on the shape of their angular light scattering behaviour measured by the **Particle Habit Imaging and Polar Scattering (PHIPS)** probe. PHIPS is an airborne in situ wing-mounted cloud probe that simultaneously measures the angular scattering function and acquires high-resolution stereo-microscopic images of individual cloud particles. Based on the amplitude of the light scattering, the size of the droplets and ice particles can be determined. Furthermore, with the microscopic images it is possible to resolve small-scale surface complexity features such as riming.

During three aircraft field campaigns, an extensive data set of individual cloud particles during more than 250 flight hours in various cloud conditions has been acquired. Due to the variability of the meteorological conditions and sampled particles, the data gathered during these three campaigns provide a representative data set for a comprehensive characterization of the microphysical properties of mixed-phase clouds.

Using the methods presented in this work, the PHIPS probe can be used to determine phase discriminated particle size distributions in mixed-phase clouds and thus bridge the gap between forward scattering probes and particle imagers in the size range between $50 < D < 200 \mu\text{m}$ where reliable phase discriminated measurements are scarce. This work will improve the in situ measurement capabilities of the phase and size of cloud particles as well as the understanding of riming and will hence contribute to the improvement of the representation of mixed-phase clouds in climate models.

1.2. Outline of this Thesis

This thesis is structured as follows:

Chapter 2 gives an overview of the theoretical background and previous works. In Section 2.1, the role of water and ice in the natural hydrological cycle is discussed and an overview of its chemical and physical properties are given. Section 2.2 explains the basics of light scattering and derives the angular scattering properties of spherical particles using Mie theory. Section 2.3 gives an introduction to the formation mixed-phase cloud

particles. Their microphysical properties are discussed in Section 2.4. Lastly, in Section 2.5, an overview of in situ measurements of cloud particles is given and state of the art airborne in situ probes are introduced.

Next, the methods used in this work are discussed. In Chapter 3, the experimental setup which was used to collect the in situ data used in this work is explained. In Section 3.1, the PHIPS probe is introduced and its setup and working principle are explained. Section 3.2 gives an overview of all the pre-existing tools and methods used to analyze and process the acquired PHIPS data. In Section 3.3, the three field campaigns during which the data were acquired are introduced: ACLOUD in the Arctic, SOCRATES in the Southern Ocean and IMPACTS over the US east coast.

Chapter 4 presents a new method to determine the phase of individual cloud hydrometeors based on the difference of distinct features in the angular scattering function of spherical and aspherical particles. The algorithm is calibrated and validated using the data set gathered during the in situ aircraft campaigns.

Chapter 5 describes the sizing of individual droplets and ice particles based on their measured angular scattering function. Combined with the phase discrimination algorithm, phase-discriminated particle size distributions are derived and compared to the results of other probes in three case studies.

The derived particle size distributions, are then used in Chapter 6 to investigate the phase composition of clouds sampled during SOCRATES and ACLOUD. The temperature dependency of the cloud phase compositions is discussed and compared to the results of previous studies and a comparison between the conditions in the Southern Ocean and the Arctic is given.

Further, in Chapter 7, the occurrence and properties of rimed particles during the three field campaigns are investigated. Section 7.3 discusses observations of ice particles carrying small, faceted rime which are oriented with respect to the crystalline axis of the host particle. This is called epitaxial riming. Next, in Section 7.4, the implication of riming on the angular scattering properties of ice particles will be discussed.

Finally, Chapter 8 concludes this thesis with a summary and discussion of the results put forward in the previous chapters and gives an outlook of the implications for future works.

2. Theoretical Background

2.1. Water and Ice in Nature

Water (H_2O) is widely regarded as the *element of life*. It is omnipresent in our everyday life and has many unique and remarkable properties. Behind molecular hydrogen (H_2) and carbon monoxide (CO), it is the third most prevalent molecule in the universe [Weingärtner et al., 2016]. It is the only chemical compound that commonly exists naturally on Earth in all three physical states: gaseous vapor, liquid water and solid ice [Reece et al., 2011].

In this section, the hydrological “life” cycle of a water “particle” is sketched, the role of water in clouds on Earth’s climate is explained and the most basic chemical and physical properties of water are discussed.

2.1.1. Hydrological Cycle

On Earth, water is most commonly found in the liquid phase. Most of it (97.4% of the total mass) is located in the oceans, which cover 71% of Earth’s surface [Weingärtner et al., 2016]. About 2.0% corresponds to ice of glaciers and the polar ice caps, covering about 8.3% of Earth’s surface [Davies, 2020]. Most of the remaining 0.6% are bound in soil moisture, groundwater, lakes and rivers. Only about $10^{-3}\%$ of the water is found in the atmosphere. For example, at room temperature ($T = 20\text{ }^\circ\text{C}$) and standard atmospheric pressure ($p_0 = 1,013.25\text{ hPa}$) the absolute humidity in the air amounts to approximately 18.3 g/m^3 , assuming a relative humidity of $\text{RH} = 100\%$ [Michell Instruments Ltd., 2015]. Nevertheless, water in the atmosphere, especially in the form of clouds, has a huge impact on our everyday life. Fig. 2.1 shows the hydrological cycle of a water molecule. Due to the radiation of the sun, the Earth’s surface heats up, causing water in lakes, oceans and water bound in soil or plants to evaporate (1). Since warm and wet air parcels have a lower density compared to their cold and dry surrounding¹, they rise up and take the water vapor higher into the atmosphere (2). When the air cools down again, the water vapor condenses or re-sublimates and forms a cloud (3, see also Section 2.3.3). There, the cloud particles² evaporate or grow (see Section 2.3.4) until they are too heavy and precipitate to the ground (4), where the cycle begins anew.

During this cycle the water changes its aggregate state (potentially repeatedly) between gaseous, liquid and solid phase. The (extraordinary) chemical and physical properties

¹Water (vapor) has a lower molar mass ($M = 18.01\frac{\text{g}}{\text{mol}}$) compared to dry air ($M = 28.96\frac{\text{g}}{\text{mol}}$) that consists of 78% molecular nitrogen (N_2 , $M = 28.01\frac{\text{g}}{\text{mol}}$) and 21% molecular oxygen (O_2 , $M = 32.00\frac{\text{g}}{\text{mol}}$) [Holleman and Wiberg, 2007].

²Note that clouds do not consist exclusively of water, but can contain a wide variety of different particulate matter such as organic and inorganic aerosols (see Section 2.3.3). However, the focus of this work lies on the description of atmospheric droplets and ice particles. Hence, over the course of this thesis, the term *cloud particle* is used synonymously with *hydrometeor* to describe atmospheric droplets and ice particles.

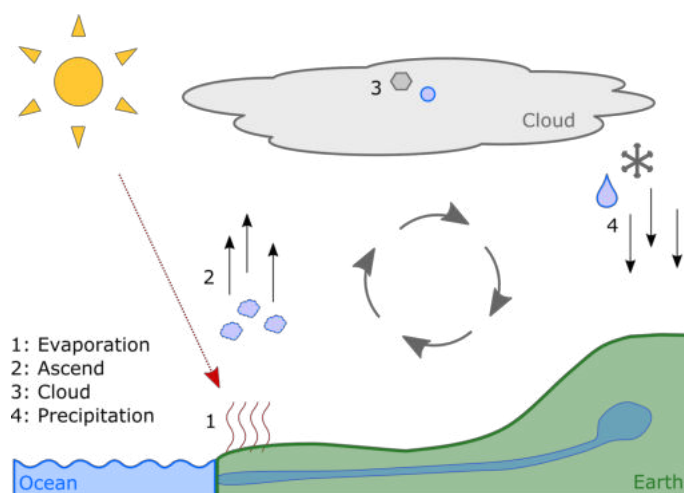


Figure 2.1.: Hydrological cycle of water in the atmosphere: Heated up by the sun (1) water evaporates and ascends (2). When it reaches colder altitudes, clouds form (3) where cloud particles grow until they precipitate back down (4).

of water in its three aggregate states will be outlined in the following. For the sake of readability, gaseous water will from now on be referred to as *vapor* and solid water as *ice*. Unless explicitly stated otherwise, the term *water*, refers to its liquid phase. Further, only one crystalline form of ice is considered (I_h , see below). Thus, in the scope of this work, “phase” is used synonymous with “aggregate state”.

2.1.2. Chemical and Physical Properties of Water and Ice

Water is the molecule with the most commonly recognized molecular formula: H_2O . Water

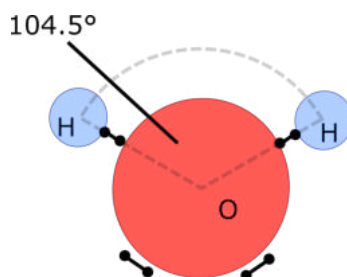


Figure 2.2.: Schematic view of a water molecule consisting of one oxygen atom ($^{16}_8\text{O}$, red) and two hydrogen atoms (^1_1H , blue). The black dots indicate the bound electrons. The binding angle between the two hydrogen atoms is 104.5° [Holleman and Wiberg, 2007].

is the product of many oxidation reactions³, for example the burning in air of hydrogen



or various carbohydrates (e.g. wood, oil, methane, ...)



The features of water are highly influenced by the intermolecular interactions between water molecules. Due to its polarity, a water molecule in the liquid or solid state is able to

³So far, it is not yet completely understood where the huge amount of water on the Earth originated. Isotope studies suggest that most of the water did not form on Earth but is the result of the impact of a huge cryometeor that impacted on Earth billions of years ago [Morbidelli et al., 2000].

form up to four hydrogen bonds between each hydrogen atom and the oxygen atom of another, neighboring molecule (see dashed lines in Fig. 2.3). Hydrogen bonds are ten times stronger than normal intermolecular *Van-der-Waals* forces [Holleman and Wiberg, 2007]. This has many implications such as the relatively high heat capacity (see Table 2.1) and boiling point at $T_{\text{boil}} = 100 \text{ }^\circ\text{C}$ (due to the high energy needed to break up the H-bonds) as well as the *density anomaly* that will be discussed in the following.

Table 2.1.: Physical properties of water in different states at standard ambient conditions ($p_0 = 1,013.25 \text{ hPa}$ and $T = 0 \text{ }^\circ\text{C}$) [Feistel and Wagner, 2006; Hale and Querry, 1973; Warren and Brandt, 2008].

	Density ρ [$\frac{\text{g}}{\text{cm}^3}$]	Refr. Index $n_{532 \text{ nm}}$	Heat Capacity c_P [$\frac{\text{J}}{\text{gK}}$]
Gaseous Vapor	0.001	1.00	2.00
Liquid Water	1.000	$1.3337 + i 1.50 \cdot 10^{-9}$	4.20
Solid (hex.) Ice	0.917	$1.3116 + i 1.49 \cdot 10^{-9}$	2.10

2.1.2.1. Phase Transitions

The phase transition points, i.e. boiling ($T_{\text{boil}} = 100 \text{ }^\circ\text{C}$, assuming standard atmospheric pressure $p_0 = 1,013.25 \text{ hPa}$) and freezing temperature ($T_{\text{freeze}} = 0 \text{ }^\circ\text{C}$) of water define the cornerstones of the Celsius temperature scale. It is important to note that phase transitions are stochastic processes. Above $100 \text{ }^\circ\text{C}$, all water is evaporated. Below that, the percentage of evaporated water depends on the temperature and *vapor pressure*. This ratio is calculated via the *Clausius–Clapeyron* equation. This is also true for the phase transition in the opposite direction: water *can* start to freeze at $0 \text{ }^\circ\text{C}$, but that does not mean that necessarily all water is frozen below $0 \text{ }^\circ\text{C}$ because any liquid needs crystallization energy to undergo the phase shift to solid. In nature the needed crystallization energy can be reduced by impurities in the water that serve as nucleation centers. In the atmosphere, in the absence of aerosols that could serve as ice nucleating particles (INP), water exists as *supercooled liquid water* over a broad temperature range. At temperatures around below $-38 \text{ }^\circ\text{C}$ all supercooled water freezes homogeneously. This will be explained in detail in Section 2.3.3.

2.1.2.2. Density Anomaly

Most materials get more dense when they cool down as a result of the reduced *Brownian motion*. When they freeze, the density is increased further since the molecules are more densely packed when embedded in a crystal lattice. Water is one of the few materials that show a *negative thermal expansion* (density anomaly) [Yasutomi, 2015]. Water reaches its maximum density at $T = 4 \text{ }^\circ\text{C}$, both above and below that, the density decreases. The expansion during the freezing process is caused by the hydrogen bonds that increase the distance between molecules. This effect is much stronger in the solid state compared to the liquid phase where the molecules can wiggle around more freely. Thus, the density of ice is about 10% lower compared to water (see Table 2.1) and hence, for example, icebergs float on the ocean.

2.1.2.3. Crystal Structure

Ice occurs naturally on earth as hexagonal crystals. Other crystal structures of ice (e.g. cubic ice, I_c [König, 1943]) are possible in theory, but occur only under extreme conditions such as very high pressure or very cold temperatures. Because they transform into hexagonal ice I_h at temperatures above -33° [Murray, 2008] they are very rare in nature and hence will not be discussed in the scope of this work.

The lattice structure (I_h) is shown in Fig. 2.3 [Bjerrum, 1952]. The oxygen atom (red) of each molecule is connected (coordinated) to four neighboring water molecules via the aforementioned H-bonds (dashed lines) to the hydrogen atoms (blue). This way, the elementary cell of the ice particle (solid black lines, center marked with an “x”) is a tetrahedron. The angle between the edges of a tetrahedron, i.e. the H-bonds, is 109.5° . This is very close to the angle between the hydrogen atoms of the elementary water molecule (104.5° [Holleman and Wiberg, 2007], see Fig. 2.2). This makes the hexagonal crystal structure of ice naturally very stable and gives it a relatively large hardness (6 on *Moh’s scale* at $T = -50^\circ\text{C}$), which is even higher than that of iron (4.5 on *Moh’s scale*) [Teichert, 1939].

Due to the hexagonal crystal structure, the basic shape of an atmospheric ice particle is a hexagonal column or plate. However, within the hexagonally symmetric crystal structure, the morphology of atmospheric ice particles still differs significantly. The formation of different habits based on the ambient conditions is discussed in Section 2.4.1.

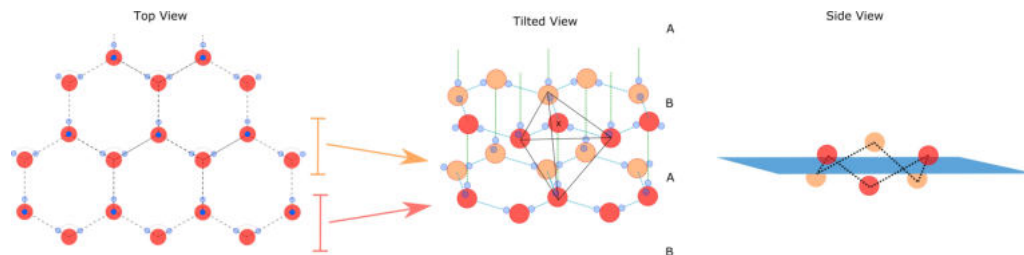


Figure 2.3.: Schematic representation of the molecular structure of hexagonal ice in top view (left), tilted view (middle) and from the side (right). Oxygen atoms are indicated by red circles, hydrogen atoms by blue circles. Hydrogen bonds between each molecule are shown with the dashed lines. The elementary, tetrahedral cell of the crystal around one molecule (marked by the “x”) is drawn in black.

2.2. Optical Properties of Droplets and Ice Particles

The optical properties of particulate matter are defined by shape, size, morphological complexity and refractive index. In the frequency of visible light, ice has only a slightly higher refractive index compared to liquid water ($n_{\text{liq}} = 1.3337$ and $n_{\text{ice}} = 1.3116$ for $\lambda = 532\text{ nm}$, see Table 2.1). For cloud particles the absorption (imaginary part) is negligible compared to the scattering (real part) in the visible wavelength. The refractive indices over the whole spectrum of water and ice are shown in Fig. 2.4.

However, despite the similar refractive index, the optical properties of droplets and ice particles differ significantly since droplets are spherical, whereas ice particles form as faceted, hexagonal crystals. For example, on a rainy day, light scattering on droplets produces a rainbow (see Section 2.2.2.1), whereas pristine hexagonal ice particles produce a halo around the sun (see Section 2.2.2.2).

The scattering of light on atmospheric cloud particles plays a vital role towards Earth’s energy budget (see Section 2.3.2). Further, a wide range of different in situ cloud sampling probes are based on light scattering measurements of cloud particles (see Section 2.5). Later in this work, the different scattering features of spherical (droplets) and aspherical (ice) particles will be utilized to develop the phase discrimination algorithm (see Chapter 4).

In this section, the theoretical physical background behind the interaction of light and matter will be explained. First, light as an electromagnetic wave is introduced and its behaviour in vacuum and a medium is described. Based on that, refraction, i.e. the interaction of a light beam on the edge from one medium to another, is discussed. However,

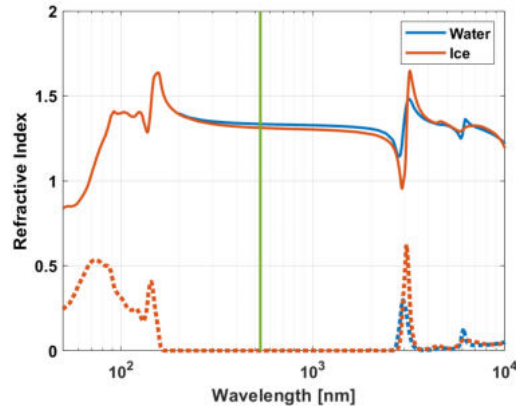


Figure 2.4.: Refractive index of water (blue) and ice (red) based on the parameterization of Hale and Querry [1973] and Warren and Brandt [2008], respectively. The solid line correspond to the real part, the dashed to the imaginary part. The green line marks $\lambda = 532$ nm.

because the size of cloud particles is in a similar order of magnitude compared to the wavelength of visible light, a complex numerical tool (i.e. Mie theory) is needed to calculate the scattering of spherical particles. Lastly, the explained theories are used to calculate theoretical scattering phase functions, i.e. how much light is scattered in which angular direction, for spherical and aspherical (cloud) particles. The introduction to light scattering and Mie theory is also published verbatim in [Waitz, 2017].

2.2.1. Light as an Electro-Magnetic Wave

Light can be understood as an electromagnetic wave propagating through time and space with the velocity $c_0 \approx 2.99792 \cdot 10^8$ m/s (in vacuum). Therefore, in order to understand the interaction of light and matter, the theoretical behaviour of electromagnetic waves must be understood first.

In 1864 James Clerk Maxwell published a set of equations that describe how electromagnetic fields are generated by charges and currents [Maxwell, 1865]. In the following section, Maxwell's equations both in vacuum and a homogeneous dielectric medium will be discussed.

2.2.1.1. Maxwell Equations in Vacuum

In vacuum, the behaviour of electromagnetic waves is described by the four Maxwell equations

$$\begin{aligned} \vec{\nabla} \cdot \vec{E} &= \frac{\rho}{\epsilon_0}, & \vec{\nabla} \cdot \vec{B} &= 0, \\ \vec{\nabla} \times \vec{E} &= -\frac{\partial \vec{B}}{\partial t}, & \vec{\nabla} \times \vec{B} &= \mu_0 \vec{j} + \mu_0 \epsilon_0 \frac{\partial \vec{E}}{\partial t}, \end{aligned}$$

with the electric field \vec{E} , the magnetic flux density \vec{B} , the charge density ρ and the electric current density \vec{j} . The two constants, $\mu_0 := 4\pi \times 10^{-7} \frac{\text{Vs}}{\text{Am}}$ (vacuum permeability) and $\epsilon_0 := \frac{1}{\mu_0 c^2}$ (vacuum permittivity), are required to match the units of \vec{E} and \vec{B} . In general, all quantities are space- and time-dependent. That means e.g. $\vec{E} = \vec{E}(\vec{r}, t)$ unless stated explicitly otherwise, but for the sake of brevity and readability, the arguments \vec{r} and t are omitted.

In the absence of any charges or currents Maxwell's equations simplify to

$$\begin{aligned}\vec{\nabla} \cdot \vec{E} &= 0, & \vec{\nabla} \cdot \vec{B} &= 0, \\ \vec{\nabla} \times \vec{E} &= -\frac{\partial \vec{B}}{\partial t}, & \vec{\nabla} \times \vec{B} &= \frac{1}{c^2} \frac{\partial \vec{E}}{\partial t}.\end{aligned}$$

Using vector algebra this system of coupled differential equations can now be decoupled and solved.

Curling the third and time-differentiating the fourth of Maxwell's equations yields

$$\vec{\nabla} \times (\vec{\nabla} \times \vec{E}) = -\vec{\nabla} \times \frac{\partial \vec{B}}{\partial t}, \quad (2.3)$$

$$\vec{\nabla} \times \frac{\partial \vec{B}}{\partial t} = \frac{1}{c^2} \frac{\partial^2 \vec{E}}{\partial t^2}. \quad (2.4)$$

Using the following vector identity and the first Maxwell equation,

$$\vec{\nabla} \times (\vec{\nabla} \times \vec{E}) = \underbrace{\vec{\nabla}(\vec{\nabla} \cdot \vec{E})}_{=0} - (\vec{\nabla} \cdot \vec{\nabla})\vec{E}, \quad (2.5)$$

and inserting the equations above into each other decouples the differential equation leading to the wave equation

$$\vec{\nabla}^2 \vec{E} + \frac{1}{c^2} \frac{\partial^2 \vec{E}}{\partial t^2} = 0, \quad (2.6)$$

which is solved by a plane wave

$$\vec{E}(\vec{r}, t) = E_0 e^{i(\vec{k} \cdot \vec{r} - \omega t)} \quad (2.7)$$

with the wavevector \vec{k} and the angular frequency $\omega = 2\pi f$. In isotropic media, the wave can propagate equally in every direction, so that $\vec{k} = k \vec{e}$, with the wavenumber $k = |\vec{k}| = \frac{2\pi}{\lambda}$ and the unity vector \vec{e} . Wavenumber and angular frequency are connected by the dispersion relation,

$$\vec{k}^2 = \frac{\omega^2}{c^2}. \quad (2.8)$$

This solution corresponds to an infinitely propagating light beam travelling with the speed of light c and intensity

$$I(\vec{r}, t) = I_0 = |\vec{E}|^2 = E_0^2. \quad (2.9)$$

2.2.1.2. Macroscopic Maxwell Equations in Medium

In the presence of matter some new effects have to be considered: all matter contains positively charged protons and negatively charged electrons. Light (i.e. electromagnetic waves) that travels through a medium polarizes said charged particles and this results in a new internal electric field, called the polarization, \vec{P} . Analogously, the \vec{B} -field results in a magnetization \vec{M} of the material. The Maxwell's equations change to

$$\vec{\nabla} \cdot \vec{D} = \rho, \quad \vec{\nabla} \cdot \vec{B} = 0, \quad (2.10)$$

$$\vec{\nabla} \times \vec{E} = -\frac{\partial \vec{B}}{\partial t}, \quad \vec{\nabla} \times \vec{H} = \vec{j} + \frac{\partial \vec{D}}{\partial t}, \quad (2.11)$$

with the electric flow density \vec{D} and magnetic field \vec{H} defined as

$$\vec{D} := \epsilon_0 \vec{E} + \vec{P}, \quad \vec{H} := \frac{1}{\mu_0} \vec{B} - \vec{M}. \quad (2.12)$$

Since the polarization \vec{P} is caused by the applied electrical field (the light), it can be expressed as a function of \vec{E} . Using Taylor expansion this yields

$$\frac{P_i}{\epsilon_0} = \sum_j \chi_{ij}^{(1)} E_j + \sum_{jk} \chi_{ijk}^{(2)} E_j E_k + \dots \quad (2.13)$$

with the (complex) susceptibility tensor $\chi(\vec{r}, t)$.

For most materials and small \vec{E} -fields, higher orders are small relative to $\chi^{(1)}$ and can be neglected in linear optics. In general, χ is a tensor and thus \vec{P} and \vec{E} are not necessarily parallel. However, for isotropic media χ is a scalar quantity and $\vec{P} \parallel \vec{E}$. Additionally, assuming constant and instant material response (for homogeneous media and negligible time-dependent effects like heating or memory effects), the polarization $\vec{P}(\vec{r}_0, t_0)$ (and hence \vec{D}) is only dependent on the electric field at the same place and time $\vec{E}(\vec{r}_0, t_0)$ and χ is a constant, only dependent on the frequency ω of the light wave and the properties of the medium.

Using this approximations, \vec{D} can be simplified to

$$\vec{D} = \epsilon_0 \epsilon \vec{E} \quad (2.14)$$

with the (complex) relative permittivity $\epsilon = \epsilon(\omega) = \epsilon' + i\epsilon'' = 1 + \chi$. The derivation above can be followed analogously for the effect caused by the \vec{B} -field, but since the materials considered in this work are not magnetic, the magnetization effect is negligible and $M = 0$ ($\mu = 1$, $\vec{H} = \frac{1}{\mu_0} \vec{B}$) is a feasible approximation and valid in most cases. Similar to the last section, the Maxwell equations and vector calculus lead to the wave equation in matter

$$\vec{\nabla}^2 \vec{E} + \frac{\epsilon}{c^2} \frac{\partial^2 \vec{E}}{\partial t^2} = 0 \quad (2.15)$$

with the similar solution

$$\vec{E}(\vec{r}, t) = E_0 e^{i(n \vec{k}_0 \cdot \vec{r} - \omega t)} \quad (2.16)$$

$$= E_0 \cdot \underbrace{e^{-n'' \vec{k}_0 \cdot \vec{r}}}_{\text{exponential damping}} \cdot \underbrace{e^{i(n' \vec{k}_0 \cdot \vec{r} - \omega t)}}_{\text{oscillating wave}}, \quad (2.17)$$

and dispersion relation

$$\vec{k}^2 = \vec{k}_0^2 n^2 = \frac{\omega^2}{c^2} n^2 = \frac{\omega^2}{c^2} \epsilon. \quad (2.18)$$

Again, the result is a plane wave, differing only in the additional factor ϵ or rather the refractive index n compared to the propagation of a wave in vacuum (k_0). The (complex) refractive index $n := n' + in''$ (sometimes defined as $n := n' - in''$) is connected to the permittivity $\epsilon = |n|^2$. These complex quantities, in first order approximation solely dependent on the light frequency ω , determine all important optical quantities of a medium. The imaginary part of ϵ corresponds to a phase shift between \vec{D} and \vec{E} .

Real and imaginary parts of permittivity and refractive index can be translated into each other according to:

$$\epsilon' = n'^2 - n''^2, \quad \epsilon'' = 2n'n'', \quad (2.19)$$

$$n' = \sqrt{\frac{\sqrt{\epsilon'^2 + \epsilon''^2} + \epsilon'}{2}}, \quad n'' = \sqrt{\frac{\sqrt{\epsilon'^2 + \epsilon''^2} - \epsilon'}{2}}. \quad (2.20)$$

The real part of the refracting index determines the dispersion of the light: The plane wave travels at reduced speed $v_{\text{phase}} = \frac{c}{\sqrt{n'}}$. The imaginary part results in extinction as the wave is losing energy as it propagates due to absorption.

2.2.2. Refraction

According to *Fermat's principle*, light travels along the path which takes the least time. When light travels, either through vacuum or a medium with refractive index n , this is simply a plane wave going forward in a straight line. But what happens at the boundary between two media?

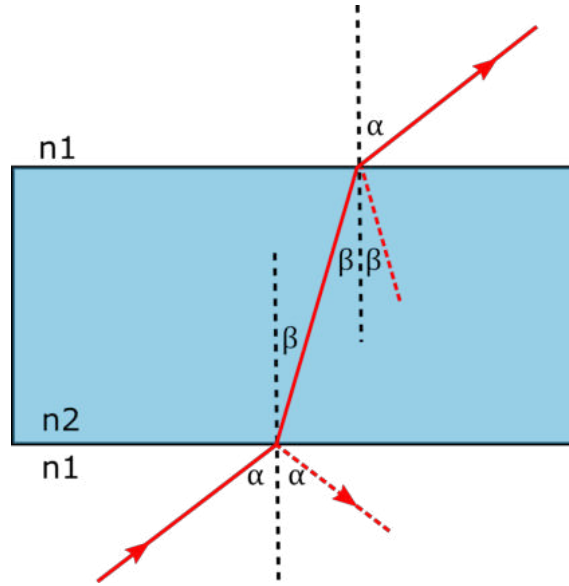


Figure 2.5.: Refraction of a light beam according to Snell's law.

Fig. 2.5 shows the refraction of an incident light beam that hits a medium with $n_2 > n_1$ under the angle α . The light is partly reflected (dashed red line) and transmitted (solid red line). The path of the light can be calculated using the boundary conditions that arise from the fact that Maxwell's equations must be valid on both sides. From Maxwell's second equation $\vec{\nabla} \cdot \vec{B} = 0$ (Eq. (2.10)) follows that the perpendicular component of the magnetic density, B^\perp , must be continuous. Combining that with $\vec{\nabla} \times \vec{E} = -\frac{\partial \vec{B}}{\partial t}$ (Eq. (2.11)) demands that the parallel component of the electric field, E^\parallel , must be continuous as well. This leads to

$$E_{\text{inc}}^\parallel + E_{\text{refl}}^\parallel = E_{\text{trans}}^\parallel \quad (2.21)$$

for the incident, reflected and transmitted light beam. Again, we assume a plane wave as from Eq. (2.7) as solution:

$$\vec{E}(\vec{r}, t) = E_0 e^{i(\vec{k} \cdot \vec{r} - \omega t)}. \quad (2.22)$$

Since the continuity must hold for all times, we can omit the temporal part and set $t = 0$. This also means that scattering is not directly dependent on the frequency (i.e. wavelength) of the light but only the wave vector and therefore the refractive index n . This results in

$$E_{0, \text{inc}} e^{i\vec{k}_{\text{inc}} \cdot \hat{x}} + E_{0, \text{refl}} e^{i\vec{k}_{\text{refl}} \cdot \hat{x}} = E_{0, \text{trans}} e^{i\vec{k}_{\text{trans}} \cdot \hat{x}} \quad (2.23)$$

where $\vec{r} = \hat{x}$ denotes the unity vector along the boundary surface.

Since the phases of the three waves are continuous, the exponents must be the same

$$\vec{k}_{\text{inc}} \cdot \hat{x} = \vec{k}_{\text{refl}} \cdot \hat{x} = \vec{k}_{\text{trans}} \cdot \hat{x} \quad (2.24)$$

and with $\vec{k} \cdot \hat{x} = |\vec{k}| \sin(\theta)$ and the dispersion relation $|\vec{k}| = n \frac{\omega}{c}$ we get

$$\underbrace{n_1 \frac{\omega}{c} \sin(\alpha)}_{\text{incident}} = - \underbrace{n_1 \frac{\omega}{c} \sin(-\alpha)}_{\text{reflected}} = \underbrace{n_2 \frac{\omega}{c} \sin(\beta)}_{\text{refracted}}, \quad (2.25)$$

where θ corresponds to the angle with respect to the boundary of the beams (α and β in Fig. 2.5). Since frequency and speed of light are constant as well, the exit angle of the reflected wave is the same as the incident. The angle of the transmitted light beam, β , is calculated via

$$n_1 \cdot \sin(\alpha) = n_2 \cdot \sin(\beta), \quad (2.26)$$

which is also known as *Snell's law*. The same process then works analogously backwards when the beam leaves the medium again (see Fig. 2.5).

2.2.2.1. Rainbow

Based on this, one common optical cloud phenomenon can be explained: the rainbow, shown in Fig. 2.6a. It is caused by the first order refraction of light in spherical droplets. Fig. 2.6b shows the schematic course of a light ray that is refracted once in a sphere: α is the entry angle with respect to the normal line (the perpendicular to the tangent), β is the angle of the beam inside the droplet.

α and β are related via Snell's law with the refraction indices $n_1 = 1$ in air and $n_2 = n_{\text{liq}}(\lambda)$. As shown in the schematic the entry (and exit) angle with respect to the horizontal calculates as

$$\gamma = 2\beta - \alpha \quad (2.27)$$

$$= 2 \arcsin\left(\frac{1}{n_{\text{liq}}} \sin(\beta)\right) - \alpha. \quad (2.28)$$

Fig. 2.6c shows the visualization of the dependence of γ and α . The greatest concentration of outgoing rays exists where the variation of the exit angle γ changes least with variation of the incident ray α , i.e.

$$\frac{d\gamma}{d\alpha} = 0 \quad (2.29)$$

which corresponds to the maximum in Fig. 2.6c. For $\lambda = 532 \text{ nm}$ and thus $n_{\text{liq}} = 1.3337$ this results in $\gamma = 21^\circ$. With respect to the incident ray ($\theta = 0^\circ$ corresponds to forward direction), the rainbow is seen at $\theta = 180^\circ - 2\gamma = 138^\circ$.

The typical color scheme of the rainbow is the result of the wavelength dependency of $n(\lambda)$ and hence the scattering angle: blue light (shorter wavelength) is scattered stronger compared to red light (longer wavelength). A weaker, secondary rainbow can be seen around $\theta = 128^\circ$ which calculates analogously for a light beam that is reflected twice inside the sphere. As the light is reflected twice, the color scheme is inverted.

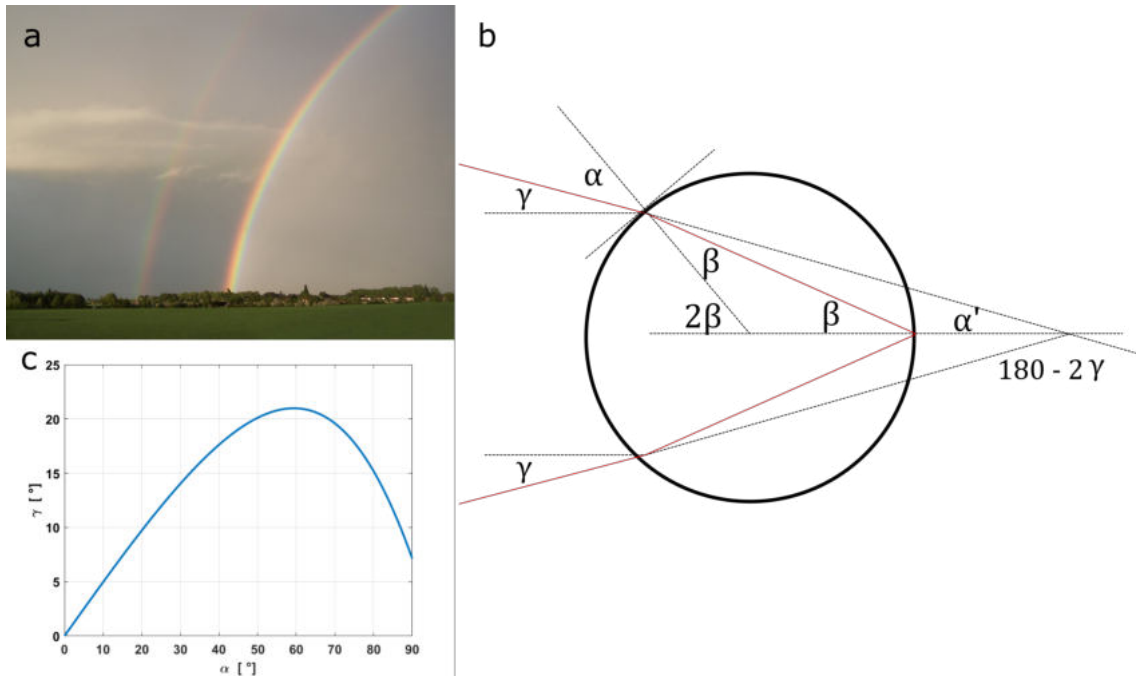


Figure 2.6.: Photography of a double rainbow around $\theta = 128^\circ$ and $\theta = 138^\circ$ (a) (photo credit: Elke Rohn), schematic view of the path of a light ray (red) in a spherical droplet (b) and the dependence of the exit angle γ of the entry angle with respect to the normal line α (c).

2.2.2.2. Halo

Another optical phenomenon is the *halo* for ice particles. When sunlight shines through a cloud which consists of randomly oriented, pristine, hexagonal ice particles, it can produce a bright ring around the sun at an angle of 22° . This phenomenon is caused by reflection of particles in a certain orientation. In order for the halo to be visible, depending on particle shape, at least 10% to 40% of the total scattering cross section needs to be contributed by pristine particles [Van Dienenhoven, 2014].

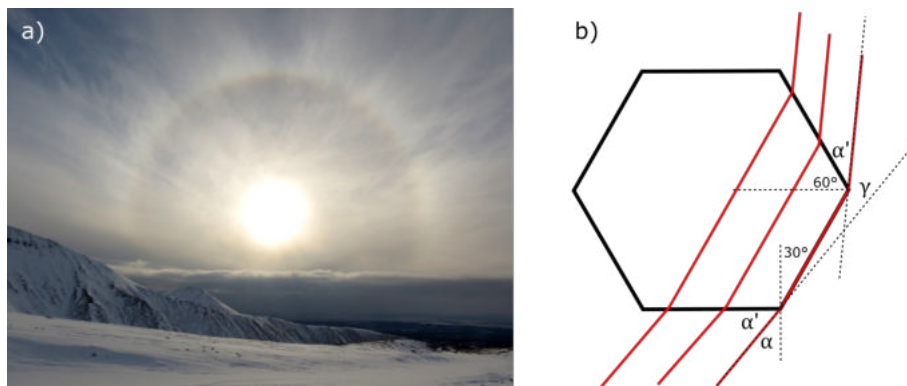


Figure 2.7.: 22° halo around the sun (a) (photo credit: Natalia Kollegova) caused by refraction of light on hexagonal ice particles as shown in the schematic view (b).

The edge case when all light is refracted horizontally and none is transmitted (i.e. the $\beta = 90^\circ$ in Fig. 2.5) is called *total internal reflection*. In case of the halo, sunlight gets reflected from hexagonal ice particle for the edge case of $\beta = 30^\circ$ in hexagonal particles that are oriented with respect to the sun as shown in Fig. 2.7. With $n_1 = n_{\text{air}} = 1.00$ and

$n_2 = n_{\text{ice}} = 1.3116$, this is the case for

$$\alpha' = 90 - \alpha = 90 - \arcsin\left(\frac{n_1}{n_2} \sin(\beta)\right) = 49.08^\circ \quad (2.30)$$

according to Snell's law. The theoretical angle at which the halo forms calculates as

$$\gamma = 180^\circ - 30^\circ - 2\alpha' = 21.84^\circ. \quad (2.31)$$

2.2.3. Mie Theory for Spherical Particles

So far, only the interaction of a single light ray with a straight edge was discussed. Now, consider a spherical particle of diameter D and refractive index $n = n' + in''$ scattering and absorbing light of wavelength λ . The task is to calculate the amount of scattered and absorbed light by said sphere. Even if the incident light beam was infinitely narrow, this problem would not be easy to solve, since parts of the light beam are scattered infinitely inside the particle and interfere with itself (see Fig. 2.8a).

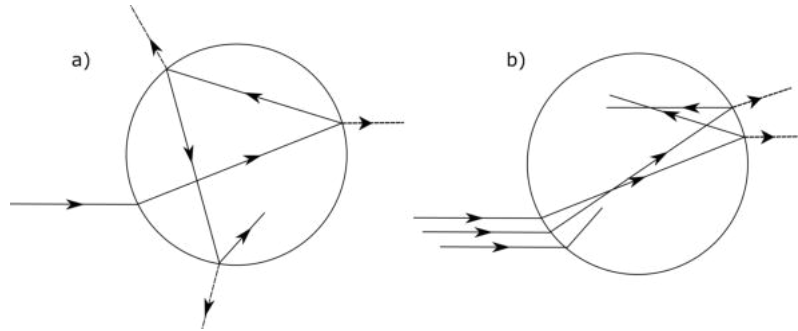


Figure 2.8.: Schematic view of multiple-scattering of a single light beam (a) and scattering of a broad light beam (b) in a spherical object.

A broad incident light beam, seen as the sum of multiple light beams, which hit the sphere under different surface angles, results in even (infinitely) more beams which interfere with each other (see Fig. 2.8b) and make this problem even harder to solve.

The exact solution for this problem was found by Gustav Mie in 1908 who solved the Maxwell's equations for the boundary value problem of a sphere. Today angular dependent scattering or absorption cross sections of spherical particles of known diameter and refractive index can be calculated numerically using scripts for e.g. Matlab or Fortran based on his calculations such as BHMIE [Bohren and Huffman, 1998]. The outline of the derivation of Mie scattering of a spherical particle will be sketched in the following. Note that 'Mie theory' is no actual theory in the physical sense but rather a term used to describe 'Mie scattering' and absorption.

2.2.3.1. Vector Spherical Harmonics

In Section 2.2.1, the Maxwell's equations were introduced and solved for light propagating through vacuum and an infinite medium. However, this time the problem is more complex: Light no longer just travels through a homogeneous medium but experiences reflections every time it interacts with the particle edge (see in Fig. 2.8).

First, to simplify the calculations, the vectorial functions \vec{E} and \vec{H} can be expressed by a scalar function $\psi(\vec{r})$: We assume a scalar function ψ (called generating function) satisfying the scalar wave equation

$$\vec{\nabla}^2\psi + k^2\psi = 0, \quad (2.32)$$

and the vector harmonics \vec{M} and \vec{N}

$$\vec{M} = \vec{\nabla} \times (\vec{r} \psi), \quad \vec{N} = \frac{\vec{\nabla} \times \vec{M}}{k}. \quad (2.33)$$

\vec{M} and \vec{N} are orthogonal, have zero divergence

$$\vec{\nabla} \cdot \vec{M} = 0, \quad \vec{\nabla} \cdot \vec{N} = 0 \quad (2.34)$$

and satisfy the wave equations

$$\vec{\nabla}^2 \vec{M} + k^2 \vec{M} = 0, \quad \vec{\nabla}^2 \vec{N} + k^2 \vec{N} = 0. \quad (2.35)$$

Therefore they fulfil all requirements of an electromagnetic field and \vec{E} and \vec{H} can be expressed by a linear combination of \vec{M} and \vec{N} . A solution for ψ yields the solution for \vec{E} and \vec{H} . Furthermore, since the particle is spherical, it is suitable to handle this problem in spherical coordinates: The scalar wave equation in spherical coordinates is

$$\frac{1}{r^2} \frac{\partial}{\partial r} \left(r^2 \frac{\partial \psi}{\partial r} \right) + \frac{1}{r^2 \sin \theta} \frac{\partial}{\partial \theta} \left(\sin \theta \frac{\partial \psi}{\partial \theta} \right) + \frac{1}{r^2 \sin^2 \theta} \frac{\partial^2 \psi}{\partial \phi^2} = 0. \quad (2.36)$$

Due to the spherical symmetry of the problem, the individual components r , θ and ϕ are independent of each other and $\psi(\vec{r})$ can be factorized as

$$\psi(r, \theta, \phi) = R(r) \Theta(\theta) \Phi(\phi). \quad (2.37)$$

Inserting this in Eq. (2.36) results in the three separated equations

$$\frac{d^2 \Phi}{d\phi^2} + m^2 \Phi = 0, \quad (2.38)$$

$$\frac{1}{\sin \theta} \frac{d}{d\theta} \left(\sin \theta \frac{d\Theta}{d\theta} \right) + \left[l(l+1) - \frac{m^2}{\sin^2 \theta} \right] \Theta = 0, \quad (2.39)$$

$$\frac{d}{dr} \left(r^2 \frac{dR}{dr} \right) + [k^2 r^2 - l(l+1)] R = 0, \quad (2.40)$$

with the separation constants m and l .

The first differential equation (Eq. (2.38)) is easily solved by the linearly independent (*even* and *odd*) solutions

$$\Phi_e(\phi) = \cos(m \phi), \quad \Phi_o(\phi) = \sin(m \phi). \quad (2.41)$$

The second equation (Eq. (2.39)) has the form of a “general Legendre equation” which can be solved by the associated Legendre polynomials

$$P_l^m(x) = \frac{(-1)^m}{2^l l!} (1-x^2)^{m/2} \frac{d^{l+m}}{dx^{l+m}} (x^2-1)^l \quad (2.42)$$

with $l = m, m+1, \dots$

The last equation (Eq. (2.40)) has the form of “Bessel’s differential equation” and is solved by the Bessel and Hankel functions

$$j_l(x) = \sqrt{\frac{\pi}{2x}} \sum_{m=0}^{\infty} \frac{(-1)^m}{m!(m+l+\frac{1}{2})!} \left(\frac{x}{2}\right)^{2m+l+\frac{1}{2}}, \quad (2.43)$$

$$y_l(x) = (-1)^{l+1} j_{-l}, \quad (2.44)$$

$$h_l^{(1)}(x) = j_l(x) + i y_l(x), \text{ and} \quad (2.45)$$

$$h_l^{(2)}(x) = j_l(x) - i y_l(x). \quad (2.46)$$

Finally, the scalar function ψ can be written as

$$\psi_{eml}^z = \cos(m\phi) P_l^m(\cos\theta) z_l(kr), \quad (2.47)$$

$$\psi_{oml}^z = \sin(m\phi) P_l^m(\cos\theta) z_l(kr), \quad (2.48)$$

where z_l is any of the four spherical Bessel functions.

Using the vector harmonics

$$\vec{M}_{e,o}^z = \vec{\nabla} \times (\vec{r} \psi_{e,o}^z), \quad \vec{N}_{e,o}^z = \frac{\vec{\nabla} \times \vec{M}_{e,o}^z}{k}, \quad (2.49)$$

\vec{E} can be expressed by an infinite series

$$\vec{E} = \sum_{m=0}^{\infty} \sum_{l=m}^{\infty} \alpha_{eml} \vec{M}_{eml}^z + \alpha_{oml} \vec{M}_{oml}^z + \beta_{eml} \vec{N}_{eml}^z + \beta_{oml} \vec{N}_{oml}^z. \quad (2.50)$$

So far we have only outlined the necessary equations, without considering physical implications. The next step is to narrow down this complex equation using physical considerations.

2.2.3.2. Fields of the Spherical Particle

As seen in Fig. 2.8a, the whole scattering problem can be divided into three fields: incident, internal and scattered field. For the incident wave, a plane, x-polarized wave $\vec{E}_{\text{inc}} = E_0 e^{ikr \cos\theta} \hat{e}_x$ is assumed, travelling towards the particle in the origin of the coordinate system at $r = 0$. Due to orthogonality reasons, all α_{eml} and β_{oml} vanish. For similar reasons, all α_{oml} and β_{eml} vanish unless $m = 1$.

This leaves us with

$$\vec{E} = \sum_{l=1}^{\infty} \alpha_l \vec{M}_{o1l}^z + \beta_l \vec{N}_{e1l}^z. \quad (2.51)$$

The corresponding magnetic part is again obtained by inserting \vec{E} in the Maxwell equation, resulting in

$$\vec{H} = -\frac{k}{\omega\mu} \sum_{l=1}^{\infty} \beta_l \vec{M}_{o1l}^z + \alpha_l \vec{N}_{o1l}^z. \quad (2.52)$$

The next step is to use boundary conditions to decide which Bessel function z_l is suitable for which parts of the wave and the determination of the expansion coefficients α_l and β_l . The first boundary condition is finiteness of the incident field at the origin $r \rightarrow 0$, which is only provided by $z_l = j_l$. Inserting this into Eq. (2.51) yields the expansion coefficients $\alpha_l = E_l$ and $\beta_l = -iE_l$ with

$$E_l := E_0 i^l \frac{2l+1}{l(l+1)}. \quad (2.53)$$

The field of the outgoing, scattered wave can include both j_l and y_l , but only $h_l^{(1)}$ corresponds to the right physics of an outgoing wave, leading to $\alpha_l = -b_l E_l$ and $\beta_l = ia_l E_l$. The internal field again must be finite in the origin, therefore $z_l = j_l$, resulting in $\alpha_l = c_l E_l$ and $\beta_l = -id_l E_l$.

Now the problem is reduced to only four unknown coefficients a_l, b_l, c_l, d_l . Those coefficients depend only on the refractive index $n = n' + in''$ and the size parameter $x := kD/2$ of the particle (with the particle diameter D and the wavenumber of the lightwave $k = \frac{2\pi}{\lambda}$). For the sake of simplicity, a refractive index of the surrounding medium $n = 1$ and a permeability of both medium and particle $\mu = 1$ are assumed.

The four coefficients a_l, b_l, c_l, d_l , which include the spherical Bessel functions, can be determined using the same boundary condition as in Section 2.2.2, namely that the fields must be continuous at the boundary of the sphere at $r = d/2$:

$$(\vec{E}_{\text{inc}} + \vec{E}_{\text{scatt}} - \vec{E}_{\text{int}}) \times \hat{e}_r = 0 \quad (2.54)$$

$$(\vec{H}_{\text{inc}} + \vec{H}_{\text{scatt}} - \vec{H}_{\text{int}}) \times \hat{e}_r = 0. \quad (2.55)$$

Now, \vec{E} and \vec{H} and thus the *Poynting vectors* \vec{S} (which represent the directional energy flux) for scattering and extinction

$$\vec{S}_{\text{scatt}} = \frac{1}{2} \text{Re} \left[\vec{E}_{\text{scatt}} \times \vec{H}_{\text{scatt}}^* \right] \quad (2.56)$$

$$\vec{S}_{\text{ext}} = \frac{1}{2} \text{Re} \left[\vec{E}_{\text{inc}} \times \vec{H}_{\text{scatt}}^* + \vec{E}_{\text{scatt}} \times \vec{H}_{\text{inc}}^* \right] \quad (2.57)$$

can be calculated. Integrating the Poynting vector \vec{S}_i over a closed surface gives the rate at which energy crosses the surface

$$W_i = \oint_A \vec{S}_i \cdot \hat{n} \, dA \quad (2.58)$$

resulting in the corresponding cross sections

$$\sigma_{\text{scatt}} = \frac{W_{\text{scatt}}}{I_{\text{inc}}} = \frac{2\pi}{k^2} \sum_{l=1}^{\infty} (2l+1) (|a_l|^2 + |b_l|^2) \quad (2.59)$$

$$\sigma_{\text{ext}} = \frac{W_{\text{ext}}}{I_{\text{inc}}} = \frac{2\pi}{k^2} \sum_{l=1}^{\infty} (2l+1) \text{Re}[a_l + b_l] \quad (2.60)$$

with

$$a_l = \frac{n^2 [x j_l(x)]' j_l(nx) - [n x j_l(nx)]' j_l(x)}{n^2 [x h_l(x)]' j_l(nx) - [n x j_l(nx)]' h_l(x)} \quad (2.61)$$

$$b_l = \frac{[x j_l(x)]' j_l(nx) - [n x j_l(nx)]' j_l(x)}{[x h_l(x)]' j_l(nx) - [n x j_l(nx)]' h_l(x)}. \quad (2.62)$$

As stated previously, these scattering cross sections depend solely on the refractive index $n = n' + in''$ and the size parameter $x = \pi d/\lambda$ and thus the ratio of sphere diameter and the wavelength of the light. The infinite but converging series of Bessel functions (j_l, h_l) can be calculated and hence the scattering cross sections can be numerically determined.

It is worth noting here that there are different approximations for edge cases of scattering: For $x \gg 1$ ($D \ll \lambda$), e.g. aerosols or even single molecules, orders higher than $l \geq 2$ can be neglected and

$$\sigma_{\text{scatt}} = \frac{24\pi^3 V^2}{\lambda^4} \left(\frac{n^2 - 1}{n^2 + 2} \right)^2, \quad (2.63)$$

with the particle volume $V = 4/3\pi r^3$. This is called the *Rayleigh approximation*. With this, we can for example explain why the sky is blue: comparing the scattering cross sections of blue and red light

$$\frac{\sigma_{\text{Blue}}}{\sigma_{\text{Red}}} = \left(\frac{\lambda_{\text{Red}}}{\lambda_{\text{Blue}}}\right)^4 = \left(\frac{650 \text{ nm}}{450 \text{ nm}}\right)^4 \simeq 4.4 \quad (2.64)$$

shows that blue light is scattered stronger than red light. For $x \ll 1$ ($D \gg \lambda$), the curvature of the sphere is so small in comparison to the wavelength that it can be approximated by a flat surface and hence solved by geometrical optics and Snell's law.

In this work, we are interested in the interaction of light in the visible spectrum with cloud particles (and their surface features) in a size range from roughly $D = 10 \mu\text{m}$ to $1000 \mu\text{m}$, i.e. D and λ are still in the scope of the similar order of magnitude and we need Mie theory to describe the scattering. For scattered Mie intensity of a spherical particle is in first order proportional to its geometrical cross section σ_{geom} and thus diameter squared (see Section 3.1.1). In the next section, the angular scattering behaviour of spherical droplets and aspherical ice particles will be explained.

2.2.4. Scattering Phase Function

Ultimately, for the impact of sun light scattering on cloud particles (see Section 2.3.2), we are interested in the amount of light that is scattered in a given solid angle

$$d\Omega = \sin \theta \, d\theta \, d\phi. \quad (2.65)$$

The intensity of scattered light in an arbitrary direction is referred to as scattering phase function p which is defined as the

$$p(\Omega) = \frac{1}{\sigma_{\text{scatt}}^{\text{tot}}} \sigma_{\text{scatt}}^{\text{diff}}(\Omega) \quad (2.66)$$

with the differential scattering cross section

$$\sigma_{\text{scatt}}^{\text{diff}}(\Omega) = \frac{d\sigma_{\text{scatt}}}{d\Omega} \quad (2.67)$$

and the total scattering cross section integrated over all solid angles

$$\sigma_{\text{scatt}}^{\text{tot}} = \int_0^{2\pi} \int_0^{\pi} \frac{d\sigma_{\text{scatt}}}{d\Omega} \, d\Omega. \quad (2.68)$$

Hence, naturally, p is normalized to unity

$$\int_0^{2\pi} \int_0^{\pi} p(\Omega) \, d\Omega = 1. \quad (2.69)$$

For spherical particles, the dependency of the azimuthal angle ϕ can be omitted due to the continuous rotational symmetry and p is only dependent on the polar angle θ

$$p(\Omega) = p(\theta). \quad (2.70)$$

In the following sections, the scattering phase functions of spherical water droplets and aspherical ice particles are discussed. This connects the theoretical features of the scattering function to methods presented in this work, namely determination of phase and size of cloud particles based on their scattering function.

2.2.4.1. Spherical Water Droplets

As discussed in the previous section, for spherical particles p can be analytically calculated using Mie theory. For water (refractive index $n = 1.33 + i 1.50 \cdot 10^{-9}$, see Section 2.1.2), the absorption part is negligible compared to scattering in the visible wavelengths. Fig. 2.9 shows p calculated for a theoretical spherical water droplet of diameter $D = 100 \mu\text{m}$, using Mie theory for a wavelength $\lambda = 532 \text{ nm}$. A scattering angle of $\theta = 0^\circ$ corresponds to the forward direction, $\theta = 180^\circ$ corresponds to backscattered light.

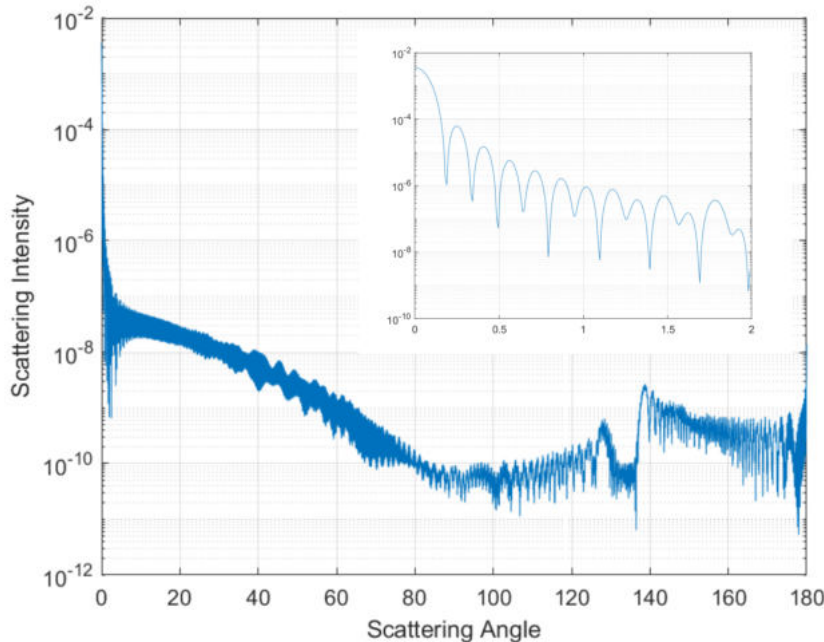


Figure 2.9.: Scattering phase function p of a spherical water droplet with refractive index $n = 1.33 + i1.50 \cdot 10^{-9}$ and diameter $D = 100 \mu\text{m}$ for a wavelength of $\lambda = 532 \text{ nm}$. The small figure within shows the angular range from $\theta = 0^\circ$ to $\theta = 2^\circ$.

Most of the light is scattered in forward direction - the scattering intensity is increased by up to 8 orders of magnitude compared to the sideways angular range (note the logarithmic scale). It can be seen, especially in the excerpt for the angular range from $\theta = 0^\circ$ to 2° , that the scattering intensity oscillates strongly depending on the scattering angle. Even within a range of $\Delta\theta = 1/10^\circ$ the scattering intensity can vary by up to one order of magnitude. These oscillations are the result of the vector spherical harmonics discussed in Section 2.2.3.1.

p is steeply decreasing with increasing scattering angle until the minimum around $\theta = 90^\circ$ (perpendicular to the incident light). Afterwards, the scattering intensity is increasing towards the rainbow angle around $\theta = 138^\circ$ (see discussion in Section 2.2.2.1). Afterwards, p is decreasing again. For $\theta \approx 180^\circ$ the intensity is again increased for the backscattered/reflected light.

2.2.4.2. Aspherical Ice Particles

Atmospheric ice particles are usually not spherical but their shapes can be rather complex as will be discussed in Section 2.4.1. There exists no analytical solution to the scattering problem of non-spherical ice particles similar to Mie theory for spherical particles, not even for the first order approximation of a hexagonal column due to the edges and lack of the continuous rotational symmetry. Hence, the scattering intensity of an individual ice particle is depending on its azimuthal orientation. For instance, given a certain azimuthal

orientation, an ice particle can experience a total internal reflection that does not happen for a different orientation. One prominent example is the halo described in Section 2.2.2.2. Further, habit, surface roughness and other complexity features significantly affect a particle's scattering phase function p [Sun and Shine, 1994; Um and McFarquhar, 2011; Järvinen et al., 2018; Schnaiter et al., 2018].

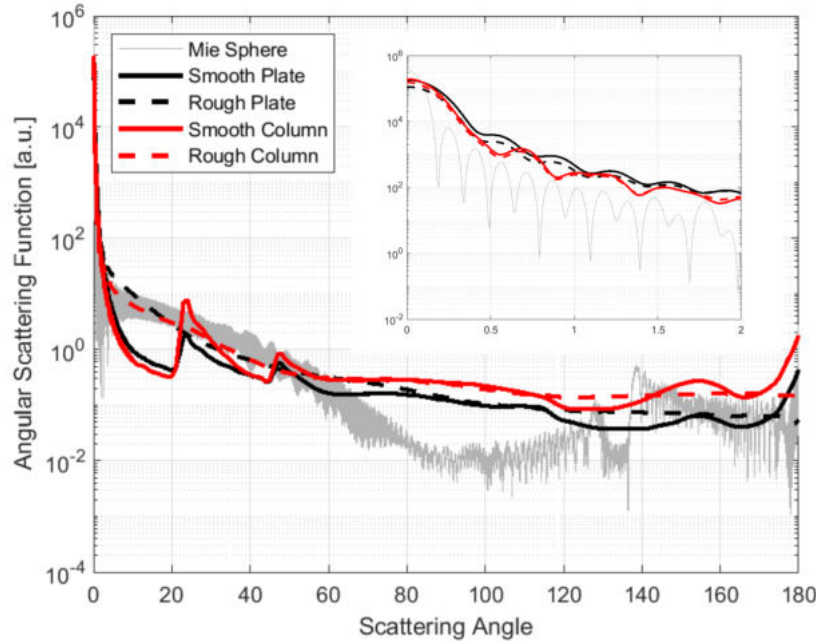


Figure 2.10.: Orientation averaged angular scattering intensities of simulated columns (red) and plates (black) with smooth (solid line) and rough surface (dashed) with maximum dimension $D = 100 \mu\text{m}$ for a wavelength $\lambda = 530 \text{ nm}$ based on [Yang et al., 2013]. The grey line shows the calculated Mie scattering intensity for a spherical droplet from Fig. 2.9 ($D = 100 \mu\text{m}$, scaled by a.u.). The small figure within shows the angular range from $\theta = 0^\circ$ to $\theta = 2^\circ$.

Even though it is not analytically solvable, p of aspherical ice particles can be simulated using geometric-optic models and Ray-tracing techniques. Previous works, e.g. [Macke et al., 1996b; Baum et al., 2011; Yang et al., 2013], have calculated p of individual as well as aggregated idealized hexagonal ice particles of various sizes, habits and surface roughness. Fig. 2.10 shows the orientation-averaged p of simulated columns and plates.

It can be seen that p has an overall similar shape compared to p of a spherical particle calculated by Mie theory. However, due to the orientation averaging, the oscillations are smoothed out. Notable differences are the steeper increase towards the forward direction and the otherwise flatter course. Especially for scattering perpendicular to the incident beam, i.e. $\theta = 90^\circ$, where the scattering of the spherical particle has its minimum, the phase function of aspherical particles remains almost constant in comparison. For smooth particles, one can clearly see the two halo features at around $\theta = 22^\circ$ and $\theta = 42^\circ$. For rough surfaces, the simulated p follow a similar course, but e.g. the halo features are more "washed out".

In this work, the discussed distinctive differences in p of spherical and aspherical particles are used to discriminate the phase of cloud particles, i.e. differentiate liquid droplets from solid ice particles. This will be explained in detail in Chapter 4. The size of cloud particles is calculated based on the amplitude of the intensity of the scattered light in Chapter 5. But first, in the following sections, the life cycle and microphysical properties of cloud particles are discussed.

2.3. Life Cycle of Mixed-Phase Cloud Particles

Fig. 2.11 shows the typical life cycle of a cloud particle. As explained previously, warm and moist air has a lower density compared to cold, dry air and hence results in an updraft of the air parcels. During their ascent through the atmosphere, the temperature and thus the vapor pressure of water decreases. Eventually, the vapor condenses as droplets or nucleates as ice depending on the availability of aerosols (see Section 2.3.3). Together, these droplets and/or ice particles form a cloud in which the cloud particles grow and eventually precipitate (or evaporate).

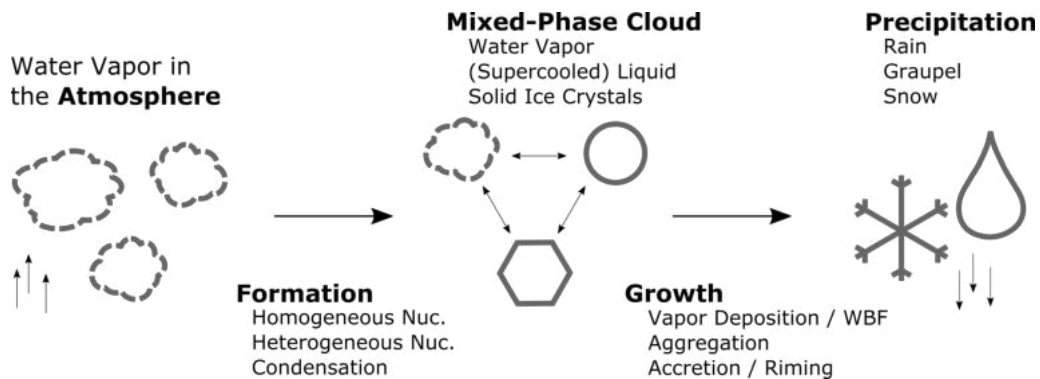


Figure 2.11.: Sketch of the typical life cycle of an MPC: Water vapor ascends in the atmosphere, cloud particles form, grow and precipitate.

One of the most significant properties of a cloud is the phase of the cloud particles. Above $T > 0$ °C, typically all cloud particles are liquid droplets. Below the homogeneous freezing point, $T < -38$ °C, clouds are in a pure ice phase. Between that, clouds can also exist as a mixture of both as mixed-phase clouds (MPCs) consisting of both droplets and ice particles. Compared to single phase clouds, MPCs are still rather poorly understood and represent a great source of uncertainty for climate models [e.g. McCoy et al., 2016]. In the following, an overview of the current knowledge MPCs and their role in Earth's climate is given (Section 2.3.2). The following sections focus on the microphysical processes related to MPC particles: The formation of droplets via condensation and the formation of ice particles via homogeneous and heterogeneous nucleation (Section 2.3.3) as well as the corresponding formation of different habits and crystal complexity features are explained. In addition, the growth mechanisms (Section 2.3.4) of ice particles via vapor deposition, aggregation, and accretion (riming, Section 2.4.3) are discussed.

2.3.1. Definition Mixed-Phase Clouds

At first glance, the definition of MPCs seems trivial: every cloud that includes water in all of its three phases — vapor, liquid droplets and solid ice particles — is technically an MPC. In practice, this definition is a lot more difficult and depends on the type of measurement as well as scale of spatial averaging. Whether a cloud is categorized as MPC depends on the classification thresholds, i.e. how much ice phase/liquid phase does it take to classify a cloud as mixed-phased instead of single phase cloud [Korolev et al., 2017].

One frequently used threshold is to classify clouds having one phase between 10% and 90% as mixed-phased [Korolev et al., 2003; Field et al., 2004]. Another problem lies in the applied metric, i.e. which measured parameter is used to quantify the "amount of the phase". Remote sensing methods (e.g. radar or lidar) detect reflectivity or cloud-layer optical depth, whereas in situ detect particle number concentration or condensed water content. Depending on the used metric, the answer whether a cloud is classified as single

or MPC, may differ. For example, a hypothetical cloud with 98% single sized droplets with diameter $D = 50 \mu\text{m}$ and 2% ice with $D = 200 \mu\text{m}$ can be classified as pure liquid cloud using the particle number concentration as primary metric. However, since the mass grows proportional to the volume $V \propto D^3$, the same cloud can also be classified as an MPC because the total liquid water content (LWC) and ice water content (IWC) are similar.

Typically, MPCs consist of many small droplets and a few larger ice particles, as the ice particles grow on the expense of the small droplets (Wegener-Bergeron-Findeisen process, see Section 2.3.4). Hence, typically, in MPCs, droplets exist at smaller sizes (in the order of $10^0 \mu\text{m} - 10^2 \mu\text{m}$) compared to ice (in the order of $10^1 \mu\text{m} - 10^3 \mu\text{m}$). Therefore, even for the same total water content (TWC), the total number concentration of droplets can exceed the number of ice particles by multiple orders of magnitude.

2.3.2. Implications for the Climate

Studies have shown that MPCs occur all over the world, from the tropics to the poles, throughout all seasons during the year, and in various meteorological conditions [Korolev et al., 2017]. MPC processes have two main implications for the climate. They influence

1. the hydrological life cycle of clouds and
2. Earth's energy budget.

Hence, uncertainties in the microphysical properties of MPCs (foremost particle phase, but also crystal complexity features like riming) transition into uncertainties in climate models and radiative transfer models and thus ultimately also towards understanding climate change.

In the following, the hydrological and radiative effects of MPCs are sketched. Apart from that, MPCs affect cloud electrification [Williams et al., 1991] as well as icing [Cober and Isaac, 2002; Hallett and Isaac, 2002, 2008], but this will not be discussed further in this work.

Life Cycle

In theory, MPCs are expected to be rather short-lived, as the classic Wegener-Bergeron-Findeisen process (see Section 2.3.4) suggests growth of ice particles until either, a) there is no more liquid to "feed" on and the cloud is purely ice or b) the ice particles get big enough to fall down as precipitation and the cloud is purely liquid or dissipates. However, multiple studies have reported stable, long-lived MPCs [Rauber and Tokay, 1991; Pinto, 1998] due to vertical oscillating air parcels [Korolev and Isaac, 2003]. Furthermore, recent studies suggest that the MPC processes are much more complex and Wegener-Bergeron-Findeisen processes are not necessarily always active in MPCs [Korolev, 2007a; Lohmann and Hoose, 2009; Fan et al., 2011a].

Cloud Radiative Effects

The main driver of Earth's energy budget is the sun. Annually and globally averaged, the Sun's total radiative flux amounts about 340 W m^{-2} [Wild et al., 2013]. The Sun emits light (short-wave electro-magnetic radiation) on the Earth's surface where parts of it are absorbed and transformed into heat (long-wave radiation). Some of the heat and light is bound chemically (e.g. in plants), some is radiated back into space. In recent centuries the burning of fossil fuels and release of radiatively active gases such as CO_2 have enhanced the natural *Greenhouse Effect* which prevents the heat from escaping Earth's atmosphere and causes global warming Hansen et al. [1997].

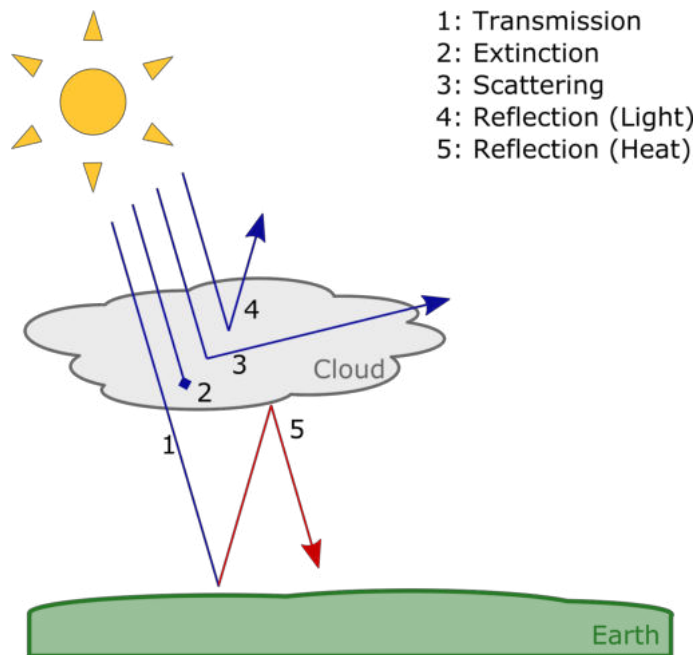


Figure 2.12.: Schematic overview of how a cloud interacts with radiation: Transmission (1), extinction (2), scattering (3) and reflection of light (4) and heat (5).

Besides greenhouse gases, clouds also play a critical role for Earth's radiative budget. Fig. 2.12 shows a schematic view of the interaction of clouds and radiation (short-wave in blue, long-wave in red). In terms of radiative effect, clouds act simultaneously as cooling (by reflecting and scattering light) and heating (by trapping heat). Which process is dominating depends on the mass as well as the microphysical properties, e.g. phase, of the cloud particles since droplets and ice particles show significantly different scattering behaviour as discussed in Section 2.2. Matus and L'Ecuyer [2017] have shown that the globally averaged net cloud radiative effect for warm liquid clouds results in a net cooling of -11.8 W m^{-2} , whereas ice clouds result in a net warming of $+3.5 \text{ W m}^{-2}$. MPCs lie *somewhere* in between that. Matus and L'Ecuyer [2017] estimated a globally averaged net cloud radiative effect of -3.4 W m^{-2} for MPCs. As this value is sensitive to the fraction of liquid and ice, the correct representation of cloud phase composition is vital for the accurate assessment of the radiative budget of the Earth. Furthermore, the implications of particle phase concerning life span of the cloud that were discussed previously also directly translate towards the radiative budget of the cloud. Hence, for the correct assessment of cloud radiative effects, both on a regional as well as global scale, it is crucial to accurately represent the phase composition of MPCs.

Further, cloud radiative effects are depending on the size of cloud particles. As shown in Section 3.1.1, the scattering cross section of a spherical particle is in first order proportional to its geometrical cross section and thus the square of its diameter. This means that for a constant TWC ($V \propto D^3$), the scattering increases and hence liquid clouds with smaller droplets contribute to a more negative net radiative effect. Lastly, the radiative effect of a cloud is dependent on morphological features such as habit and crystal complexity of ice particles as discussed in Järvinen et al. [2018]; Järvinen et al. [2021b] and Section 7.4. The formation and microphysical properties of MPC particles will be discussed in the following sections.

2.3.3. Particle Formation

2.3.3.1. Condensation

The number of water molecules that can be “stored” in the air as vapor is limited. The more vapor in the air, the higher its *partial pressure*. If the partial water pressure (e) is higher than the *saturation pressure* with respect to water (e_w) the air is supersaturated (saturation $S_w = e/e_w > 100\%$). As a result, the water vapor falls out of the gaseous phase and (*homogeneously*) condenses as droplets. If the partial pressure is lower ($S_w < 100\%$), droplets evaporate.

This is again a stochastic process — water evaporates and condenses at all temperatures or saturations, but at different rates. Given enough time, one process exceeds the other and dictates the equilibrium state. This also means that over limited periods of time, saturations well over 100% can exist.

The saturation pressure with respect to water is dependent on the temperature and is calculated via the empiric Magnus-formula [Alduchov and Eskridge, 1997] as

$$e_w = 6.112 \text{ hPa} \cdot \exp\left(\frac{17.62 T}{243.12 \text{ }^\circ\text{C} + T}\right). \quad (2.71)$$

The temperature to which the air must be cooled down to be saturated, is called *dew point*.

Note that the Magnus-formula is only valid for flat surfaces. For (spherical) droplets, the partial pressure over the curved surface is larger. Known as the *Kelvin effect*, this process depends on particle size and increases for small particles. This means that if small droplets do not grow fast enough past a critical diameter (typically in the order of $D \approx 0.1 \mu\text{m}$, [Petters et al., 2007]), they do not persist and evaporate again. Depending on the temperature, supersaturations much higher than 100% are necessary for the formation of droplets.

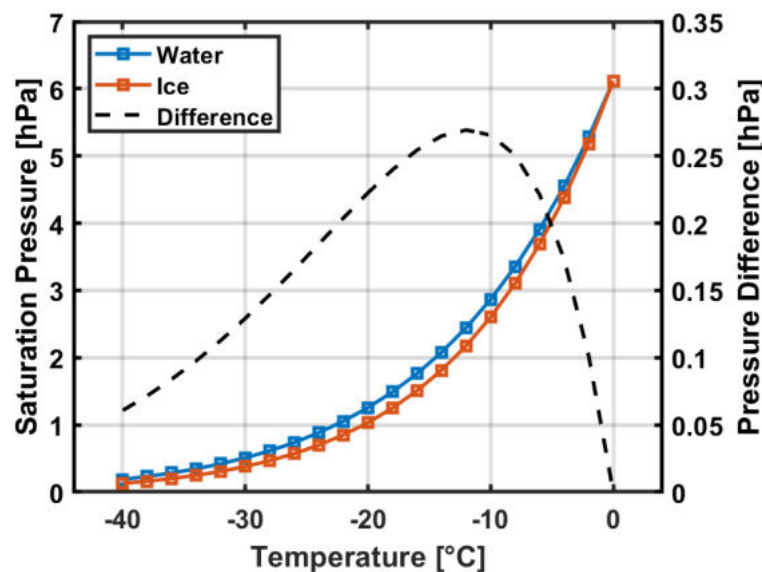


Figure 2.13.: Saturation pressure of vapor over water, e_w , (blue) and ice, e_i , (red) from the parameterization of [Murphy and Koop, 2005]. The difference between the saturation pressure over water and ice is shown by the dashed black line with the maximum difference at around $T \approx -12 \text{ }^\circ\text{C}$.

Via *heterogeneous* deposition condensation on certain aerosols, so-called cloud condensation nuclei (CCN), the critical diameter can be exceeded and condensation at low supersaturations is possible. The inclusion of soluble aerosols further alters the saturation pressure.

Empiric parameterization are given in Murphy and Koop [2005]; Koop and Murray [2016] and shown in blue in Fig. 2.13. The same applies for the phase transition from vapor to ice (deposition growth), which will be discussed in Section 2.3.4.

2.3.3.2. Nucleation of Ice Particles

As stated previously, water can exist as solid ice at temperatures below 0 °C (assuming standard atmospheric pressure). However, for the phase transition from liquid to solid, a significant amount of crystallization energy is needed. Hence, pure liquid droplets in the atmosphere usually do not freeze until temperatures below $T < -38$ °C are reached [Pruppacher and Klett, 1997]. This is known as *homogeneous freezing*. Since this process occurs only at rather low temperatures, it does not play a major role for MPCs.

Similar to what was already discussed for condensation, certain aerosols can serve as crystallization centers. INP lower the needed phase transition energy and cause freezing at higher temperatures. This is called *heterogeneous freezing*.

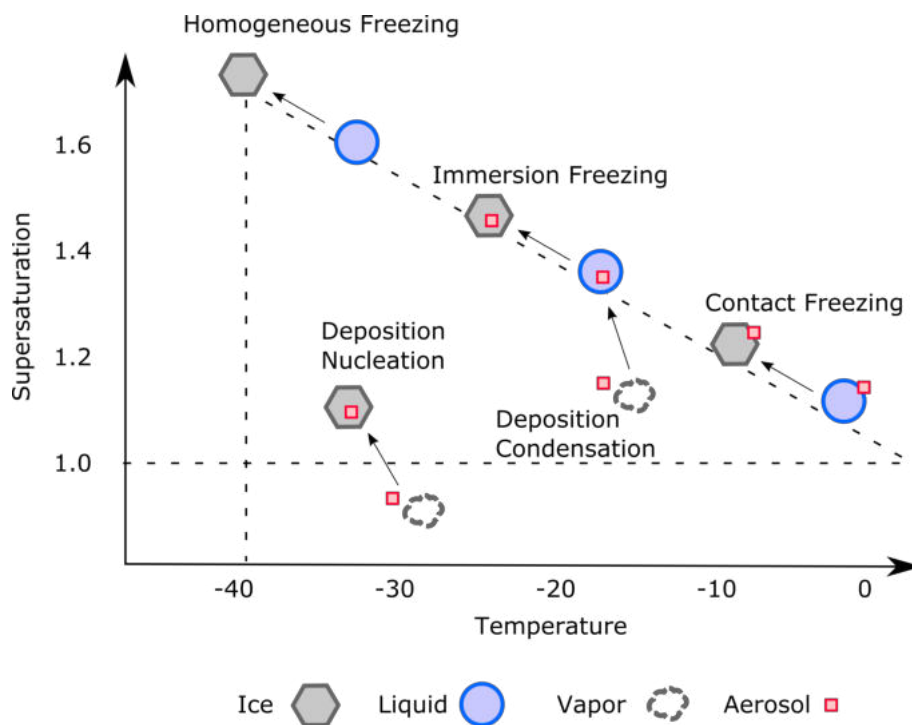


Figure 2.14.: Schematic overview of typical freezing and condensation mechanisms, adapted from [Hoose and Möhler, 2012]. The horizontal line indicates the saturation line with respect to ice, corresponding to the red line in Fig. 2.13. Below that, the equilibrium state is gaseous, above, ice is the stable phase. The vertical line indicates the threshold below which droplets freeze homogeneously. The diagonal line corresponds to the ice saturation ratio at liquid water saturation where supercooled liquid water is in equilibrium with the vapor phase (i.e. the equivalent of the horizontal line, but for liquid water, blue line in Fig. 2.13). Above that, vapor condenses on droplets, below droplets evaporate.

Fig. 2.14 shows a schematic overview of different phase transition modes, adapted from Hoose and Möhler [2012]:

1. **Contact Freezing** — supercooled droplets freeze upon colliding with INP.
2. **Immersion Freezing** — freezing of supercooled droplets with immersed INP.
3. **Deposition Nucleation** — vapor deposits (re-sublimates) directly, skipping the liquid phase.

4. Homogeneous Freezing — supercooled droplets freeze without the influence of INP.

Typically, the number of CCN surpasses the number of ice active INP by multiple orders of magnitude [Haarig et al., 2019; Ansmann et al., 2021] and thus the number concentration of supercooled droplets can surpass the ice concentration, even at colder temperatures where the solid state is thermodynamically favoured (see Chapter 6).

2.3.3.3. Secondary Ice Production

In the previous section, the primary process of the formation of ice particles was explained. However, it has been frequently observed that the number of ice particles in MPCs exceeds the number of available INPs [Huang et al., 2017; Scott, 2019; Sotiropoulou et al., 2021; Phillips et al., 2018; Järvinen et al., 2021a]. Similar to aerosols, fragments of pre-existing ice particles (e.g. sedimentating from another cloud above or due to an updraft from lower levels) can also serve as INP that initiate the formation of new ice particles. This is called *ice multiplication* or *secondary ice process* [Field et al., 2017].

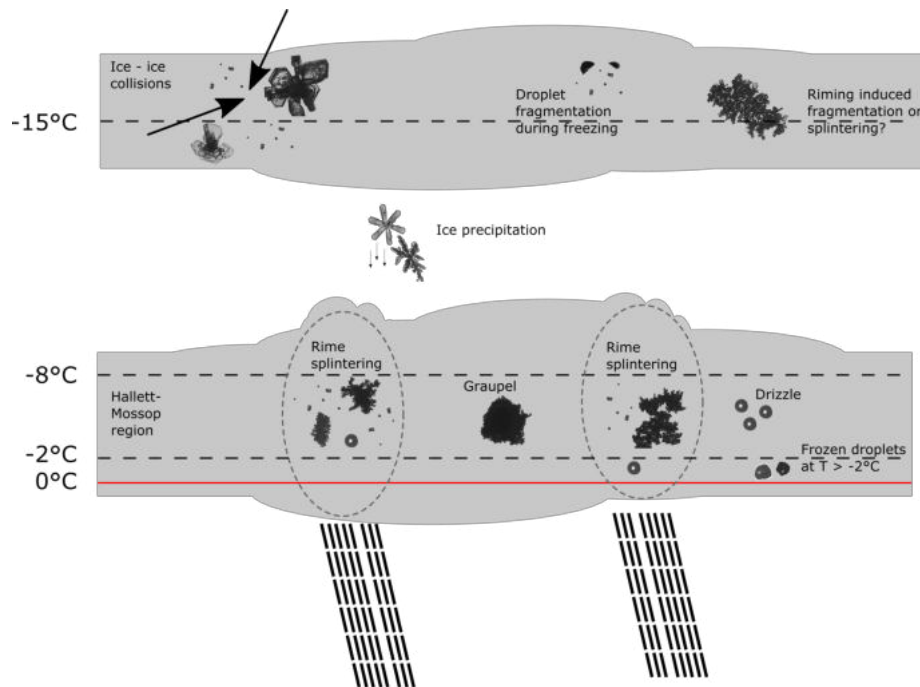


Figure 2.15.: Schematic representation of secondary ice processes caused by shattering due to collision of ice particles, fracturing of freezing drizzle droplets and rime splintering, adapted from Järvinen et al. [2021a].

Fig. 2.15 shows possible ways how small ice fragments can be generated:

- Fragmentation of freezing drizzle droplets due to internal tension [Lauber et al., 2018; Keinert et al., 2020].
- Ice-ice collision [Vardiman, 1978; Yano and Phillips, 2011].
- *Rime splintering*, also known as *Hallett-Mossop process*, which is most prevalent at temperatures around $T = -8\text{ °C}$ to $T = -2\text{ °C}$ [Hallet and Mossop, 1974; Choulaton et al., 1978; Mossop, 1980]. Riming will be discussed in Section 2.4.3 and Chapter 7.

The shattering/splintering fragments can initiate contact freezing of the surrounding supercooled droplets as explained in the previous section. The newly formed ice particles grow quickly, either via deposition growth or accretion and can shatter again to trigger

the same process anew or grow until they precipitate. This way abnormally high ice concentrations in the absence of INPs can be explained.

2.3.4. Growth of Ice Particles and Wegener-Bergeron-Findeisen Process

In an MPC, water is present in all three of its phases: gaseous, liquid and solid. Based on temperature and partial vapor pressure, the phases can acquire mass on the expense of another as indicated in Fig. 2.11. Once a cloud particle has formed via homogeneous or heterogeneous condensation or nucleation, there are three main modes via which the particle can grow: deposition of gaseous vapor or collision with other particles of either the same or of a different phase. Droplet-droplet collisions are called coalescence [Bartlett, 1966], ice-ice collisions can result in aggregation (or also the inverse effect, shattering). Lastly, the accretion of droplets by ice particles is called riming. It is discussed in Section 2.4.3. In this section, the growth of ice particles via vapor deposition is discussed.

As discussed in the previous section, atmospheric phase transition processes, and hence particle growth rates, are dictated by the partial vapor pressure of the air, e . Fig. 2.13 shows the saturation pressure of water (e_w , blue) and ice (e_i , red) based on the empiric parameterizations given in Murphy and Koop [2005]; Koop and Murray [2016]. The lines correspond to the equilibrium states, i.e. where statistically, the same amount of vapor deposits and evaporates from the droplet or ice particle, respectively. For $e > e_{w,i}$, more vapor deposits on the particles and they grow, for $e < e_{w,i}$, droplets evaporate or ice sublimates.

Since $e_w > e_i$, vapor deposition on ice particles is energetically preferred and thus ice particles grow faster than droplets (assuming they are of the same size and ignoring effects like solved aerosols that change the phase transition energy as discussed previously). Further, this means that, especially in the region between the two curves, $e_w > e > e_i$, droplets evaporate and ice particles grow on their expense. This is called *Wegener-Bergeron-Findeisen process* [Wegener, 1911]. Hence, MPCs usually consist of lots of small droplets and few large ice particles, as discussed previously in this section. The inverse process, the growing of liquid droplets on the expense of ice particles, is not possible at MPC conditions between $-40\text{ °C} < T < 0\text{ °C}$. Below this, water freezes homogeneously, whereas above this, ice particles melt.

Note that the difference between e_w and e_i (black dashed line in Fig. 2.13) is temperature dependent, with the maximum around $T \approx -12\text{ °C}$. This results in different typical growth rates of cloud ice particles. The growth rate of ice particles significantly affects their shape and morphology — their *habit*.

2.4. Microphysical Properties of MPC Ice Particles

2.4.1. Ice Particle Habit

Depending on ambient conditions like temperature and supersaturation and thus growth rate, atmospheric ice particles grow into different habits. Fig. 2.16 shows the *Nakaya diagram* which gives a schematic overview of different habits based on temperature and supersaturation. Over the past decades, many different iterations of this figure were proposed [Bailey and Hallett, 2009; Pruppacher and Klett, 1997; Magono and Aburakawa, 1969; Hueholt et al., 2020; Libbrecht, 2005]. Fig. 2.17 shows exemplary particles of different habits that were acquired using the PHIPS probe during the IMPACTS campaign. Even though the morphology of individual ice particles differs significantly, the underlying

crystal structure is still always a hexagonal prism. There are two main growth modes: along the basal and along the prismatic face of the crystal. Dominating one-dimensional growth on the basal face (along the *c*-axis) results in long *columnar* crystals. Two-dimensional growth along the prismatic face result in flat *plate*-like crystals. For high supersaturations and temperatures between $-20 \leq T \leq 0^\circ\text{C}$, the particles grow faster, resulting in *needles* and *dendrites*, respectively. At lower temperatures, concentric poly-crystalline particles (*bullet rosettes* and *side planes*) are common.

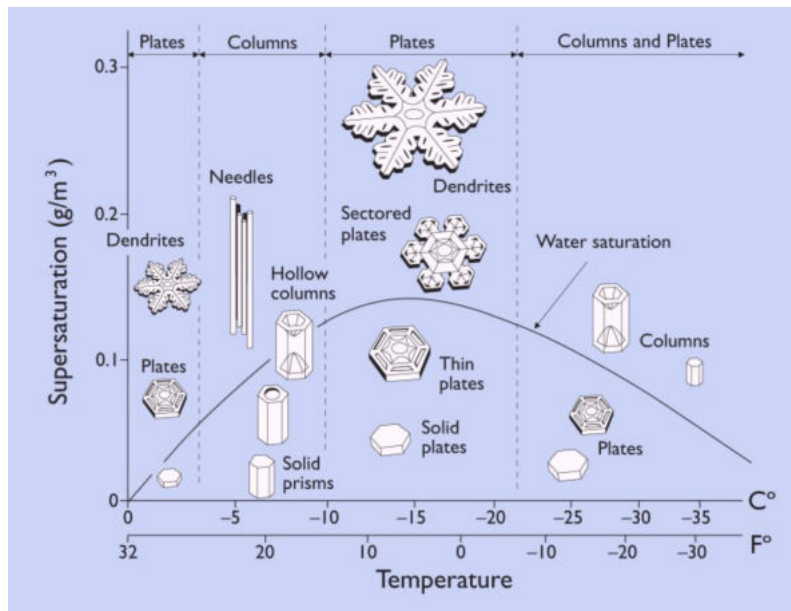


Figure 2.16.: Ice particle habit (Nakaya) diagram as a function of temperature and supersaturation, taken from [Libbrecht, 2005].

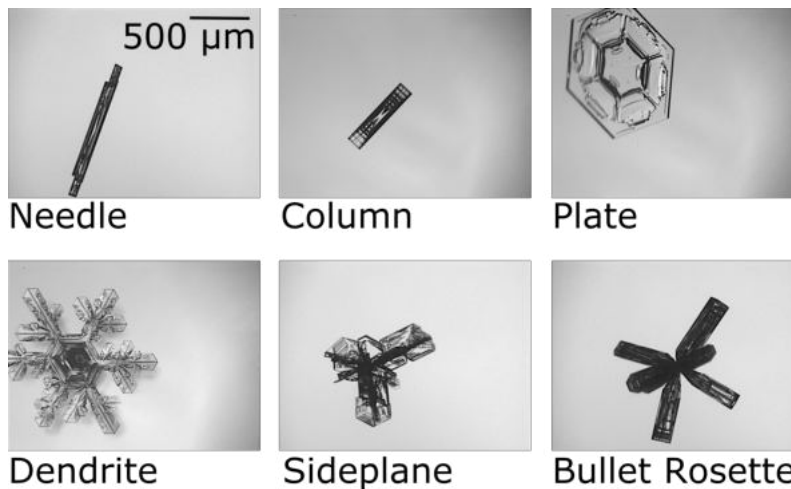


Figure 2.17.: Exemplary ice particles of different habit (needle, column, plate, dendrite, side plane and bullet rosette) acquired using the PHIPS probe during the IMPACTS campaign.

If particles grow at varying conditions, they form as a mixture of different habits. For example, if a particle starts to grow as a column in a certain environment, but is then moved in an updraft into a regime where growth along the prismatic faces is favoured, so-called *capped columns* are formed (sometimes referred to as *TIE fighter crystals*, comparing to the distinctive shape of the fictional aircraft in the Star Wars movies). Similarly, “antennas” can form on the basal faces of particles which have previously grown along their prismatic

faces. Examples are shown in Fig. 2.18.

Not all ice particles can be easily classified into one of the six mentioned habit classes. Even though those are typically the most common habits, a significant amount of atmospheric ice particles are classified as irregular [e.g. Lawson et al., 2019]. Furthermore, numerous habit sub-classes exist, for example differentiating between solid columns and hollowed columns.

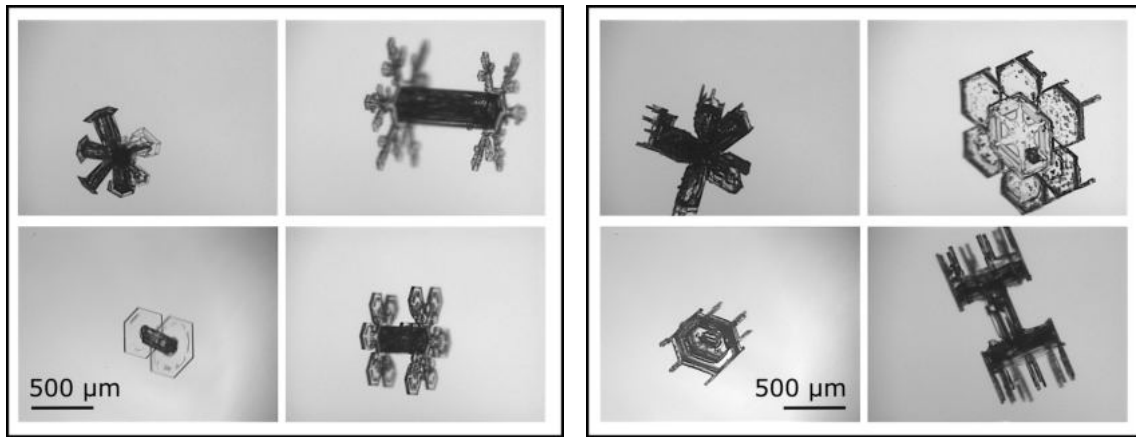


Figure 2.18.: PHIPS images of capped columnar particles (left) and particles with antennas on the basal face, acquired during the IMPACTS campaign.

2.4.2. Crystal Complexity

Even if particles can be attributed to a certain habit, their morphology can differ significantly. Järvinen et al. [2021b] have defined the term *crystal complexity* to describe "any morphological deviation from that of a pristine, ideal hexagonal prism". It has been shown that ice particles with a high degree of crystal complexity can dominate a cloud's microphysical properties and lead to an overall net negative (cooling) cloud radiative effect in the order of multiple $W m^{-2}$ [Yi et al., 2013; Schnaiter et al., 2016; Järvinen et al., 2018].

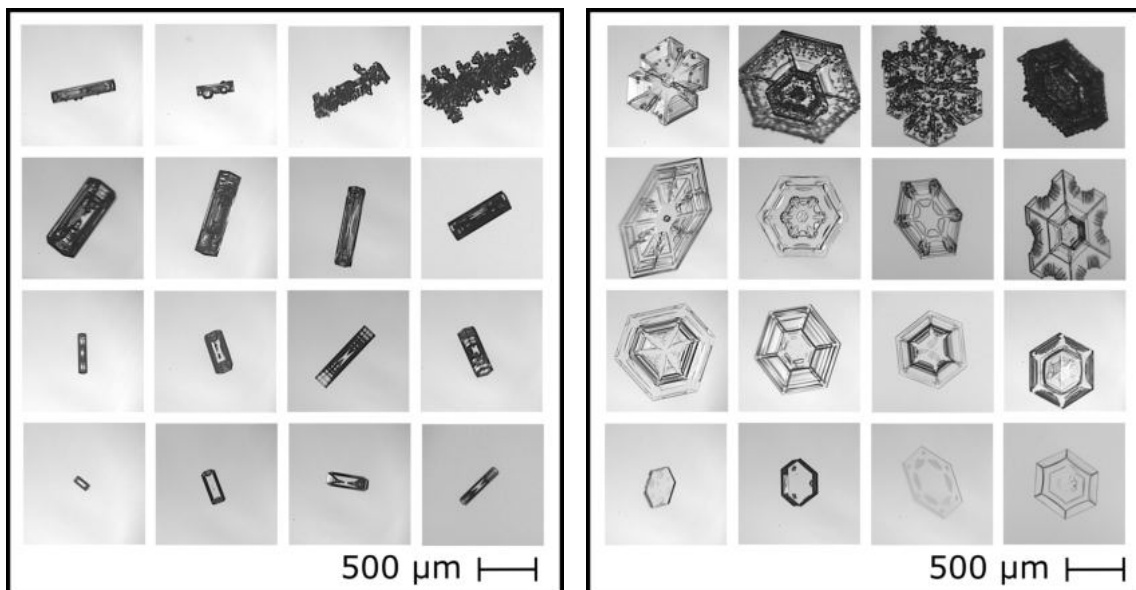


Figure 2.19.: Exemplary PHIPS images of columns (left panel) and plates (right panel) acquired during the IMPACTS campaign with different visual degree of crystal complexity ranging from pristine particles with little to no crystal complexity to heavily rimed particles in the top right.

Fig. 2.19 shows representative images of columns (left panel) and plates (right panel) sampled by PHIPS during the IMPACTS campaign. The particles differ strongly in terms of crystal complexity, ranging from pristine particles with little to no crystal complexity to heavily rimed particles in the top right. There exists a wide variety of different crystal complexity types, ranging from sub-nanometer to millimeter scale. Fig. 2.20 gives an overview of different types of crystal complexity on the nano-, meso- and micro- to macro-scale as well as corresponding exemplary particles for each category.

One type of surface complexity that is directly linked to the interaction of droplets and ice is riming, the accretion of small droplets on the surface of ice particles as shown in Fig. 2.20.9 and the top rows of Fig. 2.19. Riming is explained in depth in the following section. Also, in situ observations of riming on ice particles in MPCs as well as the implications for their light scattering properties are presented in Chapter 7. The other types of crystal complexity will not be discussed in further detail in this work.

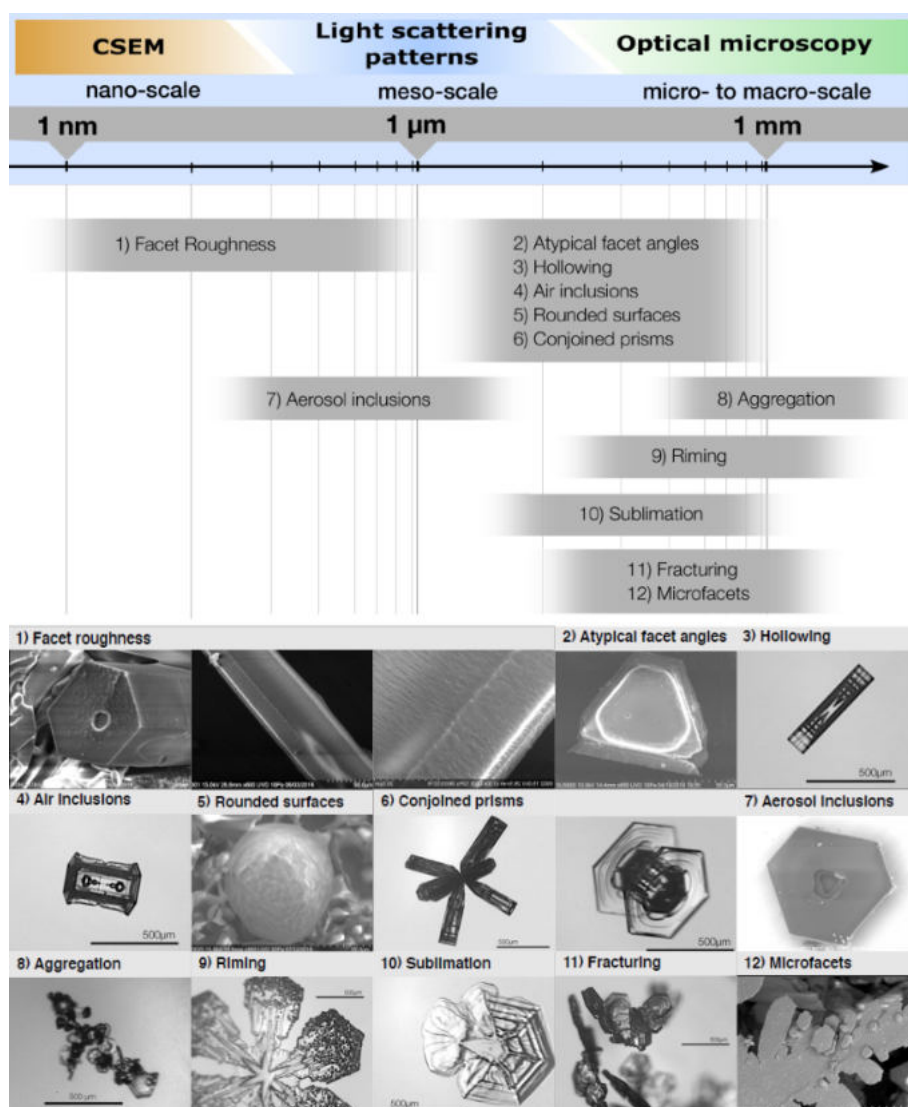


Figure 2.20.: Overview of different types of crystal complexity on nano-scale (observable via cryoscopic scanning electron microscopy), meso-scale (observable via light scattering patterns) and micro- to macro-scale (observable via optical microscopy) as well as corresponding exemplary particles for each category imaged via cryoscopic scanning electron microscopy (CSEM) (1, 2, 5, 7 and 12) and PHIPS (rest), adapted from Järvinen et al. [2021b].

2.4.3. Riming

One of the main growth modes of ice particles in MPCs is *riming*. Riming refers to the accretion of supercooled liquid droplets on the surface of ice particles. Riming can be divided into two (not always easily distinguishable) sub-topics: riming of small ice particles (diameter $D \approx 100 \mu\text{m} - 1000 \mu\text{m}$) in clouds and riming of large (D between $\geq 1000 \mu\text{m}$ and $5000 \mu\text{m}$) precipitating ice, graupel and snow particles. The typical life cycle of an exemplary rimed crystal is usually as follows:

1. The ice particle is formed, e.g. due to deposition nucleation or immersion freezing on an INP (see Section 2.3.3.2).
2. The ice particle grows by vapor deposition (see Section 2.3.4) until it has reached a critical minimum size (depending on shape and habit, e.g. $D \geq 60 \mu\text{m}$ for columns [e.g. Ono, 1969; Ávila et al., 2009]).
3. The ice particle collects small, supercooled droplets (around $D = 10 \mu\text{m} - 40 \mu\text{m}$ [e.g. Harimaya, 1975; Wang and Ji, 2000]) that freeze on the crystal's surface until it is too heavy and precipitates.
4. Whilst falling, the ice particle can accrete even more droplets and grow further until it reaches the ground as graupel or snow.

In principle, riming can occur everywhere where ice particles and supercooled droplets coexist. So far, the exact processes that influence the riming of cloud particles are not well understood. A deterministic parameterization of when and where to expect how much riming does not exist. The riming efficiency of an ice particle is a function of (i) its collection efficiency and (ii) the number of supercooled droplets, integrated over (iii) the time the ice particle spends in the cloud and during precipitation. These three quantities depend on numerous parameters, such as the temperature [Kneifel and Moisseev, 2020], the habit and size of the ice particle [Ono, 1969; Wang and Ji, 2000; Ávila et al., 2009], the size of the supercooled droplets [Saleeby and Cotton, 2008] as well as the turbulence and vertical velocity [Herzogh and Hobbs, 1980; Garrett and Yuter, 2014]. In situ observations of the correlation of riming with some of those parameters are part of this work and will be discussed in detail in Chapter 7.

The implications of riming are manifold, affecting the life cycle of clouds as well as the microphysical properties of ice particles:

- Ice particles grow, both in size and mass, until they precipitate [Pruppacher and Klett, 1997].
- Subsequently, the scavenging of (supercooled) liquid water affects droplet size distribution and number concentration and thus liquid water content (LWC) as well as aerosol concentration [Baltensperger et al., 1998; Hegg et al., 2011].
- This growth consequently changes the clouds lifetime and radiative properties.
- Since the ice particles are of higher mass and more compact, their fall speed and terminal velocity are increased [Locatelli and Hobbs, 1974; Lin et al., 2011; Garrett and Yuter, 2014].
- *Rime splintering* (Hallett-Mossop-process) can initiate secondary ice processes [Hallett and Mossop, 1974], thus leading to formation of new ice particles (see Section 2.3.3.3).
- Riming leads to increased surface roughness and crystal complexity and hence change the ice particle's light scattering properties, as shown in e.g. Schnaiter et al. [2016]; Järvinen et al. [2018]; Järvinen et al. [2021b] as well as Section 7.4.

Most studies on riming are either conducted in the laboratory [e.g. Takahashi, 1979a] or on freshly fallen snow [e.g. Ono, 1969; Moisseev et al., 2017]. In recent years, multiple studies have used radar measurements to retrieve information about snow and riming density based on their vertical Doppler-velocity [Mosimann et al., 1993; Leinonen and Szyrmer, 2015; Leinonen et al., 2018; Mason et al., 2018; Kneifel and Moisseev, 2020]. Those methods proved to be fit to determine the riming state of large, precipitating snow and graupel particles. However, they cannot resolve the fine structure of small or freshly rimed ice particles inside clouds if the radar signal is dominated by large graupel particles in the size range around $D = 1 \mu\text{m} - 10 \text{mm}$.

In situ studies with high-resolution cloud imaging probes that investigate the properties of individual rimed particles sampled directly in the cloud are scarce. The difficulty is to resolve the riming features and discriminate between rimed and irregular particles. Further, analysis of particle images is quite complex and hence difficult to automate, and manual assessment of particle properties is very laborious.

Consequently, the riming of ice particles is often times poorly (or not at all) represented in climate models. Most models account for the riming degree only in the sense of a *subtype* for hydrometeors (e.g. *cloud ice*, *graupel*, *snow*, COSMO, [Blahak and Seifert, 2015], www.cosmo-model.org/). Riming is neglected completely in most model studies of the Arctic [e.g. Fan et al., 2011b; Ovchinnikov et al., 2014; Stevens et al., 2018].

In the following section, different methods and instrumentation to measure microphysical properties will be introduced and the strengths and challenges of the different measurement techniques are discussed. Occurrence and properties of rimed ice particles will be discussed in detail in Chapter 7.

2.5. In situ Measurement of Cloud Particles

To describe a cloud, the most basic questions and corresponding observables are:

- How dense is the cloud - i.e. what is the total number **concentration** of cloud hydrometeors per unit volume?
- How much water is in the cloud - i.e. what is the condensed total water content (TWC) that is present in the form of droplets or ice particles per unit volume (the sum of LWC and IWC)?
- What is the **phase** of the cloud particles - i.e. are the hydrometeors liquid droplets or ice particles?
- What is the **size** the cloud particles?

The direct way to answer these questions is via in situ measurements using airborne wing-mounted cloud probes. There exists two main methods to measure the properties of cloud particles using aircraft cloud probes — via images and via light scattering. In the following, the different methods are discussed and the most common in situ instruments are introduced.

2.5.1. Particle Sizing

Based on images

There are different methods to generate images: via shadow and microscopic imaging (see Section 2.5.5). Taking an image of a cloud particle produces a 2D projection of it. Based on this, the maximum dimension (D_{max}) and geometric cross section (area) equivalent

diameter (D_{geom}) can be determined. D_{max} is simply the largest distance within the particle or illustratively the diameter of a circle around the particle. D_{geom} is calculated based on the geometric cross section (σ_{geom} , equivalent to the area of the image) as if it was circular

$$D_{\text{geom}} = \sqrt{\frac{4}{\pi} \sigma_{\text{geom}}}. \quad (2.72)$$

For spherical particles, which result in a circular projection, D_{max} and D_{geom} are identical. For aspherical particles, D_{max} and D_{geom} can differ significantly. For example, assume a columnar ice particle with length $L = 100 \mu\text{m}$ and basal width $b = 20 \mu\text{m}$. If this column is imaged from one of its prismatic sides, the projection is simply a rectangle with the sides L and b and cross section $\sigma_{\text{geom}} = b \cdot L$ resulting in $D_{\text{max}} = \sqrt{b^2 + L^2} = 101.98 \mu\text{m}$ and $D_{\text{geom}} = 50.46 \mu\text{m}$.

Further, the measured size of the particle strongly depends on the orientation of measurement. If the same hypothetical column was imaged from the front, i.e. facing the basal face, the resulting projection is a hexagon with $D_{\text{max}} = b = 20 \mu\text{m}$ and cross section $\sigma_{\text{geom}} = \frac{3\sqrt{3}}{8}b^2$ and thus $D_{\text{geom}} = 18.19 \mu\text{m}$.

Based on scattering measurement

Another possible definition of the size of a cloud particle is its scattering equivalent diameter D_{scatt} . It is defined similarly to D_{geom} as

$$D_{\text{scatt}} = \sqrt{\frac{4}{\pi} \sigma_{\text{scatt}}^{\text{tot}}} \quad (2.73)$$

based on the total scattering cross section instead of the geometrical.

Typically, scattering based in situ cloud measurement probes do not measure the total scattering cross section ($\sigma_{\text{scatt}}^{\text{tot}}$) but rather the differential cross section over a certain solid angle ($\sigma_{\text{scatt}}^{\text{diff}}(\Omega) = \frac{d\sigma_{\text{scatt}}}{d\Omega}$, see Section 2.2.4). As shown in Section 3.1.1, the partial scattering cross section is approximately proportional to the geometrical cross section for spherical particles. This proportionality factor can be determined using empiric calibration.

In this work, a method is described to determine the scattering equivalent diameter of cloud particles based on their angular scattering function measured by PHIPS. The sizing method is calibrated using the area equivalent diameter deducted from the corresponding images. This will be discussed in Chapter 5.

2.5.2. Phase Discrimination

As discussed in the previous section, to correctly determine the size of cloud particles, it is important to know their phase. Further the microphysical as well as radiative properties of liquid cloud particles differ strongly compared to aspherical particles as discussed previously. Furthermore, the concentration of droplets can surpass the amount of ice particles by up to multiple orders of magnitude. Hence, reliable and precise phase discrimination of single cloud particles is crucial for the correct representation of clouds.

Based on images

The most common phase discrimination method is based on sphericity measurement based on imaging probes [Holroyd, 1987; McFarquhar et al., 2018]. However, image based discrimination methods have uncertainties discriminating quasi-spherical ice particles

[Cober et al., 2001]. Fig. 2.21 shows stereo-images of a droplet (a) and a quasi-spherical ice particle (b) acquired by PHIPS during the SOCRATES campaign. It shows how the phase of the particles can be hard to discriminate based on the images alone. This leads to a high uncertainty in phase discrimination, especially for slightly out of focus or smaller particles ($D \lesssim 200 \mu\text{m}$) as well as for probes with a limited optical resolution. Fig. 2.21c shows the corresponding angular scattering behaviour which differs significantly and can be used to determine the phase of the particle as discussed in the following.

Particle imagers with higher resolution have the downside that the time needed for acquisition and saving of the images increases and hence limits acquisition frequency and thus temporal and/or spatial resolution.

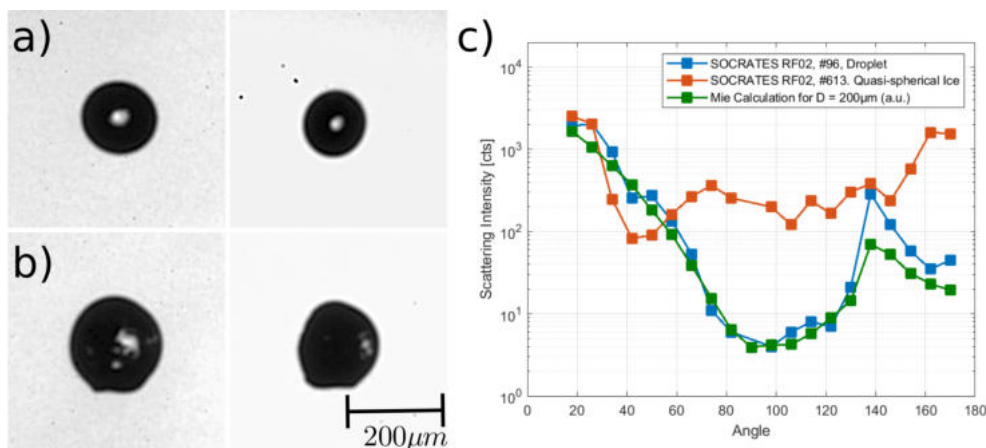


Figure 2.21.: Stereo micrograph of a droplet (a) and a quasi-spherical ice particle (b) taken by the PHIPS probe. In the stereo micrograph, the two views of the particle have an angular distance of 120°. The instrument concurrently recorded the angular light scattering functions of the imaged particles as displayed in (c). The theoretical scattering function calculated for a droplet with a diameter of 200 μm calculated using the Mie theory is shown for comparison in (c). The calculated scattering-intensity is integrated over the field of view of each of PHIPS' 20 polar nephelometer channels so it can be compared to the measurement (see Section 3.1.1 for details).

Based on scattering measurements

As discussed in Section 2.2.4, the scattering properties of spherical droplets and aspherical ice particles differ significantly. These differences can be used to discriminate cloud particles based on light scattering measurements.

One method is the measurement of spatially resolved scattering patterns in the forward direction. Based on the shape of the 2D scattering patterns (rings for spherical droplets, "lines" and irregular patterns for pristine and rough ice particles, see Section 2.5.5.4 and Fig. 2.23). However, coincidence of multiple droplets leads to overlap of scattering pattern or artifacts results in the misclassification of droplets as ice particles [Vochezer et al., 2016].

Another method is phase discrimination based on (de-)polarization measurements of backscattered light. Backscattering of spherical droplets does not change the polarization state of the incident light, whereas backscattering of randomly oriented ice particles results in a depolarization ratio of roughly 30% [Liou and Schotland, 1971; Liou and Lahore, 1974; Sassen, 1991; Nichman et al., 2016].

A third method is based on polar nephelometer probes that measure the angular scattering function of cloud particles over a broad angular range. Fig. 2.21c shows the angular scattering functions of a droplet and quasi-spherical ice particle. While those particles are

hard to discriminate based on visual inspection, the angular scattering functions differ significantly and allow for a confident determination of the phase of the particles.

In this work, a novel phase discrimination method based on the angular scattering function of single particles measured by PHIPS is presented. This will be explained in detail in Chapter 4.

2.5.3. Particle Size Distributions

After determining their phase and size, the most common way to combine the measurement of a set of particles is to derive particle size distributions (PSDs). The PSD describes the concentration N of droplets and ice particles per unit volume resolved by size

$$N(D) = \int_{D_1}^{D_2} \frac{n(D)}{V(D)} dD \quad (2.74)$$

where n is the number of particles with diameter $D_1 \leq D < D_2$ measured within the measurement volume

$$V_{\text{sens}}(D) = A_{\text{sens}}(D) \cdot v \cdot \Delta t \quad (2.75)$$

that was sampled during a given time (typically $\Delta t = 1$ s or $\Delta t = 10$ s). v is the relative airspeed of the aircraft, i.e. difference of aircraft velocity and the surrounding air parcels (typically around $v \approx 150$ m/s). A_{sens} is the sensitive detection area of the instrument in which particles are sampled. In most cases, A_{sens} is size dependent (see Section 3.1.3).

Typically, an PSDs is normalized by bin width and plotted as $\frac{dN}{dD}$ or $\frac{dN}{d \log(D)} = D \frac{dN}{dD}$ over D or $\log(D)$, respectively. This way, the PSD is not dependent on the width of the chosen size bins (D_1, D_2) and results between probes with different size bin edges can be compared.

2.5.4. Condensed Water Content

Based on the PSD of a cloud, the mass of water that is present in the form of droplets and ice particles can be estimated. For spherical particles, this is trivial as the mass of a spherical droplet (LWC) is simply

$$m_{\text{liq}}(D) = \rho_{\text{water}} \cdot V_{\text{particle}} = \frac{\pi \rho_{\text{water}}}{6} D^3. \quad (2.76)$$

For aspherical ice particles, the IWC can be estimated in a similar fashion as

$$m_{\text{ice}}(D) = a \cdot D^b \quad (2.77)$$

using empiric parameterization where a and b are calibration parameters. However, the mass-dimension-relationship is strongly dependent on their habit as well as definition of the used diameter (see discussion above). In this work, the parameterization proposed by Ham et al. [2017] based on Yang et al. [2000] for a mixture of habits ($a = 0.497, b = 3.296$) is used to estimate LWC and IWC based on PSDs as

$$\text{Water content} = \int m(D) N(D) dD. \quad (2.78)$$

The cloud water content can also be measured directly with e.g. hot-wire probes. These instruments as well as other common in situ cloud probes are introduced in the following section.

2.5.5. In situ Aircraft Cloud-Particle Measurement Instruments

One of the main goals of this work is to present a new method to derive phase discriminated cloud PSDs in MPCs, where droplets and ice particles are present at the same time. This will be done based on data acquired by the PHIPS probe, which will be explained in depth in the next chapter. But first, the most common wing-mounted in situ probes to study the microphysical properties of cloud particles will be introduced shortly. Remote sensing and ground based methods will not be discussed.

2.5.5.1. Hot-Wire Probes

Hot-wire probes, such as the King or Nevzerov instruments, are designed to measure LWC [King et al., 1978; Korolev et al., 1998]. The instrument consists of a heated wire that is exposed to the incoming particle stream. When droplets impact the wire, they evaporate and the wire loses heat. Based on the lost energy, i.e. energy that is needed to heat the wire back to its original temperature, the mass of the droplet can be estimated. Ice particles are supposed to bounce off the wire and not change the temperature of the wire. However, it was shown that "residual ice effects", i.e. the small amount of lost heat during the collision of ice particles can significantly overestimate the measured LWC [Korolev et al., 2003]. Simultaneously, the LWC can be underestimated for drizzle droplets $D \geq 50 \mu\text{m}$ that (partly) bounce off the wire and do not entirely evaporate.

The TWC is measured using a similar setup with a heated hollow cone in addition to the wire. Droplets as well as ice particles get caught in the cone, evaporate and the mass is calculated based on the heat loss. Based on the difference between TWC and LWC the IWC is estimated.

Hot-wire probes have the advantage that they directly measure LWC and IWC and are hence not reliant on (habit dependent) mass-diameter-parameterizations and hence avoid the corresponding uncertainties. They typically have a high temporal resolution and large sensing volume which reduces statistical uncertainties. However, hot-wire probes measure large bulks of particles at once and cannot resolve the microphysical properties of individual particles.

2.5.5.2. Optical Array Probes

The most common instrument class for the investigation of cloud particle microphysics are optical array probes (OAPs) such as the Cloud Imaging Probe (CIP) and Precipitation Imaging Probe (PIP) (both DMT, Longmont, USA), or the Two-dimensional Cloud Probe (2D-C) and Two-dimensional Stereo Probe (2D-S) (both SPEC Inc., Boulder, USA). The core setup of OAPs consists of two opposing arms. A light source, which is guided through one arm, illuminates the path between the two arms and casts a shadow image of particles within on the second arm. Located in the second arm there is a set of charge coupled device (CCD) sensors (the optical array) which measure the intensity of the shadows of the particles within the instruments field of view (FoV). The 2D-S, which consists of two pairs of arms, is shown in Fig. 2.22a on the wing of the National Center of Atmospheric Research (NCAR) C-130 aircraft. Fig. 2.22b shows example data of the 2D-S acquired in a cirrus cloud.

Based on those shadow images, the maximum and area equivalent size of the particles is calculated. Further, the particle phase can be estimated based on its sphericity [Holroyd, 1987; Cober et al., 2001; McFarquhar et al., 2018]. OAPs have the advantage that they have a large sensitive volume ($V_s \approx 0.1 \text{ L s}^{-1} - 10 \text{ L s}^{-1}$) and fast acquisition rate of multiple MHz as well as fairly wide detection range for $D = 10 \mu\text{m}$ to $100 \mu\text{m}$ and are hence established to produce cloud PSDs. One disadvantage of OAPs is their limited optical resolution

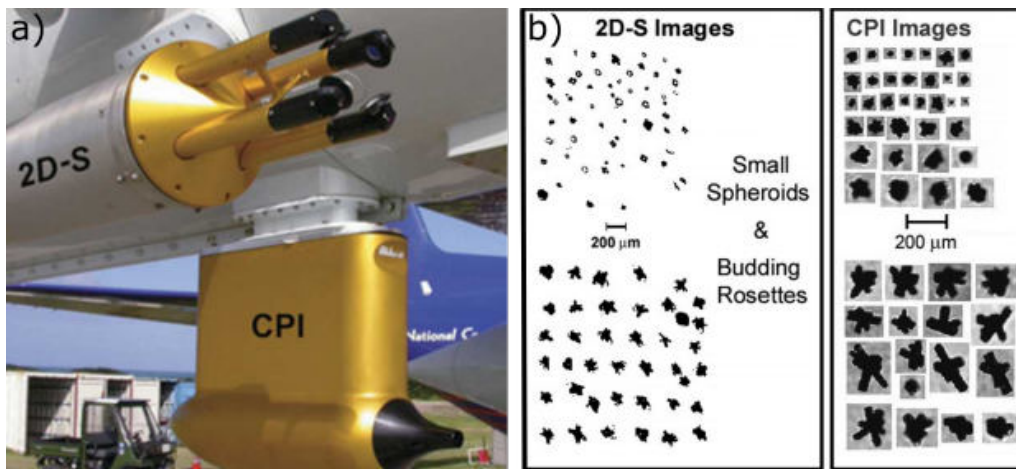


Figure 2.22.: Photographs of the 2D-S and CPI probes installed on the NCAR C-130 (a) and examples of images from the 2D-S and CPI acquired in a cirrus cloud (b). Both figures are taken from [Lawson et al., 2006].

(e.g. $25\ \mu\text{m}$ for the 2D-C) which leads to uncertainties in size and sphericity for small particles ($D < 200\ \mu\text{m}$) that consist of just a few pixels, especially for “fogged” or out of focus particles [Korolev, 2007b; Wu and McFarquhar, 2016].

2.5.5.3. Particle Imaging Probes

At first glance, the setup of particle imaging instruments is similar to the setup of OAPs: particles fly through the sensitive area, get illuminated by a light source (typically a laser) and are imaged. However, the key difference lies within the imaging unit: the particles are not imaged by an optical array but a high resolution camera including a magnification optical setup. Hence, imaging probes usually do not have the same open path symmetry as OAPs but instead the particles are guided through the instrument. One common imaging probe is the Cloud Particle Imager (CPI) (SPECinc, Boulder, USA) which is shown in Fig. 2.22a.

The advantage of particle imagers is that they have a much higher optical resolution compared to OAPs. Fig. 2.22b shows exemplary images acquired by the CPI. The high optical resolution allows for a precise determination of particle size and sphericity analysis for small particles down to $D = 35\ \mu\text{m}$ [McFarquhar et al., 2013]. Further, the microscopic images offer much more detail about the particle such as particle habit as well as surface complexity features such as riming. However, since the camera needs to be precisely focused on a single particle, the sensing area is a lot smaller compared to OAPs which results in a lower temporal resolution. Also, the closed geometry makes the instrument more prone to shattering as ice particles have more chance to collide within the inlet compared to OAPs (see Section 5.2).

2.5.5.4. Light Scattering Probes

Another method to derive the size of cloud particles is based on their light scattering properties.

The Cloud Droplet Probe (CDP) (DMT, Longmont, USA), Small Ice Detector Mark 3 (SID-3) [Vochezer et al., 2016] (shown in Fig. 2.23a) and Particle Phase Discriminator (PPD) [Hirst and Kaye, 1996; Kaye et al., 2008; Vochezer et al., 2016; Mahrt et al., 2019] are in situ instruments that measure the light scattering in forward direction of small cloud particles in a size range from $D = 1\ \mu\text{m}$ to $50\ \mu\text{m}$. These scattering probes have the advantage that

they operate with a very high acquisition frequency and are hence well established to measure cloud PSDs for small particles. However, the light scattering intensity alone allows no conclusion about the phase of the particles. Hence, the SID-3 or PPD also measure the spatially-resolved scattering pattern for a subset of particles, from which information about their phase as well as surface roughness can be concluded (see Fig. 2.23b-d).

The *Cloud and Aerosol Spectrometer with Polarization* (CAS-POL, DMT, Longmont, USA, [Glen and Brooks, 2013]) is an instrument that measures the light scattered by single cloud particles and aerosols in a size range of $0.6\mu\text{m} \leq D \leq 50\mu\text{m}$ in the forward and backward directions. Based on the polarization ratio of the backscattered light, the sphericity of the cloud particles can be estimated [Sassen, 1991; Nichman et al., 2016]. However, recent studies have suggested that particle phase discrimination of polarization-based measurements can misclassify up to 80% of the ice particles as droplets in the presence of small, quasi-spherical ice [Järvinen et al., 2016]. Simultaneously, slightly aspherical droplets (see e.g. Section 4.5) also result in a depolarization of the backscattered light [Bi et al., 2018] and can hence be misclassified as ice. Further, due to the integration over a finite solid angle around $\theta = 180^\circ$, even perfectly spherical droplets show a non-zero depolarization ratio and can hence be misclassified as ice [Glen and Brooks, 2013].

Polar Nephelometers (PNs) are instruments that measure the angular scattering properties of cloud particles in one polar plane over a wide angular range [Gayet et al., 1997; Jourdan et al., 2003]. The difference in the phase function of spherical and aspherical particles can be used to discriminate droplets and ice particles as discussed in Section 2.2.4. However, current PN instruments have the disadvantage that they measure a large ensemble of cloud particles at the same time, hence single particles remain undetected which leads to biases for e.g. low concentrations of ice in dense liquid cloud and vice versa.

In this work, the PHIPS probe is used. It is an airborne cloud probe that combines the aspects of a particle imager and a polar nephelometer. Its setup and working principle is explained in the following chapter.

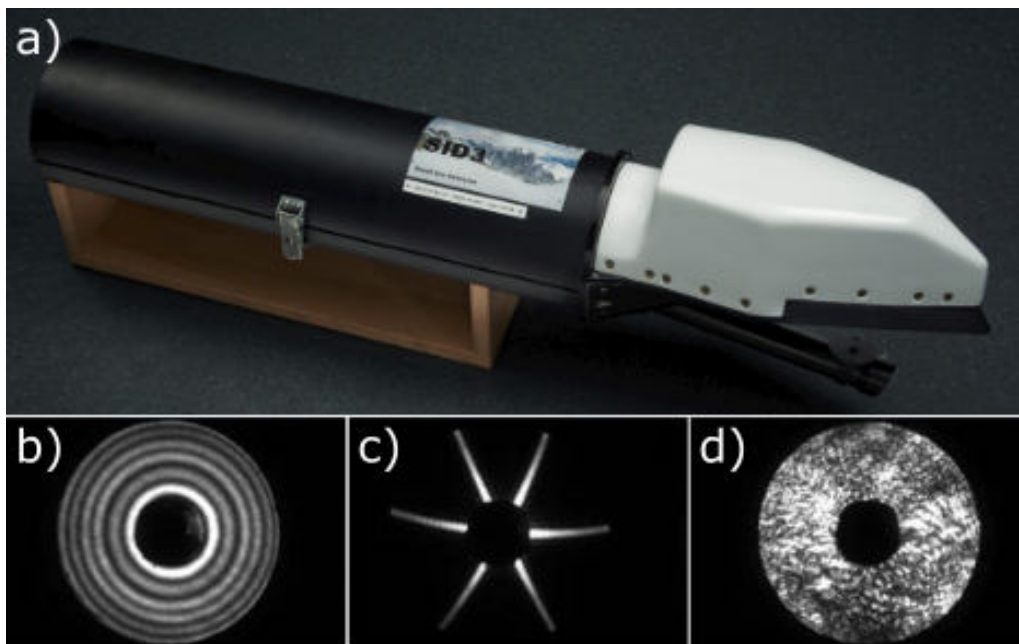


Figure 2.23.: Photo of the SID-3 probe (a, image credit: KIT/ Markus Breig) and scattering patterns of a droplet (b), pristine column (c) and rough ice particle (d) acquired by the SID-3.

3. Experimental Setup

3.1. The Particle Habit Imaging and Polar Scattering Probe (PHIPS)

The Particle Habit Imaging and Polar Scattering (PHIPS) probe is an airborne, wing-mounted, in situ cloud probe that simultaneously measures the microphysical and scattering properties of individual cloud particles [Abdelmonem et al., 2016; Schnaiter et al., 2018]. Fig. 3.1a shows PHIPS on the wing of the P3 aircraft during the IMPACTS campaign. The optical and processing unit are shown with opened covers in Fig. 3.1b and Fig. 3.1c.

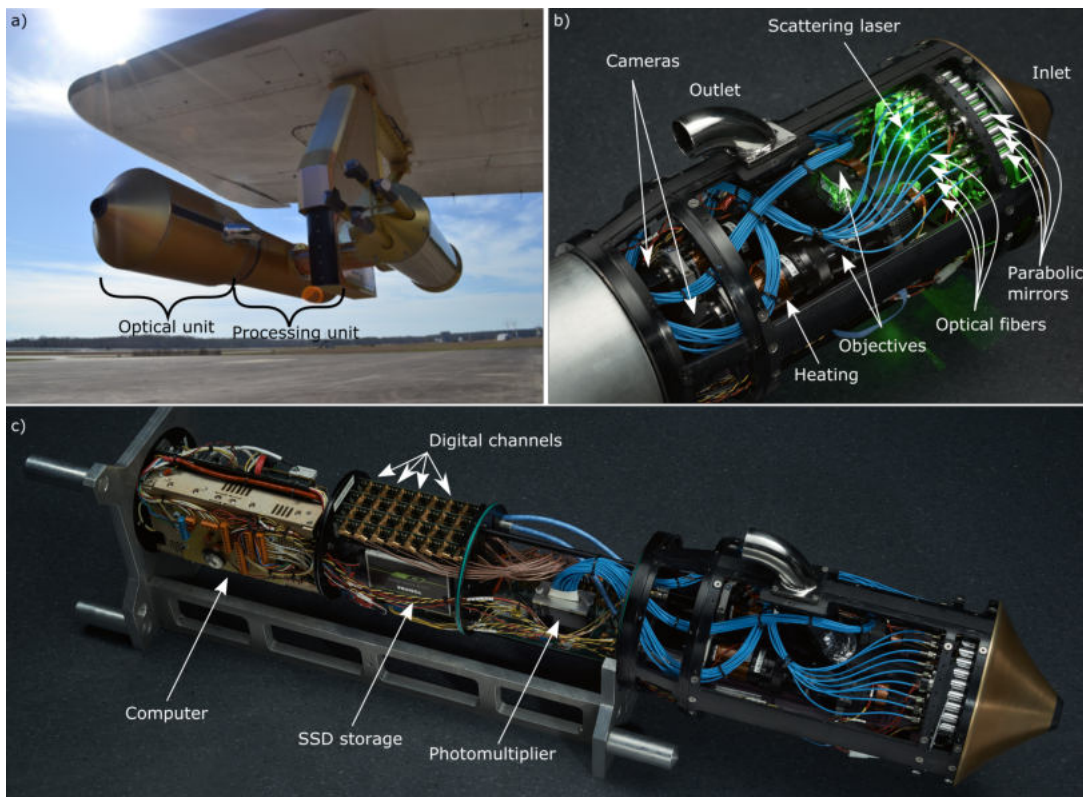


Figure 3.1.: PHIPS on the wing of the P3 aircraft during the IMPACTS campaign (a, on the left), close up view of the optical unit with running scattering laser (b, image credit: KIT/ Markus Breig) and view of the whole instrument including processing unit (c, image credit: KIT/ Markus Breig).

Fig. 3.2 shows the working principle of PHIPS. When the aircraft flies through a cloud, cloud particles stream through the inlet (blue line in Fig. 3.2). If the particle is large enough, it is detected by the trigger sensor (which is located below the base plate and hence not shown in the figure). The trigger then initiates two things: a scattering measurement

(green in Fig. 3.2) of 20 scattering channels and the acquisition of stereo images via two microscopic cameras (red in Fig. 3.2). This way, PHIPS measures the differential scattering cross sections over 20 angular positions and acquires corresponding stereo images of the same individual cloud particle. It combines the measurement principles of a particle imager (such as the CPI) and a single particle polar nephelometer (such as the PN, see Section 2.5.5). Fig. 3.3 shows the stereo images of two exemplary particles, a droplet¹ and an ice particle² as well as their corresponding More information about the trigger sensor, the scattering system and the image acquisition are given in the following sections. An algorithm to discriminate droplets and ice based on their light scattering properties is introduced in Chapter 4.

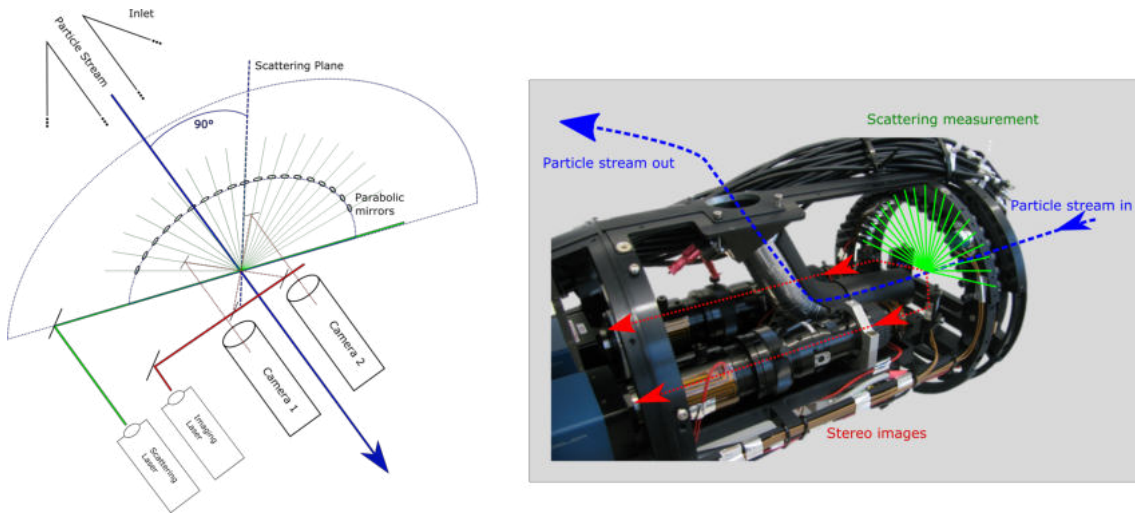


Figure 3.2.: Sketch of the measurement principle of PHIPS. The particle stream is marked in blue, the scattering measurement in green and the image acquisition in red.

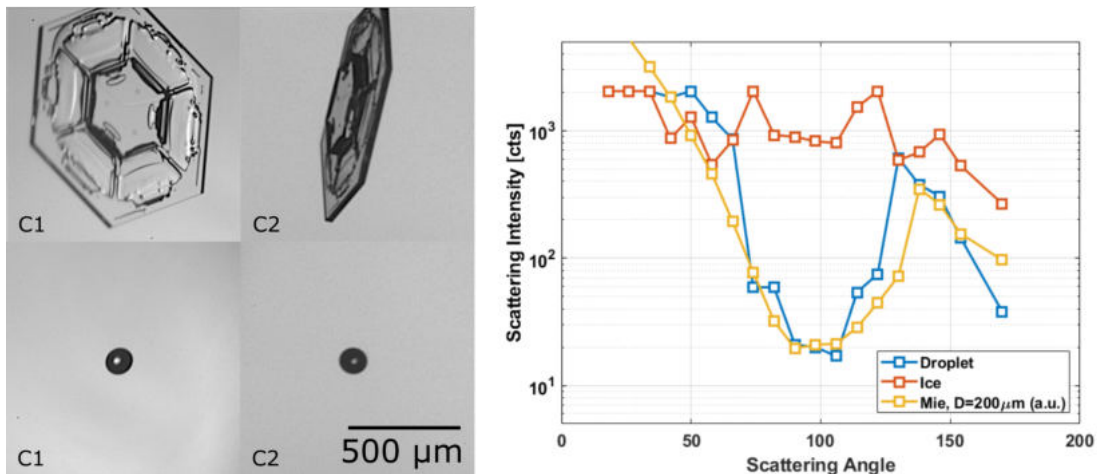


Figure 3.3.: Stereo images of an exemplary deformed droplet and ice particle acquired during the IMPACTS campaign and their corresponding angular scattering functions as well as the calculated angular scattering function of a spherical particle ($D = 200 \mu\text{m}$) using Mie theory. The theoretical angular scattering function is scaled by a constant factor that accounts for the laser power and the conversion from counts to W of the MAPMT.

¹IMPACTS, flight 20200118 #37611

²IMPACTS, flight 20200118 #13506

3.1.1. Scattering Measurement

Fig. 3.4 shows a schematic view of the setup of PHIPS' angular scattering measurement. The scattering laser is a green Nd:YAG continuous wave laser with a wavelength $\lambda = 532 \mu\text{m}$ and laser power between 76 mW for ACLOUD and 55 mW SOCRATES. The laser has a Gaussian beam-shape and a $1/e$ diameter of roughly $D_{\text{Laser}} = 0.86 \text{ mm}$ (see Section 3.1.3). When triggered, the 20 channels measure the light that is scattered by the particle. The 20 channels are located in 8° steps from 18° to 170° perpendicular to the particle stream. The light is collected via parabolic mirrors with a radius $R = 5 \text{ mm}$ which are located $r = 83 \text{ mm}$ from the scattering center. The half opening angle of the parabolic mirrors is $\alpha = \arctan\left(\frac{R}{r}\right) = 3.5^\circ$. The light is then guided via optical PMMA (polymethyl methacrylate) fibers to a multi-anode photomultiplier array (MAPMT) (Hamamatsu, model H7260) in the electronic part of the probe. A custom made fibre-coupler was designed to minimize crosstalk between individual fibers (see Appendix A.1) for the transition between fibers and MAPMT. The maximum temporal resolution, i.e. acquisition frequency of scattering data is 3.5 kHz.

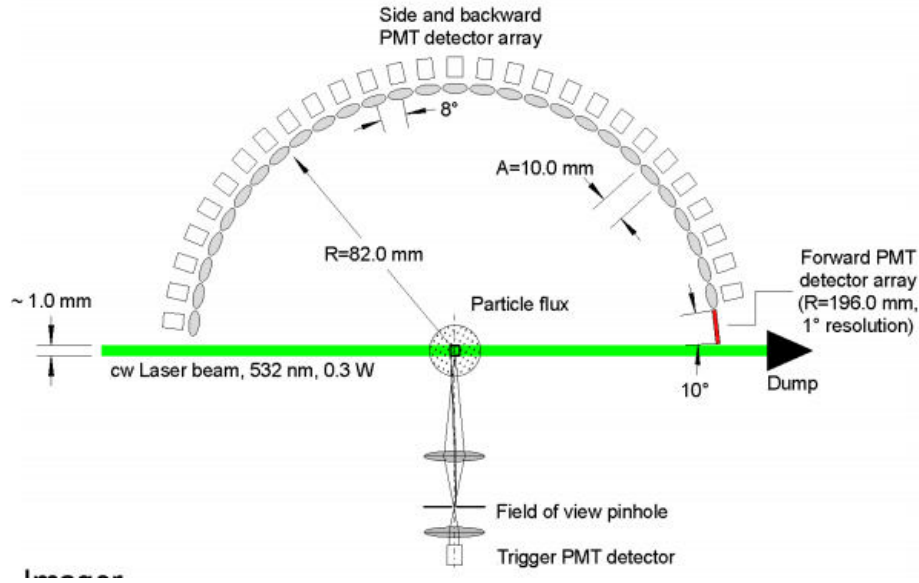


Figure 3.4.: Schematic view of PHIPS' scattering setup (figure adapted from Stegmann et al. [2016])

Nephelometer Field of View

The total amount of measured light per channel I_{channel} is calculated as the integral over the surface of the detector A , i.e. the total intensity that arrives in the solid angle Ω of each parabolic mirror

$$I_{\text{channel}} = \int \int_A I(\Omega) d\Omega = \int \int_A I(\theta) dA \quad (3.1)$$

Due to the azimuth symmetry of the detectors, it is only depending on the polar angle θ . The surface of a circular detector with the center at θ_0 is calculated via

$$\int dA = 2\pi r \int_{\theta_0-\alpha}^{\theta_0+\alpha} x(\theta) d\theta \quad (3.2)$$

where $x(\theta)$ is the width perpendicular to the scattering plane of the detector as shown in Fig. 3.5. It is calculated as

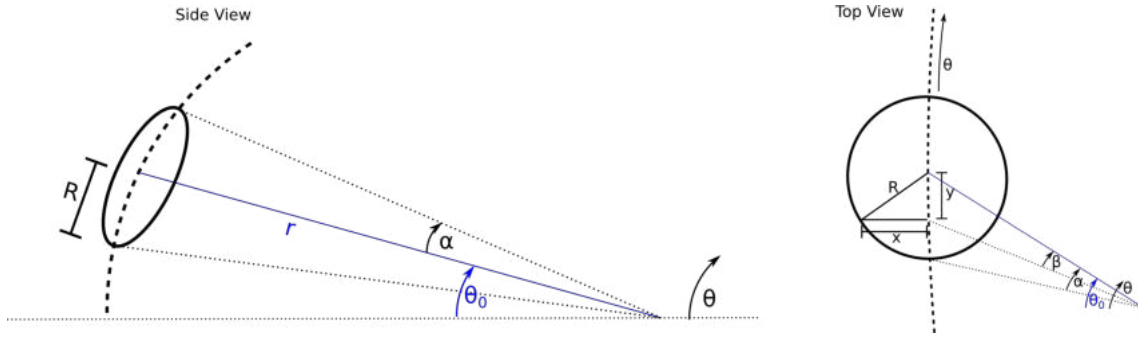


Figure 3.5.: Sketch of the angular range of PHIPS' polar nephelometer channel, left: side view, right: top view (not to scale).

$$x = \sqrt{R^2 - y^2} \quad (3.3)$$

$$= \sqrt{r^2 \tan^2(\alpha) - y^2} \quad (3.4)$$

$$= \sqrt{r^2 \tan^2(\alpha) - r^2 \tan^2(\theta - \theta_0)}. \quad (3.5)$$

Finally, to account for curvature of the surface, this has to be corrected to

$$x \rightarrow r \cdot \arctan\left(\frac{x}{r}\right). \quad (3.6)$$

The final integrated intensity per detector at the position θ_0 reads

$$I(\theta_0) = 2\pi r^2 \int_{\theta_0 - \alpha}^{\theta_0 + \alpha} I(\theta) \cdot \arctan\left(\sqrt{\tan^2(\alpha) - \tan^2(\theta - \theta_0)}\right) d\theta. \quad (3.7)$$

This can be converted to the differential scattering cross section

$$\sigma_{\text{scatt}}^{\text{diff}}(\theta_0) = I(\theta_0)/I_{\text{inc}} \cdot \pi \cdot D_{\text{laser}}^2/4, \quad (3.8)$$

with I_{inc} and D_{laser} the power and diameter of the incident laser beam, respectively.

Angular Scattering Function

In Section 2.2.4, the phase functions of spherical and aspherical cloud particles have been discussed. As PHIPS measures the differential scattering cross sections over 20 angular positions, it does not measure the complete phase function. Hence, to any confusion, in this work the angular resolved scattering intensity measured by PHIPS is referred to as ASF.

Fig. 3.6 shows the comparison of the theoretical phase function of a spherical particle with $D = 200 \mu\text{m}$ calculated using Mie theory (blue) and the corresponding ASF how PHIPS would measure the same particle (red). Due to the coarse angular resolution fine features such as the oscillations vanish. The distinct scattering features of the scattering phase function p discussed in Section 2.2.4.1 such as the decrease towards the minimum around $\theta = 90^\circ$ and the increase towards the rainbow at $\theta = 138^\circ$ are still clearly visible in the ASF. The measured ASF of real droplets and ice particles measured by the PHIPS are shown in Fig. 3.3.

Fig. 3.7 shows the calculated ASF for spherical droplets of different size. It can be seen that shape of the ASF is only very weakly depending on the particle diameter. It can be further

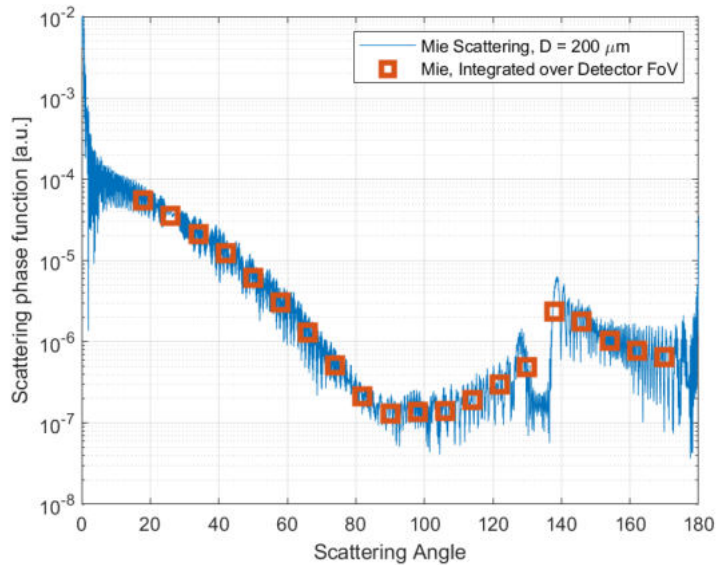


Figure 3.6.: Calculated phase function p of a droplet with $D = 200 \mu\text{m}$ (blue) and the same differential scattering cross sections (angular scattering function (ASF)) integrated over the FoV of PHIPS' nephelometer channels (red).

seen that the ASF is in good approximation proportional to the geometrical cross section (i.e. proportional to diameter squared) of the particle.

In this work, the distinctive differences in the ASFs of spherical and aspherical particles are used to discriminate the phase of cloud particles, i.e. differentiate liquid droplets from solid ice particles. This will be explained in detail in Chapter 4. The size of cloud particles is calculated based on the amplitude of their ASFs in Chapter 5.

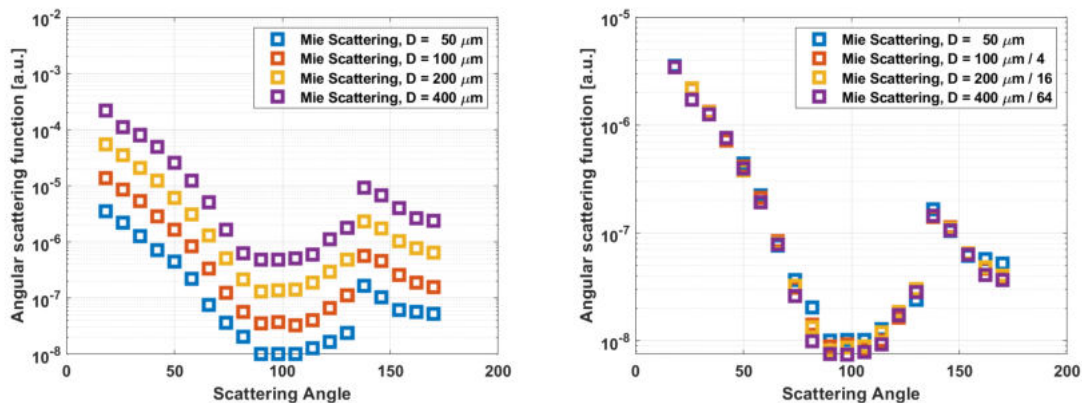


Figure 3.7.: Calculated Mie intensity for droplets of various size (left) and the same graph normalized by diameter squared (right).

3.1.2. Image Acquisition

The setup of PHIPS' imaging unit is shown in Fig. 3.8. Simultaneous to the scattering measurement, PHIPS takes stereo images of the triggered particles using two cameras (GE1380, Allied Vision Technologies Inc., Canada) with a 2/3" 12 bit CCD sensor with 1360x1024 pixel resolution which corresponds to a pixel size of $6.45 \mu\text{m} \times 6.45 \mu\text{m}$. The cameras are fit with microscopic zoom objectives (Zoom 6000, Navitar Inc., USA) with a variable magnification. This setup consisting of camera and zoom objectives is referred

to as camera telescope assembly (CTA). For CTA2, the magnification ranges from 1.4 to 9.0, which corresponds to a FoV ranging from $6.27 \text{ mm} \times 4.72 \text{ mm}$ to $0.98 \text{ mm} \times 0.73 \text{ mm}$, respectively. The optical resolution ranges from $7.2 \text{ }\mu\text{m}$ to $2.35 \text{ }\mu\text{m}$ for the low ($1.4\times$) and high ($9.0\times$) magnification, respectively. A typical operating optical resolution is approx. $5.3 \text{ }\mu\text{m}$ (at $4\times$ magnification) with a FoV of approx. $2.19 \text{ mm} \times 1.65 \text{ mm}$. For CTA1, the magnification is 10% higher, i.e. 1.54 to 9.9. The optical path of CTA1 and CTA2 is aligned via mirrors so that the cameras are focused on particles within the sensitive trigger area at angles $\pm 60^\circ$ with respect to the particle path which corresponds to $\theta = 30$ and $\theta = 150^\circ$. They are oriented perpendicular to the scattering plane, in the same plane as the particle path.

To acquire the image, the particles are illuminated from behind using a 40 ns incoherent pulsed diode laser (Cavitar, model Cavilux, $\lambda = 690 \text{ nm}$, 400 W, Class 4), producing a bright field microscopic image. The flash laser beam is divided using a beam-split and aligned with mirrors onto the optical path of the cameras as indicated in Fig. 3.2. Due to the incoherent light, diffraction effects are suppressed [Guenther, 2015] and the short illumination time ensures a sharp image without any motion blur despite the high relative velocity of $v = 150 \text{ m/s}$ to 200 m/s of the aircraft.

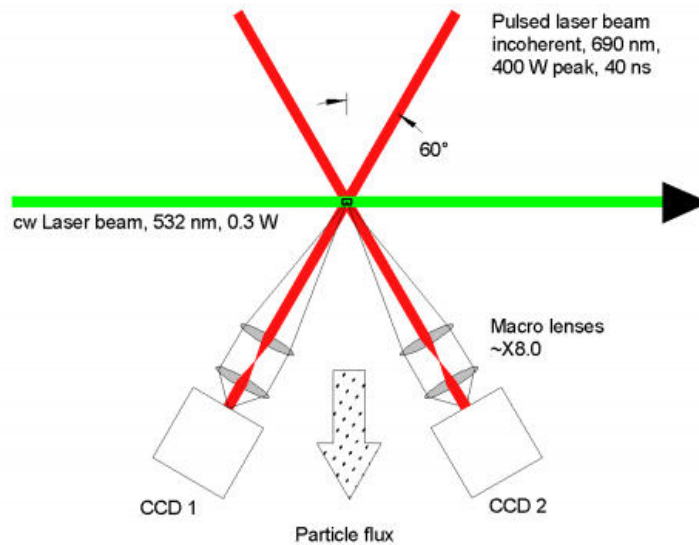


Figure 3.8.: Schematic view of PHIPS' imaging setup (figure adapted from Stegmann et al. [2016]).

After getting triggered, the camera have a shutter latency of $3.9 \text{ }\mu\text{s} \pm 0.03 \text{ }\mu\text{s}$ after which the shutter is opened for roughly $10 \text{ }\mu\text{s}$. The opening time of the shutter is negligible, as the acquisition time is dictated by the illumination time of the flash laser which is pulsed with $4 \text{ }\mu\text{s}$ delay for 40 ns. In practice, it has been observed that acquisition rates near the maximum can lead to data loss of individual images during the acquisition and saving process. Hence, the acquisition rate is limited to 3 Hz. This means that the temporal resolution of scattering and image acquisition differ significantly — whereas the ASF of every triggered particle is measured, stereo-images are available only for a subset of particles. For the remaining triggered particles only the ASF is measured. It is essential that the assignment of which pair of stereo images belongs to which corresponding ASF works for every particle. The scattering measurement and the image acquisition have independent internal clocks that are synced with the PHIPS computer. However, due to variable data processing time in the computer, the timestamps can vary and a careful image assignment has to be conducted. This, as well as detailed information about the

image post-processing and image analysis, will be explained in Section 3.2.

3.1.3. Trigger Sensor and Sensitive Area

In principle, the trigger sensor is set up similar compared to the scattering channels, but not with a parabolic mirror but with a collection lens. The trigger sensor is located at $\theta = 90^\circ$ below the base plate (see Fig. 3.4) and its FoV is slightly bigger compared to the scattering channels. The FoV is displaced 0.4 mm in front of the FoV of the images to account for particle movement during the shutter delay of the cameras (see following section). The scattering measurements are taken in the position of the trigger point. Further, a trigger delay, i.e. waiting time until the trigger signal is given to scattering measurement and image acquisition, can be introduced to correct for slower flight speed, e.g. during calibration in the laboratory.

The trigger sensor detects the light scattered of a particle by the $\lambda = 532$ nm scattering laser. If the intensity in the trigger channel exceeds a set threshold for a set time, this is interpreted as there is a particle detected in the FoV and the instrument is triggered. Additionally, once every 0.7 second, the instrument is "force triggered", i.e. measures the background scattering intensity without a particle present in the FoV.

Naturally, the trigger intensity threshold introduces a size threshold since the ASF of a particle is size dependent (see Section 3.1.1). Also, since the scattering properties of spherical and aspherical particle differ strongly near $\theta = 90^\circ$ (see Section 2.2), where the trigger sensor is located, (aspherical) ice particles have a lower trigger size threshold compared to (spherical) droplets. This has the positive effect that even in clouds which are dominated by lots of smaller droplets and have few large ice particles, those ice particles can be detected and are not "overflow" by the small droplets. A typical setting for the trigger threshold, which was e.g. used for the SOCRATES campaign, results in a lower detection limit of $D \geq 50 \mu\text{m}$ and $D \geq 20 \mu\text{m}$ for spherical and aspherical particles, respectively.

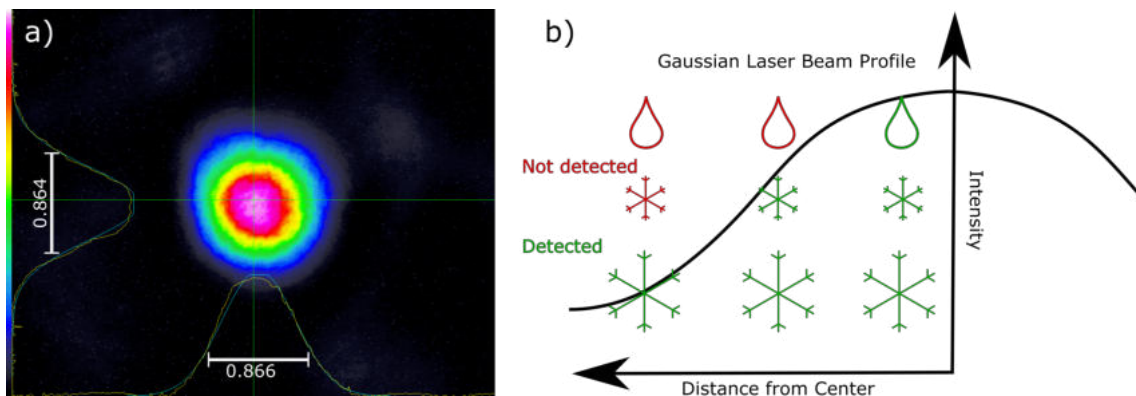


Figure 3.9.: a) Shape of the beam profile of PHIPS' scattering laser before the SOCRATES campaign. The yellow lines show the vertical and horizontal intensity distribution and the corresponding Gaussian fits are marked in green. The $1/e^2$ diameter is approximately 0.865 mm. b) Schematic visualization of the size and phase dependency of the sensitive area of PHIPS' trigger system. Due to the Gaussian shape of the laser beam profile, whether or not a particle at a given distance from the center of the laser beam is detected by the trigger sensor is dependent on their size and shape.

Since the scattering laser has a Gaussian beam-shape (see Fig. 3.9a) the sensitive area A_{sens} , i.e. the location where a particle is detected by the trigger system, is phase and size dependent, as visualized in Fig. 3.9b. As discussed in Section 2.2.4, (aspherical) ice particles usually have different differential scattering cross sections compared to (spherical) droplets, especially in side scattering directions where the trigger optics is located. Particles with a

small scattering cross section (spherical or small size) are only triggered when they are in the center of the beam, whereas large or aspherical particles are also triggered further off center.

The size of the A_{sens} was calculated using the optical engineering software FRED (Photon Engineering, LLC, USA), which combines light propagation by optical raytracing simulations with 3D computer aided design (CAD) visualization [Waitz et al., 2021a] and confirmed for spherical particles using a piezo-driven droplet generator on an adjustable micrometer stage. As shown in Fig. 3.10, A_{sens} is > 25% larger for ice particles compared to water droplets of the same size. The derived A_{sens} is used to calculate the effective volume sampling rate for the determination of PSDs in Section 5.1.

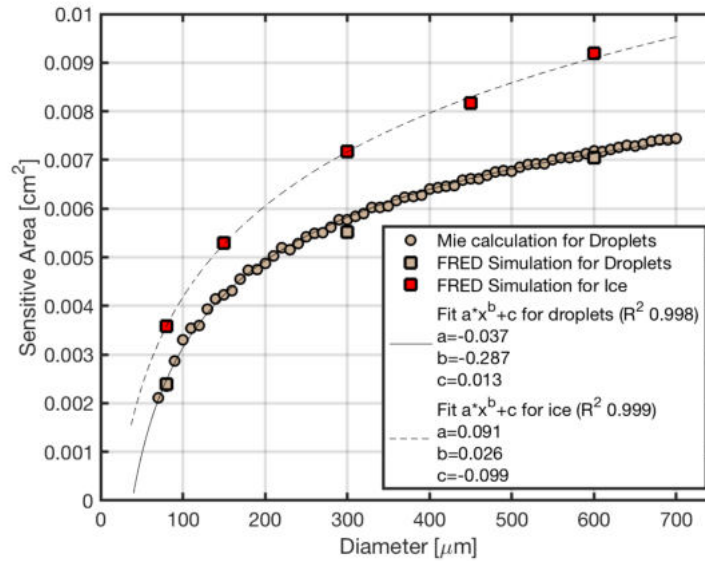


Figure 3.10.: Sensitive area based on FRED simulations for ice (red) and droplets (grey).

3.2. Image Processing

PHIPS stereo images are 8-bit gray-scale images that can be interpreted as 1360×1024 -arrays with integer values between 0 (black) and 255 (white). In the following, the procedure and preparation for image analysis and image enhancement including background (BG) correction will be briefly explained.

3.2.1. Image Analysis

Most of the methods for PHIPS' image analysis were developed and explained in depth by Roland Schön during his doctoral thesis [Schön et al., 2011; Schön, 2007]. The image analysis software is written in *IDL* (Interactive Data Language, RSI Research Systems Inc., Harris Geospatial Solutions). The key points will be briefly outlined in the following.

In the first step of the image analysis, the grey-scale image is background corrected³, processed (edges are smoothed, border objects are removed) and binarized. Then, the

³For previous campaigns, this empty image was manually hand-picked for every flight (each one for CTA1 and CTA2). Alternatively, the average over enough (about 1000) images with small, randomly distributed particles approximates an empty image as well, since the few black pixels (i.e. the particle) average out. A demonstration is shown in Appendix A.2. In future projects, PHIPS will take an empty image every 100th image, which allows accurate BG subtraction for the image analysis and enhancement.

image is translated into a vector chain that follows the perimeter of the particle. Fig. 3.11 shows an exemplary particle⁴ during different stages of the image processing.

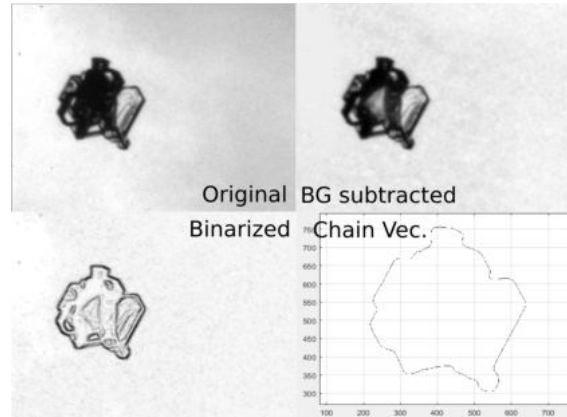


Figure 3.11.: Exemplary image during different stages of the image processing: original image (top left), removed BG (top right), final binarized image with all processing measures (bottom left) and the resulting chain vector (bottom right).

Based on the chain vector, the relevant geometrical parameters of the particle such as maximum dimension (D_{\max}), Projection area (A) and area equivalent diameter assuming a circular particle ($D_{\text{geom}} = 2\sqrt{A/\pi}$), are calculated.

This is done independently for the images of both CTAs. In general, the size measurement of the two CTAs agree very well. However, as already discussed in Schnaiter et al. [2018], high magnification settings can lead to a slight overestimation of the size of small particles as they blur due to the lower resolution. This effect can be corrected by fitting an empirical function ($y = a \cdot \exp(-x/b)$) to the relative size difference. For example, for the SOCRATES campaign, the magnification settings were $\times 6.6$ for CTA1 and $\times 4$ for CTA2. Fig. 3.12 shows the area equivalent diameter of CTA1 and CTA2 of the whole SOCRATES campaign. Fig. 3.13 shows the corresponding relative difference between area equivalent diameter of CTA1 and CTA2, $1 - D_{C1}/D_{C2}$. On average, the size of small particles below $50\ \mu\text{m}$ is overestimated by up to 20%. The correction fit through the diameter bin averages is shown by the red line.

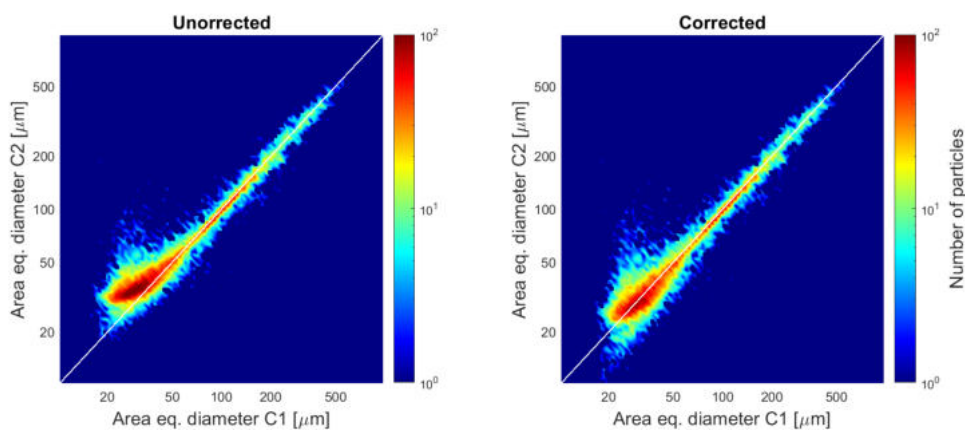


Figure 3.12.: Uncorrected and corrected area equivalent diameter of CTA1 and CTA2 of the whole SOCRATES campaign. The 1:1 line is marked in white.

⁴SOCRATES, RF11, #0079, CTA1

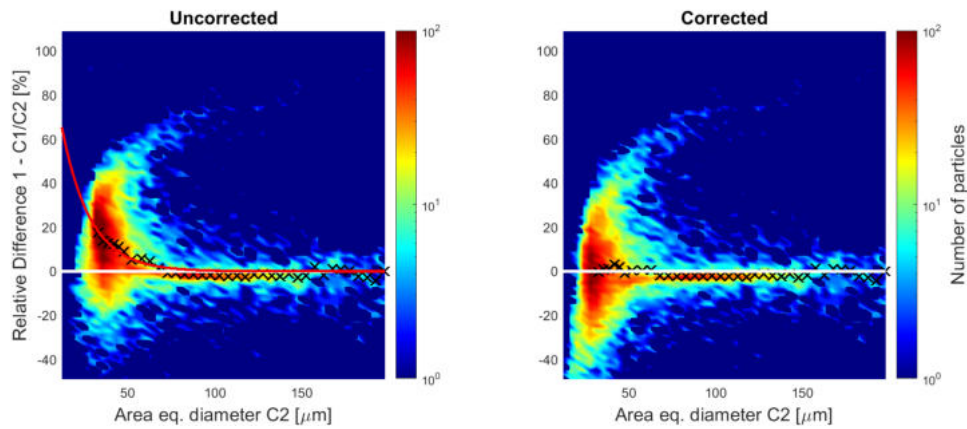


Figure 3.13.: Relative difference between area equivalent diameter of CTA1 and CTA2 of the whole SOCRATES campaign, uncorrected (left) and corrected (right). The black markers show the mean per diameter bin. The red line shows the exponential fit through the bin means.

3.2.2. Image Post-processing

To make details like surface properties more visible and to get rid of artifacts in the image for e.g. the manual classification or display in publications, the images are enhanced via Gaussian smoothing, noise reduction and logarithmic scaling of the gray-scale image to enrich the contrast. Further, a similar BG correction as explained in Section 3.2.1 is conducted. Finally, the BG intensity of different images, CTA1 compared to CTA2 and especially of different campaigns can be different. Hence, the BG is equalized based on the median of all images. This will be explained in detail in the following.

Fig. 3.14 shows the images (upper panel) and corresponding intensity histograms (lower panel) of three exemplary particles during different steps of the image post-processing process: an epitaxially rimed⁵ column⁶ (1), a plate⁷ (2) and a chain aggregate⁸ (3).

The first column (1a, 2a, 3a) shows the original⁹ images. The second column (1b, 2b, 3b) shows the enhanced images. The third (1c, 2c, 3c) and fourth (1d, 2d, 3d) panel show the same image with BG subtraction as well as BG equalization, respectively. It can be seen that the final post-processed images are brighter, have higher contrast and an overall higher image quality. Hence, details like surface features can be seen more easily. The lower panel shows the corresponding intensity histograms for the 3×4 images. The x-axis of the histograms shows the relative occurrence of grey-scale value per pixel (a value of 0 corresponds to a black pixel, 1 is a white pixel). The histograms usually show two peaks: one for the background (at rather bright grey-values at around 80%) and one for the particle (darker, at around 20%). The figures will be explained further in the following.

⁵The concept behind *epitaxially riming* is explained in depth in Section 7.3.

⁶IMPACTS, flight 20200201, #00769, CTA1

⁷IMPACTS, flight 20200118, #13506, CTA1

⁸CapeEx2019, flight 20190729, #05784, CTA1

⁹The images are flipped vertically to account for the mirrors in the optical path.

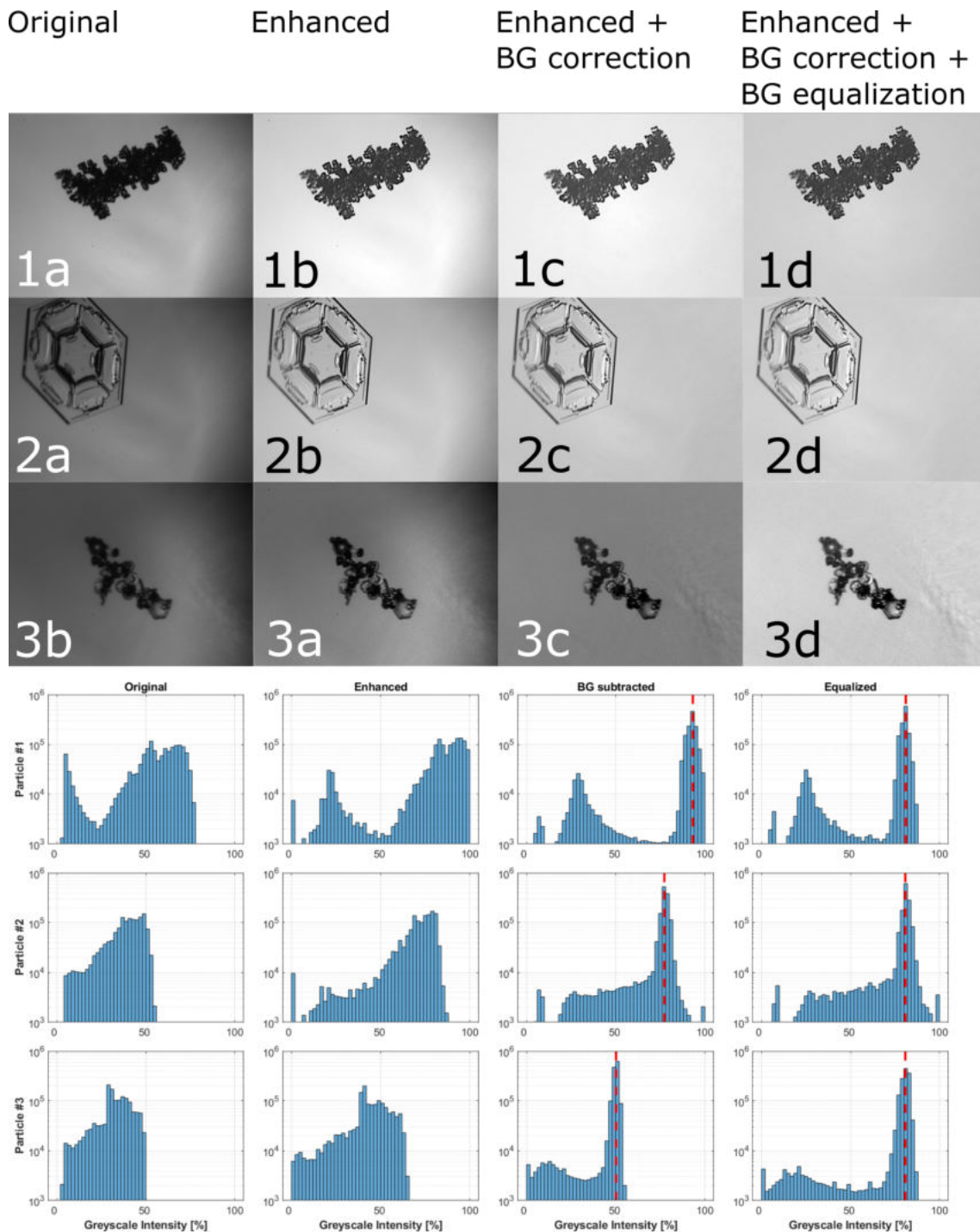


Figure 3.14: Illustration of the image post-processing. The upper panel shows 3 exemplary images throughout different stages of the image post-processing: a) original, b) enhanced, c) enhanced + BG correction and d) enhanced + BG correction + BG equalization. The lower panel shows the corresponding intensity histograms (0 corresponds to black pixels, 100% means white). More information is given in the text.

3.2.2.1. Image Background Subtraction

To remove artifacts and reflections that appear in every image but are not associated with the sampled particle, the BG intensity of an empty image¹⁰ is subtracted from each image.

¹⁰The empty image is manually hand-picked for every flight or generated by averaging over lots of images with small particles as discussed in Appendix A.2.

To subtract the BG from the original image (A_o), the images are inverted first:

$$\bar{A}_o = 255 - A_o \quad (3.9)$$

and thus $0 \equiv$ white and $255 \equiv 100\% \equiv$ black. This way, subtracting a white pixel, does not change the original image. However, subtracting a pixel that is black in the BG (e.g. a dust particle on the lens) will make the pixel in the corrected image brighter. The inverse transformation works similar:

$$A_p = \bar{\bar{A}}_p = 255 - (255 - A_p) \quad (3.10)$$

For the BG subtraction in Section 3.2.1, the intensity of the empty BG image is just subtracted and the (inverted) processed, BG-subtracted image A_p simply calculated as

$$\bar{A}_p = \bar{A}_o - \bar{BG}. \quad (3.11)$$

This works well for the image analysis, since the final product is a binary image. However, it can destroy e.g. the fine surface structure of the crystal which we want to investigate with the enhanced images. Hence, for the image post-processing, the BG subtraction must be more "subtle": instead of subtracting the whole BG intensity, only the derivation of the mean of the BG is subtracted. This means, compared to Eq. (3.11), the (inverted) processed image is calculated as

$$\bar{A}_p = \bar{A}_o - \left[\bar{BG} - \text{mean}(\bar{BG}) \right]. \quad (3.12)$$

Essentially, this means that only dark regions are made brighter and the light regions are made darker, or, in technical terms, the intensities of pixels that are lower than the mean are added, the others are subtracted. The impact of the BG correction can be seen by comparing column b) and c) of Fig. 3.14. Shadows and spotlights at the edges of the images are removed and the BG is overall smoother. Details like surface features on the particle surface remain unchanged and clearly visible. Fig. 3.15 shows a magnified segment of one of the particles, 2b and 2c. The left part is the enhanced image and the right shows the same image with subtracted background. The red arrow points to an artifact (likely a dust particle on the camera lens) that is removed via this method.

In the intensity histograms (lower panel of Fig. 3.14) it can be seen that the main peak (around a gray-scale of 50% to 100%) that corresponds to the BG is much narrower which means a more uniform BG. Also, for particle #3 it can be seen that the peak around 15% that corresponds to the particle itself, sticks out more distinct.

3.2.2.2. Image Background Equalization

The last step for the image post-processing is the BG equalization. As can be seen in column c) of Fig. 3.14, the BG of the images (which are from different flights and campaigns) differ in brightness. This can also be seen clearly in the histograms in the lower panel: The BG peaks of the corresponding images are located at around 90%, 80% and 50% grey-scale intensity as indicated by the dashed red lines in Fig. 3.14. Since the BG dominates the intensity histogram (note the logarithmic scale), even for very large particles, the mean intensity of the BG can feasibly be approximated as the mean over the whole image, i.e.

$$I_{\text{mean}} = \text{mean}(BG) \approx \text{mean}(A_0). \quad (3.13)$$

The main idea for the BG equalization is to "squeeze" these histograms so that the BG intensities match (i.e. the BG peaks are at the same grey-scale level, see Fig. 3.14d), so that

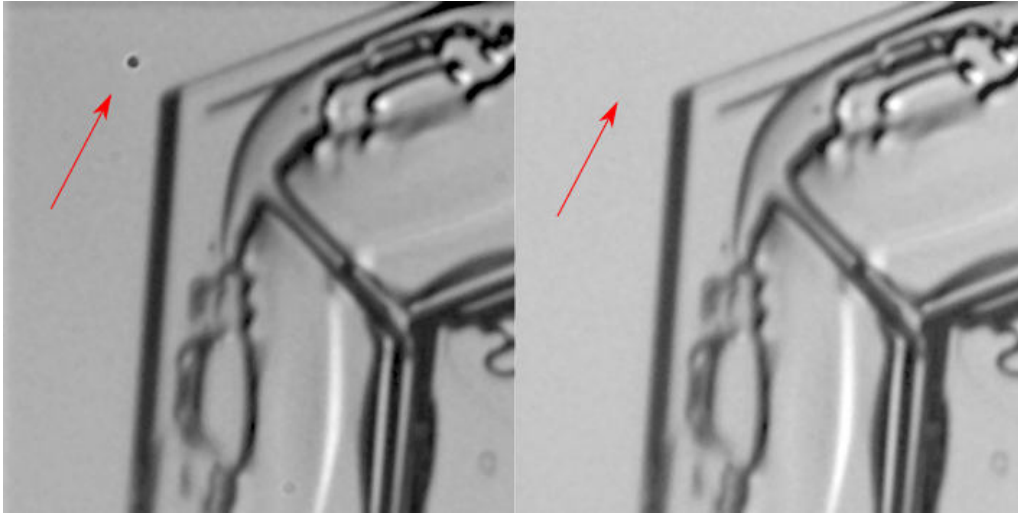


Figure 3.15.: Parts of an image before and after background subtraction. The red arrow points to an artifact (likely a dust particle on the camera lens) that is removed via this method.

the BG is similarly bright for every image and hence particles from different flights and even campaigns are better comparable.

To which absolute value the images are squeezed can be chosen freely. It has been found suitable to set the reference value (to which the dashed red lines are shifted) at around $I_{\text{ref}} = 80\%$. The final equalized image (A_{eq}) is simply calculated by multiplying the intensity¹¹ of each pixel (A_p) with the ratio of I_{mean} to I_{ref} :

$$A_{\text{eq}} = A_p \times \frac{I_{\text{mean}}}{I_{\text{ref}}} . \quad (3.14)$$

The result can be seen in the right column (d) of Fig. 3.14. All images have similar brightness. All details and surface features are still clearly visible.

3.2.3. Manual Habit Classification

Additionally to the numerical image analysis regarding particle size, as discussed in the previous section, there are other important particle properties such as habit or surface features as introduced in Section 2.4.1. Those properties are usually so complex that it is very hard to automate this analysis. So far, for PHIPS, this assessment is done manually. Using a custom-built Matlab tool, cloud particles are manually classified based on their stereo images.

They are classified according to their habit into the following categories (see Section 2.4.1):

- **Plates** with the sub-categories **Skeleton Plates**, **Sectored Plates** and **Stellar Plates**
- **Columns** with sub-categories **Hollow Columns**, **Sheath Columns** and **Capped Columns**
- **Needles**
- **Dendrites**
- **Droplets**

¹¹Since in this step we only do multiplicative operations (no additive) it does not matter whether or not the images are inverted.

- **Frozen Droplets**
- **Graupel**
- **Bullet Rosettes**
- **Side Planes**
- **Irregulars**

Further, the images are given additional attributes, like like

- **Rimed or Pristine**
- **Aggregation and Chain Aggregation**
- **Sublimation**
- a flag marking images that show **Multiple Particles** or indicate potential **Shattering**
- or that have an **Empty, Cut off** or **Not Classified** image.

3.2.4. Manual Riming Classification

Additionally to the habit classification, a subset of particles was again manually classified in a second step for the riming studies (see Chapter 7). Similarly to the first classification step, this was again done using a custom built Matlab tool. To reduce the time needed for the manual classification, this subset of images included only images of particles that were sampled in riming-relevant cloud segments (i.e. temperatures of $T \geq -17$ °C, see Zhu et al. [2015]; Kneifel and Moisseev [2020] and Chapter 7). Further, particles that were classified as *irregular* in the first step and had a diameter $D_{\text{scatt}} \leq 100$ μm were ignored as those might be potential shattering cases and the limited optical resolution makes it hard to unambiguously classify the riming state.

The categories are:

- Estimated **surface riming degree (SRD)** similar to the definition of riming degree used in previous studies such as e.g. Magono and Lee [1966]; Bruintjies et al. [1987]; Mosimann et al. [1993, 1994]; Mosimann [1995]:
 - **Unrimed** — SRD = 0%, no visible riming
 - **Slight Riming** — SRD \lesssim 25% of the particles surface is covered with riming, i.e. a few scattered droplets on the particle's surface
 - **Medium Riming** — 25% \lesssim SRD \lesssim 50%, i.e. up to half of the particle's surface is covered by droplets
 - **Heavy Riming** — 50% \lesssim SRD \lesssim 100%, most or all of the particle's surface is covered by rime and
 - **Graupel** — SRD \gg 100%, the whole particle surface is covered by multiple layers of rime, so that the structure of the underlying particle is no longer recognizable.
- **Epitaxial Riming** — Particles with (poly-)crystalline build-ups instead of round (droplets) on the surface. This is explained in detail in Section 7.3.
- Estimated diameter of the rimed droplets, **Small Droplets** (smaller than 20 μm) or **Large Droplets**
- Discrimination whether the particle is uniformly rimed or only on **one side**.

Examples of crystals with different riming properties are shown in Fig. 3.16. The correlation of SRD with ambient meteorological parameters is discussed in Section 7.2. Note that the classification based on riming fraction and size is based on visual estimation.

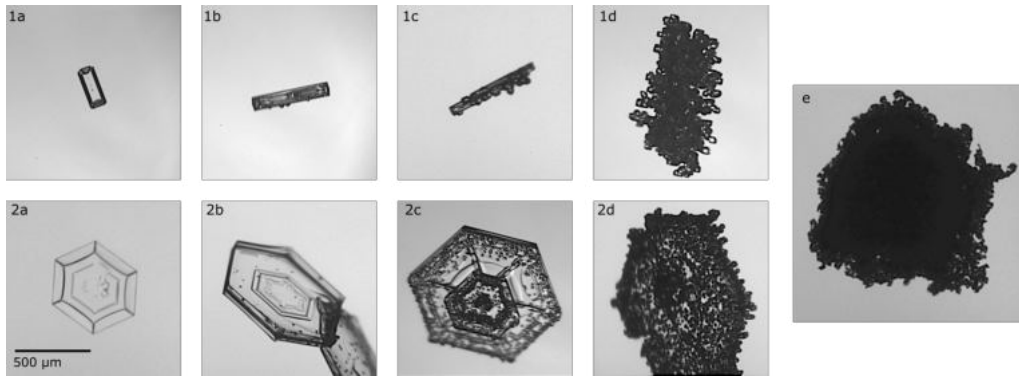


Figure 3.16.: Examples of (1) columnar particles and (2) plates with different degrees of riming depending on the surface riming degree (SRD): unrimed (a, $\text{SRD} = 0\%$), slightly rimed (b, $0\% < \text{SRD} < 25\%$), moderately rimed (c, $25 \leq \text{SRD} \leq 50\%$), heavily rimed (d, $50\% < \text{SRD} \leq 100\%$) and graupel particle (e, $\text{SRD} \gg 100\%$).

3.3. Field Campaigns

In this work, experimental in situ data gathered during three airborne field campaigns:

1. **Arctic C**loud Observations Using airborne measurements during polar **D**ay (ACLOUD), May/June 2017 based in Svalbard (Spitsbergen, Norway) with the AWI Polar 6 aircraft,
2. **S**outhern **O**cean **C**louds, **R**adiation, **A**erosol **T**ransport **E**xperimental **S**tudy (SOCRATES), Jan/Feb 2018 based in Hobart (Tasmania, Australia) with the NCAR Gilstream-V aircraft and
3. **I**nvestigation of **M**icrophysics and **P**recipitation for **A**tlantic **C**oast-**T**hreatening **S**nowstorms (IMPACTS), Jan/Feb 2020 based in Wallops (VA, USA) with the NASA P3 aircraft.

Fig. 3.17 shows the tracks of all research flights during the three campaigns.

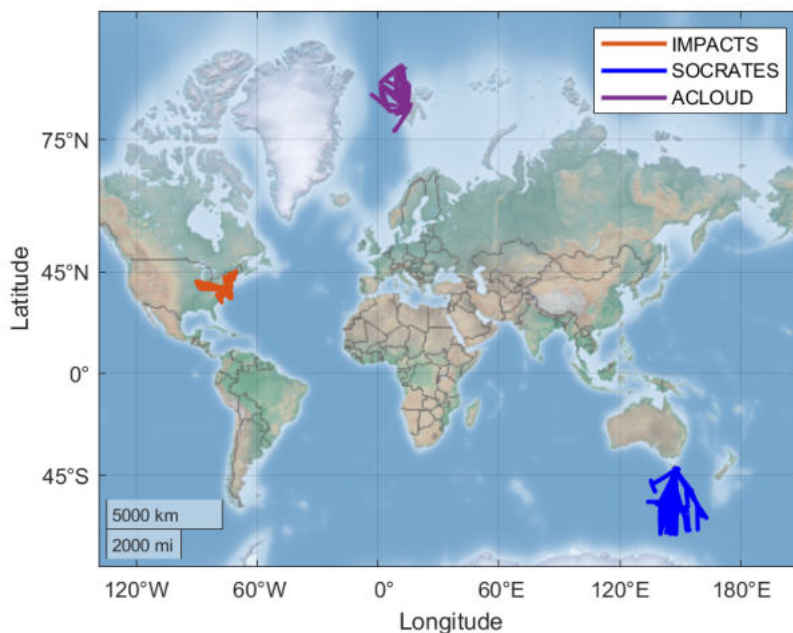


Figure 3.17.: Overview of the flight tracks of all flights of the ACLOUD (purple), SOCRATES (blue) and IMPACTS (red) field campaign.

Even though the focus of the three campaign lied on MPCs, the sampling included a wide variety of different cloud conditions: warm clouds, supercooled liquid clouds, ice clouds and mixed-phase clouds. Clouds sampled ranged in altitude from boundary layer clouds below 200 m to mid-level clouds between 4000 m and 6000 m above sea level. Temperatures ranged from $-35\text{ }^{\circ}\text{C}$ to $+9\text{ }^{\circ}\text{C}$. The sampled ice particles covered a wide range of different particle shapes and habits (columns, plates, needles, bullet rosettes, dendrites and irregulars, including rough, rimed and pristine particles) as well as sizes (c.f. below).

Due to the variability of the meteorological conditions and sampled particles, the data gathered during these three campaigns provide a suitable and representative data set for a comprehensive characterization of the microphysical properties of MPC particles. In the following, a brief overview of the instrumentation and meteorological conditions during the three campaigns is presented. An overview of the properties of the sampled PHIPS data is given in Section 3.3.4.

3.3.1. ACLOUD

The ACLOUD campaign took place as part of the AC³ project (*Arctic Amplification Climate relevant Atmospheric and surfaCe processes and feedback mechanisms*) from May 27 to June 26 in 2017 in Svalbard (Spitsbergen), which is an archipelago in the Arctic Ocean north of Norway at approx. 78°N . The general goal was to obtain a comprehensive data set of a diversity of atmospheric parameters that to understand and quantify specific physical processes in, above, and below Arctic clouds to estimate their role for the amplified climate change in Polar regions.

The sampling strategy was the following: The Polar 6 aircraft flew north-west towards the Arctic, sampling mostly MPCs as far north as 82°S in altitude from mid-level clouds around 3,000 m to boundary layer clouds below 100 m. Temperatures ranged from $-15\text{ }^{\circ}\text{C}$ to $+5\text{ }^{\circ}\text{C}$. The flight tracks are shown in Fig. 3.18.

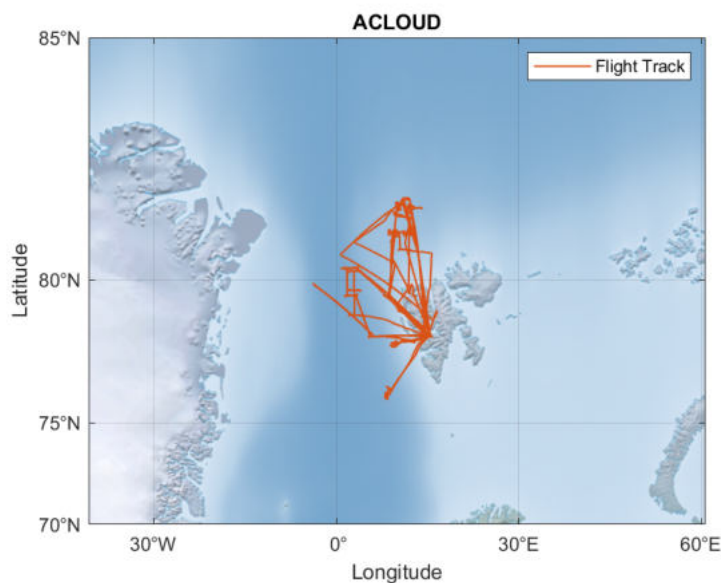


Figure 3.18.: Overview of the flight tracks of all flights of the ACLOUD campaign.

In total, the ACLOUD campaign [Knudsen et al., 2018; Wendisch et al., 2019] collected data over 19 research flights and 165 flight hours. Besides the PHIPS probe, the instrumentation included the cloud particle microphysics probes SID-3, CDP and CIP (see Section 2.5.5).

All raw data acquired during ACLOUD that is used in this work can be found at Ehrlich et al. [2019].

PHIPS' instrument settings were set to measure single cloud particles in a size range from $50 \mu\text{m} \leq D \leq 700 \mu\text{m}$ and $20 \mu\text{m} \leq D \leq 700 \mu\text{m}$ for droplets and ice particles, respectively. The image acquisition rate of the microscopic system was limited to 3 Hz in these campaigns, while single-particle scattering data could be acquired up to a maximum rate of 3.5 kHz. The magnification settings of the cameras corresponded to an optical resolution of approximately $3.3 \mu\text{m}$. Due to a misaligned FoV, the $\theta = 34^\circ$ channel was measuring erroneously low scattering intensities and is thus excluded from analysis in this work.

3.3.2. SOCRATES

The SOCRATES campaign took place from January 15 to February 26 in 2018 in Hobart, the capital of Tasmania, which is a large island south of Australia's mainland at approx. 42°S . The general goal of the campaign was to improve the understanding of clouds, aerosols, air-sea exchanges, and their interactions over the Southern Ocean.

The NSF (national science foundation) NCAR Gulfstream-V (G-V) aircraft flew south towards the Antarctic, sampling cirrus and MPCs as far south as 62°S in altitude from boundary layer clouds below 200 m to mid-level clouds between 4000 m and 6000 m above sea level. Temperatures ranged from -35°C to $+5^\circ\text{C}$. The flight tracks are shown in Fig. 3.19. The sampling strategy consisted of a transit flight to a southernmost point and a return flight consisting mostly of a repeating combination of "saw tooth" pattern (ascending and descending up and down through the cloud) as well as "stair way" pattern (sampling above, in and then below the cloud).

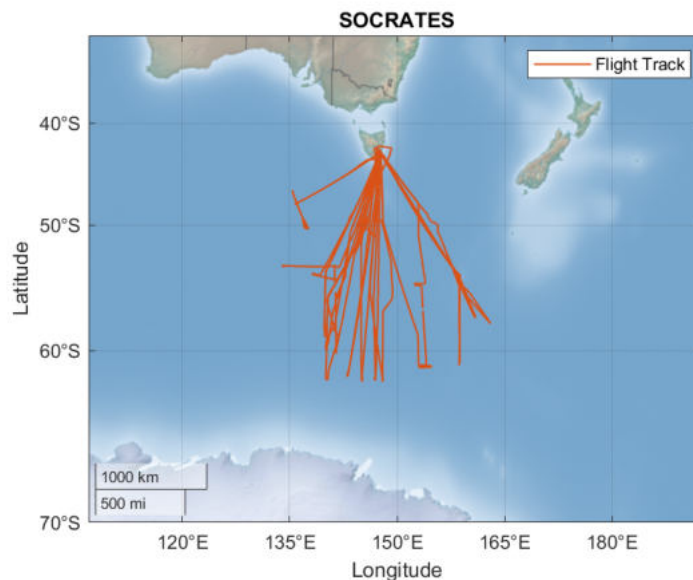


Figure 3.19.: Overview of the flight tracks of all flights of the SOCRATES campaign.

In total, the SOCRATES campaign [McFarquhar et al., 2019, 2021] collected data over 15 research flights and 165 flight hours. Besides the PHIPS probe, the instrumentation included the cloud particle microphysics probes CDP, 2D-C, 2D-S and CPI (see Section 2.5.5) as well as the HIAPER Cloud Radar (HCR) [EOL, 2018b]. All raw data acquired during SOCRATES that is used in this work can be found at EOL [2018a].

PHIPS' instrument settings were set similar as during ACLOUD to measure single cloud particles in a size range from $50 \mu\text{m} \leq D \leq 700 \mu\text{m}$ and $20 \mu\text{m} \leq D \leq 700 \mu\text{m}$ for droplets

and ice particles, respectively. The image acquisition rate of the microscopic system was limited to 3 Hz and single-particle scattering data could be acquired up to a maximum rate of 3.5 kHz. The magnification settings of the cameras varied between a corresponding optical resolution of approximately 3.3 μm to 4 μm . During the first flight, PHIPS was not recording images due to malfunction of the imaging laser and for RF01 only ASF data are available. Due to a problem with the scattering laser during the first four hours of RF06 PHIPS was measuring erroneously low scattering intensities and these data are thus also excluded from analysis in this work.

3.3.3. IMPACTS

The IMPACTS campaign [McMurdie et al., 2019] involves three 6-week deployments that were initially planned for consecutive years, but the two latter deployments were postponed by one year due to the global CoVid-19 pandemic until 2022 and 2023. All IMPACTS data that is used for the analysis in this work was acquired during the 2020 deployment of the IMPACTS project.

The campaign took place from January 11 to March 02 in 2020 in Wallops Island (VA, US), which is a small island on the east coast of the United States, about 150 km east of the capital Washington DC at a latitude of approx. 38°N. The general goal of the campaign was to better understand the formation of narrow, heavy snow bands and improve forecasts of these extreme weather events near the US east coast.

The National Aeronautics and Space Administrations (NASA) P3 flew mostly along the coast over land. Two flights were conducted over the sea. For one flight, the P3 was relocated to Dayton (Ohio, US), sampling generating cells over central US. The P3 sampled mostly MPCs with generating cells altitude from clouds below 1,500 m up to 7,000 m above sea level. Temperatures ranged from $-32\text{ }^{\circ}\text{C}$ to $+9\text{ }^{\circ}\text{C}$. The flight tracks are shown in Fig. 3.20. The sampling strategy consisted of mostly "race track" patterns, i.e. long legs of back and forth sampling in the same cloud, repeating in different altitudes.

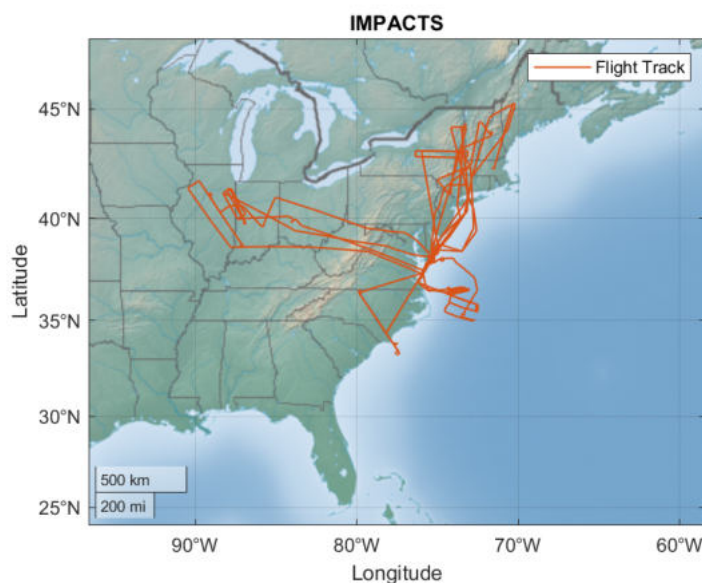


Figure 3.20.: Overview of the flight tracks of all flights of the IMPACTS campaign.

In total, the IMPACTS campaign collected data over 9 research flights and 53 flight hours. Besides the PHIPS probe, the instrumentation included the cloud particle microphysics probes 2D-S, CDP and CPI (see Section 2.5.5). Detailed information about the campaign

setup, instrumentation as well as raw data acquired during IMPACTS that is used in this work can be found at McMurdie et al. [2019].

During IMPACTS the scientific focus was on larger ice particles so the trigger threshold as well as the magnification were increased to trigger only particles larger than $D \geq 100 \mu\text{m}$ for droplets and $D \geq 40 \mu\text{m}$ for ice. The magnification settings of the cameras corresponded to an optical resolution of approximately $4 \mu\text{m}$ and the maximum camera acquisition rate was varied between 3 to 10 Hz, which corresponds to a maximum spatial resolution of roughly one stereo-image per 15 m.

3.3.4. Overview of the Experimental Data Set

During the aforementioned campaigns in total 41,196 (ACLOUD), 233,241 (SOCRATES) and 406,650 (IMPACTS) particles were sampled by PHIPS and single particle scattering data were acquired. Out of this, corresponding pairs of stereo-microscopic were acquired for 22,393 (54.3%), 30,159 (12.9%) and 123,347 (30.3%) of the particles, respectively. The images were analyzed and processed according to the methods described in Section 3.2. Fig. 3.21 shows the relative frequency of particle sizes based on the area equivalent diameter (mean of CTA1 and CTA2 images) of the three campaigns.

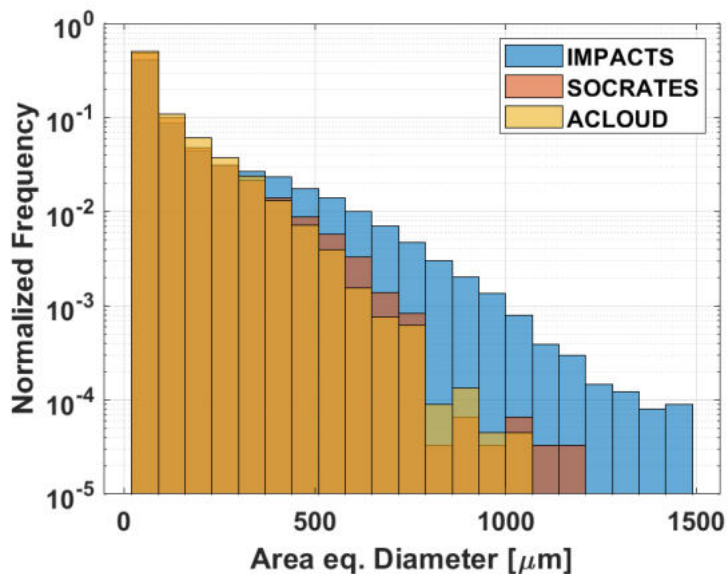


Figure 3.21.: Overview of the mean area equivalent diameter all sampled particles during ACLOUD, SOCRATES and IMPACTS.

The relative distribution of particle sizes for ACLOUD and SOCRATES are very similar. Most particles are in the size range $20 \leq D \leq 700 \mu\text{m}$. Few particles $D > 700 \mu\text{m}$ were sampled, however the particles in that size range were often times only partly imaged and had saturated scattering signals. During SOCRATES more particles larger than $D > 500 \mu\text{m}$ were sampled compared to ACLOUD during the transit segments in the first part of the flights. During IMPACTS, the size range of the sampled particles was larger due to the lower intensity gain (higher trigger threshold) and lower optical magnification setting. The size of sampled particles exceeded $D > 1500 \mu\text{m}$. Particles below $D < 40 \mu\text{m}$ were exclusively multiple particle events (likely shattering fragments).

Further, the images acquired during the ACLOUD and SOCRATES campaigns were manually classified according to the classification scheme discussed in Section 3.2.3. The classification was performed by several persons. Out of the 22,393 and 30,159 stereo images, 8,341 (37.2%) and 12,220 (40.5%) particles could be assigned to a certain habit class for

ACLOUD and SOCRATES, respectively. The remainder were image pairs that showed shattering cases, empty images, out-of-focus or only partly images particles. These were excluded from further analysis. Out of the 8,341 (ACLOUD) and 12,220 (SOCRATES) images, 1,853 (19.0%) and 2,284 (18.7%) were classified as droplets. 7,885 (81.0%) and 9,936 (81.3%) were classified as ice particles, out of which 3,302 (33.9%) and 4,591 (37.6%) were small ($D \leq 100 \mu\text{m}$) irregulars that might be potential shattering cases. An overview of the habits of the particles sampled by PHIPS during ACLOUD and SOCRATES is shown in Fig. 3.22 and Fig. 3.23.

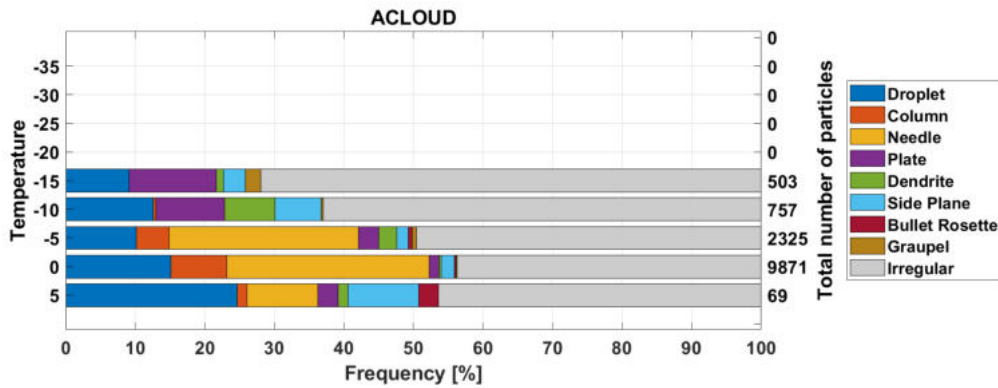


Figure 3.22.: Overview of the habit of the manual classified particles of ACLOUD in different temperature regimes.

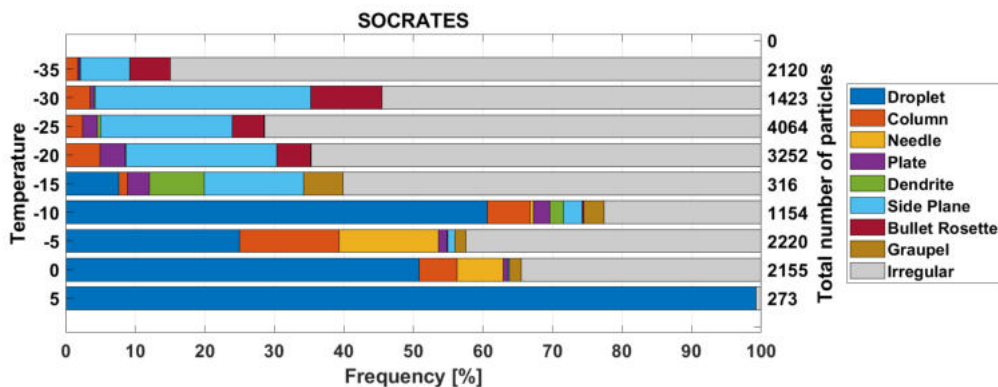


Figure 3.23.: Overview of the habit of the manual classified particles of SOCRATES in different temperature regimes.

It can be seen that PHIPS observed supercooled liquid droplets down to temperatures below $T = -15 \text{ }^\circ\text{C}$ during both campaigns. Simultaneously, a large portion of the manually classified particles sampled at positive temperatures $T \geq +0 \text{ }^\circ\text{C}$ were classified as ice ($>80\%$ for ACLOUD, $\approx 50\%$ during SOCRATES). Most of the ice particles ($> 50\%$) were classified as irregulars. This fraction increases towards colder temperatures. At warm temperatures between $-10 \leq T \leq +5 \text{ }^\circ\text{C}$, the most common habits were columns and needles. Plates and dendrites were most commonly found at temperatures between $-20 \leq T \leq -10 \text{ }^\circ\text{C}$ and poly-crystalline particle such as side planes and bullet rosettes were most common at lower temperatures $T \leq -20 \text{ }^\circ\text{C}$. This agrees well with the theory discussed in Section 2.4.1.

As discussed in Section 3.2.4, the subset of ice particles with $D \geq 100 \mu\text{m}$ sampled at temperatures $T \geq -17 \text{ }^\circ\text{C}$ was again manually classified in a second step for the riming studies (3,957 particles from ACLOUD and 1,413 from SOCRATES, see Chapter 7). Due to the increased image acquisition rate, over 123,000 stereo-image pairs were sampled during the IMPACTS campaign, so no manual image classification was done within the time frame of this thesis and only the set of images used for the case study presented

in Section 7.3.1 were manually inspected. Also, due to the high trigger threshold, most detected particles were ice and the IMPACTS campaign is not used for the calibration of the phase discrimination algorithm that will be discussed in the following chapter.

4. Phase Discrimination of Individual Cloud Particles based on their Angular Scattering

As discussed in Section 2.2.4, the scattering phase functions and hence the angular scattering functions (ASFs) of spherical droplets and aspherical (ice) particles can differ significantly. Hence, it is possible to differentiate the phase of individual cloud particles by looking into differences in the angular light scattering behaviour in the angular regions where spherical particles exhibit unique features, like the minimum around $\theta = 90^\circ$ and the rainbow around $\theta = 138^\circ$. In this section, four distinct scattering features are introduced and an algorithm is developed that is able to classify each particle based on the combined information from multiple features of the ASF (see Fig. 4.1).

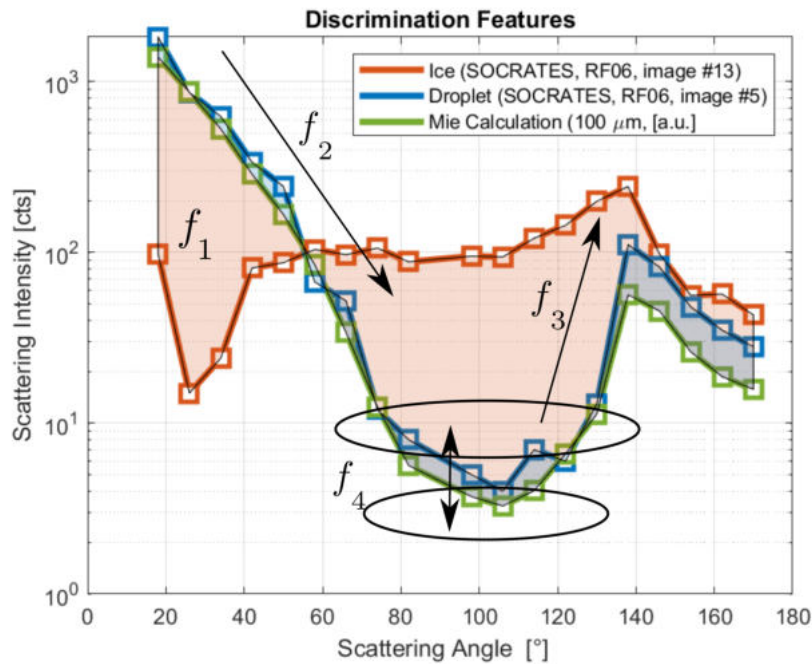


Figure 4.1.: Visualization of the four classification features: f_1 = Mie comparison (shaded area between curves and Mie calculation), f_2 = down slope, f_3 = up slope before the rainbow feature and f_4 = ratio around the minimum at 90° . The green line shows the calculated ASF for a theoretical spherical particle. The blue and red lines show the measured ASF of an exemplary droplet ($D = 119.6\mu\text{m}$) and ice particle ($D = 165.8\mu\text{m}$) from the SOCRATES campaign.

The basic concept of the development procedure for the single-particle phase discrimination algorithm will be explained in this chapter and is shown in Fig. 4.2. In the first step, ASFs calculated by Mie theory (BHMIE, Bohren and Huffmann [1998]) for spherical particles using the refractive index for water ($n_{\text{refr}} = 1.332$) are compared to modelled ASFs of aspherical

ice particles [Baum et al., 2011; Yang et al., 2013]. Based on the differences in the ASFs, four features are determined that are characteristic for spherical or aspherical particles as shown in Fig. 4.1:

- f_1 - Comparison of the shape of the ASF with the calculated ASF of a theoretical Mie-sphere.
- f_2 - *Down slope* between the forward scattering and the minimum at $\theta = 90^\circ$.
- f_3 - *Down slope* between the minimum $\theta = 90^\circ$ and the rainbow peak around $\theta = 138^\circ$.
- f_4 - The ratio of the scattering intensity around the minimum at $\theta = 90^\circ$.

The algorithm is then calibrated and validated using PHIPS data from the two field campaigns that were introduced in the previous section. This data set consists of about 23,000 representative single cloud particles of various phase, habit and size for which stereo micrographs as well as the corresponding ASFs are available. Those particles are manually classified as spherical or aspherical based on their appearance in the stereo micrographs. The calibration of the phase discrimination algorithm is then based on the ALOUD data set only. This way, a classification probability for every feature is determined. The different features are then weighted and combined to a final discrimination probability for every single particle. Based on data acquired during the SOCRATES campaign, the discrimination algorithm is validated and discrimination accuracy as well as special cases and limitations are discussed. Lastly, a comparison to machine learning approaches used in other studies is given. The methods presented in this chapter are also published verbatim in Waitz et al. [2021a].

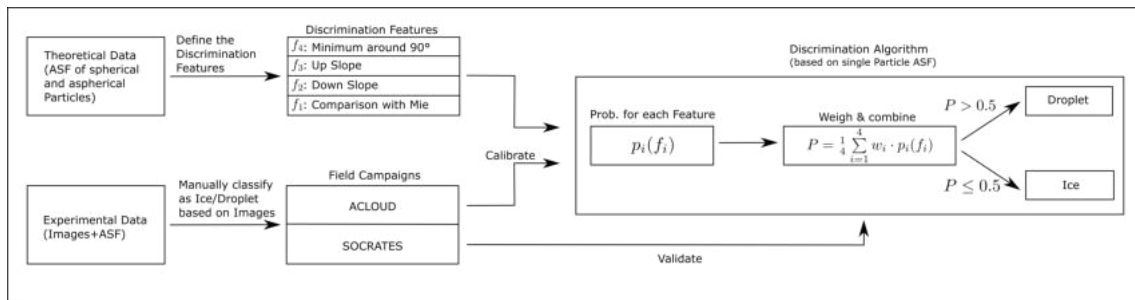


Figure 4.2.: Schematics showing the basic working principle of the phase discrimination algorithm.

4.1. Discrimination Features

4.1.1. f_1 : Comparison with Mie Scattering

One approach to discriminate between spherical and aspherical particles is to compare the shape of a particle's ASF with the shape of the calculated ASF of a theoretical sphere using Mie theory. To estimate the deviation of the observed ASF from the calculated Mie scattering, the integrated difference between measurement and calculation are evaluated (shaded area between the curves in Fig. 4.1). Fig. 4.3 shows a step-by-step explanation of the determination of the f_1 parameter based on two exemplary droplets: a droplet (d1) with $D = 119.6 \mu\text{m}$ (the same particle as in Fig. 4.1) and a theoretical Mie-sphere (d2) with $D = 200 \mu\text{m}$. Fig. 4.3a shows the ASF for the two particles as well as the ASF of the reference Mie-sphere with $D = 100 \mu\text{m}$.

The ratio between the measured intensity I_{exp} of an individual particle and the Mie calculation I_{Mie} for a spherical reference particle with a diameter of $100\ \mu\text{m}$ for every nephelometer angle θ_i is defined as

$$q(\theta_i) = \frac{I_{\text{exp}}(\theta_i)}{I_{\text{Mie}}(\theta_i)} \quad (4.1)$$

as shown in Fig. 4.3b. To be comparable to the measured intensities, the calculated theoretical Mie scattering function was integrated over the FoV of the polar nephelometer channels (see Section 3.1.1). Ideally, this ratio q_i should be calculated with a theoretical

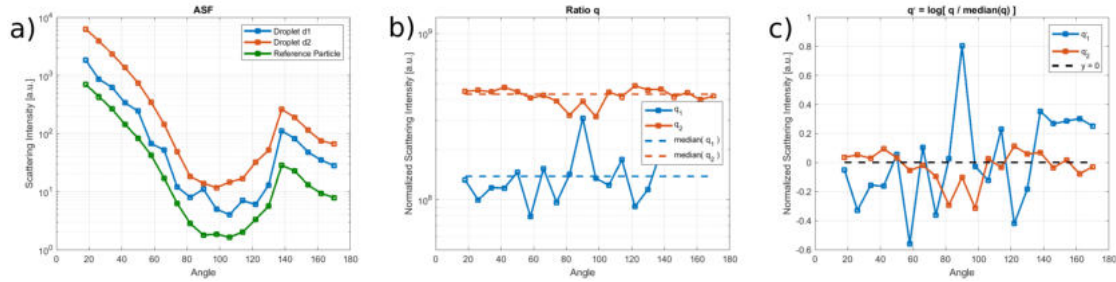


Figure 4.3.: Determination of the feature parameter f_1 of two exemplary droplets: Droplet d1 (blue) is the same particle as in Fig. 2.21. Droplet d2 (red) is a theoretical Mie-sphere with $D = 200\ \mu\text{m}$. The plots show the particles' ASF (a), q and \bar{q} (b) and q' (c). The resulting f_1 is then calculated as the integral over all channels (i.e. area between each curve and $y = 0$). The resulting values are $f_1 = 3.7$ for d1 and $f_1 = 2.2$ for d2.

reference particle with the same diameter as the detected particle. However, the diameter of the measured particle is not known without applying a size calibration first. To circumvent this, each q_i is normalized by the median over all channels \bar{q} (dashed line in Fig. 4.3b).

For a spherical particle, the ASF is approximately proportional to its diameter squared and thus $I_{\text{Mie}}(\theta, d)/D^2 \approx \text{const.}$, (see Fig. 3.7 in Section 3.1.1) and thus q is $\approx \text{const.}$. Since we do not know the diameter of the measured particle without applying a size calibration, q is normalized by the median over all channels \bar{q} and the influence of the approximately constant factor can be neglected. This also has the advantage that we do not need to calibrate the conversion factor from counts to power unit (W) of the MAPMT array which can change for different campaigns, gain settings and changes in laser power. Thus, the discrimination algorithm works for different campaigns and settings without further calibration.

Furthermore, as we are interested in the shape in log-scale, the deviation in 'both directions' from the calculated Mie intensity have to be weighted equally, i.e. $q_i = 2$ and $q_i = \frac{1}{2}$ should be equivalent. Therefore, we make the transformation $q'_i \rightarrow \log(q_i/\bar{q})$. The resulting 'feature parameter' is then finally defined as the logarithm of the integral over all angles θ_i :

$$f_1 = \log \left(\int |q'_i| d\theta_i \right) = \log \left(\int \left| \log \left(\frac{q_i}{\bar{q}} \right) \right| d\theta_i \right) \quad (4.2)$$

which corresponds to the area under the curves in Fig. 4.3c.

To demonstrate that this feature is representing a distinctive difference between spherical and aspherical particles, the distribution of the feature parameter value f_1 of representative, manually classified spherical and aspherical particles from the experimental in situ aircraft measurement campaigns introduced in Section 4.3, are shown in Fig. 4.6a. It can be seen that, roughly, if a given particle has a feature value of e.g. $f_1 < 4.5$, it is likely spherical, and if $f_1 > 5$, it has a high probability of being an aspherical particle. Phase discrimination

based on this feature alone would already allow for a reasonable discrimination, but there also exist spherical particles with e.g. $f_1 > 5$ that would be misclassified by using this approach. Hence, multiple features are taken into account to increase the discrimination accuracy.

4.1.2. $f_2 + f_3$: Down and Up-Slope

When looking at Fig. 4.1, the most distinctive differences between the ASF of spherical and aspherical particles are the minimum around $\theta = 90^\circ$ and the rainbow maximum around $\theta = 138^\circ$ for spherical particles (see Section 2.2.2.1), whereas aspherical particles often show a flatter angular scattering behaviour. One way to extract those features is to evaluate the 'exponential slope'

$$f_2 = \frac{\log(I(\theta_2)) - \log(I(\theta_1))}{\theta_2 - \theta_1} \quad (4.3)$$

in the region before and after the minimum around $\theta = 90^\circ$. This results in two features: the negative slope before the minimum and the positive slope between minimum and rainbow around $\theta = 138^\circ$. In general, steeper slopes mean that a given particle is likely to be spherical. The first 'slope feature' (f_2) is the *down slope*, which is simply the linear slope from $\theta_1 = 42^\circ$ to $\theta_2 = 74^\circ$. The first three scattering channels ($\Theta = 18^\circ, 26^\circ, 34^\circ$) are not taken into account here because they have a larger possibility to be saturated for larger particles. The slopes are determined by applying a linear fit to the logarithmic intensities in the channels between θ_1 and θ_2 .

The second slope feature (f_3), the *up slope*, is calculated as the (logarithmic) slope from the minimum around $\theta = 90^\circ$ to the maximum of the rainbow peak. Since the scattering intensity can be very low and, therefore, comparable to the magnitude of the background noise (especially for small particles), hence the 'lower end' is averaged over multiple channels from $\theta = 74^\circ$ to 106° . The upper end of the slope is not fixed either, but rather chosen dynamically as the angular position of the rainbow peak can vary within four scattering channels between $\theta = 130^\circ$ and 154° . Thus, we define the slope feature f_3 as

$$f_3 = \frac{\log(\max[I(130^\circ \text{ to } 154^\circ)]) - \log(\text{mean}[I(74^\circ \text{ to } 106^\circ)])}{\theta_2 - \theta_1}, \quad (4.4)$$

with the corresponding angle of the rainbow maximum θ_2 and the minimum $\theta_1 = 90^\circ$. This way, even small particles and elongated particles with a shifted rainbow peak (see Section 4.5) can be classified correctly.

4.1.3. f_4 : Ratio around the 90° Minimum

Another possible way to depict the depth of the 90° minimum (see Section 2.2.4.2) is to directly compare the intensities in the vicinity around $\theta = 90^\circ$ with channels that are farther away (see Fig. 4.1). Hence, the 'Mid Ratio' feature is defined as

$$f_4 = \log\left(\frac{\text{mean}[I(58^\circ, 66^\circ, 114^\circ, 122^\circ)]}{\text{mean}[I(74^\circ, 82^\circ, 90^\circ, 98^\circ, 106^\circ)]}\right). \quad (4.5)$$

With the distinct shape of the ASF of droplets around the 90° minimum, one could argue that an intensity threshold might be enough to discriminate between spherical and aspherical particles (e.g. classifying every particle with $I(\theta = 90^\circ)$ smaller than a certain threshold I_{thresh} as spherical). However, looking at absolute values would prove impractical as the ASF scales with particle size: a very small aspherical particle could still fulfil $I(\theta = 90^\circ) < I_{\text{thresh}}$

as well as a rather large spherical particle $I(\theta = 90^\circ) > I_{\text{thresh}}$, respectively. Hence, the discrimination features presented here are all based on relative values, slopes and ratios instead of discrete thresholds. Further, all discrimination features are based on the scattering signal of multiple channels instead of only one channel to minimize the impact of noise. This allows the discrimination algorithm to be used for multiple campaigns (even with differing settings or minor hardware changes or malfunction) without additional calibration (see Section 4.4).

4.1.4. Unused Discrimination Features

In theory, a third slope feature after the rainbow peak could be calculated from the maximum in said range to the end (i.e. between $138 \lesssim \theta \lesssim 170$). However, in comparison to the other features, the histogram of the potential third slope feature would show a much bigger overlap (see Fig. 4.4). Possible explanations for this could be the limited amount of available channels in the backwards direction or shifting of the rainbow peak due to deformation of elongated droplets (more on that in Section 4.5). Further, depending on particle orientation, specular reflections on pristine ice particles can lead to large peaks in the ASF. Such a peak could erroneously "trigger" this third slope feature parameter. Hence, since the inclusion of this feature could not increase the phase discrimination accuracy, it is not used further as a classification feature.

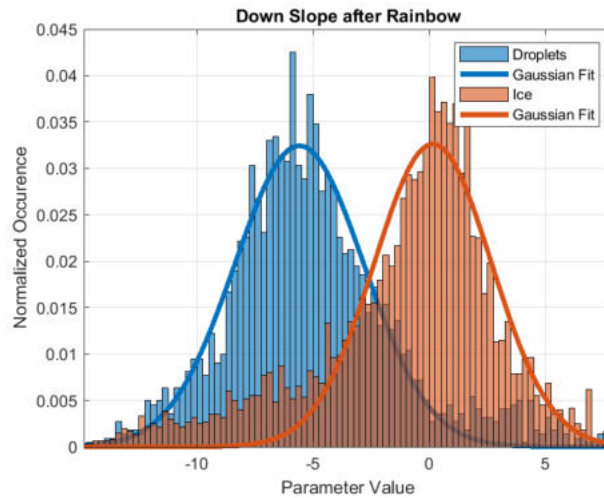


Figure 4.4.: Distribution of the feature parameter for the down slope after rainbow peak, based on the manually classified images from the SOCRATES campaign.

To compensate for the impact of specular reflections (i.e. those peaks being falsely identified as very steep slopes and ice particles are misclassified as droplets), it was considered to look at the slope of every individual channel, i.e. the ratio to the next channel

$$m_i = \log \left(\frac{I(\theta_{i+1})}{I(\theta_i)} \right). \quad (4.6)$$

As already utilised for the down slope (f_2) feature, according to Mie theory, the scattering intensity for spherical droplets descends continuously for increasing θ until the minimum around 90° . Hence, if the scattering intensity suddenly increases during the down slope, this could be caused by a specular reflection peak. Analogously, the same goes for peaks during the up slope (f_3).

However, for small particles with scattering signal near the magnitude of the background of only a couple counts, noise can falsely be interpreted as a specular reflection peak. Also,

similar to the down slope after the rainbow, the histogram of the feature distribution also show large overlaps and implementing one or more specular reflection peak features could not improve the discrimination accuracy. Hence, in an effort to keep the discrimination algorithm simple and the number of discrimination features low, specular reflection peaks are not taken into account.

4.2. Simulation of the Feature Parameters

To investigate if the defined set of discrimination features reliably discriminates between spherical and aspherical particles, the feature parameter values f_i are calculated based on theoretical phase functions. For droplets, Mie theory is used for spherical particles with diameters from $50 \mu\text{m} \leq D \leq 700 \mu\text{m}$. For ice, modelled orientation-averaged ASF of ice particles of different habits and roughness are calculated based on the databases from Baum et al. [2011] and Yang et al. [2013] in the size range from $20 \mu\text{m} \leq D \leq 700 \mu\text{m}$. Similarly as explained beforehand, the scattering intensities are integrated over the FoV of the polar nephelometer channels.

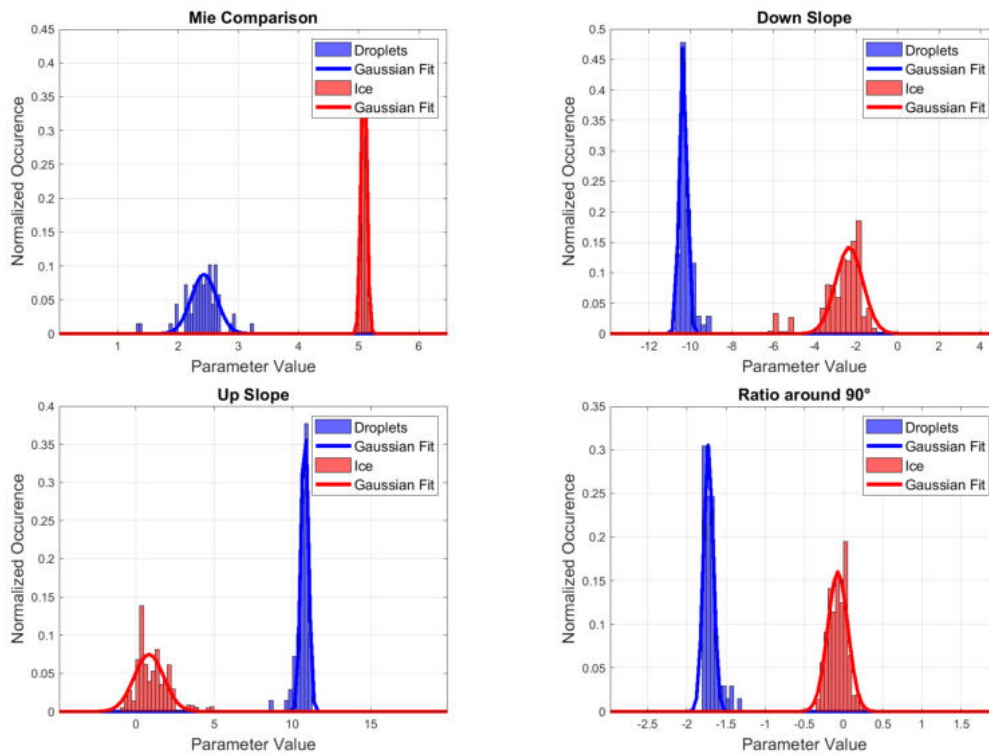


Figure 4.5.: Normalized histograms of the discrimination features, f_i , evaluated for theoretical ASFs. Simulated ASFs were calculated using Mie theory in case of droplets (blue) and by selecting typical ice particle habits (red) from the light scattering databases by Baum et al. [2011] and Yang et al. [2013]. Normal distribution fits to the data are depicted by solid lines in the graphs. Note that the simulations provide orientation-averaged ASF whereas the observed particles by PHIPS have random but fixed orientation.

The distribution of feature parameters is shown in Fig. 4.5. It can be seen that the resulting values differ significantly for droplets and ice. This indicates that the aforementioned features are in fact fit to discriminate the ASF of spherical and aspherical particles. From now on, particles that appear spherical in terms of their angular light scattering behavior are assumed to be droplets and particles that appear aspherical in their ASF are ice. Note that this includes also deformed droplets (see Section 4.5) as well as quasi-spherical ice as shown in Fig. 2.21.

However, it is important to note that the simulated values correspond to theoretical, idealized particles that do not represent real ice crystals which can inherit various kinds of complexity features beyond surface roughness (see Section 2.4.2). Further, the simulated ASF are based on orientation averaged phase functions of simulated particles. Measured particles however always have a (usually random but) fixed orientation. In the next section, the derived feature parameters of real ice particles measured by PHIPS are used to calibrate the phase discrimination algorithm and the values are compared to the simulated particles.

4.3. Calibration

The next step is to calibrate the discrimination algorithm, i.e. determine empiric thresholds that determine whether a particle with a given set of feature parameters $\{f_i\}$ is classified as liquid or ice. The discrimination features were applied to experimental data sets of real cloud particles. In situ data of representative, manually classified single particles are used to validate the calculated features. This experimental data was then used to calibrate the algorithm (i.e. the classification probability functions $P_i(f_i)$ for every feature), in order to have a numerical function that calculates a classification probability for every feature of a given particle, and later a combined probability that can be used to discriminate every single particle based on its phase.

The experimental data sets used for the calibration and verification of the discrimination algorithm is based on manually classified particles from the ACLOUD and SOCRATES campaigns (see Section 3.3). During the first flight of SOCRATES, PHIPS was not recording images due to malfunction of the imaging laser, hence RF01 is excluded from the calibration and analysis. RF15 was dominated by precipitation (such as seen in Fig. 4.11) and was hence excluded as well, as those particles are not representative (see discussion in Section 4.5) and would negatively affect the calibration.

As it is the goal to develop an algorithm that is suitable without any further calibration for upcoming campaigns, the calibration and verification data sets are entirely disjunct: the ACLOUD data set is used for calibration, the verification is done using the SOCRATES data set. The ACLOUD and SOCRATES campaigns comprise 14 and 15 research flights, during which, in total about 41,000 and 235,000 single particles were detected by PHIPS, respectively. More details about sizes and habits of the manually classified particles used for the calibration can be found in Section 3.3. Because the imaging component of PHIPS has a limited temporal resolution, this results in about 22,000 and 32,000 events with matching stereo micrographs for the ACLOUD and SOCRATES flights, respectively. Based on these stereo micrographs, all imaged particles were manually classified as ice or droplets. To ensure a representative data set, only clearly distinguishable particles were taken into account, whereas images that show multiple particles and particles that are only partly imaged, out of focus or not clearly distinguishable, were ignored. Hence, the resulting data set used for the calibration (based on the ACLOUD campaign) includes 1,853 droplets and 7,885 ice particles. The data set used for the validation and determination of the discrimination accuracy (see Section 4.4) contains of 2,284 droplets and 9,936 ice particles from the SOCRATES campaign. The chosen data sets consist of representative cloud particles which cover a wide range of different particle shapes and habits (columns, plates, needles, bullet rosettes, dendrites and irregulars, including rough, rimed and pristine particles) as well as sizes $D_{\text{geom}} = 20 - 700 \mu\text{m}$ and $D_{\text{geom}} = 50 - 700 \mu\text{m}$ for ice and droplets, respectively.

The left panels of Fig. 4.6 show, similar to the simulations in Fig. 4.5, the relative amount $n(f_i)$ of particles that share a certain feature parameter value X . To account for the different amount of measured droplets and ice particles in the data set ($N_{\text{ice}} \approx 3 \cdot N_{\text{droplet}}$), the number

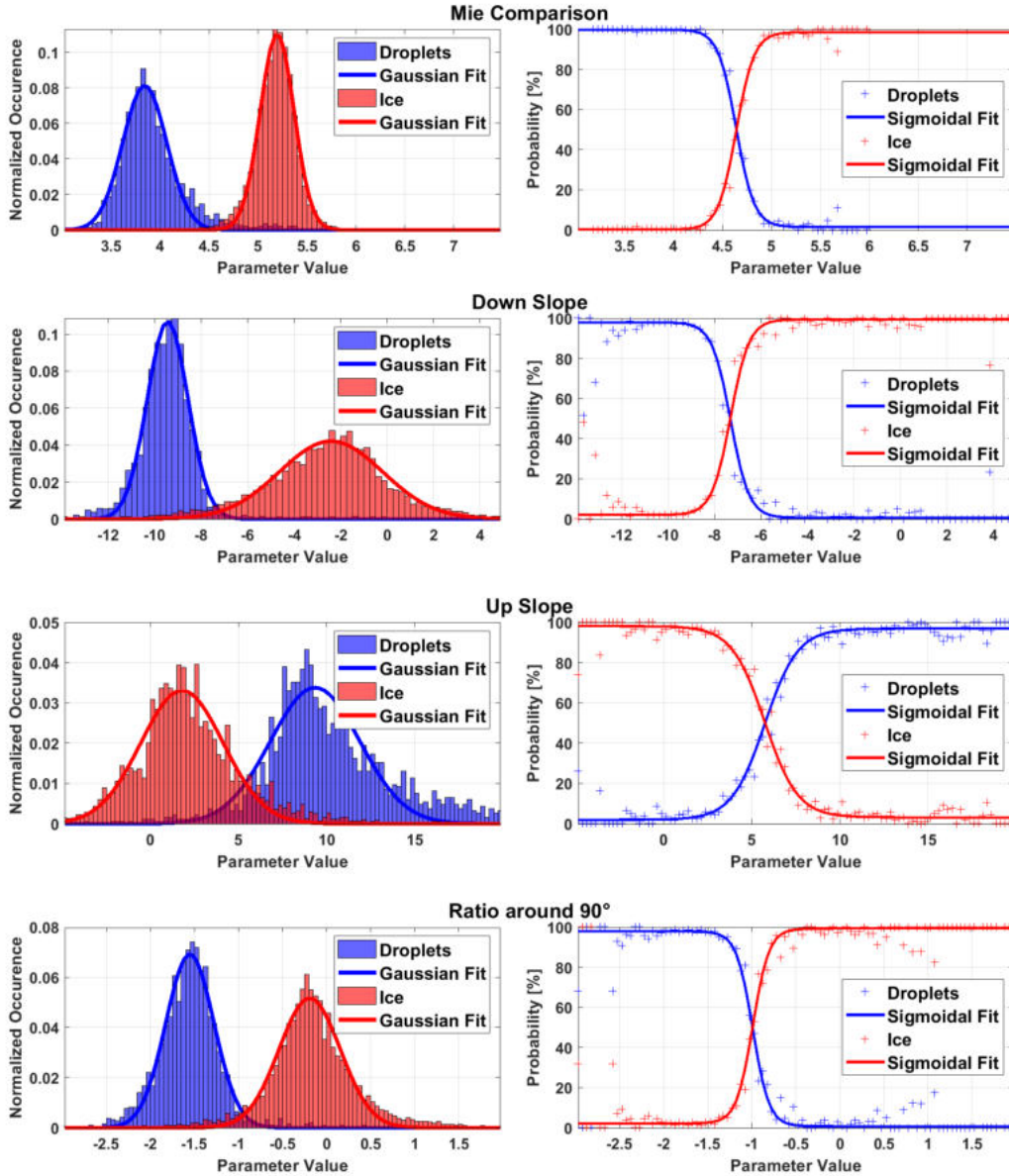


Figure 4.6.: Left: normalized histograms of the discrimination features, f_1 , f_2 , f_3 and f_4 , of all manually classified particles (blue: droplets, red: ice) from the ALOUD campaign that were used for the calibration of the discrimination algorithm. The histograms can be nicely fitted by normal distributions (solid lines). Right: corresponding probability for a given particle with a given feature parameter value to be classified as ice or droplet, including sigmoidal fits. The fit parameters are shown in Appendix A.4.

frequencies $n_{\text{droplet/ice}}$ are normalized by the total amount of droplets and ice particles. The plots show that the distribution of the four aforementioned feature parameters are clearly distinct for droplets and ice and thus represent features that can be used to discriminate droplets from ice. Further, it can be seen that these normalized occurrences $n(f_i)$ are normally distributed.

The distributions of the four feature parameters based on the measurements (Fig. 4.6) show a similar trend to the simulations (Fig. 4.5). The width of the distributions of feature parameters for measurements is much broader compared to the simulations. This can be explained by the single-orientation of the measured crystals compared to the orientation-averaging that was used in the simulations. Orientation-averaging tends to smooth out features in the ASF and thus cause more narrow feature parameters. It should be also noted that the theoretical computations are for idealised crystals. Nevertheless, the mean values of the distributions agree very well. The only exception to this is the mean value of the distribution of droplets for f_1 , which is shifted slightly to larger values compared to the simulations. This is to be expected because the "Mie-comparison-feature" f_1 is based on the relative difference between the measured and calculated ASF. This difference is much smaller for simulated particles.

However, Fig. 4.6 also shows that the ice and droplets modes are not always clearly separable for every feature and for every measured particle. Therefore, instead of using a sharp threshold, a classification probability

$$P_i(f_i) = \frac{n_{\text{ice}}(f_i)}{n_{\text{ice}}(f_i) + n_{\text{droplet}}(f_i)}, \quad (4.7)$$

that a particle is classified as ice (or with $1 - P_i(f_i)$ as a droplet) based on the ratio between $n_{\text{droplet}}(f_i)$ and $n_{\text{ice}}(f_i)$ for each feature (see right panels of Fig. 4.6), is defined. Assuming that the $n_i(f_i)$ follow normal distributions with comparable widths, $P_i(f_i)$ can be approximated and fitted by a sigmoid function (see Appendix A.3). Following that, the probability functions $P_i(f_i)$ are determined by using a sigmoidal fit for every feature based on the empiric data. The corresponding fit parameters are shown in Table A.1 and Table A.2 in Appendix A.4. These probabilities, P_i , for each feature are combined to

$$P_{\text{combined}} = \frac{1}{n} \sum_{i=1}^n w_i \cdot P_i(f_i) \quad (4.8)$$

with empiric weights w_i that are determined using recursive, linear optimization.

4.3.1. Determination of the Optimum Weight

The determination of the optimum weight is done via the following steps:

1. Generate randomized training data set (2/3 of the whole data set).
2. Generate a random starting point (set of weights).
3. Variate one weight (chosen randomly) in coarse steps ($\Delta w = 1$) from 0 to 10, calculate the total combined classification probability P for every particle of the training data set and count how many particles are misclassified.
4. Select the weight with the least amount of misclassified particles, use this set of weights as the starting point and start over with step 3 and variate another weight from 0 to 10, until a (local) minimum is reached, i.e. every weight has been varied and the discrimination accuracy does not change any further.

5. Repeat the same procedure as 3 with finer steps, i.e. variate a randomly chosen w_i from $w_{i, \text{old}} - 1$ to $w_{i, \text{old}} + 1$ in $\Delta w = 0.2$ steps until a minimum is reached.
6. Start over with step 2 and generate a new randomized starting point. This is repeated for e.g. $k = 50$ times and each time the "best" set of weights with the least amount of misclassified particles is saved.
7. Start over with step 1., generate a new randomized training data set and repeat the steps above for e.g. $l = 10$ times.
8. Finally, these resulting $k \cdot l = 500$ potential candidates for the best set of weights are tested using the whole data set and the one particular set of weights with the least amount of misclassified particles (over the whole data set, not only the training data set) is declared as the winner.

To avoid over-fitting and creating a lookup table, the data set is split (randomly) 2:1 and only 2/3 of the hand-classified data set is used as "training data". Further, to make sure that we do not end up in the same local minimum over and over again, the start point (i.e. the starting weight) is chosen randomly.

Because there is one remaining degree of freedom that means e.g. the set of weights $w = [1 \ 1 \ 1 \ \dots]$ and $w = [2 \ 2 \ 2 \ \dots]$ are equivalent, the weight of one feature can be chosen freely (e.g. $w_1 = 1$) and the remaining weights are chosen in respect to that.

Coincidentally, the optimum weight is to weigh all four features equally, i.e. $w_1 = w_2 = w_3 = w_4 = 1$ and thus $P_{\text{combined}} = \text{mean}(P_i)$. Finally, this results in a classification probability for every given particle with a set of calculated feature parameter values $\{f_1, f_2, f_3, f_4\}$, which is then classified based on P_{combined} as a droplet ($P \leq 50\%$) or ice particle ($P > 50\%$).

4.4. Discrimination Accuracy

4.4.1. Cross-correlation of the Feature Parameters

In Section 4.3 it was argued that one feature alone is not sufficient to reliably classify all cloud particles due to the particles that lie in the overlap between the two peaks in Fig. 4.6. Now the question is, how dependent are the four features and whether or not a particle that cannot be confidently (or is even falsely) classified by e.g. f_3 , i.e. that lies in the overlap of the feature space, can be confidently classified by the other feature parameters or if it lies in the overlap for the other features as well.

Fig. 4.7a shows the correlation of the classification confidence based on only one feature parameters f_3 and of the combined result for all 4 features for all manually classified ice particles of the ACLOUD campaign. It can be seen that lots of particles that cannot be classified with high confidence by the first feature ($P(f_3) < 66\%$) are classified with high confidence by the other features ($P_{\text{combined}} > 66\%$).

The corresponding statistics are displayed in a confusion matrix in Fig. 4.7b. Most of the particles (87.5%) are correctly and confidently classified based on f_3 alone (column 4). But out of the 992 particles that are not classified confidently and correctly based on f_3 (i.e. sum of column 2 and 3), most (805) are confidently classified based on the combination of all four features. This shows that the usage of multiple features significantly improves the discrimination accuracy. Hence, by combining all four different features, a high combined classification confidence and accuracy can be achieved.

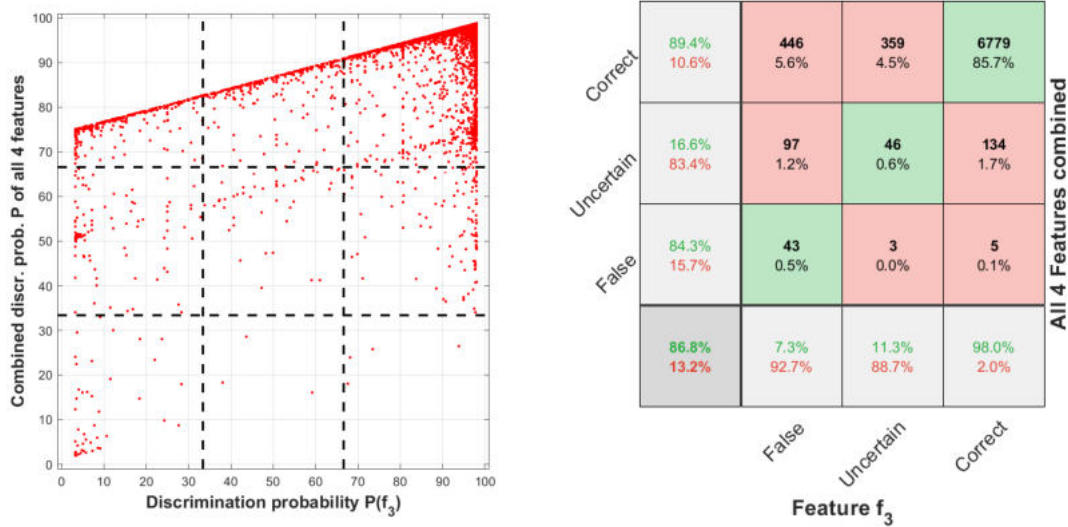


Figure 4.7.: a) Correlation of the classification probability of feature parameters f_3 alone and the combination of all four features. The dashed lines mark the confidence limits. $P(f) > 66\%$ corresponds to particles that are classified correctly with high confidence, $33 < P(f) \leq 66\%$ means the classification is uncertain and particles with $P(f) \leq 33\%$ are classified falsely as droplets with high confidence. b) shows the corresponding statistics of the plot in a confusion matrix. The squares correspond to the dashed lines in a).

4.4.2. Validation of the Discrimination Algorithm

Discrimination algorithms often run in danger of *overtraining* or creating a *lookup table*, resulting in seemingly very good discrimination accuracies that, in reality, are just recreating the training data used for calibrating the system but fail to classify new, unknown data sets. In order to avoid this, the *training* and *test* data set are not only disjunct, but from entirely different field campaigns: The calibration of the discrimination algorithm is purely based on the experimental in situ data gathered during the ACLOUD campaign, whereas the determination of the discrimination accuracy is tested also on the SOCRATES data set. Furthermore, this proves that the algorithm is able to function independently for different campaigns without further calibration.

The confusion matrices [Fawcett, 2006] for the discrimination algorithm for the two campaigns are shown in Fig. 4.8. For the SOCRATES data set, 99.7% of ice particles could be correctly classified as ice and only 29 out of 9,936 were misclassified as droplets. 95.8% droplets were classified correctly and 95 out of 2,284 were misclassified as ice. In total, out of all particles, 99.0% were classified correctly. Respectively, if a particle is classified as ice (droplet) by the algorithm, the expected error (i.e. the probability that the initial particle was actually a droplet) amounts to 0.9% (1.3%). Also, 100% of the theoretical particles used in Section 4.2 (which were not used for the calibration) were classified correctly. More details about the discrimination accuracy and misclassified particles can be found in the following section.

Note that during ACLOUD, one channel ($\theta = 34^\circ$) was malfunctioning and is hence excluded from the analysis. During SOCRATES, the $\theta = 90^\circ$ channel was affected by the background noise in case of droplets and was thus excluded. However, due to the design of the discrimination features (i.e. averaging over multiple channels), the implications on the discrimination are reduced and the same parameterization still works well for the SOCRATES data set.



Figure 4.8.: Confusion matrices that visualize the classification accuracy of the ice discrimination algorithm. The discrimination algorithm was applied to all manually classified particles from both the ALOUD (left) and SOCRATES (right) data sets. In both cases the combined probability P_{combined} from the ALOUD calibration was used to calculate the classification probability of each individual particle.

4.5. Special Cases, Limitations and Misclassified Particles

The phase discrimination algorithm does not only give a binary classification result (e.g. 0 = ice, 1 = droplet) but also a discrimination confidence. Fig. 4.9a shows that correctly classified particles are usually classified with high confidence (close to 0 or 100%), whereas misclassified particles are often times quite unclear and the classification confidence is near 50%, i.e. the different features are equally strong leaning towards both sides. This can be used to manually check the ASF (or image, wherever available) of individual particles, where the classification of the algorithm is not conclusive.

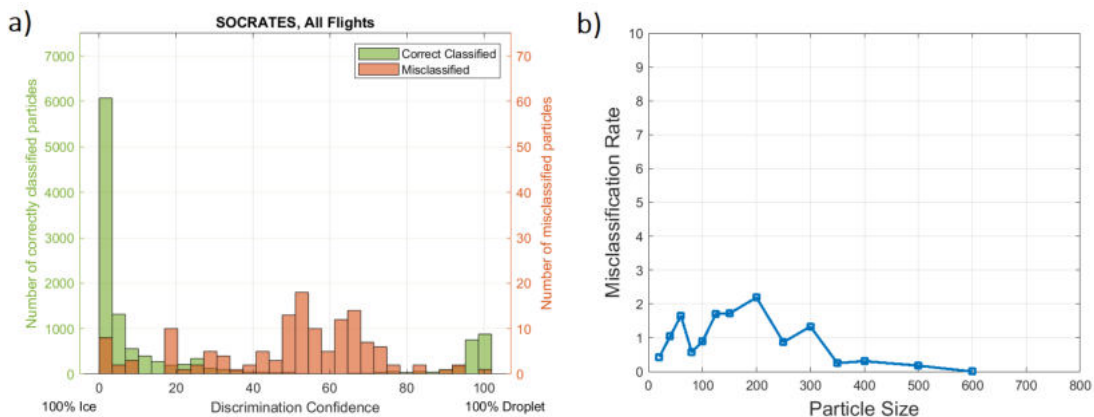


Figure 4.9.: a) Discrimination confidence of all correctly classified (left) and misclassified particles (right). b) Correlation of misclassification rate (= 100% - discrimination accuracy) and particle size. The size binning is the same as used previously.

In Table 4.1, the discrimination accuracy for the various particle habits for the SOCRATES data set is shown. It can be seen that the discrimination accuracy is relatively constant for the different habits and the algorithm is not biased towards certain shapes. Also, no

correlation of discrimination accuracy and particle size was found (see Fig. 4.9b.). In this section, examples of typical particle types that are sometimes misclassified, are presented.

Table 4.1.: Discrimination accuracy for different particle habits for the SOCRATES data set.

Particle Shape	Droplets (all)	Elongated Droplet	Drizzle	
Number True	2189	267	13	
Number False	95	40	6	
Accuracy [%]	95.8	87	68.4	
Particle Shape	Ice Particles (all)	Column	Plate	Needle
Number True	9907	788	2456	423
Number False	29	6	2	2
Accuracy [%]	99.7	99.2	99.9	99.5
Particle Shape	Bullet Rosette	Graupel	Frozen Droplet	Irregular
Number True	618	127	56	5339
Number False	0	0	1	20
Accuracy [%]	100	100	98.2	99.6
Particle Shape	Pristine	Rimed	Aggregate	
Number True	136	640	724	
Number False	2	1	2	
Accuracy [%]	98.6	99.8	99.7	

Elongated Droplets

The largest challenge for the presented discrimination algorithm is the correct classification of "elongated" droplets as seen in Fig. 4.10. Elongated droplets are droplets that are deformed due to the pressure difference in the inlet of the probe. This affects about 12% of all droplets and is dependent on the relative airspeed and particle size. Due to this deformation, the droplets are no longer spherical and harder for the algorithm to classify correctly¹. Whereas droplets usually show a steep decline in scattering intensity towards the side (i.e. the minimum around 90°), elongated droplets tend to scatter more light in the sideways direction. Also, the rainbow peak can be shifted. Still, despite their asphericity, the algorithm can still detect some features and classifies about 87% of all elongated droplets correctly.

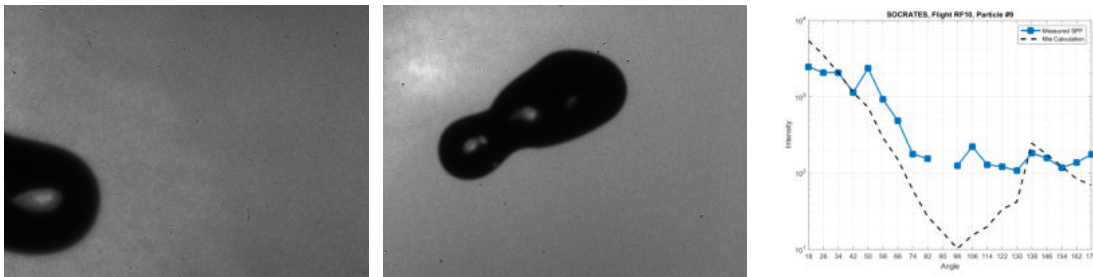


Figure 4.10.: Example of a typical elongated droplet, stereo images (left: CTA1, middle: CTA2) and the corresponding ASF (right) including the theoretical Mie ASF of a spherical particle ($D = 200\mu\text{m}$) for comparison.

¹Note that since the algorithm discriminates spherical and aspherical particles, these particles are technically not misclassified, as the droplets are in fact aspherical at the moment of measurement. However, as discussed previously, the goal of this work is to discriminate particles based on their phase. Hence, the algorithm is tuned to also discriminate elongated droplets as droplets and (quasi-)spherical ice as ice.

Large Drizzle Droplets

Another difficult case is the classification of very large particles which cause a lot of the scattering channels to be saturated. Since saturated channels are excluded from the analysis, the slope features cannot be calculated for such particles. Because the integrated area between the ASF and Mie calculation (see Mie feature f_1) is very large (see ASF in Fig. 4.11), such particles are usually classified as ice. Generally, this is reasonable, since large particles $D > 500 \mu\text{m}$ are usually ice particles. However, deformed precipitating drizzle droplets (see Fig. 4.11) can be misclassified. Such cases are, however, very rare.

A similar issue exists for very small particles with ASF near the background. If a particle shows an equally low scattering intensity over all channels, the resulting slopes are relatively horizontal and the integral between the Mie calculation large. The particle is hence usually classified as ice. This, however, is not a problem as PHIPS does not trigger on droplets below $50 \mu\text{m}$ and all smaller particles can thus be assumed to be ice.

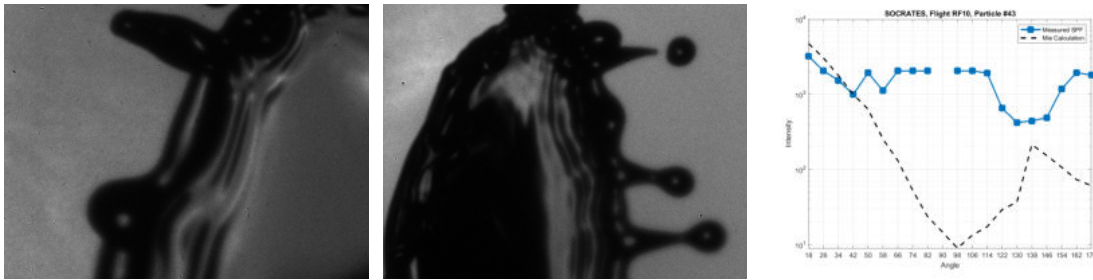


Figure 4.11.: Example of a typical misclassified large drizzle droplet with multiple saturated channels.

Other Misclassified Particles

Fig. 4.12 shows an example of a particle that is visually inspected clearly a pristine ice particle, which is misclassified because the ASF resembles all typical features of a droplet's: the minimum around 90° , the steep slopes. There is even a specular reflection in the angular range of the rainbow peak. Note that the lower ASF in the first scattering angles compared to the theoretical ASF does not influence the classification result, since the first channels are not taken into account as they are often times saturated. Approaches that, for example, only exclude the first channels if they are saturated and include them otherwise, were tried and could be able to correctly classify particles as this one, but resulted in an overall decrease of the discrimination accuracy (i.e. particles that are classified correctly now would then be misclassified). The algorithm was calibrated to optimize the overall discrimination accuracy, i.e. that the highest fraction of particles is classified correctly. Hence, if a particle's ASF happens to look like this, it will be misclassified. Fortunately, such cases are very rare.

4.6. Machine Learning

Binary classification problems like the one presented in this work are typically well fit to be solved using machine learning (ML) algorithms [Kumari and Srivastava, 2017]. For example, in recent works, Mahrt et al. [2019]; Touloupas et al. [2020]; Atlas et al. [2021] have presented different methods to employ ML to discriminate ice and liquid cloud particles using the PPD-HS, HOLIMO and 2D-S, respectively. Depending on the chosen classification problem, ML algorithms can be very easy and quick to set up: basically all that is needed is a (pre-classified) training data set. There exists software, such as e.g.

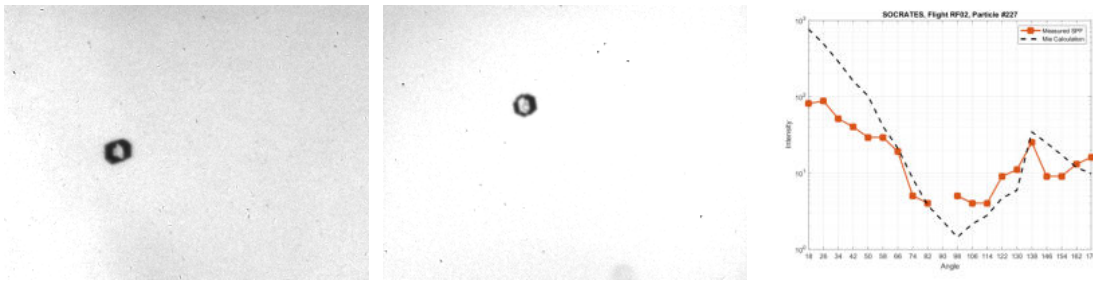


Figure 4.12.: Example of a particle that is clearly a pristine ice particle that is misclassified because the ASF resembles all typical features of a droplet's.

TensorFlow (Google LLC, CA) that is specialised on ML, however, nowadays most common analysis software such as e.g. *Matlab* or *Mathematica* have built-in ML toolboxes that make working with ML quite easy, fast and comfortable. In general, the main idea is that the ML algorithm is able to identify systematic differences and common features of the different "types" on its own (even such that could be hard to find for humans) and divide the data set accordingly. This way, the ML can classify even new, unknown data sets. Given a large enough training data set, ML algorithms can achieve high discrimination accuracies.

For comparison with the analytical approach used in this work, the classified data set was analysed using two different, basic supervised ML methods, using a) fine decision tree and b) linear support-vector machine (SVM). This was done once for the raw data, i.e. just the scattering intensity of the 18 scattering channels (the $\theta = 34^\circ$ and $\theta = 90^\circ$ were removed) as well as using the four features $[f_1, f_2, f_3, f_4]$ presented in this work as well as using both raw intensity and derived features. Again, the algorithm was trained using the ACLOUD data set and tested against the SOCRATES data set. All particles that had any NaN or INF values were discarded. The corresponding discrimination accuracies are shown in Table 4.2. It can be seen that the different ML methods already show good results. Also, this shows once more that the presented features $[f_1, f_2, f_3, f_4]$ are indeed fit to represent the difference in the ASF. With more fine tuning, especially the discrimination accuracy of the SVM approach might reach the 99% of the analytical approach.

Table 4.2.: Classification accuracies for different ML approaches and different input information.

Used data set	Fine Decision Tree	Linear SVM
Raw ASF data	96.4%	94.4%
Derived features	97.9%	98.4%
Both	97.6%	98.4%

However, despite the discussed advantages, ML also has one main disadvantage: it is hard to understand what the algorithm is doing in detail. Basically, what you end up with, is a *black-box* that classifies input data with a given confidence, but you cannot tell why. Hence, it is very hard to analyze which features are relevant for the classification. Further, since the ML knows only statistics, not physics, it is possible that the ML algorithm links the classification to "un-physical parameters" that can introduce systematical biases. For example, it could be possible that the ML algorithm learns that large particles (with a corresponding high total scattering intensity) are typically ice, whereas droplets are typically smaller and hence scatter less light. Thus, it would look at the "amplitude", rather than the "shape" of the ASF and classify all "large particles" as ice. Since the number of large droplets in the used data set is rather small, the overall discrimination accuracy would be quite high, however there would be the systematical bias that the few large droplets would tend to be misclassified.

Hence, and because it yields better discrimination accuracy, the analytical approach was chosen over ML for this work. Also, the presented method has the advantage, as discussed previously that it works without calibration for further campaigns, even when single scattering channels are malfunctioning (such as e.g. the $\theta = 34^\circ$ channel during ACLOUD) or the laser power is changed (since it takes only the shape, not the amplitude into account). Nevertheless, the presented analytical method works similarly to the ML approach.

4.7. Summary

In this chapter, a novel method to discriminate the phase of single cloud particles in the size range from $20 \mu\text{m} \leq D \leq 700 \mu\text{m}$ was presented. Based on the comparison of the theoretical phase function for spherical and aspherical particles, four parameters were derived that represent the distinct differences in their scattering behaviour. This way, an algorithm to discriminate individual (spherical) droplets from (aspherical) ice particles based on the shape on their ASF was derived.

The proof of concept of the discrimination methods was demonstrated using calculated phase functions using Mie theory for spherical particles and a database of modelled, aspherical ice particles. The algorithm was then calibrated and validated using disjunct sets of manually classified data acquired during two in situ aircraft campaigns. It was shown that the algorithm is able to reliably discriminate droplets and ice with a confidence above 98%.

Since the algorithm was calibrated with data from one campaign and validated using the data acquired during another campaign, it has been proven that the same algorithm can be applied for future campaigns without further calibration. It has been demonstrated that the algorithm still functions when single scattering channels are missing (e.g. due to malfunction or saturation) as all derived feature parameters are based on the slope or average over multiple scattering angles. Furthermore, as the method is not depending on absolute values of the scattering amplitude but rather the relative shape of the ASF, the discrimination algorithm is not influenced by changes or fluctuations of the incident laser power. Also, even though the algorithm was calibrated and tested using only PHIPS data, the method is not tied to the setup of PHIPS but works analogously for every polar nephelometer that measures the ASF of particles in a similar angular range.

In the following chapter, the phase discrimination algorithm presented in this chapter will be combined with a particle sizing method to derive phase discriminated PSDs based on the ASFs of single particles measured by PHIPS. These results are compared to data measured by other probes for three representative case studies.

5. Derivation of Particle Size Distributions based on Single Particle Polar Nephelometer Data

In the previous chapter, a novel method to discriminate the phase of individual cloud particles on the **shape** of their ASF was introduced. In this chapter, the **amplitude** of the ASF is used to determine the size of droplets and ice particles. This way, phase discriminated particle size distributions (PSDs) based on the ASFs of single particles of PHIPS can be determined.

Further, the detection of shattering artefacts and statistical uncertainties are discussed. The combined methods are applied to three representative case studies and the PSDs are compared to data of other instruments. The methods and case studies presented in this chapter are also published verbatim in Waitz et al. [2021a].

5.1. Particle Sizing based on Angular Scattering Function

As discussed in Section 3.1.1, PHIPS measures the differential scattering cross section of individual cloud particles via 20 detector channels. The differential scattering cross section for the detector at the angular position $\theta = \theta_0$ corresponds to

$$\sigma_{\text{scatt}}^{\text{diff}}(\theta_0) = I(\theta_0)/I_{\text{inc}} \cdot \pi \cdot D_{\text{laser}}^2/4 \quad (5.1)$$

with I_{inc} and D_{laser} the power and diameter of the incident laser beam, respectively. Integrating Eq. (5.1) over all nephelometer channels gives a partial scattering cross section

$$\sigma_{\text{scatt}}^{\text{partial}} = \pi \cdot D_{\text{laser}}^2/(4 \cdot I_{\text{inc}}) \cdot \int I(\theta) d\theta \quad (5.2)$$

of the particle as defined for the PHIPS measurement geometry. For spherical particles, $\sigma_{\text{scatt}}^{\text{partial}}$ is approximately proportional to their geometrical cross section $A = \pi \cdot D_{\text{geom}}^2/4$, with the particle diameter D_{geom} (see Section 3.1.1).

Assuming that there is a similar dependence between $\sigma_{\text{scatt}}^{\text{partial}}$ and D_{geom} for ice particles as well, the scattering equivalent particle diameter D_{scatt} can be deduced from the PHIPS intensity measurement $I(\theta)$

$$D_{\text{scatt}} = a \cdot \left(\int I(\theta) d\theta - c_{\text{BG}} \right)^{\frac{1}{2}}. \quad (5.3)$$

In Eq. (5.3), a is a calibration coefficient that describes the incident laser properties (beam width and incident laser power), the detection characteristics of the polar nephelometer (e.g. the MAPMT gain settings) as well as the angular light scattering properties of the particle, and c_{BG} the integrated background intensity. As already discussed in the previous section, ice and droplets have vastly differing angular scattering characteristics, i.e. scattering cross sections $\sigma_{scatt}^{diff}(\theta)$. Hence, different a coefficients are needed and the calibration is done separately for ice and droplets. The coefficient a is calibrated based on the area equivalent diameter D_{geom} derived from the stereo micrographs. A correction for the slight size overestimation of the CTA2 for small particles due to the lower magnification is applied (see Section 3.2.1).

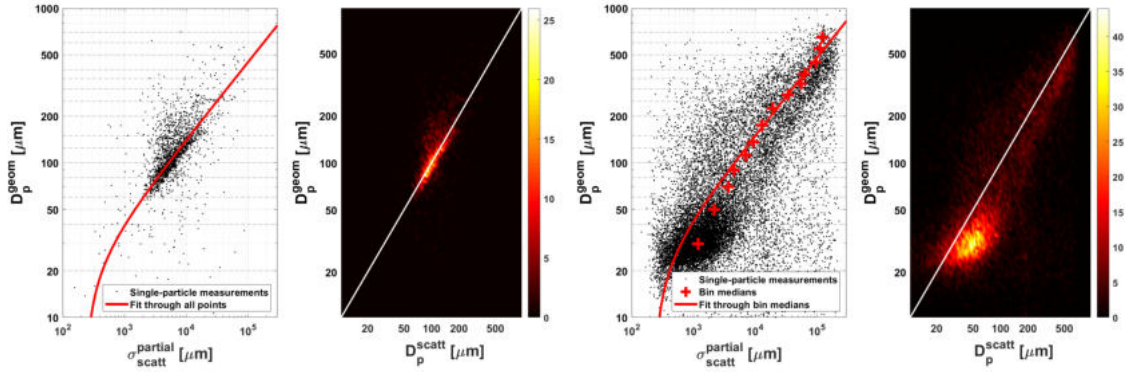


Figure 5.1: Calibration of the PHIPS integrated light scattering intensity measurement, expressed by the partial scattering cross section $\sigma_{scatt}^{partial}$, against the geometric diameter D_{geom} deduced from the concurrent stereo micrographs. Stereo micrographs from the SOCRATES data set were manually classified for droplets (left) and ice particles (right).

The experimental data set used for the calibration of the phase discrimination algorithm described in Section 4.3. The data are binned with respect to the particle's geometrical area equivalent diameter. The bin edges are the same as used for the final PSD data product. Those are 20 μm , 40 μm , 60 μm , 80 μm , 100 μm , 125 μm , 150 μm , 200 μm , 250 μm , 300 μm , 350 μm , 400 μm , 500 μm , 600 μm and 700 μm . For ice, the coefficient a is determined by fitting Eq. (5.3) through the median of each bin. For droplets, the function is fitted through all data points since the data points are distributed over fewer size bins. The background intensity c_{BG} is determined as the integrated intensity from forced triggers averaged over time periods when no particles were present. c_{BG} is the same for droplets and ice. The calibration is performed for each campaign separately, assuming that the instrument parameters remain unchanged over the duration of one campaign. The resulting calibration of the scattering equivalent diameter for the SOCRATES campaign is shown in Fig. 5.1a and Fig. 5.1b for droplets and ice, respectively. The corresponding fit parameters are $a_{ice} = 1.4167$ and $a_{droplet} = 1.4441$. The background measurement value is $c_{BG} = 238.12$. In a similar fashion, particle sizing calibrations are determined for the ACLOUD and IMPACTS campaigns (plots not shown here).

In order to calculate a PSD per volume from the single particle sizing data, as shown in Fig. 5.2, the volume sampling rate of the instrument has to be known. This sampling rate is the product between the speed of the aircraft and the sensitive area A_{sens} of the trigger optics (see Section 2.5.3). The size of the sensitive area A_{sens} is determined using optical engineering software. This is presented in Section 3.1.3.

PSDs can also be calculated based on D_{geom} deduced from PHIPS' micrographs. However, since only a sub-sample of the PHIPS particle events produce a stereo micrograph (i.e. maximum imaging rate of 3 Hz in ACLOUD and SOCRATES), PSDs that are based on the analysis of the images can only be calculated with a limited statistics. Furthermore, particle

sizing might be biased for particles with sizes smaller than $30\ \mu\text{m}$, due to the limited optical resolution of the PHIPS imaging system (see Schnaiter et al. [2018] and Section 3.2.1).

Fig. 5.2 shows the comparison of the PSDs based on the images (D_{geom} , solid lines) and the ASFs (D_{scatt} , dotted lines) averaged over all flights of SOCRATES for both ice (red) and droplets (blue). The PSDs for droplets agree very well. The PSD based on D_{scatt} slightly overestimates the concentration of large droplets. This might be caused by deformed droplets (see Section 4.5) that have an increased ASF compared to spherical particles of the same size. For ice, the PSDs also agree well, however the PSD based on D_{scatt} underestimates the concentration of particles in the smallest bin ($20 \leq D \leq 40\ \mu\text{m}$) whilst overestimating the concentration of large particles. That means, on average, particle sizing based on the ASF results in a slightly higher D compared to the image analysis and the PSD is shifted to the right. One potential reason for this are surface complexity features such as riming which increase the ASF compared to an unrimed particle of the same D_{geom} (see Section 2.4.2 and Section 7.4 and hence result in a larger D_{scatt} . Another potential reason is the underestimation of D_{geom} of particles due to the 2D image projection, i.e. for instance when a column is captured from the basal plane (see discussion in Section 2.5.1).

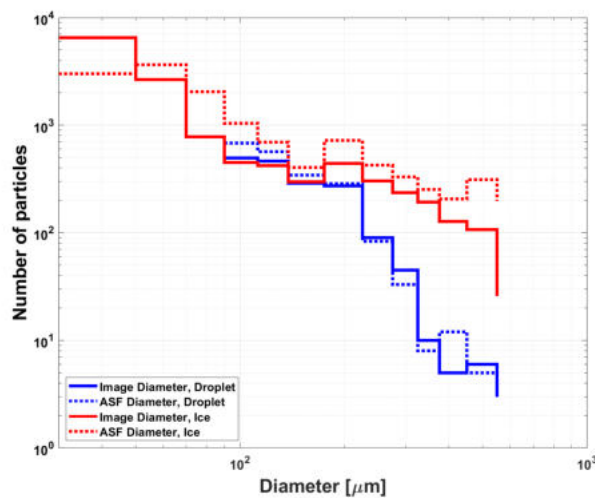


Figure 5.2.: Comparison of PSDs based on D_{scatt} calculated from the single particle ASFs using the calibration defined in Eq. (5.3) (dotted line) and PSDs based on D_{geom} derived from stereo micrographs (average of CTA1 and CTA2, solid line) for droplets (blue) and ice particles (red). The data are from all flights recorded during SOCRATES. Only particles with stereo micrographs that showed only one, completely imaged particle were taken into account. The same particles were used for both PSDs.

5.2. Identification of Shattering Artefacts

One major source of uncertainty for wing mounted probes is shattering of ice particles on the instrument's outer mechanical structures or breakup of particles in the instrument inlet. Fig. 5.3 shows a typical example of a shattering event. Fig. 5.4 shows the microscopic stereo images of a case where a large aggregate was broken up into multiple small fragments.

Shattering can lead to a significant overcounting of ice particles (e.g. in some studies up to a factor of five using a fast forward scattering spectrometer probe (FSSP), Field et al. [2003]) and a bias in the PSD towards smaller sizes. In this section, the frequency of shattering events in the SOCRATES data set is characterized and a method to detect shattering events within the PHIPS data sets is presented. Even though the geometry of PHIPS was designed to minimize disturbances and turbulences in the instrument (e.g. sharp edges at the front

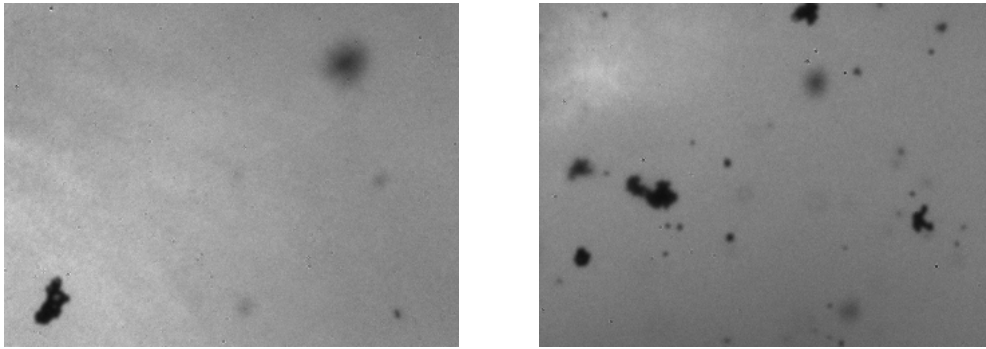


Figure 5.3.: Example of a shattering event during the transit leg of SOCRATES RF06. The images (left CTA1, right CTA2) show one representative shattering event during this time period.

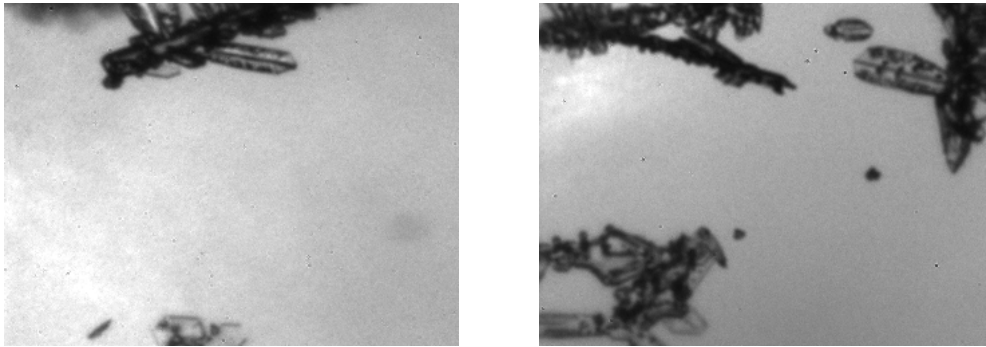


Figure 5.4.: Example of a shattering event (left CTA1, right CTA2) during another segment of RF06, indicating the breaking up of aggregates.

of the inlet and an expanding diameter of the flow tube towards the detection volume (see Abdelmonem et al. [2016]), shattering can still be an issue, especially in clouds where large cloud particles and aggregates with $D > 1$ mm are present.

Since the FoV of the CTA is much larger (typically ≈ 1.5 mm \times 1 mm) compared to the sensitive trigger area ($A_{\text{sens}} \approx 0.2 - 1$ mm², see Section 3.1.3), the stereo micrographs can be used to detect shattering events. However, as only a subset of detected particles is imaged, a shattering correction based on inspection of the stereo micrographs is not a practical and reliable solution. Still, manual examination of the stereo micrographs can be helpful to determine whether or not a cloud segment was affected by shattering in individual cases.

5.2.1. Interarrival Time Analysis

The most common method to detect shattering that is based on the analysis of particle interarrival times [Field et al., 2003]. If two (or more) particles are detected in very short succession, those particles are identified as shattering fragments and removed. Fig. 5.5 shows a histogram of interarrival times (τ) of ice particles (left) and droplets (right) measured during two flights of SOCRATES. For ice, it is apparent that the otherwise approximately log-normal distributed interarrival times show a second, lower mode between $0.1 \leq \tau \leq 0.5$ ms (equivalent to spatial separation of 1.5 to 7.5 cm, assuming a relative air speed of $v = 150$ ms⁻¹) that is likely caused by shattering. For droplets, the second mode is not visible, since droplets tend to less fragment when entering the instrument inlet.

Whereas the interarrival time analysis method is used in multiple OAPs (2D-S, 2D-C, Field et al. [2003]), the application is limited for single-particle instruments, like PHIPS, due to

their small sensitive area. Near the detection volume, the inlet has a diameter of 32 mm, whereas the sensitive area measures only about 0.7 mm (depending on phase and size, as discussed in Section 3.1.3), which means that the probability to detect two (or more) fragments of the same shattering event is very low and hence the instrument would detect only one shattered particle. Furthermore, the instrument has a dead time of $t = 12 \mu\text{s}$ after each trigger event [Schnaiter et al., 2018]. Additional shattering fragments that pass during this time, are not detected.

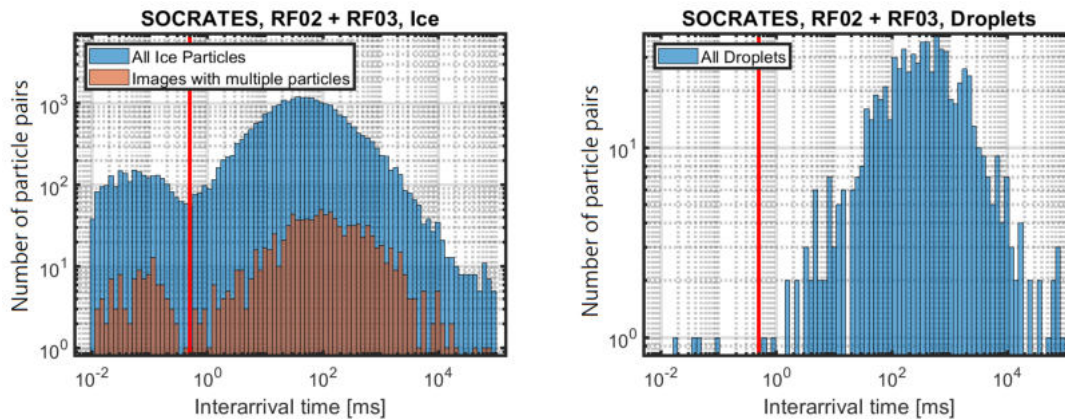


Figure 5.5: Histogram of interarrival times of ice particles (left) and droplets (right) measured during SOCRATES flights RF02 and RF03. Comparison of the interarrival times of all particles (blue) and only particles whose images were manually classified as shattering events (red). The red vertical line marks the $\tau \leq 0.5$ ms threshold. The lowest measured interarrival time is limited by the dead time of $t = 12 \mu\text{s} = 0.012$ ms after each trigger event.

As shown in Fig. 5.5, only a small percentage of the particles whose images were manually classified as shattering (red), could be identified as shattering using the interarrival time analysis method. Hence it can be concluded that interarrival time analysis alone is not fit as a reliable shattering flag, either. Nevertheless, all particles with a low interarrival time $\tau \leq 0.5$ ms are removed and excluded from the analysis. In the next section, a shattering flag is introduced which marks segments which are affected by particle shattering, so they can be excluded from further analysis.

5.2.2. Shattering Flag based on the Presence of Large Particles

It is known that a particles shattering probability is strongly size dependent. Large particles and aggregates are much more prone to shattering compared to small particles. To overcome the limitation of the interarrival time method to eliminate shattered particles, a shattering flag based on the presence of large particles is introduced. Fig. 5.6a shows the total number concentration of particles in the size overlap region of PHIPS and 2D-S ($200 \mu\text{m} \leq D \leq 500 \mu\text{m}$, see Section 2.5.5.2) for all SOCRATES flights. The data are averaged over 30 s segments. Only segments with $N_{2\text{D-S, overlap}} \geq 0.5 \text{ L}^{-1}$ are taken into account. The colour-code indicates the fraction of 2D-S particles in the size range of $D_{\text{max}} \geq 200 \mu\text{m}$ that are larger than $800 \mu\text{m}$. The diagonal lines mark the median ratio between $N_{\text{PHIPS}}/N_{2\text{D-S}}$ of each colour. Fig. 5.6b shows the correlation of the difference between PHIPS and 2D-S in the overlap region and the ratio of large particles. It can be seen that the two probes agree very well in segments with only a few large particles.

In segments that consist of more than 10% large particles, PHIPS and 2D-S tend to disagree and PHIPS can overestimate particle concentrations in the size range $200 \mu\text{m} \leq D \leq 500 \mu\text{m}$

by up to a factor > 10 . This can be explained by the shattering of large particles on the instrument inlet tip or wall or disaggregation of large aggregates due to shear forces in the inlet flow.

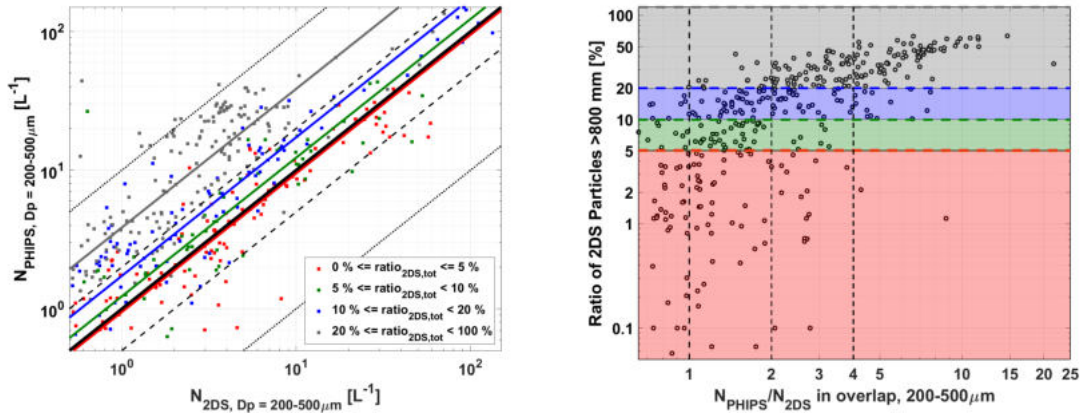


Figure 5.6.: a) Comparison of the total number concentrations of 2D-S and PHIPS. Each point is averaged over 30 s. The colour-code is based on the ratio of large 2D-S particles with $D_{\text{max}} \geq 800 \mu\text{m}$. The thick black line marks the 1:1 line, the dashed and dotted lines factor 2 and 10. b) Correlation of the ratio of number concentrations of PHIPS and 2D-S and the presence of large 2D-S particles. The horizontal line marks the 10% threshold. The colour-code is the same as in a).

Therefore, said marker for the presence of large particles will be used as a shattering flag to mark cloud segments that are potentially affected by shattering. In segments where the 2D-S did not detect any particles or was not measuring 2D-C data are used instead. That means, cloud segments with more than 10% large particles are removed for future analysis. For the SOCRATES data set, 44% of all 1s segments are flagged as shattering. This means that about half of all 30s segments in MPCs and approximately 75% of pure ice clouds are affected. Droplet dominated cloud segments are not affected by this shattering flag. Due to the small A_{sens} PHIPS cannot reliably detect multiple shattering fragments and it is hence not possible to correct the data but the corresponding segments that are affected are removed.

5.3. Statistical Significance of Particle Size Distributions

The sampled cloud volume V_{sens} per unit time t calculates as $V_{\text{sens}} = A_{\text{sens}} \cdot v \cdot t$, where v is the relative air speed and A_{sens} the probe's sensitive area. A_{sens} is dependent on particle phase and diameter, as discussed in Section 3.1.3. Assuming a relative air speed of $v = 150 \text{ m s}^{-1}$, the resulting sample volume amounts about $V_{\text{sens}} = 0.08$ (0.026, 0.12) L s^{-1} for ice particles with diameter $D = 200$ (50, 500) μm , respectively. This is somewhat larger compared to other single-particle cloud instruments (e.g. the CPI, $V_{\text{sens}} = 0.009 \text{ L s}^{-1}$ [Lawson et al., 2001]), comparable to e.g. the SID-3 ($V_{\text{sens}} = 0.071 \text{ L s}^{-1}$ [Vochezer et al., 2016]), but is significantly smaller compared to the OAPs like the 2D-C ($V_{\text{sens}} \approx 0.1 - 10 \text{ L s}^{-1}$ [Wu and McFarquhar, 2016]). This has consequences for the averaging time needed in order to achieve statistically significant information on total particle concentrations.

The statistical uncertainty in example situations for the total number concentration for the size range from $D = 20 - 200 \mu\text{m}$ is investigated. This size range was chosen since at sizes below $D < 200 \mu\text{m}$ the phase information from PHIPS is of interest as phase detection based on traditional imaging methods can be challenging for small particle sizes.

In order to reach statistical uncertainty $\propto n^{-0.5}$ of less than 10%, the number of particles per size bin need to be larger than $n > 100$. Table 5.1 shows the calculated averaging time in seconds that is needed until $n = 100$ particles are sampled per bin ($t_{n=100}$), the estimated number of particles that would be sampled during 30 s of sampling ($n_{t=30s}$), as well as the corresponding statistical uncertainty $n^{-0.5}$ for a sampling period of 30 s ($n_{t=30s}^{-0.5}$) for the chosen size range. All particles were assumed to be ice.

Table 5.1.: Averaging time that is needed until $n = 100$ particles are sampled as well as the total number of particles sampled during an averaging time of 30 s, calculated for the size bin of $20 \leq D < 200 \mu\text{m}$ and exemplary particle concentrations.

$D_{\text{lower edge}}$	$D_{\text{upper edge}}$	Concentration [L^{-1}]	$t_{n=100}$ [s]	$n_{t=30s}$	$\sqrt{n_{t=30s}^{-1}}$ [%]
20	200	1	1688.5	1.8	75.0
20	200	10	168.9	17.8	23.7
20	200	56.3	30.0	100.0	10.0
20	200	100	16.9	177.7	7.5
20	200	1000	1.7	1776.8	2.4

It can be seen that the ice particle concentrations need to be larger than 56.3 L^{-1} in order to achieve a statistical uncertainty below 10% within 30 s. For ice particle concentrations of $1 (10) \text{ L}^{-1}$ an averaging time of 28 (2.8) min would be needed, which at least in the case of low ($< 10 \text{ L}^{-1}$) ice particle concentrations would likely exceed the typical sampling duration that is in the order of tens of seconds. For OAPs, assuming a sampling volume of $V_{\text{sens}} = 1.5 \text{ L s}^{-1}$ the corresponding sampling times would be 66.7 s and 6.7 s for concentrations of 1 and 10 L^{-1} . This shows that in order to get statistically significant size distributions, it is important to properly consider adequate averaging time and/or bin size, especially in segments with low particle concentration.

5.4. Case Studies: Verification of Phase Discrimination and Particle Sizing Methods

In this section, the previously presented methods are applied for three representative case studies from the SOCRATES campaign in altitudes below 2000 m for one purely liquid cloud and two MPCs which were not affected by shattering and the results are compared to the measurements of other instruments during the same cloud segments.

5.4.1. Case Study 1 — Pure Liquid Cloud

Fig. 5.7a shows meteorological and microphysical data collected during SOCRATES research flight RF04 on January 24th, 2018. Taking off in Hobart, Australia, the aircraft flew south-west sampling in different types of clouds ranging from deep precipitating clouds to layer clouds in various altitudes. The probing pattern was alternating between above cloud sampling (for aerosol measurements) and in cloud sampling (to investigate the microphysical properties of cloud hydrometeors).

A low-level supercooled liquid cloud was probed in an altitude of approximately 2,100 m at a temperature of about $-8.5 \text{ }^\circ\text{C}$ at around 55°S , 141°E . The vertical wind velocity was at a constant value of -0.5 m s^{-1} , indicating a weak downdraft. The relative humidity with respect to ice averaged about 105%. The LWC measured with the CDP averaged around 0.1 g L^{-1} and the TWC measured with the 2D-S was around 0.5 g L^{-1} . The lower panel shows the radar reflectivity measured by the HCR, which shows a single non-precipitating

cloud layer from 4:02 UTC onwards. The HCR beam was in nadir pointing mode for all three presented case studies.

The trigger threshold of PHIPS was set in a way that the instrument started to trigger on droplets with diameters larger than $50\ \mu\text{m}$ (see Section 3.3). This remained unchanged over the whole campaign. Fig. 5.7b shows PSDs measured with the CDP, 2D-S and PHIPS. The PSD has a maximum at around $15\ \mu\text{m}$ and the maximum particle sizes are found at $300\ \mu\text{m}$. All the PSDs agree well with each other.

The stereo micrographs from this flight segment (Fig. 5.7c) show the presence of large drizzle droplets with diameters from $100\ \mu\text{m}$ to $200\ \mu\text{m}$. No indication of the presence of ice particles was seen in the PHIPS images. Information on the phase of the particles with $D > 100\ \mu\text{m}$ can be acquired from the PHIPS ASF measurements. The phase discrimination algorithm classified every particle in the presented segment as droplet, which is in agreement with the stereo micrographs. This shows that this cloud, despite the low temperature and the particle sizes up to $300\ \mu\text{m}$, consists purely of supercooled liquid droplets.

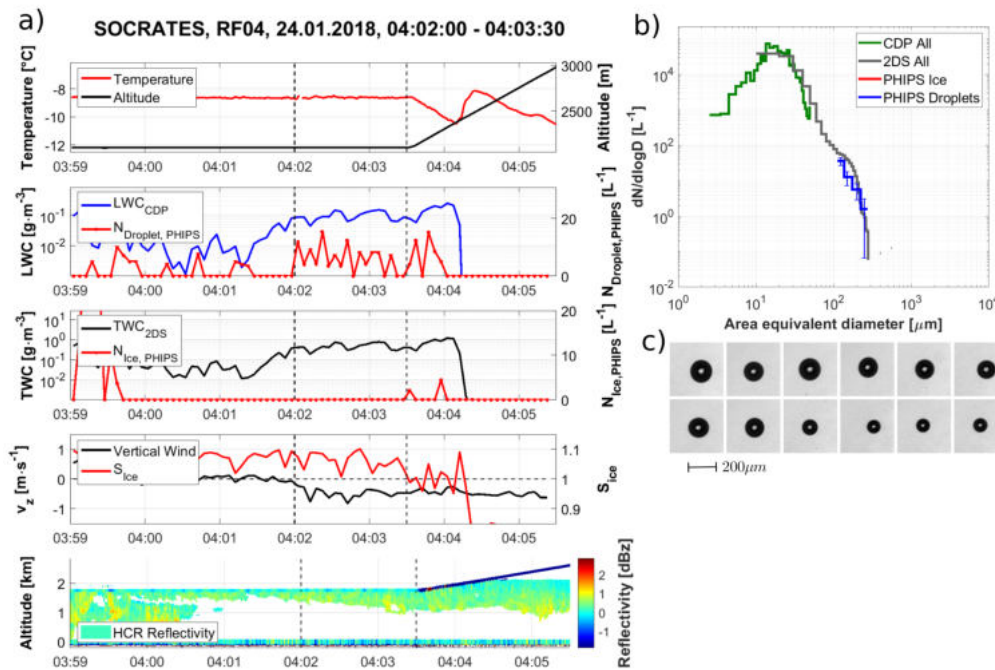


Figure 5.7.: Example of PHIPS data acquired in a low-level supercooled liquid cloud over the Southern Ocean during the SOCRATES campaign (research flight RF04). a) overview of meteorological parameters, CDP, 2D-S and PHIPS number concentrations (based on the ASF data) as well as HCR radar data. b) the comparison of the PSDs measured by CDP, 2D-S and PHIPS including statistical uncertainty bars $n^{-0.5}$ as discussed in Section 5.3. c) representative stereo micrographs of particles during that segment measured by PHIPS.

5.4.2. Case Study 2 — Heterogeneous Mixed-Phase Cloud

Low-level MPCs were investigated during SOCRATES research flight RF07 on January 31st, 2018. During this flight, the aircraft sampled clouds south-east from Hobart, including an overpass over Macquarie island. The aircraft flew at cruising altitude towards the most southward point, where it descended down to lower altitude, probing multiple thin and persistent supercooled and MPCs on its way back to Hobart.

Fig. 5.8a shows a cloud segment at around -58°N , 162°E , shortly after the turnaround at the most southward point. The cloud was probed in an altitude of $1,800\ \text{m}$ at a temperature of

about -10°C . The vertical wind velocity was slightly below zero and the relative humidity with respect to ice averaged about 107%. The maximum of the CDP LWC was 0.5 g L^{-1} and the maximum of the 2D-S TWC was 2 g L^{-1} . Fig. 5.8b shows the PSDs between 04:16:40 and 04:21:00 UTC. The PSD has a maximum at $15\text{ }\mu\text{m}$ and the maximum particle sizes are found at $700\text{ }\mu\text{m}$. All the probes agree well.

Based on the PHIPS phase information, the whole segment can be divided in two sub-segments. Until 04:19:30, PHIPS detects only supercooled liquid droplets, after that only ice particles. This is backed up by PHIPS' representative stereo micrographs from the two sub-segments. In the first sub-segment, Fig. 5.8c shows supercooled drizzle droplets with diameters from $50 - 200\text{ }\mu\text{m}$ similar to the pure liquid case. During the second sub-segment, Fig. 5.8d shows irregular and columnar ice particles with sizes from $100 - 500\text{ }\mu\text{m}$, some of which appear to be rimed or faceted. This coincides with the high reflectivity area measured by the HCR (lower panel in Fig. 5.8a) and the decrease in LWC measured by the CDP. No ice particles were present on stereo micrographs taken during the first sub-segment and no droplets during the second, respectively. This shows that PHIPS can detect and distinguish local concentration of supercooled liquid and ice within a single cloud.

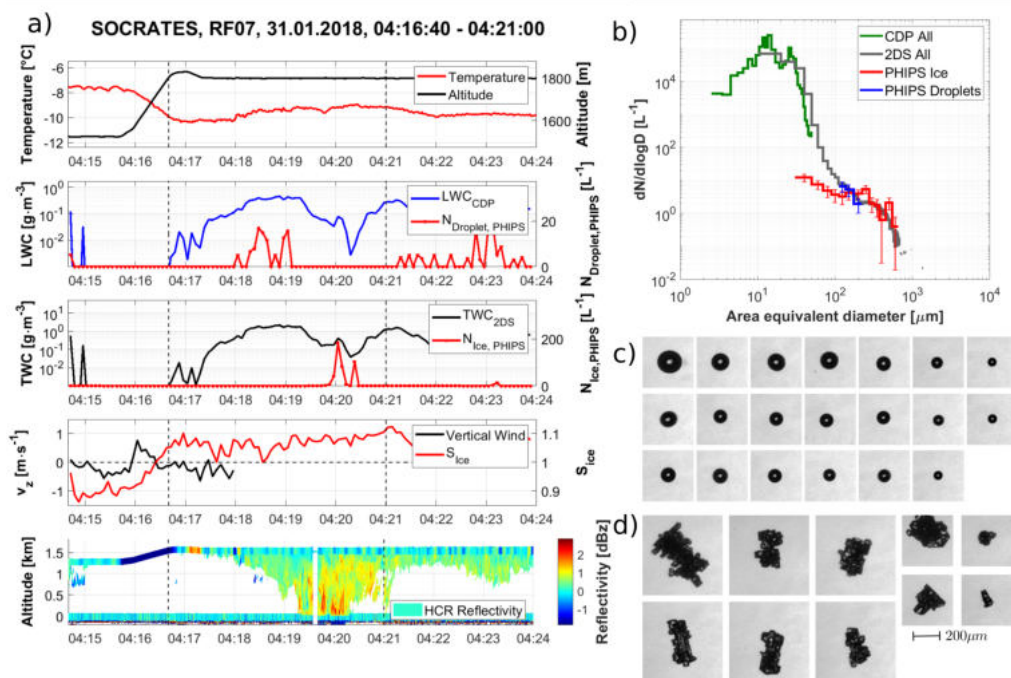


Figure 5.8.: Same as in Fig. 5.7 but for a low-level droplet-dominated MPC during a transit leg of SOCRATES research flight RF07. All supercooled droplets (c) were sampled between 04:16:40 - 04:19:30, whereas the ice particles (d) were sampled between 04:19:30 - 04:21:00.

5.4.3. Case Study 3 — Ice dominated Mixed-Phase Cloud

Fig. 5.9a shows a low-level MPC of SOCRATES research flight RF08 on February 4th, 2018. Due to a low pressure system south of Tasmania, cold air was expected advecting north from the Antarctic. During this flight, the aircraft flew straight southwards from Hobart. After turning back at the most southward point, the flight path back to Hobart was alternating between a "saw-tooth" pattern (going up and down through the clouds) and a "staircase" pattern (10 minutes above the cloud, then 10 minutes inside the cloud and 10 minutes below, as explained previously).

The presented case study shows one segment during the ascend of the final saw-tooth leg around -51°N , 147°E in a thin MPC in the Hallett-Mossop temperature regime (see Section 2.3.3.3). The cloud was approximately 700 m thick and the temperature within the cloud ranged between -5°C at cloud base at 700 m and 0°C at the cloud top at 1400 m. The vertical wind velocity was fluctuating around zero and the relative humidity with respect to ice was between 80 and 100%. The maximum of the CDP LWC was 0.5 g L^{-1} and the 2D-S TWC was 3 g L^{-1} .

Fig. 5.9b shows the PSDs between 05:13:10 and 05:15:35 UTC. The PSD has a maximum at $15\text{ }\mu\text{m}$ and the maximum particle sizes are found at up to $800\text{ }\mu\text{m}$. Again, all three probes agree well. Contrary to the previous case, the stereo micrographs in Fig. 5.9c+d are almost exclusively ice particles. The sizes range from $20\text{ }\mu\text{m}$ to $500\text{ }\mu\text{m}$. Observed ice particle habits throughout the cloud were mostly needles with some hollow columns and small irregulars – all with different degrees of crystal complexity and riming. Also, a few supercooled droplets were present. The presence of supercooled droplets is also confirmed by the scattering measurements. This shows that the presented method is also able to detect and correctly classify single large supercooled drizzle droplets in MPCs which are otherwise dominated by ice in that size range.

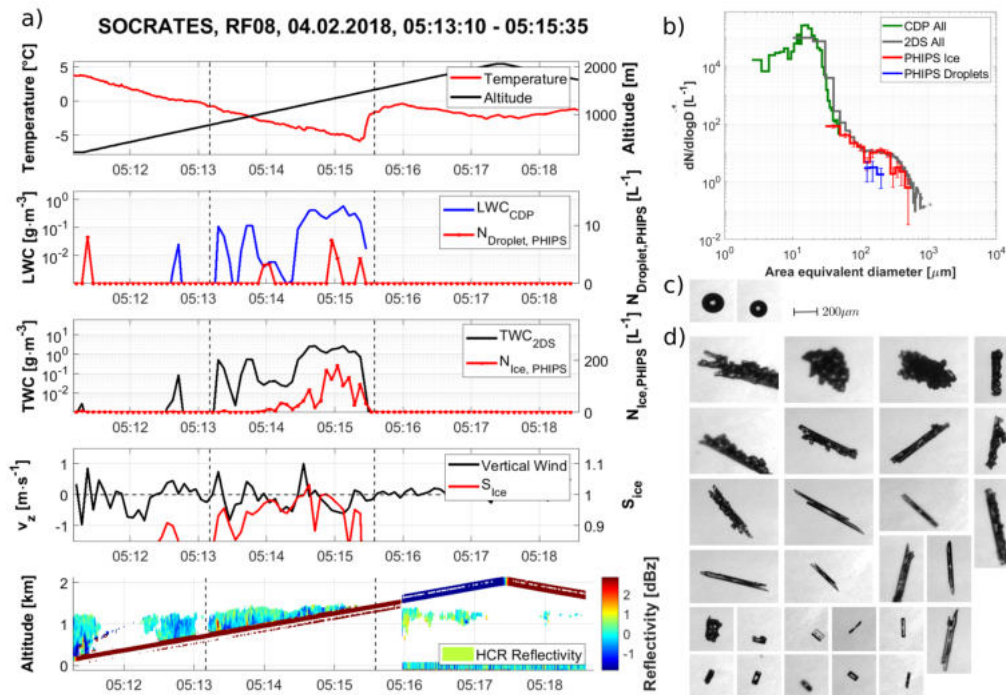


Figure 5.9.: Same as in Fig. 5.7 and Fig. 5.8 but for a low-level MPC of SOCRATES research flight RF08.

5.5. Summary

In this chapter, a method to determine the diameter of single particles based on their ASF measured by PHIPS was introduced. The particle sizing algorithm was calibrated using the area equivalent diameter based on the corresponding stereo micrographs measured by PHIPS for the same individual particles. Combined with the phase discrimination algorithm presented in the previous chapter and the determination of A_{sens} (see Section 3.1.3), this allows to calculate phase discriminated PSD based on the ASF of single particles in a size range of $50 \leq D \leq 700\text{ }\mu\text{m}$ and $20 \leq D \leq 700\text{ }\mu\text{m}$ for droplets and ice, respectively.

The newly developed data analysis algorithms were applied to three representative case studies. Comparison with the PSDs from other instruments showed a good agreement. The presented case studies show that PHIPS can provide unique and detailed insight about the phase composition of clouds, where phase discrimination based solely on particle size or aspect ratio could potentially be difficult, such as e.g. in MPC conditions where large droplets and small ice particles coexist. With these methods available, PHIPS can provide additional information on the microphysical properties of MPCs.

However, it was shown that a significant amount of the data are afflicted with uncertainties due to shattering of particles in the inlet of the probe. Multiple methods were discussed to detect segments that are affected by shattering based on interarrival time analysis and the presence of larger particles. Despite that, it is possible that segments that are not categorized as potential shattering cases by the presented shattering flag are still affected by shattering. Even though it has been shown that shattering is most prominent in segments with larger particles, the shattering of smaller particles cannot be completely ruled out. The interarrival time method does not reliably detect multiple fragments of the same particle due to the small A_{sens} and it is not possible to correct the measured concentrations and retrieve the original size of the shattered particles. Hence, PHIPS PSDs have to be considered as upper estimate of ice particle concentrations. Manual investigation of the stereo-images can help to identify shattering, but this process is laborious and images are only available for a subset of detected particles.

Despite that, due to the reliable single-particle phase-discrimination method, PHIPS data can be used to qualitatively detect e.g. individual small ice particles in liquid dominated clouds that might otherwise be classified as a pure liquid phase cloud. Further, the PSDs can be used to determine LWC and IWC as the total mass does not change during the shattering process and biases of increased concentration and decreased particle size theoretically cancel out.

In the following chapter, PSDs of PHIPS are combined with data from other cloud probes to determine the fraction of ice, liquid and MPCs during SOCRATES and ACLOUD. The PSDs are only used to estimate LWC and IWC to avoid the discussed uncertainties due to shattering.

6. Phase Composition of MPC in High Latitudes

As discussed in Chapter 2, life cycle as well as radiative and microphysical properties of cloud are strongly dependent on the phase of cloud hydrometeors, i.e. whether they are pure liquid, pure ice or mixed phase. In Section 2.5, the different state-of-the-art methods to measure phase, size and concentration of cloud particles using airborne in situ probes were discussed. In the previous chapters, a new method to determine cloud particle phase, size and concentration using the PHIPS was introduced and case studies of single phase and MPCs were presented. In this chapter, an overview of the cloud phase compositions (CPCs) of the sampled clouds during the ALOUD and SOCRATES campaigns¹ will be given and the following key questions will be discussed:

- Which fraction of clouds are pure liquid, ice or MPC?
- What are the fractions of liquid and ice in MPC?
- How do the results compare to previous studies?
- Are there systematic differences between the cloud phase composition (CPC) in the Southern Ocean and the Arctic?

6.1. Approach and Experimental Data-Basis

As discussed in Section 2.3, the definition whether a cloud is single- or mixed-phased lies within the applied metric on which the discrimination is based on. Korolev et al. [2003] have proposed the phase-composition coefficient based on water content

$$\mu = \frac{IWC}{TWC} = \frac{IWC}{LWC + IWC} \quad (6.1)$$

with the thresholds $\mu_{liq} = 0.1$ below which a cloud is classified as liquid, $\mu_{ice} = 0.9$ above which it is classified as pure ice cloud. Segments with $\mu_{liq} \leq \mu \leq \mu_{ice}$ are classified as MPC. A detailed comparison to the methods and results of Korolev et al. [2017] is given in Section 6.3.1.

The total concentration N_{tot} is calculated based on the PSD data-sets integrated over the corresponding size range

$$N_{tot} = \int_{D_1}^{D_2} \frac{dN}{dD} dD = \int_{D_1}^{D_2} \frac{1}{D} \frac{dN}{d \log D} dD \quad (6.2)$$

¹The IMPACTS campaign is not part of this analysis as phase-discriminated 2D-S data products were not yet available at the time of writing this thesis. Further, PHIPS' trigger threshold was set in a way to detect only large particles ($D \geq 100 \mu\text{m}$ for droplets, see Section 3.3.3).

for each cloud segment. The water content is calculated in a similar fashion as

$$\int_{D_1}^{D_2} m(D) N_{\text{tot}} dD, \quad (6.3)$$

using the mass-diameter relationship parameterization

$$m = aD^b, \quad (6.4)$$

proposed by Ham et al. [2017] based on Yang et al. [2000]. For liquid droplets, which are assumed to be spherical, the parameters are $a = \pi/6 \cdot \rho_{\text{liq}} = 0.480$ and $b = 3$. For ice, the parameterization for a mixture of habits is used, $a = 0.497$ and $b = 3.296$. The used data-sets include all flights from ALOUD and SOCRATES. The temporal averaging is $\Delta t = 10$ s. This corresponds to a spatial averaging of approximately $\Delta s \approx 150$ m assuming a flight speed of $v_s = 150$ m/s. Only segments with a TWC > 0.01 g m⁻³ are taken into account. Due to the coarse averaging scale of $\Delta s \approx 150$ m ($\Delta T = 10$ s) spatial phase heterogeneity, i.e. small pockets of ice/droplets in a liquid/ice cloud, cannot be resolved and are hence not discussed in the following.

As discussed in Section 2.5.5, there exists no in situ cloud probe that reliably measures ALL cloud particles as common cloud probes are only sensitive over a given size range. In this analysis, scattering probes are used for small (mostly liquid) particles ($D < 50$ μm) and OAP for large (primarily ice) particles (200 $\mu\text{m} \leq D < 2000$ μm). PHIPS is used for the in-between diameter range (50 $\mu\text{m} \leq D < 200$ μm for droplets and 20 $\mu\text{m} \leq D < 200$ μm for ice). The probes used for the analysis of the two campaigns are explained in the following.

6.1.1. Cloud Probe Data during SOCRATES

For SOCRATES, the CPC is determined based on data measured by the CDP, PHIPS and 2D-S. The CDP data are used for the size range 2 $\mu\text{m} \leq D < 50$ μm . Despite the fact that the CDP is designed to measure droplet concentrations and LWC (hence the name), it also measures ice. However, the CDP has no phase discrimination method available. Hence, all CDP data are considered to be liquid and the droplet concentration and LWC is to be considered an upper estimate.

The small ice particles in the size range 20 $\mu\text{m} \leq D < 50$ μm are measured by PHIPS where it only detects ice and not droplets due to the design of the trigger FoV (see Section 3.1). In the size range 50 $\mu\text{m} \leq D < 200$ μm , the CPC is also based on PHIPS data. The particle phase is determined based on the phase discrimination algorithm presented in Chapter 4.

Information of larger particles in the size range 200 $\mu\text{m} \leq D < 2000$ μm is based on shadow images measured by the 2D-S. Reliable particle phase information is retrieved based on sphericity analysis of the images [McFarquhar et al., 2018]. Note that the 2D-S measures shadow images of cloud particles down to $D = 50$ μm . However, quasi-spherical or irregular ice particles smaller than $D < 200$ μm can be misclassified due to the limited optical resolution, especially for out-of-focus particles (see discussion in Section 2.5). Hence, the PHIPS data are used for this intermediate size range. An overview of the droplet and ice concentration as well as LWC and IWC of the three probes in the respective size ranges of all cloud segments acquired during SOCRATES are shown in Fig. 6.1.

6.1.2. Cloud Probe Data during ALOUD

For ALOUD, the analysis is based on data measured by the SID-3, PHIPS and CIP probe. The corresponding size ranges used for the analysis are identical to the ones used for the SOCRATES data.

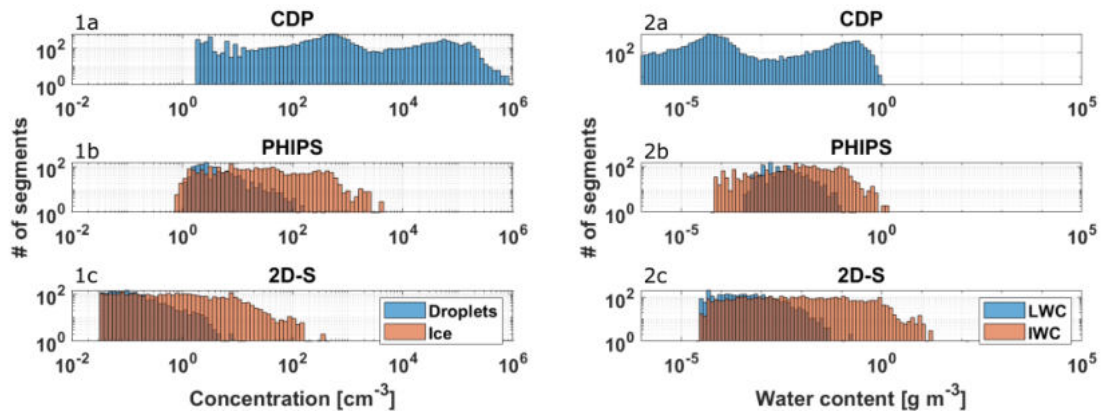


Figure 6.1.: Histograms of concentration (1) and water content (2) of droplets (blue) and ice (red) measured by the CDP (a), PHIPS (b) and 2D-S (c) during SOCRATES.

Similar to the CDP for SOCRATES, all SID-3 data are assumed to be liquid. As discussed in Section 2.5.5, SID-3 measures not only the total scattering intensity over a certain room angle (as does the CDP), but also measures the scattering pattern from $\theta = 3^\circ$ to 8° which gives information about the particle phase (circular rings for droplets, cross pattern or irregular "freckles" for ice, see Fig. 2.23). However, the scattering patterns are acquired for a subset of particles only (see Section 2.5.5.4). Further, coincidence of multiple droplets can lead to a distorted scattering pattern and thus results in a misclassification as ice [Vochezer et al., 2016]. Thus, for ALOUD no phase-discriminated PSDs were available. Hence, all SID-3 data are considered to be liquid. This way, the approach is consistent with the use of the CDP data from the SOCRATES campaign and the results of the two campaigns are more comparable. The size range for the analysis of the SID-3 data is identical to the CDP's: $2 \mu\text{m} \leq D < 50 \mu\text{m}$.

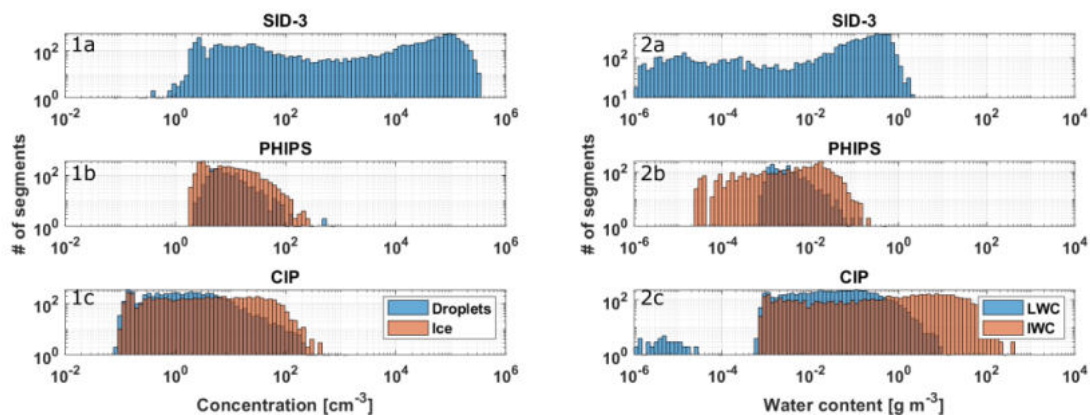


Figure 6.2.: Histograms of concentration (1) and water content (2) of droplets (blue) and ice (red) measured by the SID-3 (a), PHIPS (b) and CIP (c) during ALOUD, analogously to Fig. 6.1 for SOCRATES.

Again, PHIPS data are used for ice in the size range $20 \mu\text{m} \leq D < 200 \mu\text{m}$ and $50 \mu\text{m} \leq D < 200 \mu\text{m}$ for droplets. The CIP is used in the same size range as the 2D-S from $200 \mu\text{m} \leq D < 2000 \mu\text{m}$. An overview of droplet and ice concentration as well as LWC and IWC of the three probes in the respective size ranges of cloud segments acquired during ALOUD are shown in Fig. 6.2.

6.2. Temperature Dependency of the Cloud Phase Composition

Fig. 6.3 shows the distribution of the phase-composition coefficient μ as defined in Eq. (6.1) for SOCRATES and ALOUD. The dashed vertical lines mark the $\mu_{\text{liq}} = 0.1$ and $\mu_{\text{ice}} = 0.9$ thresholds.

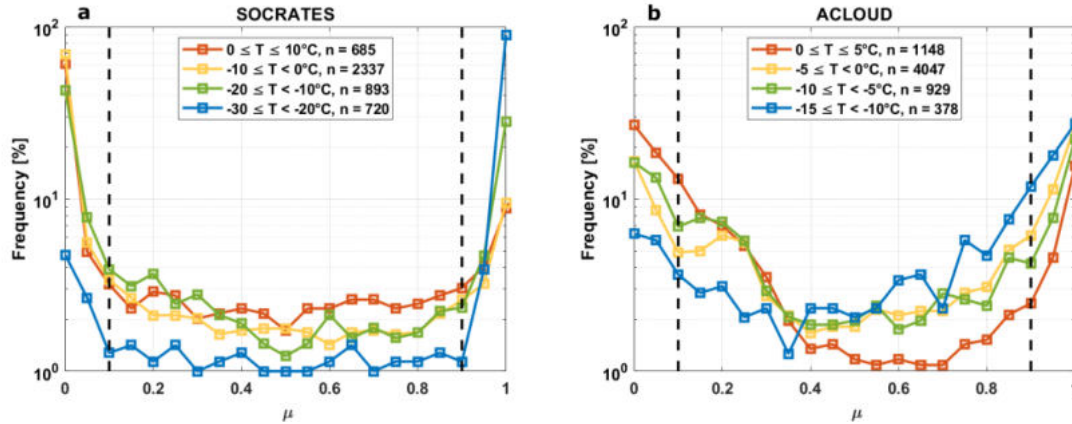


Figure 6.3.: Frequency of occurrence of phase-fraction coefficient μ of cloud segments sampled during SOCRATES (a) and ALOUD (b). The dashed vertical lines mark the $\mu_{\text{liq}} = 0.1$ and $\mu_{\text{ice}} = 0.9$ thresholds. The color-code corresponds to different temperature regions (note the logarithmic y-scale and the different temperature binning for SOCRATES and ALOUD).

Both SOCRATES and ALOUD show a distinctive "U-shape" with a high frequency of segments with $\mu < \mu_{\text{liq}} = 0.1$ and $\mu > \mu_{\text{ice}} = 0.9$ at the edges and a low, nearly constant level in between for MPC (note the logarithmic y-scale). This is in accordance with previous works [Mazin, 2006; Korolev et al., 2017; D'Alessandro et al., 2021] (see Section 6.3.1).

Compared to SOCRATES, the curves for ALOUD show a similar shape, but the frequency of μ values in the MPC regime ($0.1 < \mu < 0.9$) is not as constant compared to SOCRATES but show a clear minimum near $\mu \approx 0.5$. Based on water content, in total 15.5% (35.0%) of cloud segments of SOCRATES (ALOUD) are classified as MPC. 2.8% (3.5%) of segments have a balanced amount of droplets and ice particles, i.e. $0.4 < \mu < 0.6$ and $\text{LWC} \approx \text{IWC}$.

Fig. 6.4 shows the CPCs for SOCRATES and ALOUD. Each data point corresponds to one cloud segment with $\Delta s \approx 150$ m ($\Delta t = 10$ s) and $\text{TWC} > 0.01$ g m^{-3} . For both campaigns, the CPCs show similar trends: For warm temperatures ($T \geq 0^\circ\text{C}$), most cloud segments are classified as pure liquid. Towards colder temperatures, the fraction of ice clouds increases for all four plots until $T = -15^\circ\text{C}$.

For SOCRATES, the fraction of ice clouds increases significantly and remains at a constant level of $\text{CPC} \approx 90\%$ for temperatures $T < -20^\circ\text{C}$. Almost all cloud segments with $T < -20^\circ\text{C}$ were sampled at high altitudes above 6,000 m asl. During ALOUD, no clouds in this height or temperature range were sampled. For the coldest temperature bin $-20 \leq T < -15^\circ\text{C}$ only $n = 85$ segments were sampled, resulting in high statistical uncertainty of $\sigma = n^{-1/2} > 10\%$. The corresponding data are shown by the faded bars in Fig. 6.4.

The CPC analysis for the two campaigns follow the same approach. Even though PHIPS is the only probe that was used during both campaigns, the other used instruments have similar measurement principles: Small particles are measured by forward scattering probes, the CDP for SOCRATES and SID-3 for ALOUD. Large particles are measured via OAPs,

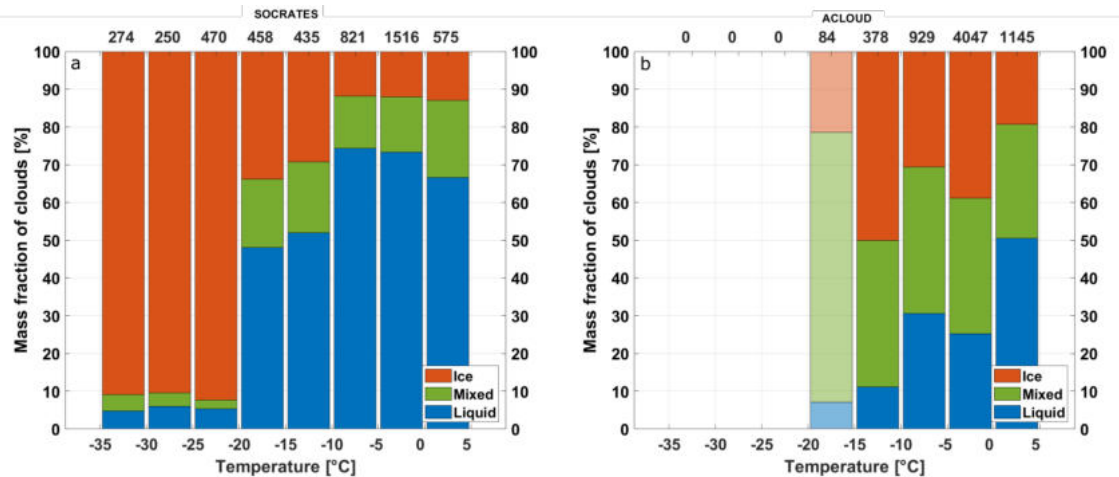


Figure 6.4.: CPC for SOCRATES (a) and ALOUD (b). The upper x-axis indicates the number of sampled cloud segments per temperature bin. The lowest temperature bin $-20 \leq T < -15^\circ\text{C}$ of ALOUD has a low number of samples ($n = 85$) and is thus shown with faded colors.

the 2D-S and CIP. The corresponding diameter ranges used for the determination of total concentration, LWC and IWC are identical: $D < 50 \mu\text{m}$ for droplets measured by CDP and SID-3, $20 \mu\text{m} \leq D < 200 \mu\text{m}$ and $50 \leq D < 200 \mu\text{m}$ for PHIPS ice and liquid and $200 \mu\text{m} \leq D < 2000 \mu\text{m}$ for 2D-S and CIP.

During both campaigns, most cloud segments were sampled in the temperature range $-10^\circ\text{C} \leq T \leq +5^\circ\text{C}$ and altitudes between 0 to 2000 m asl. During SOCRATES, some cirrus clouds between 6000 m to 8000 m asl down to temperatures $T \leq -35^\circ\text{C}$ were also sampled during transit periods. For ALOUD, no cloud segments were sampled at temperatures below $T \leq -17^\circ\text{C}$.

In terms of CPC, both campaigns show a similar decrease of liquid cloud fraction towards colder temperatures. Apart from that, the ALOUD result differs compared to SOCRATES as the fraction of ice and MPC segments is significantly increased. For SOCRATES, the fraction of MPC segments is almost temperature independent at around 17% whereas it ranges from 32% to 41% for ALOUD.

The low fraction of ice and MPCs is explained by the lack of INP over the Southern Ocean due to long distance from continental air sources [Bigg, 1973; Burrows et al., 2013; McFarquhar et al., 2021]. Despite that, the fraction of ice and MPC during SOCRATES for warm temperatures $T > 0^\circ\text{C}$ is relatively high, comparable with the CPCs of ALOUD. This is in accordance with observation of "warm ice" in the Southern Ocean by Zaremba et al. [2021] as well as e.g. the case study presented in Section 5.4.3.

6.3. Discussion

6.3.1. Comparison with Previous Studies

Recently, D'Alessandro et al. [2021] have reported a phase discrimination method that relies on a decision tree algorithm based on total number concentrations, particle size and water content measured by the CDP and 2D-S. The phase discrimination of the individual probes for each cloud segment is based on the Rosemont Icing detector (RICE, [Mazin et al., 2001]) for the CDP and multinomial logistic regression [Kwak and Clayton-Matthews, 2002] for the 2D-S. PHIPS data were not used. Fig. 6.5a shows the CPC based on their

analysis with $\Delta t = 1$ s. It compares nicely to the derived CPC for SOCRATES shown in Fig. 6.6a in this work (note the different color code for liquid and ice).

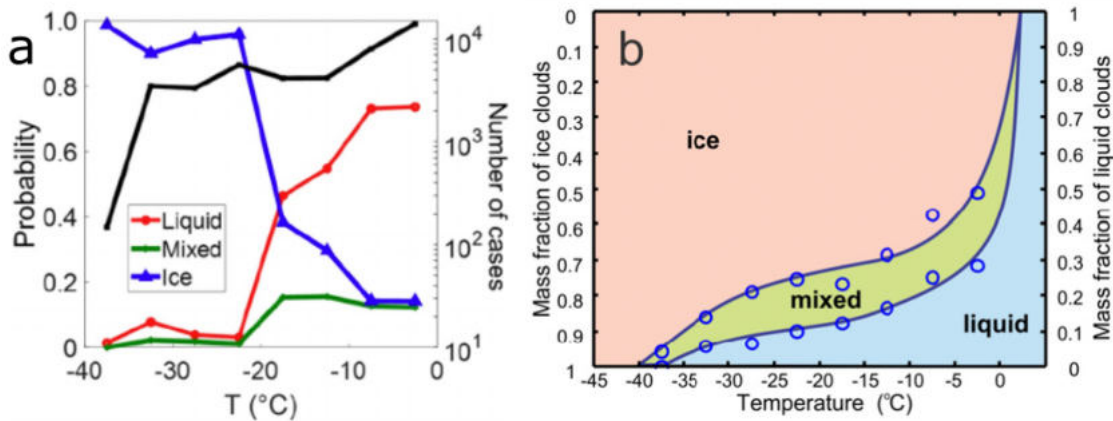


Figure 6.5.: (a) Relative frequency distribution of CPCs during SOCRATES taken from D’Alessandro et al. [2021]. The black line shows the number of cloud samples. (b) Relative CPCs based on LWC and IWC measured by the Nevzorov hot-wire probe during 5 in situ aircraft field campaigns over Canada, taken from Korolev et al. [2017].

Korolev et al. [2003] and Mazin [2006] have presented extensive studies analyzing the CPC of clouds sampled over Canada and the former Soviet Union. The data set of Korolev et al. [2003] consists of 5 in situ aircraft campaigns over 6 years from the year 1994 to 2000 with combined 93 flights and a total in-cloud path length of 44,000 km. The sampled temperature and altitude of measurements ranged from $-35^{\circ}\text{C} < T < 0^{\circ}\text{C}$ and from 0 to 6 km asl. Most of the data were collected at temperatures in the range $-15 < T < 0^{\circ}\text{C}$.

The CPC was calculated based on LWC and IWC measured by Nevzorov hot-wire probes (see Section 2.5). Complementary information from other instruments such as forward scattering spectrometers and OAP were used qualitatively to identify misclassified clouds (e.g. in the case of drizzling clouds due to uncertainties between collection efficiencies of the LWC and IWC (TWC) sensors). The cloud TWC threshold ($> 0.01 \text{ g m}^{-3}$) as well as the phase-composition coefficient thresholds for the discrimination of CPC ($\mu_{\text{liq}} = 0.1$ and $\mu_{\text{ice}} = 0.9$) were the same as used in this work. The scale of averaging per cloud segment was $\Delta t = 0.1$ s.

Fig. 6.5b shows the CPC published by Korolev et al. [2017] based on recalculated data from Korolev et al. [2003]. It shows a similar trend of increasing ice fraction towards colder temperatures and only weakly temperature dependent MPC fraction around 20% which is in accordance with the results presented in this work. However, the ice fraction is much higher ranging from 50% ($T < 0^{\circ}\text{C}$) to over 90% ($T < -35^{\circ}\text{C}$) compared to the results shown in Fig. 6.4, especially for the warmer temperature range.

Mazin [2006] combined the data set of Korolev et al. [2003] with observations from seven aircraft sounding stations in the former Soviet Union carried out from 1953 to 1958. CPC was determined based on visual inspection of oil slides as well as ice deposition on any part of the aircraft construction as well as optical phenomena such as e.g. halos. Fig. 6.6 again shows the CPC for SOCRATES and ACLOUD shown in the stacked histograms in Fig. 6.4. For temperatures above $T > -20^{\circ}\text{C}$, the CPCs follow a linear trend. The dashed lines represent the parameterization by Mazin [2006]. The faded lines represent the linear fits through the data points from $-20 \leq T < +5^{\circ}\text{C}$. Fit parameters are shown in Table 6.1. For ACLOUD, the lowest temperature bin ($-20 \leq T < -15^{\circ}\text{C}$) is excluded because of the high statistical uncertainty due to the low number of samples measured in this temperature regime.

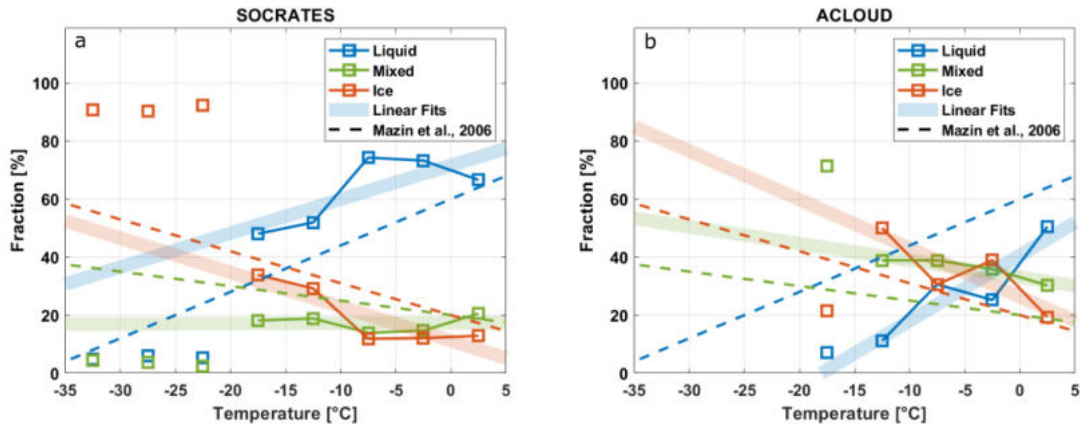


Figure 6.6.: CPC of cloud segments of SOCRATES (a) and ACLOUD (b). The faded lines correspond to the linear fits through the data points from $-20 \leq T < +5$ °C. Fit parameters are shown in Table 6.1. Again, for ACLOUD, the lowest temperature bin is excluded due to the low number of measured cloud segments in this temperature regime. The dashed lines correspond to the parameterization from Mazin [2006].

Table 6.1.: Linear fit parameters for the CPC parameterization shown in Fig. 6.6 based on SOCRATES and ACLOUD as well as the parameterization from Mazin [2006].

Linear Fit ($y = a \cdot x + b$)	Cloud Phase	a	b	R^2
SOCRATES	Liquid	1.17	71.61	0.58
	Mixed	0.01	17.29	0.72
	Ice	-1.18	11.10	0.76
ACLOUD	Liquid	2.25	40.62	0.80
	Mixed	-0.58	33.06	0.84
	Ice	-1.68	26.32	0.69
Mazin et al. (2006)	Liquid	1.6	60	
	Mixed	-0.5	20	
	Ice	-1.1	20	

The linear fits have a reasonable goodness ($0.58 \leq R^2 \leq 0.80$). The slopes of the linear regressions agree very well with the parameterization by Mazin [2006]. However, the lines are offset by +11.6% for liquid and -8.9% for ice compared with SOCRATES and -19.4% (liquid) and +6.3% (ice) for ACLOUD.

One possible explanation for this is the aforementioned potential bias towards liquid clouds due to the fact that CDP and SID-3 are considered as all liquid due to the lack of reliable discrimination methods.

Furthermore, the data set presented by Korolev et al. [2003] only contain cloud segments in the temperature range $T \leq 0^\circ\text{C}$ whereas during both SOCRATES and ACLOUD a significant portion of clouds were sampled at positive temperatures. As shown in Fig. 6.4, though cloud segments in this temperature region are dominated by liquid clouds, there were some ice and MPC clouds sampled in this temperature range as discussed previously. This does not agree with the extrapolation (solid line and shaded area) in Fig. 6.5b which shows exclusively liquid CPC for positive temperatures.

Another difference of previously discussed studies compared to this work lies within the temporal resolution and spatial averaging. Due to the constrained sensitive area from PHIPS (see discussion in Section 5.3) the averaging time per cloud segment is $\Delta t = 10$ s compared to $\Delta t = 1$ s of the previously discussed studies. Hence, small-scale heterogeneities, i.e. pockets of ice/liquid in a liquid/ice cloud are not discussed in this work.

6.3.2. Sensitivity Analysis: Impact of PHIPS Measurements

In Fig. 6.4, the CPC for SOCRATES and ACLOUD was discussed. Fig. 6.7 shows same CPC analysis, once including PHIPS (i.e. identical to Fig. 6.4) shown by the narrow, solid bars as well as excluding PHIPS data from the analysis (i.e. only based on CDP and 2D-S for SOCRATES and SID-3 and CIP for ACLOUD) shown by the broad, faded bars.

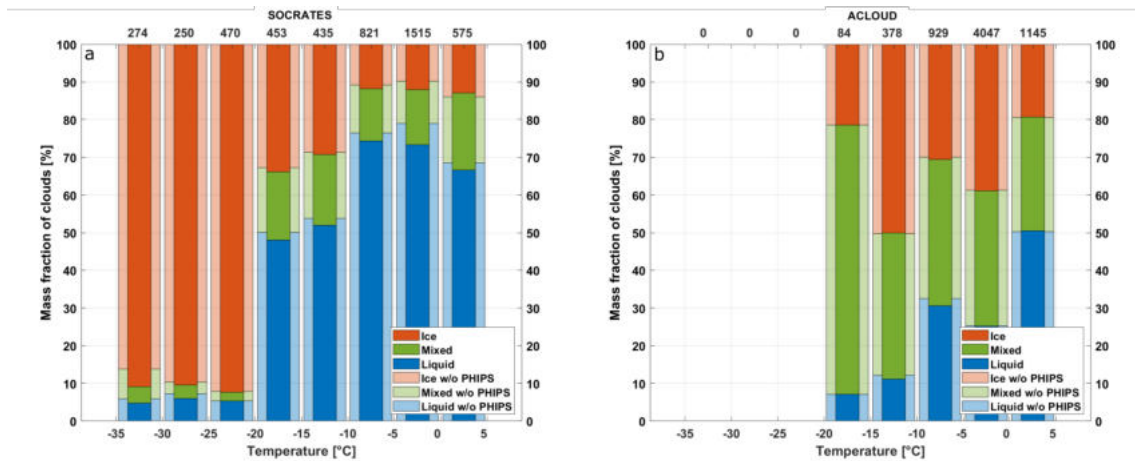


Figure 6.7.: CPC for SOCRATES (a) and ACLOUD (b) identical to Fig. 6.4 (narrow solid bars) as well as the same analysis without taking PHIPS data into account (faded bars).

For ACLOUD, the results differ only slightly depending on whether PHIPS data are included or not. For SOCRATES, the amount of identified ice cloud segments by including PHIPS is increased compared to the analysis without PHIPS, especially for the temperature range below $T < -20^\circ\text{C}$ (up to a difference of 92% ice fraction compared to 86% without PHIPS for the lowest temperature bin $-35^\circ\text{C} \leq T < -30^\circ\text{C}$). In the temperature range $-20 \leq T < 5^\circ\text{C}$, the fraction of ice clouds increases by roughly +2% and the fraction of MPCs by +4%. This can be explained by particles that are misclassified by the OAP or falsely attributed as liquid due to the lack of reliable phase discrimination for particles $D < 50 \mu\text{m}$ detected by the forward scattering probes.

6.3.3. Concentration-based Phase-Composition Coefficient

One disadvantage of the mass-based phase-composition coefficient used in this work is that contrary to the hot-wire probes used in e.g. Korolev et al. [2003], the aforementioned probes used in this work do not measure LWC and IWC directly but those values are calculated based on the PSDs. Thus, the water content is dependent on the chosen parameterization of the mass-diameter relationship (see Eq. (6.4)) which is strongly habit dependent [Ham et al., 2017].

As discussed in Section 2.3, there exist alternative possible definitions of CPC, e.g. based on particle number concentration. Analogous to Eq. (6.1) it would be calculated as

$$\mu_{\text{conc}} = \frac{N_{\text{tot, ice}}}{N_{\text{tot, liq}} + N_{\text{tot, ice}}}. \quad (6.5)$$

However, the concentration-based analysis also has its disadvantages: The main problem lies within the chosen classification thresholds. Similar thresholds as for mass-based phase-composition coefficient of $\mu_{\text{liq}} = 0.1$ and $\mu_{\text{ice}} = 0.9$ do not work as the number of droplets typically exceed the concentration of ice particles by multiple orders of magnitude whereas LWC and IWC are more comparable (see discussion in Section 2.3.1 as well as Fig. 6.1 and Fig. 6.2). That means that, as discussed in Section 2.3.1, a hypothetical MPC with balanced LWC and IWC could be classified as pure liquid cloud since most of the small particles (which dominate the total number concentration) are liquid.

The solution to this issue could be to lower those thresholds, e.g. down to $\mu_{\text{liq}} = 0.001$ so that the MPC can be detected even if there exists only 1 ice particle per 1000 droplets. However, this would not work due to the limited discrimination accuracy - even though PHIPS has a rather high discrimination accuracy of $> 98\%$, such a strong threshold could in return falsely classify pure liquid clouds as MPC.

A similar problem exists for forward scattering probes such as the CDP which have no reliable way of determining the phase of cloud particles. This way, small ice particles in a pure ice cloud that detected by the CDP and erroneously assumed to be liquid could classify this cloud as mixed-phase or even pure liquid cloud.

6.4. Summary

In this chapter, data acquired via multiple cloud probes during two in situ aircraft field campaigns were combined. This data set gives information about the phase and size (and hence water content) of cloud particles over a wide range of particles from $1 \mu\text{m} \leq D \leq 2000 \mu\text{m}$.

Even though different instruments were used during the two campaigns, the measurement principles behind the instruments are similar and hence the results are comparable. Small particles ($1 \mu\text{m} \leq D < 50 \mu\text{m}$) were measured by forward scattering probes (CDP for SOCRATES, SID-3 for ACLOUD) and large particles ($200 \mu\text{m} \leq D < 2000 \mu\text{m}$) via OAP (2D-S for SOCRATES, CIP for ACLOUD). The PHIPS probe was used for both campaigns for particles in a size range from $20 \mu\text{m} \leq D < 200 \mu\text{m}$ for ice particles and $50 \mu\text{m} \leq D < 200 \mu\text{m}$ for droplets.

Phase and size of the measured cloud particles are determined based on their shadow images for the OAP and via the new methods based on their ASF for PHIPS as described in Chapter 4 and Chapter 5. In the small diameter range, particle sizing is determined based on the light scattering intensity in forward direction. For small particles $D < 50 \mu\text{m}$

no phase information is available from the forward scattering probes and all measured particles are assumed to be liquid. This results in an overestimation of LWC in clouds with small ice particles. However, this bias is reduced by the detection of ice in the range from $20 \leq D < 50 \mu\text{m}$ by PHIPS.

Based on this data set the CPC of all cloud segments with $\text{TWC} > 0.01 \text{ g m}^{-3}$ with a temporal resolution of $\Delta t = 10 \text{ s}$ was determined. The CPC is calculated based on the fraction of IWC to TWC with thresholds $\mu_{\text{liq}} = 0.1$ and $\mu_{\text{ice}} = 0.9$ analogous to previous studies.

It was shown that the CPC is dominated by liquid for warm temperatures near $T = 0^\circ\text{C}$ and decreases towards colder temperatures. The MPC fraction was found to be relatively temperature independent at around 17% for SOCRATES and slightly decreasing from 32% to 41% for ACLOUD. High level clouds below $T < -20^\circ\text{C}$ were found to be largely pure ice phase with a liquid and MPC fraction down to 5% each. These findings are in accordance with previous works. Further, the CPCs of cloud segments sampled during SOCRATES and ACLOUD were compared and hence differences of clouds over the Southern Ocean and the Arctic were discussed.

In the next chapter the interaction of liquid droplets and ice particles in MPCs in the form of riming will be discussed.

7. Observations of Riming in High Latitude Mixed-Phase Clouds

As introduced in Section 2.4.3, riming, the accretion of small droplet by ice particles, is one of the main growth modes of ice particles in MPCs. Even though riming significantly affects the microphysical properties of ice particles as well as lifetime and radiative properties of MPCs, riming on sub-mm particles is rarely represented in climate models. In situ studies with high-resolution cloud imaging probes investigating the properties of individual rimed particles sampled directly in the cloud are scarce.

In this chapter, the formation conditions and microphysical properties of rimed particles are investigated. Further, rimed ice particles that show crystalline, faceted build up which is aligned along the crystal structure of the underlying particle are described. For these, so far not well described particles, the term "epitaxial riming" is proposed. Riming state (rimed, unrimed, epitaxially rimed) as well as surface riming degree are correlated with ambient meteorological parameters based on in situ observations during the ACLOUD and SOCRATES campaign. Finally, the angular light scattering properties of rimed particles are investigated. The results presented in this chapter are also published verbatim in Waitz et al. [2021b].

7.1. Statistical Analysis and Correlation with Ambient Conditions

In general, the average number of rime found on an ice particle is calculated as the integrated riming rate over the particle trajectory. The riming rate is a function of the relative flux of available droplets and hence droplet number concentration and relative velocity with respect to the ice particle. Further, it is dependent on the collision probability (and hence the cross sections of ice particles and droplets) as well as on the collection efficiency, i.e. the probability that a colliding droplet sticks as rime. The trajectory of the ice particle and thus the time it spends in the cloud is dependent on its mass and the vertical (updraft) velocity.

It is not possible to know each of those parameters for each particle at every given moment. Hence, as already mentioned above, such detailed description of riming on a particle-by-particle basis is not present in current climate prediction models and riming is only accounted for in terms of graupel and snow and rarely for smaller, less densely rimed particles. Here, riming of sub-millimeter ice particles is investigated based on experimental data and correlate the relative occurrence of rimed and unrimed ice particles with ambient meteorological parameters. Note that the measured conditions do not necessarily represent the environment where the particles were rimed but rather where they were sampled.

This statistic is based on 5,370 manually classified images from the ACLOUD and SOCRATES campaign. Fig. 7.1a shows the correlation of riming fraction and ambi-

ent temperature. Here, "riming fraction" refers to the relative amount of rimed particles compared to total amount of classified ice particles (rimed + unrimed). Most riming was observed in a temperature range between $-10^{\circ}\text{C} \leq T \leq 0^{\circ}\text{C}$ where up to almost 50% of all ice particles were rimed. The high riming fraction around -17°C is due to a very high rimed fraction during a single cloud segment of RF09 of SOCRATES. It is based on a low number of total particles and is therefore not assumed to be a generalizable feature. The corresponding fit parameters for all histograms are shown in Table 7.1.

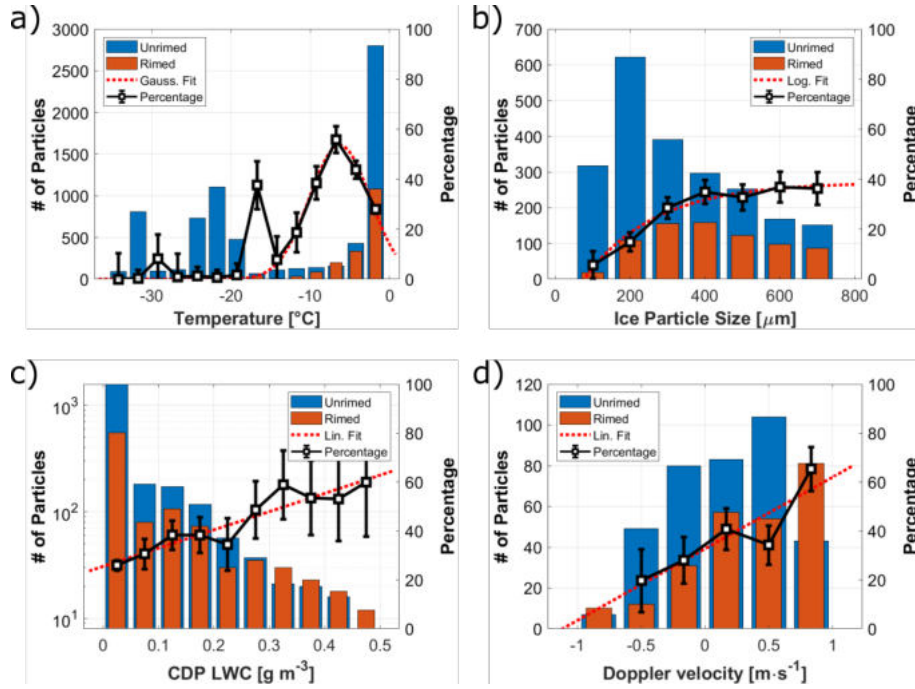


Figure 7.1: Histograms showing the absolute number of classified unrimed (blue) and rimed (red) particles during ALOUD and SOCRATES as well as the riming fraction (relative percentage $n_{\text{rimed}}/n_{\text{all}}$, black, right axis) in correlation with different ambient parameters: Temperature (a), area-eq. diameter of the underlying ice particle measured by PHIPS (b), CDP LWC (c) and vertical HCR Doppler velocity (d). The red dotted line shows a fit to the riming fraction (see text). The corresponding fit parameters for all histograms are shown in Table 7.1. The statistical uncertainty bars correspond to the number of particles per bin ($n^{-1/2}$). Only bins with $n \geq 20$ are considered for the fit. Correlation plots with further parameters (CDP mean droplet diameter, ambient vertical velocity, relative cloud height, supersaturation with respect to ice), which show only a weak dependency are shown in Fig. A.3 in the Appendix.

For the following analysis, apart from Fig. 7.1a, only particles sampled at $T \geq -17^{\circ}\text{C}$ are considered. Fig. 7.1b shows riming statistics as a function of ice particle's area equivalent diameter retrieved from the stereo-microscopic images. It can be seen that the percentage of rimed particles increases with particle size. The riming fraction increases from below 5% for particles smaller than $D_{\text{im,A}} \leq 150, \mu\text{m}$ to over 35% for particles larger than $D_{\text{im,A}} \geq 400, \mu\text{m}$. Above that, the riming fraction is only weakly dependent on particle size. The smallest ice particle where riming was observed was a column with an area equivalent diameter of $D_{\text{im,A}} = 116.1 \mu\text{m}$ and maximum dimension $D_{\text{im,max}} = 193.7 \mu\text{m}$ is shown in Fig. 7.2. This is a larger riming onset size compared to e.g. Ono [1969]; Ávila et al. [2009]), who reported a critical minimum diameter of $D \geq 60 \mu\text{m}$ for riming on columns collected via glass slides and analyzed by optical microscopy.

The correlation of riming fraction and cloud LWC measured by the CDP is shown in Fig. 7.1c. The riming fraction increases from 25% in cloud segments with low LWC below 0.05 g m^{-3} to 60% for $\text{LWC} \geq 0.5 \text{ g m}^{-3}$. Rimed droplets had a size around roughly $D_{\text{max}} \approx 20$ and

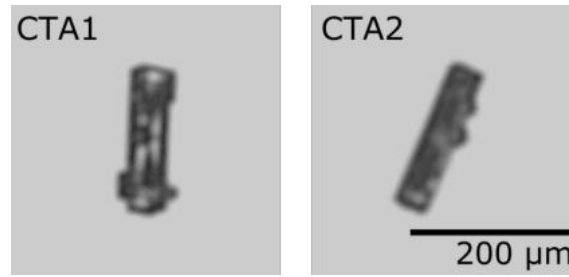


Figure 7.2.: Stereo image of one of the smallest particles that is conclusively classified as riming and showed no indication of shattering had an area equivalent diameter of $D_{im,A} = 116.1 \mu\text{m}$ and maximum dimension of $D_{im,max} = 193.7 \mu\text{m}$ (SOCRATES, RF12, #217).

Table 7.1.: Fit parameters to the riming percentage histograms shown in Fig. 7.1.

		Fit function	R^2
Temperature		$y = -0.952 x^2 - 12.2 x + 11.9$	0.940
Ice particle diameter	(PHIPS)	$y = 38.7 - \exp[-52.8 (x-769)]$	0.964
Liquid water content	(CDP)	$y = 74.7 x + 25.5$	0.863
Vertical Doppler velocity	(HCR)	$y = 29.3 x + 32.7$	0.790

50 μm as shown in Fig. 7.3a, b for two exemplary particles. This is in agreement with results presented by e.g. Kikuchi and Uyeda [1979]; Harimaya [1975], who reported sizes of rimed droplets between 10 and 60 μm . Comparison with CDP mean droplet diameter showed a slight correlation with a maximum riming fraction at $D_{drop, mean} = 20 \mu\text{m}$ (see Fig. A.3f in the Appendix). Fig. 7.3c, d show drizzle-rimed ice (*ice lollies*). Such contact freezing of relatively large droplets compared to the size of ice particle was reported by [Uyeda and Kikuchi, 1978; Keppas et al., 2017]. Such particles were, even though only very few, also observed during the ACLOUD and SOCRATES campaigns. Due to the low number, no correlation with sampled PHIPS drizzle droplet concentration was found and no detailed statistical analysis was conducted.

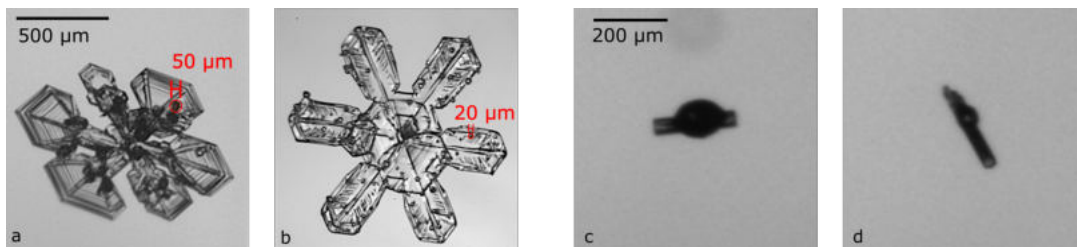


Figure 7.3.: Exemplary rimed particles showing the size of rimed droplets on the surface (a, b) and drizzle rimed ice (*ice lollies*, c, d).

Fig. 7.1d shows the correlation with the Doppler radial velocity measured by the HCR [EOL, 2018b] which is the sum of vertical wind velocity and particle fall speed, corrected by the vertical motion of the aircraft. Negative velocity corresponds to downward direction, positive to updrafts. Since the HCR has a dead zone of 145 m around the aircraft in which data are not usable, there is no data available at the location of the aircraft. One data point corresponds to the average over the whole vertical column. HCR data are only available for the SOCRATES campaign. The HCR was typically rotated to point in zenith direction when flying beneath or ascending through boundary layer clouds and nadir at other times. It can be seen that there is a clear trend of increasing positive (upward) Doppler velocity with riming fraction. Due to the updraft, the ice particles remain in the cloud longer and

hence the probability that they collide with droplets increases. Previous studies have reported increased fall speeds for rimed particles [Locatelli and Hobbs, 1974; Lin et al., 2011; Garrett and Yuter, 2014] which indicates that the particles are still in the cloud and not yet precipitating.

The measurement of ambient vertical velocity around the aircraft shows a slight correlation towards both higher positive and negative values (see Fig. A.3h in the Appendix). This could indicate a correlation with turbulent air motion, as riming is expected to be more likely if particles remain longer in the cloud, having a longer total travel path and hence a higher chance of collecting droplets. However, at the same time, a lot of one sided rimed plates were observed during the campaigns (see Fig. 7.4), which would be unlikely if all riming would necessarily be correlated with turbulent air motion. This confirms observations of fallen snow by Ono [1969]; Rango et al. [2003]. Roughly 15% of all plates at warm temperatures $T > -10^\circ\text{C}$ are one-sided (see Fig. A.6a and the corresponding discussion in the Appendix) and almost none at colder temperatures.

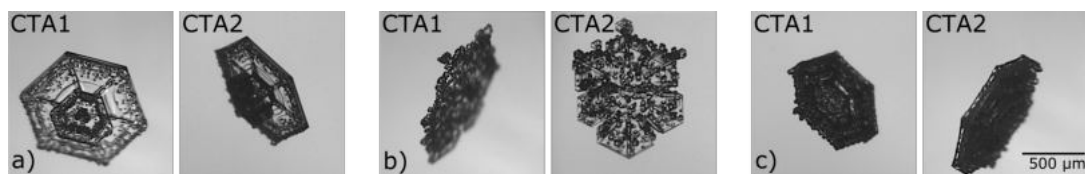


Figure 7.4.: Three exemplary one-sided rimed particles shown from different perspectives by the two camera telescope assemblies (CTA1 and CTA2). Note that the particle orientation in the stereo image does not reflect the orientation within the cloud.

No significant correlation (R^2 below 0.5) or only very minor dependency of riming fraction and CDP droplet number concentration, CDP mean droplet diameter, ambient vertical velocity, relative cloud height and supersaturation with respect to ice were found. The corresponding plots are shown in Fig. A.3 in the Appendix. No significant difference was found between the occurrence of riming during ALOUD and SOCRATES.

7.2. Riming Degree

All rimed ice particles were manually classified concerning their *riming degree*, i.e. their estimated surface riming degree (see Section 3.2.3). This classification was done manually based on visual inspection of the particle's individual stereo-images. Exemplary particles are shown in Fig. 7.5.

Fig. 7.6 shows the relative distribution of SRD with three ambient parameters: temperature (Fig. 7.6a), ice particle size (Fig. 7.6b) and vertical Doppler velocity (Fig. 7.6c). A correlation is seen between temperature and SRD. At colder temperatures ice particles are more heavily rimed. At temperatures $T \leq -15^\circ\text{C}$, more than 80% of all rimed particles are heavily rimed or graupel, whereas most slightly rimed particles are found at warm temperatures between -5°C and 0°C . The relative fraction of heavily rimed particles is only moderately temperature dependent.

A correlation is also visible between SRD and ice particle size: Most small particles around $D_{\text{im},A} \leq 250 \mu\text{m}$ show only slight riming whereas heavy riming is mostly found on larger particles. These typically large graupel particles correlate with an increased negative (downwards) Doppler velocity (Fig. 7.6c) as they are almost spherical and hence more densely packed compared to aspherical ice particles. This is in agreement with Doppler radar studies presented by Mosimann [1995]. However, apart from that, no correlation of SRD with vertical Doppler velocity is visible. The weak but positive trend of SRD and

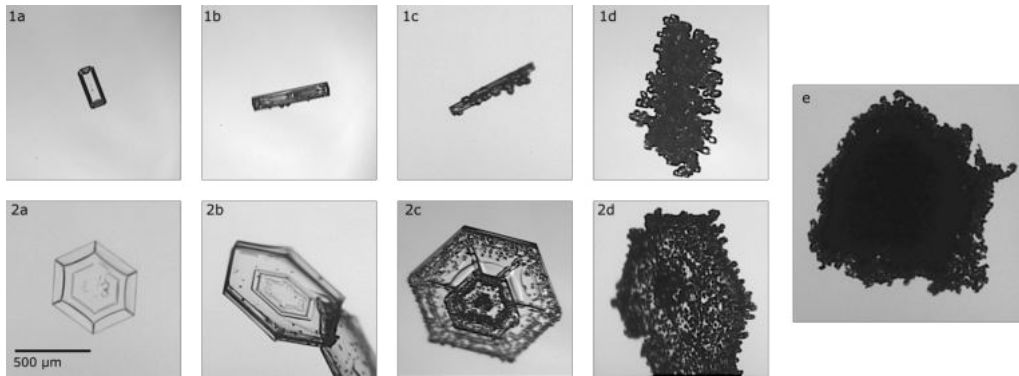


Figure 7.5.: Examples of (1) columnar particles and (2) plates with different degrees of riming depending on the SRD (unrimed (a, $\text{SRD} = 0\%$), slightly rimed (b, $0\% < \text{SRD} < 25\%$), moderately rimed (c, $25\% \leq \text{SRD} \leq 50\%$), heavily rimed (d, $50\% < \text{SRD} \leq 100\%$) and graupel particle (e, $\text{SRD} \gg 100\%$).

downward Doppler velocity presented by Mosimann [1995] is not seen here. A possible explanation is that the increased fall speed due to the increase SRD cancels out with updrafts of the air parcels (see Fig. 7.5d and corresponding discussion) that cause the increased SRD in the first place.

Comparisons with LWC and the other previously discussed parameters (plots shown in the Appendix) show no apparent correlation. Since the classification of SRD is only based on visual inspection, no further numerical analysis was conducted and no fit parameters are presented.

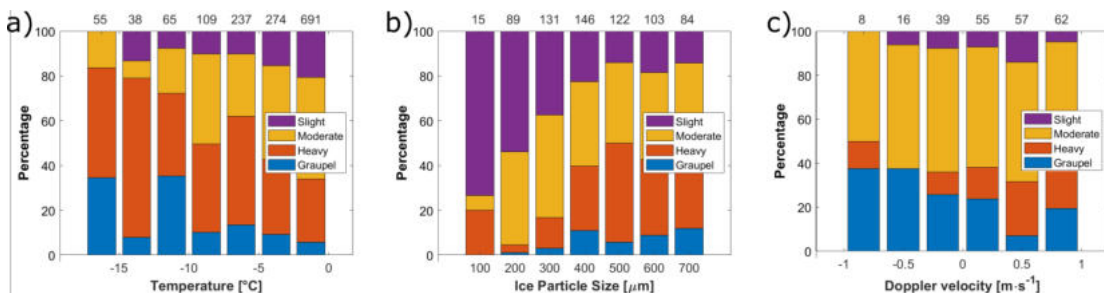


Figure 7.6.: The relative occurrence of particles of different SRD as defined in Fig. 7.5: slight (purple), moderate (yellow) and heavy riming (red) as well as graupel (blue) in correlation with ambient temperature (a), ice particle size (b), and HCR Doppler velocity (c) similar to Fig. 7.1a-c. The values on the upper x-axis correspond to the total number of particles per bin.

7.3. Epitaxial Riming

Rimed ice particles are usually understood as ice particles which have round accretion (rime). However, during their ageing process, the form of accretion can change significantly. Fig. 7.7 shows exemplary rimed ice particles with differently structured rime: round rime (Fig. 7.7a) and crystalline, faceted rime (Fig. 7.7b-e). The latter can be explained by ageing (vapor deposition growth) of rimed particles. In the following, round rime on ice particles will be referred to as *normal riming*.

Particles with faceted rime have been reported in the past. Korolev et al. [2020] have reported a case study with "a few ice particles with small faceted particles stuck to their surfaces" which they refer to as "aged rimed ice particles" that had possibly originated from

"vapor deposition regrowth of rime into faceted particles". Libbrecht [2016] has reported "oriented freezing" of rimed droplets that "freeze with their molecular lattices matching the pre-existing lattice underneath" which results in "faceted rime particles". Since not all aged rimed particles show small faceted particles on the surface and the attribute "faceted" is often used in other context for ice particles (pristine plates, e.g. Libbrecht et al. [2015]; Korolev et al. [2020]), I propose the term *epitaxial riming* to avoid any confusion. In general, epitaxy refers to crystalline growth of a material on the surface of another particle along the lattice structure of the underlying particle [Pashley, 1956]. The epitaxial growth of ice on the surface of crystalline substrates, such as e.g. feldspar, has been the topic of many previous works [e.g. Bryant et al., 1960; Kiselev et al., 2016]. Here, the growth of small ice particles on the surface of larger ice particles along the same crystal axis is described. Thus, the term *epitaxial riming* refers to faceted, rimed particles, underlining the important property that the small "rimed" particles on the surface inherit the same lattice structure as the underlying host particle and share the same c-axis as shown in Fig. 7.7.

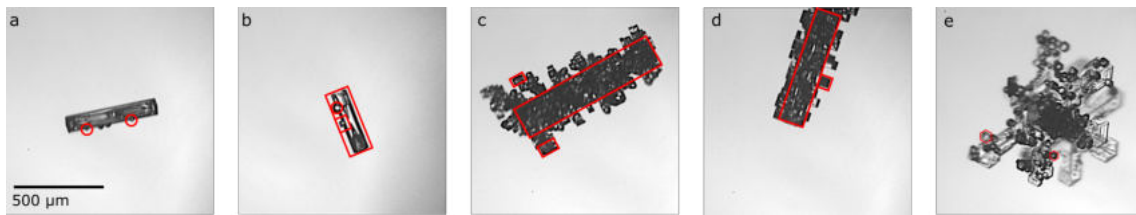


Figure 7.7.: Exemplary rimed ice particles sampled during the IMPACTS campaign: "normally rimed" column (a), column with both normal and epitaxial riming (b), heavily epitaxially rimed columns (c, d) and a epitaxially rimed plate (e).

Multiple studies exist investigating the orientation of the freezing of rimed droplets, both in-vitro [Magono and Aburakawa, 1969; Takahashi, 1979b; Mizuno, 1984; Mizuno and Wakahama, 1983] and in situ [Uyeda and Kikuchi, 1980]. It has been shown that the crystal structure of rimed (still round) droplets matches the underlying lattice structure. At warm temperatures $-10^{\circ}\text{C} \leq T \leq 0^{\circ}\text{C}$, most small droplets ($D \lesssim 40 \mu\text{m}$) freeze as single crystals whereas at colder temperatures ($T \leq -15^{\circ}\text{C}$), rimed droplets tend to freeze as polycrystals. However, to our knowledge, so far no studies exist that analyze the properties and formation conditions of the aforementioned epitaxially rimed particles. In the following, detailed observations of such ice particles are presented and it is shown that they are the result of vapor deposition on rimed particles.

Fig. 7.8 shows the relative occurrence of normally and epitaxially rimed particles during the ACLOUD and SOCRATES campaign in correlation with ambient meteorological parameters. The corresponding fit parameters for all histograms are shown in Table 7.2. Again, only particles sampled at a temperature $T \geq -17^{\circ}\text{C}$ with diameter $D \geq 100 \mu\text{m}$ that were distinctively classified according to the aforementioned manual classification are included.

Fig. 7.8a shows that there is a tendency to find more epitaxial riming at warmer temperatures near $T = 0^{\circ}\text{C}$, where up to almost 40% of all rimed particles show epitaxial riming. Between -5 and -10°C , the fraction of epitaxial riming slightly decreases from 40% to 30%. Below $T < -10^{\circ}\text{C}$, the percentage of epitaxial riming decreases below 20%, although it should be noted that the statistics for this temperature region are weak. This temperature dependency is in accordance with the aforementioned studies showing that the rimed droplets tend to freeze as single crystals along the c-axis of the underlying particle.

Fig. 7.8b shows a slight correlation of the occurrence of epitaxial particles with the size of the underlying particle. For small particles below $D \leq 150 \mu\text{m}$, the fraction of epitaxially rimed particles is 20%. This increases to up to 40% for ice particles larger than $D \geq 300 \mu\text{m}$.

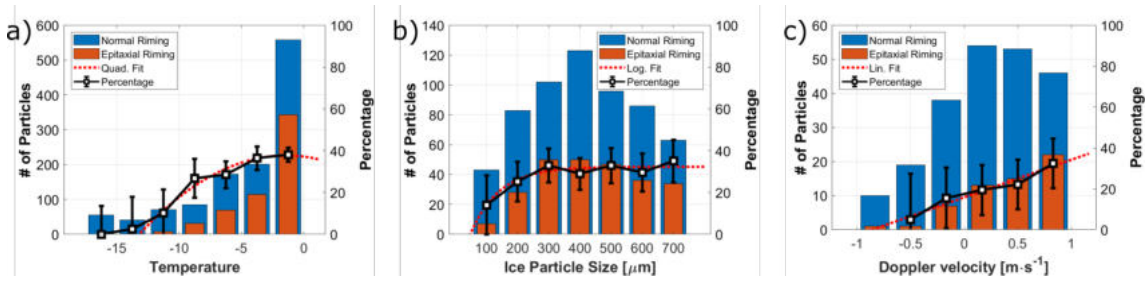


Figure 7.8.: Absolute number of analyzed particles for normal (blue) and epitaxial (red) riming and fraction of epitaxially rimed particles as a function of ambient temperature (a), ice particle size (b) and HCR Doppler velocity (c).

Above that, the fraction of epitaxially rimed crystals is only weakly dependent of particle size. The correlation of particle size with the presence of epitaxial riming can be explained by the fact that epitaxial riming is caused by vapor deposition during the ageing process of rimed particles which naturally also causes the particle to grow on their main surfaces.

Fig. 7.8c shows a trend towards higher upward vertical velocity, indicating a correlation with updrafts. Again, comparisons with LWC and the other previously discussed parameters show no significant correlation (plots shown in the Appendix).

Next, a case study of an MPC sampled during the IMPACTS campaign is presented. The assumption that the ice particles with epitaxial riming are the result of ageing of rimed particles is investigated further and the formation process of epitaxially rimed particles is discussed in detail.

Table 7.2.: Fit parameters to the riming percentage histograms shown in Fig. 7.8.

	Fit function	R ²
Temperature	$y = -0.312 x^2 + -1.37 x + 36.6$	0.93
Ice particle diameter (PHIPS)	$y = 32.3 - \exp[-109 (x-367)]$	0.898
Vertical Doppler velocity (HCR)	$y = 15.5 x + 18$	0.856

7.3.1. Case Study — Epitaxial Riming on Columns

Fig. 7.9a shows meteorological and microphysical data collected on February 1st during the 2020 IMPACTS campaign. The MPC segment discussed in this case study was probed from 12:42:30 - 12:49:00 UTC ($\Delta t = 06:30$ min, which corresponds to $\Delta s = 58.5$ km) in an altitude of approximately 4,300 m at a temperature of about -12 °C around $36^\circ\text{N}/73^\circ\text{W}$, roughly 300 km near the US east coast. The vertical wind velocity was at a constant value around ± 0 m s⁻¹. The relative humidity with respect to ice averaged about 100%. The LWC measured with the CDP averaged around 0.1 g m⁻³ and the TWC measured with the 2D-S was around 0.5 g m⁻³. The number-weighted mean particle diameter was around 20 μm for droplets and between 200 μm to 800 μm for ice particles based on the measurements of CDP and 2D-S, respectively.

The trigger threshold of PHIPS was set in a way that the instrument started to trigger on droplets with diameters larger than $D > 100$ μm. In this segment, in total, 1,589 particles were triggered and 575 stereo images were acquired. Examples of stereo micrographs of particles from this flight segment are shown in Fig. 7.9b. Of the 575 stereo images, 259 (45%) were not classified since they were identified as potential shattering fragments smaller than $D = 100$ μm. Of the remaining ice particles (320) most are classified as columnar particles (173) and 33 as needles. These particles show a wide spectrum of riming degree,

ranging from unrimed (43) to slightly (44), moderately (42) and heavily rimed particles (124). Ice particles show different types of riming, most are epitaxially rimed (87), 56 show normal riming. Furthermore, there are numerous particles with evidence of both normal and epitaxial riming on the same particle (20), which are referred to as *mixed riming* in the following. Apart from that, there are 3 large drizzle droplets with diameters $200\ \mu\text{m} - 300\ \mu\text{m}$ as well as rimed dendrites (30) and graupel (48) particles. 35 particles were classified as irregulars. Similar particle shapes are observed on the CPI imagery (not shown here).

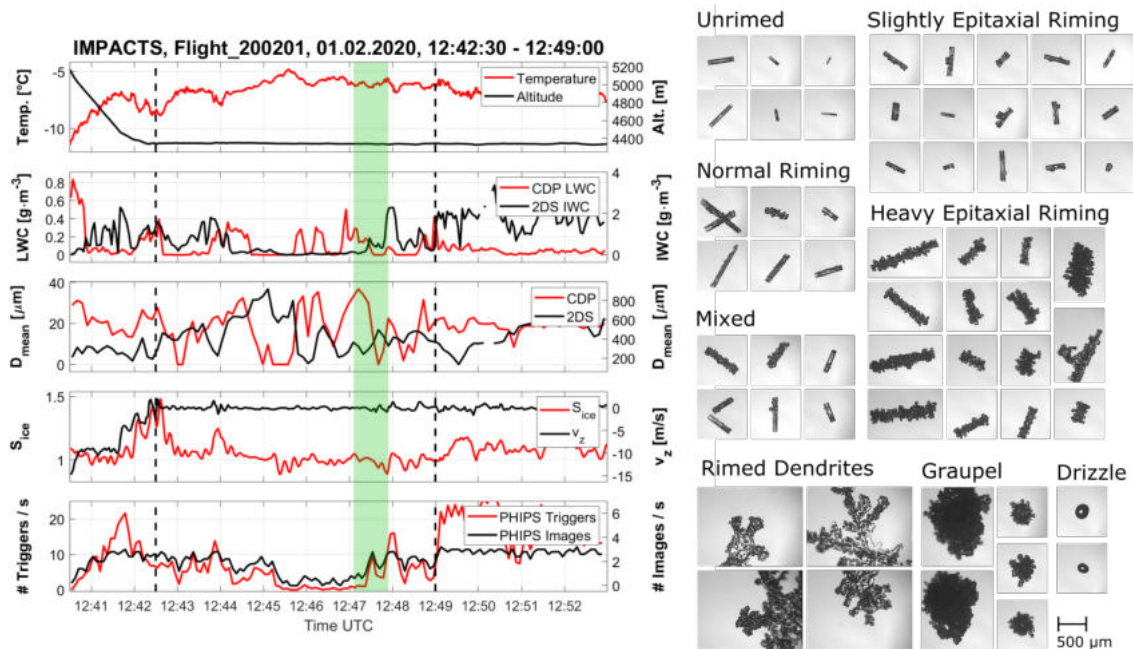


Figure 7.9.: Example of PHIPS data acquired in an MPC near the US east coast sampled during the IMPACTS campaign on February 1st, 2020. Left: overview of meteorological parameters, CDP LWC, 2D-S TWC, CDP and 2D-S number-weighted mean particle diameter and number of PHIPS images and total triggers. Right: representative PHIPS images of particles during the segment marked by the dashed black lines. The green shaded area marks a 45 s segment during which the four particles shown in Fig. 7.10 were acquired.

The lower panel of Fig. 7.10 shows four exemplary ice particles that were sampled within a 45 s window (12:47:07 - 12:47:52 UTC, corresponding to a distance of 6.7 km) that is indicated by the shaded green area in Fig. 7.9. The particles that were sampled within this period show columnar particles during different stages of the riming process: an unrimed (a), a normally rimed (b), a mixed rimed (c) and epitaxially rimed column (d). Since normal and epitaxial riming is observed not only within the same segment in near spatial vicinity, but also on the same singular particles, this shows that normal and epitaxial riming are, as hypothesized, interlinked. As proposed by Korolev et al. [2020], this shows that epitaxial riming is the result of the ageing (deposition growth) of normally rimed particles as sketched in the upper panel of Fig. 7.10: An unrimed ice particle (a) accretes a supercooled droplet and forms the initial primarily "normal" riming (b). Ambient water vapour deposits on the rime matching the lattice structure of the underlying particle and thus forming the faceted surface. It is further possible that older rime grows on the expense of recently accreted droplets that partly evaporate due to latent heat during the freezing process. More droplets are accreted such that normal and epitaxial riming can be observed on the same particle (c). The process repeats and the particle grows further until, eventually, the whole surface is covered by epitaxial rime (d).

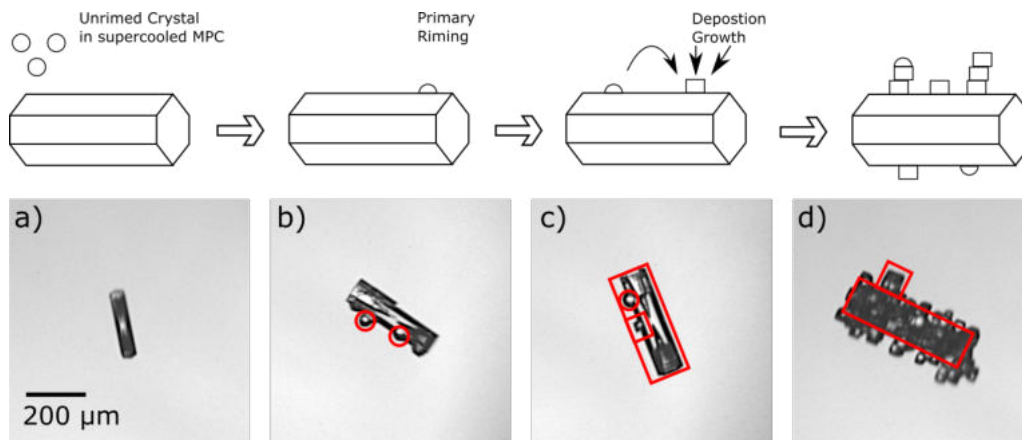


Figure 7.10.: Schematic sketch of an epitaxially rimed column during different stages of the ageing process: unrimed (a), normally rimed (b), mixed (c), and epitaxially rimed column (d). The lower panel shows corresponding exemplary PHIPS images (#1309, #1325, #1320, and #1368) acquired within a 45 s segment in the presented case-study (shaded green area in Fig. 7.9).

7.4. Angular Light Scattering of Rimed Particles

As discussed in Section 3.1, PHIPS measures the ASF of individual particles for 20 channels from $\theta = 18^\circ - 170^\circ$ in 8° steps in polar direction along the scattering plane using a continuous wave laser with a wavelength of $\lambda = 532$ nm. The scattered light is collected by parabolic mirrors over $\pm 3.5^\circ$ around the center of each channel. In the following, the implications of riming on a particle's angular scattering properties are investigated by combining the riming classification with the singly particle ASF measurements.

Fig. 7.11a,b show normalized median ASF of all unrimed (blue), epitaxially rimed (green), and "normally rimed" (i.e. all rimed particles excluding epitaxial riming, red) columns and needles larger than $D \geq 100 \mu\text{m}$ sampled during the ALOUD and SOCRATES campaign in cloud segments warmer than $T \geq -17^\circ\text{C}$. The ASF of the individual particles are normalized by the particle area ($D_{\text{im,A}}$) that is calculated based on the images. Only particles that are completely captured on at least one image are included in the analysis. Images that show multiple particles are excluded from the analysis. During ALOUD, the scattering channel at $\theta = 34^\circ$ was malfunctioning and is hence excluded from the analysis. During SOCRATES, the $\theta = 90^\circ$ channel was affected by background noise and is thus excluded as well. Also, saturated channels are excluded from the analysis. This affects mostly the first two channels (51% for $\theta = 18^\circ$, 39% for $\theta = 26^\circ$). Figs. 7.11c,d show the ASF of unrimed (blue), slightly rimed (red), moderately rimed (green) and heavily rimed (purple) columns and needles.

The side-scattering intensity averaged over the angular range from $\theta = 42^\circ$ to 170° of normally rimed columns (needles) increases by +51.7% (+63.9%) compared to unrimed particles. The side-scattering intensity of epitaxially rimed columns (needles) increases by +67.9% (+70.0%) compared to unrimed particles. Based on the SRD, the average ASF increases by +44.7% (+13.5%) for slightly rimed, +31.7% (+38.9%) for moderately rimed and +107.0% (+135.6%) heavily rimed columns (needles) compared to unrimed particles.

It has been shown by both theoretical [Macke et al., 1996a; van Diedenhoven et al., 2014] as well as experimental studies [Schnaiter et al., 2016; Järvinen et al., 2016] that in general, increasing surface complexity results in higher side scattering and hence a lower asymmetry parameter (g) in the visible wavelengths. As shown by Järvinen et al. [2018], a decrease in g leads to a negative cloud radiative effect (net cooling) in the order of multiple W m^{-2} . This

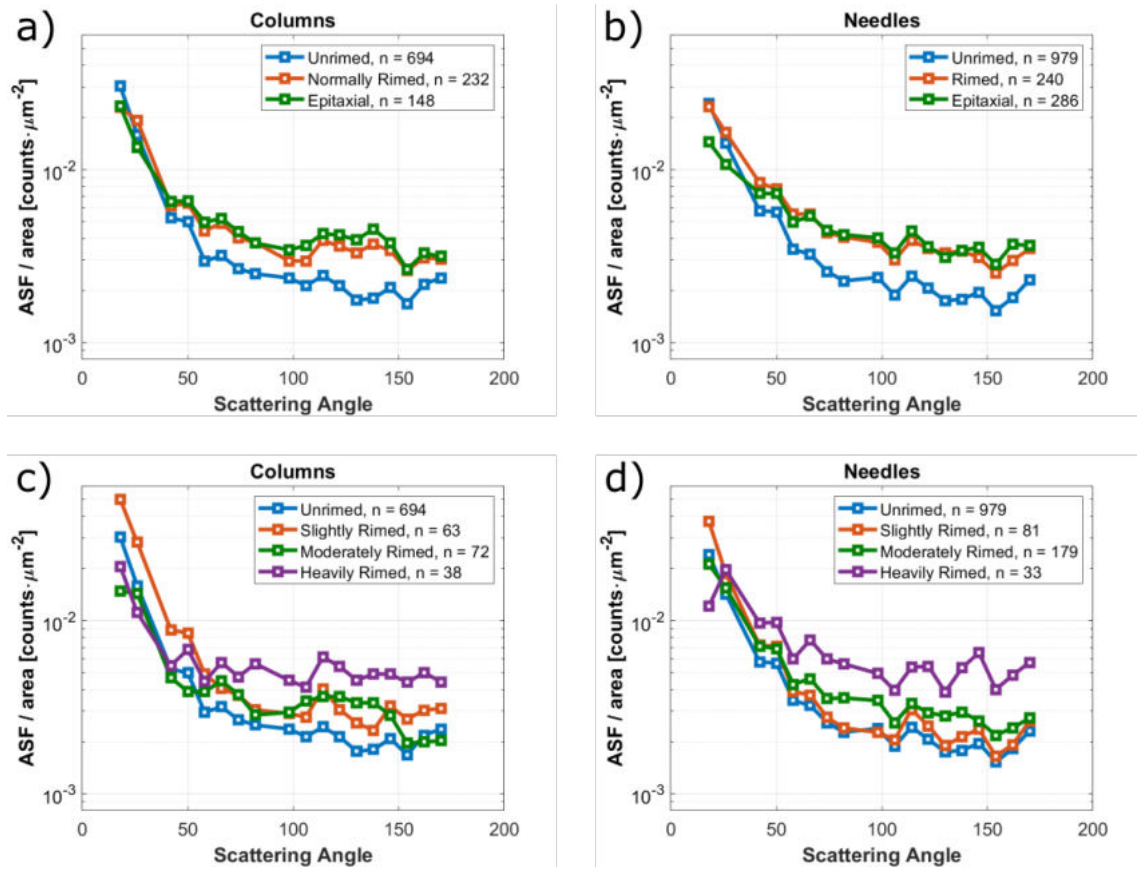


Figure 7.11.: Median ASF normalized by particle area (based on the image) of unrimed (blue), normally rimed (red) and epitaxially rimed (green) columns (a) and needles (b). The lower panel shows similar plots for unrimed (blue), slightly rimed (red), moderately rimed (green) and heavily rimed (purple) columns (c) and needles (d).

shows further that in order to correctly calculate Earth's radiative budget and to predict e.g. the impact of climate change, it is important to include riming features on (individual) ice particles and the corresponding scattering response in climate models.

7.5. Summary

In this chapter, in situ observations of rimed particles using the PHIPS probe during three aircraft campaigns targeting MPCs in the Arctic, the Southern Ocean and US east coast are presented. Ice particles in a size range from $100 \mu\text{m} \leq D \leq 700 \mu\text{m}$ and in the temperature range between $-17^\circ\text{C} \leq T \leq 0^\circ\text{C}$ were manually classified regarding their riming status (rimed or unrimed) and SRD.

It is shown that riming is most prevalent at temperatures around -7°C , where, on average, 43% of the investigated particles showed evidence of riming. It is shown that riming fraction increases with ice particle size (<20% for $D \leq 200 \mu\text{m}$, 35% to 40% for $D \leq 400 \mu\text{m}$) and LWC (25% for $\text{LWC} \leq 0.05 \text{ g m}^{-3}$, up to 60% for $\text{LWC} = 0.5 \text{ g m}^{-3}$).

Riming features such as SRD, size of rimed droplets and one-sided riming were investigated based on visual inspection of individual stereo-images of ice particles imaged by PHIPS during these campaigns. It is shown that the SRD increases with decreasing temperature and increasing ice particle size.

Furthermore, ice particles with faceted, crystalline build-up which is aligned to the lattice structure of the underlying particle were presented. This is called *epitaxial riming* that is differentiated from round "normal riming". Epitaxial riming is most notable in the temperature range from $-10^\circ\text{C} \leq T \leq 0^\circ\text{C}$ where epitaxial riming is visible on 32%-37% of all rimed particles. A case study was presented that demonstrates that normal and epitaxial riming can be observed in the same cloud segments and even simultaneously on the same single ice particles. It is shown that epitaxially rimed particles are the result of deposition growth of water vapor on primarily rimed particles during their ageing process.

Lastly, it is shown that both types of riming increases the light scattering in the angular range from $\theta = 42^\circ$ to 170° by up to 135% for normally and epitaxially rimed columns, respectively, compared to unrimed particles, which has implications for the radiative properties of rimed ice particles.

Currently, the implications of riming towards the climate are not yet well understood as most present day climate models lack a parameterization of riming and consider riming only for large particles ($D \geq 1 \text{ mm}$) in the sense of graupel and snow. Riming on smaller particles is usually not considered. The presented correlation between riming fraction and ambient meteorological parameters can be used as a basis for first steps towards such a riming parameterization for climate models. It was shown that epitaxial riming is prevalent on a significant portion of rimed particles, but further studies are needed to investigate the exact growth mechanisms of epitaxial riming, for example in laboratory studies. Also, some implications of epitaxial riming are still unclear. It is still unknown, for instance, whether rime splintering appears more or less often and with more or less smaller or larger fragments compared to normal riming and how this affects secondary ice production.

8. Conclusion

8.1. Summary

The main objective of this work was to develop tools for better microphysical characterisation of MPCs. In the present day, the biggest challenge and source of uncertainty for the understanding of MPCs is the accurate representation of size and concentration of cloud droplets and ice particles. Hence, the first task of this thesis was to derive a method to determine the phase and size of individual cloud particles based on their ASF in the angular range between $\theta = 18^\circ$ and 170° .

The developed methods were calibrated with, and afterwards applied to, in situ data gathered during three aircraft field campaigns in the Arctic and the Southern Ocean using the PHIPS probe. Based on the derived PSDs, the CPC of cloud segments in the temperature range $-20^\circ\text{C} \leq T \leq +5^\circ\text{C}$ was investigated. Further, the interaction of droplets and ice in the form of riming is discussed and formation, ageing and light scattering of rimed particles was investigated.

The results of this thesis will advance the understanding of the composition and implications of MPCs and lay ground for further studies using the data analysis tools presented in this work. The main scientific contributions of this work are summarized in the following. Suggestions for future research as well as for instrument optimization inspired by the insights gained throughout this work are discussed at the end of this chapter.

Phase-discriminated PSDs

Based on the distinct difference in the theoretical scattering phase functions (SPFs) of spherical droplets and aspherical ice particles a robust method was determined that is able to discriminate individual droplets and ice based on the shape of their ASF. The algorithm was calibrated and validated using disjunct experimental data sets gathered during two in situ aircraft campaigns which consist of over 20,000 pairs of manually classified stereo-micrographs and corresponding ASFs. The discrimination accuracy exceeds 98%.

Because the phase discrimination method is independent of absolute values, it remains valid for future measurement campaigns. This works even when e.g. the laser power changes between campaigns or individual channels have to be excluded from the analysis. Similarly, the sizing method can easily be re-calibrated for future campaigns using the calibration method via the size from the automated image analysis. No additional calibration in the laboratory is needed. Furthermore, the presented method is not tied to the PHIPS probe but can be used for other polar nephelometer instruments that measure the ASF of cloud particles in a similar angular range.

Complementary to the phase discrimination, a method to determine the area equivalent diameter of droplets and ice particles based on the amplitude of their ASF was presented.

Combined with the determination the size and shape dependency of the instruments sensitive area this allows to calculate phase discriminated PSDs in a size range of $50 \mu\text{m} \leq D \leq 700 \mu\text{m}$ and $20 \mu\text{m} \leq D \leq 700 \mu\text{m}$ for droplets and ice, respectively, based on the single particle ASFs measured by PHIPS.

Comparison with the PSDs from other instruments for three representative case studies showed a good agreement in segments that are not affected by shattering. This demonstrates how PHIPS closes the gap between forward scattering instruments and OAPs and provides unique and detailed insight about the phase composition of clouds.

However, it was shown that a significant amount of the particles sampled by PHIPS are potential shattering fragments due to collisions at the inlet of the probe. This leads to a significant overestimation of particle concentrations and underestimation of particle size. Methods presented in this work can help to identify data that are affected by shattering, but due to PHIPS' small sensitive area it is not possible to correct the measured concentrations and retrieve the original size of the shattered particles. Despite that, due to the reliable single-particle phase-discrimination method, PHIPS data can be used to qualitatively detect e.g. individual small ice particles in liquid dominated clouds that might otherwise be classified as single liquid phase cloud.

Cloud phase composition

Based on the derived PSDs for SOCRATES and ACLOUD, the fraction of liquid, ice and MPC segments were determined for different temperature regimes and compared to the results of previous studies. It was described how the fraction of liquid clouds decreases towards lower temperatures and that the fraction of MPCs is only weakly dependent on temperature. Comparison of the sampled clouds during SOCRATES and ACLOUD showed a significantly higher number of liquid clouds in the Southern Ocean compared to Arctic clouds in the same temperature range. During both campaigns, more than 10% of all clouds in the temperature range $0^\circ\text{C} \leq T \leq +5^\circ\text{C}$ were pure ice clouds.

Riming

Based on manual, visual inspection of the PHIPS stereo-microscopic images, all particles larger than $D \geq 100 \mu\text{m}$ sampled during SOCRATES and ACLOUD were classified in terms of their riming state (unrimed, rimed, aged riming) and SRD (percentage of particle surface covered by rime). Over 30% of all classified particles in the size range $100 \mu\text{m} \leq D \leq 700 \mu\text{m}$ sampled in the temperature range from $-10^\circ\text{C} \leq T \leq 0^\circ\text{C}$ showed evidence of riming. Based on correlation with measured ambient parameters, the influence of meteorological conditions on the formation of riming was discussed. Further, it was shown that riming increases the light scattering in the angular range from $\theta = 42$ and 170° by up to 135% compared to unrimed particles.

Currently, the implications of riming towards the climate are not yet well understood as most present day climate models lack a parameterization of riming and consider riming only for large particles ($D \geq 1 \text{mm}$) in the sense of graupel and snow. Riming on smaller particles is usually not considered. The presented correlation between riming fraction and ambient meteorological parameters can be used as a basis for first steps towards a parameterization of riming fraction for climate models.

Furthermore, ice particles were described which show faceted, crystalline build-up that is aligned to the lattice structure of the underlying particle. To differentiate from the round "normal riming", the term *epitaxial riming* is proposed. Epitaxial riming was visible on 32% - 37% of all rimed particles in the temperature range from $-10^\circ\text{C} \leq T \leq 0^\circ\text{C}$. It was shown in a case study that normal and epitaxial riming can be observed within the same

cloud segments and even simultaneously on the same single ice particles. It is hence argued that epitaxially rimed particles are the result of deposition growth of water vapor on primarily rimed particles during their ageing process.

8.2. Outlook

Advancement of measurement techniques

Currently, the biggest source of uncertainty for PSDs measured by PHIPS is the shattering of ice particles in the inlet of the probe. Due to the narrow FoV, conventional shattering detection methods based on interarrival time are not applicable as the probability to detect two fragments of a shattering event is very low. An additional scattering detector analogous to the trigger channel with a wide FoV could serve as a simple particle counter to detect bursts of multiple particles that would be identified as shattering fragments. Further, an automated shattering analysis based on images which show multiple distinct particles at the same time could be useful to detect segments that are affected by shattering.

Another potential improvement of PHIPS' measurement setup is the addition of the polarization of the backscattered light. Given two scattering channels at the same angular position, one with and one without polarization filter, the depolarization ratio of the backscattered light can be determined. Even though the accuracy of the presented phase discrimination algorithm already exceeds 98%, the depolarization measurement could help classify e.g. pristine particles with a specular reflection near the rainbow angle and thus further improve the discrimination accuracy.

The particle sizing method as well as trigger threshold depend on the illumination intensity by the scattering laser. Even though the laser power is included in the calibration parameters, variation over the course of a campaign or fluctuations due to e.g. temperature shifts introduce uncertainties. With a simultaneous and continuous measurement of the laser power via a power-meter at the position of the beam-dump behind the scattering center, power fluctuations could be corrected to rule out potential biases. Further, the introduction of a beam-shaping element would achieve a uniform top-hat profile instead of the Gaussian beam profile. This way the phase and size dependency of the sensitive area would be resolved and potential biases of the scattering intensity based on the spatial position of the particle in the sensitive area would be avoided.

So far, the habit classification of ice particles was done manually via visual inspection of the stereo-micrographs in a laborious, time consuming process. In recent years, multiple works have presented methods to determine the habit of ice particles based on optical imagery using different ML approaches [Lindqvist et al., 2012; Praz et al., 2018; Xiao et al., 2019; Wu et al., 2020]. The existing database of manually classified images acquired during the previous campaigns represents an ideal basis to develop a similar ML based method to automate the habit classification of PHIPS images. The habit classification of individual particles can be used to investigate the difference in the scattering properties between habits.

Riming

In this work, the formation and ageing processes of rimed ice particles were discussed using data from in situ aircraft campaigns. However, in situ studies can only give a snapshot of the current conditions at a given time. In vitro studies are needed to confirm the findings of this work, for example in a cloud chamber (e.g. AIDA [Möhler et al., 2001]). For that, a microscopic particle imaging unit for AIDA is needed. Another possibility to study riming processes is by levitating ice particles in an electrodynamic balance which allows

the investigation of the accretion of droplets via slow motion videography [Rzesanke et al., 2012; Lauber et al., 2018].

It was shown that epitaxial riming is prevalent on a significant portion of rimed particles and that it is caused by vapor deposition during their ageing process. However, further studies are needed to investigate the exact growth mechanisms of epitaxial riming, for example in laboratory studies. Also, the implications of epitaxial riming are still unclear. It is still unknown, for instance, whether rime splintering appears more or less often and with more or less smaller or larger fragments compared to normal riming, and how this affects the production of secondary ice particles.

It was discussed how the riming state and degree affect the side scattering properties of ice particles. This should be compared to theoretical simulations of rimed particles using optical engineering software such as FRED.

In recent years, multiple studies were presented that study riming based on remote sensing methods such as Doppler radar observations (see discussion in Section 2.4.3). However, such measurements are usually dominated by large, precipitating graupel particles ($D > 1$ mm). A manual riming classification for cloud segments based on PHIPS images as presented in this work would provide the possibility to link the riming state and riming degree of smaller cloud particles with remote sensing measurements. For this, it is necessary to combine in situ and remote sensing measurements. This is challenging, as the aircraft in situ measurements only measure in the immediate vicinity whereas airborne remote sensing methods typically have a dead zone for the first few meters. Combination with ground based or satellite remote sensing methods are challenging as well, as the overflow passage is very short and hence the overlap of the measurement is narrow. One solution is to have two aircraft that fly over each other and sample the same cloud, one from above via radar, one inside the cloud via e.g. PHIPS. This setup was given for the IMPACTS 2020 campaign, however no final radar data was available at the time of the writing of this thesis. Further, a similar setup will be flown during the second deployment of the IMPACTS project in early 2022. With this, remote sensing shattering flags can be calibrated and potential limitations can be analyzed. Additionally, this would allow to further investigate the correlation of riming with updrafts and fall speed.

Implementation in models

One of the main motivations for this work is the poor representation of MPCs in climate models. Hence, the experimental results presented in this work need to be implemented into models to investigate, for instance, whether they correctly represent the CPCs and how predictions could be improved. One possible improvement is the introduction of a riming parameterization into models and compare the riming observations presented in this work with pre-existing models over the proxy of graupel. For this, a co-operation with A. Possner from the Goethe-university of Frankfurt already started.

Further, the scattering effects of the presented results need to be investigated, both in terms of CPC and the increase in side scattering intensity due to the increase of crystal complexity caused by riming.

A. Appendix

A.1. Crosstalk

As described in Section 3.1.1, the detected scattering light of 20 channels is guided via PMMA fibers to the MAPMT photo-multiplier. To prevent light from "crosstalking" from one channel to the neighbouring, a fiber coupler consisting of cylindrical gradient index lenses is installed as discussed in Schnaiter et al. [2018]. This way, the crosstalk is decreased from up to 20% to less than 3%.

The crosstalk intensity was measured after the SOCRATES campaign using a piezo-driven droplet injector. All fibers but one were detached from the instrument and blindfolded. The scattering intensity of all channels was measured. This was repeated for every fiber. Fig. A.1 shows the average relative crosstalk intensity over all channels to their respective neighbouring channels. It can be seen that the crosstalk to first-order neighbours is below 3% and below 1% for second-order.

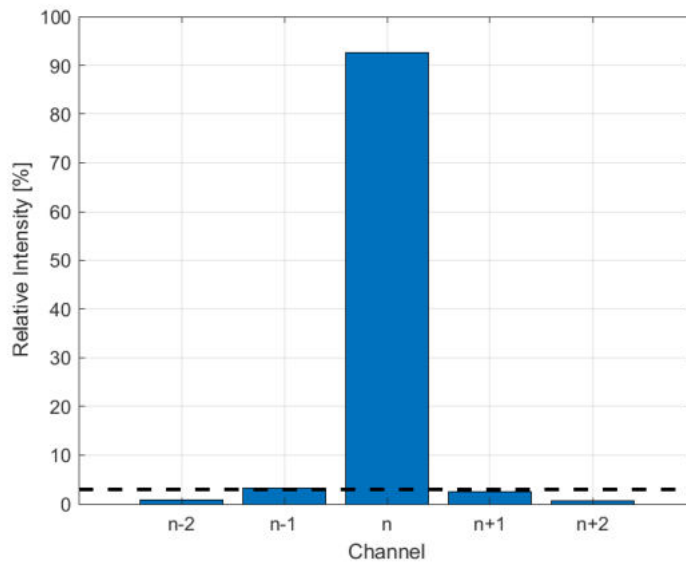


Figure A.1.: Average crosstalk intensity to neighbouring channels measured between the SOCRATES and IMPACTS campaign. The dashed black line marks 3%.

A.2. Averaging the Background Intensity of an Empty Image

For the background (BG) correction used for the image analysis (Section 3.2.1) and image post-processing (Section 3.2.2), an empty image that shows no particles but only the BG.

For most previous campaigns, this empty image was manually hand-picked for every flight (each one for each camera, CTA1 and CTA2). In the IMPACTS campaign, the ice particle concentrations were very high and shattering (see REF) was often prevalent. Hence, Given enough images, the average over a lot of images ($n \approx 1000$) with ideally small, randomly distributed particles approximates an empty image very well, since the few black pixels (i.e. the particle) average out. In future projects, PHIPS will take an empty image every 100th image which allows accurate BG subtraction for the image analysis and enhancement.

Fig. A.2 shows the comparison of an actual empty image (1a) and the average over the first 1000 images of the same flight (1b). On the very right (1c), the calculated difference between the two image is shown. The lower panel shows the corresponding intensity histograms (2a, 2b, 2c). It can be seen that both the actual image as well as the intensity histogram of the averaged image compare very well to the actual empty image. There is no indication of any residue or noise caused by any particles.

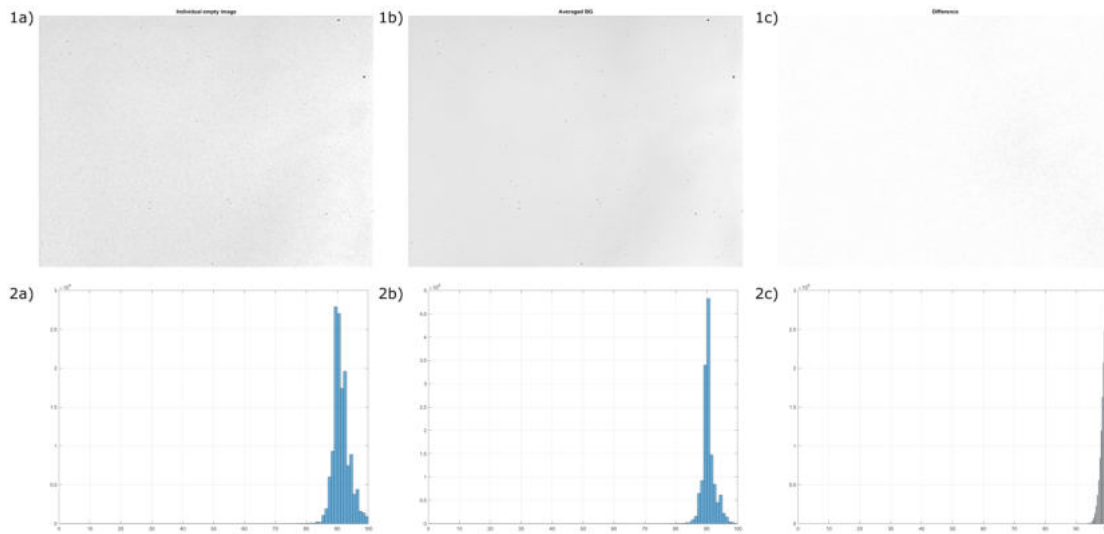


Figure A.2.: Comparison of 1a) an empty image (SOCRATES, RF04, #0003, CTA1) and 1b) the averaged intensity over images #1 to #999 of the same flight. 1c) shows the difference between 1a) and 1b). The lower panel (2a, 2b, 2c) shows the corresponding intensity histograms.

A.3. Proof Sigmoid function

As explained in Section 4.3, the classification probability/confidence $P(X)$ for each feature has the form

$$P(X) = \frac{n_1(X)}{n_1(X) + n_2(X)} \quad (\text{A.1})$$

$$= \frac{1}{1 + \frac{n_2(X)}{n_1(X)}} \quad (\text{A.2})$$

with on the relative/normalized percentage/amount/ratios $n_{droplet/ice}$ of droplets and ice particles, which follow a Gaussian distribution of the form

$$n_i(x) = a_i \cdot \exp\left(-\frac{(x - c_i)^2}{b_i}\right) \quad (\text{A.3})$$

Given that, we now want a simple¹ fit function for the classification probability $P(X)$.

For the sake of legibility, let's look at $\frac{n_2}{n_1}$ first:

$$\frac{n_2}{n_1} = \frac{a_2 \cdot \exp\left(\frac{x-c_2}{b_2}\right)^2}{a_1 \cdot \exp\left(\frac{x-c_1}{b_1}\right)^2} \quad (\text{A.4})$$

$$= \frac{a_2}{a_1} \cdot \exp\left[\left(\frac{x-c_1}{b_1}\right)^2 - \left(\frac{x-c_2}{b_2}\right)^2\right] \quad (\text{A.5})$$

$$= \frac{a_2}{a_1} \cdot \exp\left[\left(\frac{x^2 - 2c_1x + c_1^2}{b_1^2}\right) - \left(\frac{x^2 - 2c_2x + c_2^2}{b_2^2}\right)\right] \quad (\text{A.6})$$

$$= \underbrace{\frac{a_2}{a_1}}_{:=a'} \cdot \exp\left[x^2 \underbrace{\left(\frac{1}{b_1^2} - \frac{1}{b_2^2}\right)}_{:=\beta} - x \underbrace{\left(\frac{2c_1}{b_1^2} - \frac{2c_2}{b_2^2}\right)}_{:=b'} + \underbrace{\left(\frac{c_1^2}{b_1^2} - \frac{c_2^2}{b_2^2}\right)}_{:=c'}\right] \quad (\text{A.7})$$

$$= a' \cdot \exp\left(\beta x^2 - b'x + c'\right). \quad (\text{A.8})$$

Further, if the width of the normal distributions for ice and droplets are similar, i.e. $b_1 \approx b_2$, then $\beta \approx 0$ and the x^2 term is negligible against the $b' \cdot x$ term and

$$\frac{n_2}{n_1} \approx a' \cdot \exp(-b'x + c'). \quad (\text{A.9})$$

Thus, the probability can be approximated as

$$P = \frac{n_1}{n_1 + n_2} \quad (\text{A.10})$$

$$= \frac{1}{1 + \frac{n_2}{n_1}} \quad (\text{A.11})$$

$$= \frac{1}{1 + a' \cdot e^{-b'x+c'}} \quad (\text{A.12})$$

which has the form of a sigmoid function.

For the sake of clarity, we can slightly reshape the function to

$$P(x) = \frac{a - d}{1 + \exp(-b \cdot (x - c))} + d. \quad (\text{A.13})$$

without any loss of generality to give the parameters a clearer physical meaning: a and d dictate the upper and lower levels, b and c correspond to slope and position of the "jump" in between.

A.4. Fit Parameters Phase Discrimination Algorithm

The to fit the normalized occurrence of the feature parameters in Fig. 4.6 (upper panels), a Gaussian fit function of the form

$$n(x) = a \cdot \exp\left(-\left(\frac{x - \mu}{2\sigma}\right)^2\right) \quad (\text{A.14})$$

Table A.1.: Fit parameters of the Gaussian fits for the distribution of the feature parameters n_i .

Feature	a_{droplet}	μ_{droplet}	σ_{droplet}
Mie	150.3 (± 7.2)	3.842 (± 0.011)	0.3184 (± 0.0167)
Down	198 (± 5.6)	-9.444 (± 0.029)	1.243 (± 0.041)
Up	62.48 (± 4.68)	9.348 (± 0.23)	3.592 (± 0.287)
Minimum	127.9 (± 3.8)	-1.553 (± 0.009)	0.3859 (± 0.0134)
Feature	a_{ice}	μ_{ice}	σ_{ice}
Mie	868.5 (± 18.7)	5.195 (± 0.004)	0.2451 (± 0.0059)
Down	331.6 (± 13)	-2.413 (± 0.101)	3.137 (± 0.131)
Up	261 (± 14.5)	1.789 (± 0.149)	3.299 (± 0.211)
Minimum	406.2 (± 14.7)	-0.1919 (± 0.0143)	0.492 (± 0.0105)

is used. The corresponding fit parameters (with 95% confidence intervals) for the four feature parameters for the ACLOUD data set are shown in Table A.1.

Since the Gaussian distributions are of similar width σ , the corresponding discrimination probabilities (Fig. 4.6, lower panels), defined as

$$P(f) = \frac{n_{\text{ice}}(f)}{n_{\text{ice}}(f) + n_{\text{droplet}}(f)}, \quad (\text{A.15})$$

can be approximated by a sigmoid function of the form

$$P(x) = \frac{a - d}{1 + \exp(-b \cdot (x - c))} + d \quad (\text{A.16})$$

as discussed in Appendix A.3. The corresponding fit parameters are shown in Table A.2.

Table A.2.: Fit parameters of the sigmoid fit for the discrimination probabilities P_i .

Feature	a	b	c	d
Mie	98.57 (± 0.83)	10.89 (± 0.57)	4.641 (± 0.006)	0.1804 (± 0.6129)
Down	99.36 (± 1.02)	2.52 (± 0.317)	-7.312 (± 0.057)	2.052 (± 1.369)
Up	98.04 (± 1.26)	-1.069 (± 0.096)	5.732 (± 0.097)	3.14 (± 1.036)
Minimum	99.27 (± 1.73)	10.78 (± 2.319)	-0.9897 (± 0.023)	2.194 (± 2.234)

A.5. Correlation Histograms Riming

In the following, the remaining correlation histograms of riming fraction (Fig. A.3), surface riming degree (Fig. A.4), fraction of epitaxial riming (Fig. A.5) as well as one-sided riming (Fig. A.6) with various meteorological parameters, including relative cloud height (Fig. A.3e, 100% corresponds to cloud top, 0% to cloud base), supersaturation with respect to ice (Fig. A.3f), CDP mean droplet diameter (Fig. A.3g), and ambient vertical velocity relative to the aircraft (Fig. A.3h) are shown. Note that fraction of one-sided particles is considered to be a lower estimate, as not every particle is imaged clearly from both sides on the stereo images and it is thus not always possible to determine whether or not both sides are rimed.

¹to keep the number of fitting parameters as low as possible

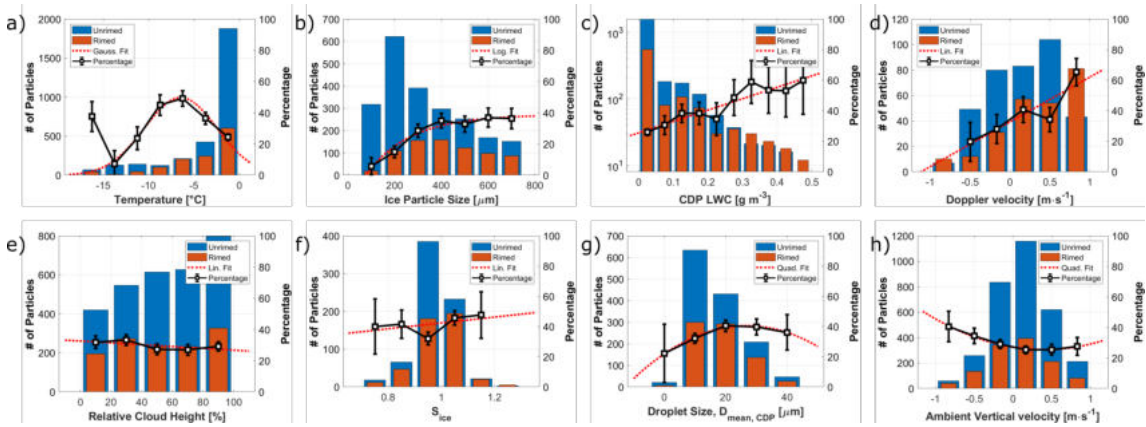


Figure A.3.: Histograms showing the absolute number of classified unrimed (blue) and rimed (red) particles during ALOUD and SOCRATES as well as the relative percentage ($n_{\text{rimed}}/n_{\text{all}}$, black, right axis) in correlation with different ambient parameters: Temperature (a), area-eq. diameter of the underlying ice particle measured by PHIPS (b), CDP LWC (c), vertical HCR Doppler velocity (d), relative cloud height (e), and supersaturation with respect to ice (f), CDP mean droplet diameter (g), ambient vertical velocity (h). The red dotted line shows a fit to the percentage values. The statistical uncertainty bars correspond to the number of particles per bin ($n^{-1/2}$). Only bins with $n \geq 20$ are considered for the fits.

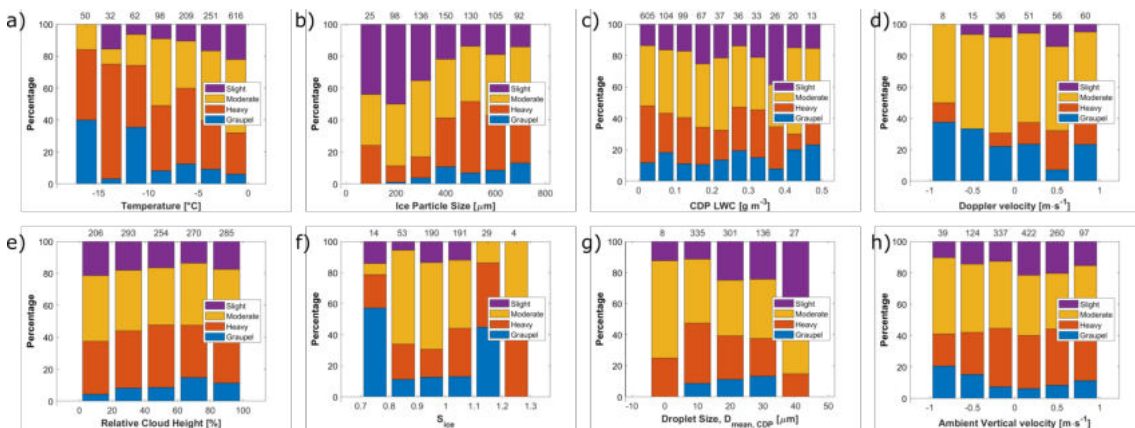


Figure A.4.: Correlation of surface riming degree with ambient parameters similar to Fig. A.3.

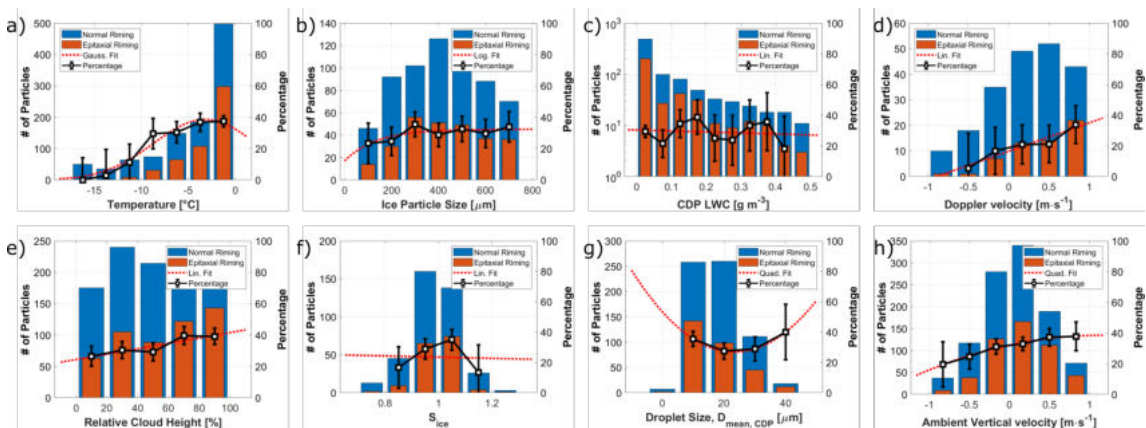


Figure A.5.: Correlation of the fraction of normally and epitaxially rimed particles with ambient parameters similar to Fig. A.3.

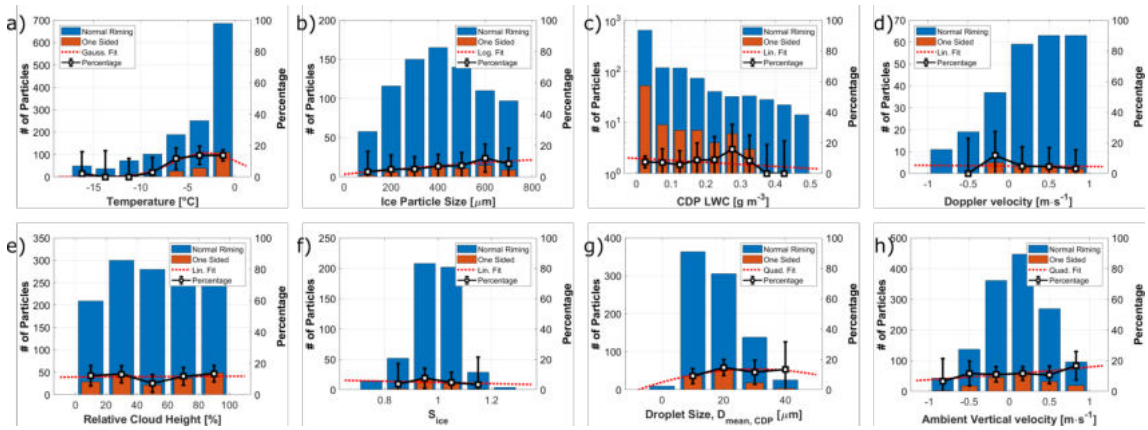


Figure A.6.: Correlation of the fraction of one-sided rimed particles with ambient parameters similar to Fig. A.3.

List of Figures

2.1. Hydrological cycle of water in the atmosphere: Heated up by the sun (1) water evaporates and ascends (2). When it reaches colder altitudes, clouds form (3) where cloud particles grow until they precipitate back down (4).	6
2.2. Schematic view of a water molecule consisting of one oxygen atom ($^{16}_8\text{O}$, red) and two hydrogen atoms (^1_1H , blue). The black dots indicate the bound electrons. The binding angle between the two hydrogen atoms is 104.5° [Holleman and Wiberg, 2007].	6
2.3. Schematic representation of the molecular structure of hexagonal ice in top view (left), tilted view (middle) and from the side (right). Oxygen atoms are indicated by red circles, hydrogen atoms by blue circles. Hydrogen bonds between each molecule are shown with the dashed lines. The elementary, tetrahedral cell of the crystal around one molecule (marked by the “x”) is drawn in black.	8
2.4. Refractive index of water (blue) and ice (red) based on the parameterization of Hale and Querry [1973] and Warren and Brandt [2008], respectively. The solid line correspond to the real part, the dashed to the imaginary part. The green line marks $\lambda = 532 \text{ nm}$	9
2.5. Refraction of a light beam according to Snell’s law.	12
2.6. Photography of a double rainbow around $\theta = 128^\circ$ and $\theta = 138^\circ$ (a) (photo credit: Elke Rohn), schematic view of the path of a light ray (red) in a spherical droplet (b) and the dependence of the exit angle γ of the entry angle with respect to the normal line α (c).	14
2.7. 22° halo around the sun (a) (photo credit: Natalia Kollegova) caused by refraction of light on hexagonal ice particles as shown in the schematic view (b).	14
2.8. Schematic view of multiple-scattering of a single light beam (a) and scattering of a broad light beam (b) in a spherical object.	15
2.9. Scattering phase function p of a spherical water droplet with refractive index $n = 1.33 + i1.50 \cdot 10^{-9}$ and diameter $D = 100 \mu\text{m}$ for a wavelength of $\lambda = 532 \text{ nm}$. The small figure within shows the angular range from $\theta = 0^\circ$ to $\theta = 2^\circ$	20
2.10. Orientation averaged angular scattering intensities of simulated columns (red) and plates (black) with smooth (solid line) and rough surface (dashed) with maximum dimension $D = 100 \mu\text{m}$ for a wavelength $\lambda = 530 \text{ nm}$ based on [Yang et al., 2013]. The grey line shows the calculated Mie scattering intensity for a spherical droplet from Fig. 2.9 ($D = 100 \mu\text{m}$, scaled by a.u.). The small figure within shows the angular range from $\theta = 0^\circ$ to $\theta = 2^\circ$	21
2.11. Sketch of the typical life cycle of an MPC: Water vapor ascends in the atmosphere, cloud particles form, grow and precipitate.	22
2.12. Schematic overview of how a cloud interacts with radiation: Transmission (1), extinction (2), scattering (3) and reflection of light (4) and heat (5).	24

- 2.13. Saturation pressure of vapor over water, e_w , (blue) and ice, e_i , (red) from the parameterization of [Murphy and Koop, 2005]. The difference between the saturation pressure over water and ice is shown by the dashed black line with the maximum difference at around $T \simeq -12$ °C. 25
- 2.14. Schematic overview of typical freezing and condensation mechanisms, adapted from [Hoose and Möhler, 2012]. The horizontal line indicates the saturation line with respect to ice, corresponding to the red line in Fig. 2.13. Below that, the equilibrium state is gaseous, above, ice is the stable phase. The vertical line indicates the threshold below which droplets freeze homogeneously. The diagonal line corresponds to the ice saturation ratio at liquid water saturation where supercooled liquid water is in equilibrium with the vapor phase (i.e. the equivalent of the horizontal line, but for liquid water, blue line in Fig. 2.13). Above that, vapor condenses on droplets, below droplets evaporate. 26
- 2.15. Schematic representation of secondary ice processes caused by shattering due to collision of ice particles, fracturing of freezing drizzle droplets and rime splintering, adapted from Järvinen et al. [2021a]. 27
- 2.16. Ice particle habit (Nakaya) diagram as a function of temperature and supersaturation, taken from [Libbrecht, 2005]. 29
- 2.17. Exemplary ice particles of different habit (needle, column, plate, dendrite, side plane and bullet rosette) acquired using the PHIPS probe during the IMPACTS campaign. 29
- 2.18. PHIPS images of capped columnar particles (left) and particles with antennas on the basal face, acquired during the IMPACTS campaign. 30
- 2.19. Exemplary PHIPS images of columns (left panel) and plates (right panel) acquired during the IMPACTS campaign with different visual degree of crystal complexity ranging from pristine particles with little to no crystal complexity to heavily rimed particles in the top right. 30
- 2.20. Overview of different types of crystal complexity on nano-scale (observable via cryoscopic scanning electron microscopy), meso-scale (observable via light scattering patterns) and micro- to macro-scale (observable via optical microscopy) as well as corresponding exemplary particles for each category imaged via cryoscopic scanning electron microscopy (CSEM) (1, 2, 5, 7 and 12) and PHIPS (rest), adapted from Järvinen et al. [2021b]. 31
- 2.21. Stereo micrograph of a droplet (a) and a quasi-spherical ice particle (b) taken by the PHIPS probe. In the stereo micrograph, the two views of the particle have an angular distance of 120°. The instrument concurrently recorded the angular light scattering functions of the imaged particles as displayed in (c). The theoretical scattering function calculated for a droplet with a diameter of 200 μm calculated using the Mie theory is shown for comparison in (c). The calculated scattering-intensity is integrated over the field of view of each of PHIPS' 20 polar nephelometer channels so it can be compared to the measurement (see Section 3.1.1 for details). 35
- 2.22. Photographs of the 2D-S and CPI probes installed on the NCAR C-130 (a) and examples of images from the 2D-S and CPI acquired in a cirrus cloud (b). Both figures are taken from [Lawson et al., 2006]. 38
- 2.23. Photo of the SID-3 probe (a, image credit: KIT/ Markus Breig) and scattering patterns of a droplet (b), pristine column (c) and rough ice particle (d) acquired by the SID-3. 39

- 3.1. PHIPS on the wing of the P3 aircraft during the IMPACTS campaign (a, on the left), close up view of the optical unit with running scattering laser (b, image credit: KIT/ Markus Breig) and view of the whole instrument including processing unit (c, image credit: KIT/ Markus Breig). 41
- 3.2. Sketch of the measurement principle of PHIPS. The particle stream is marked in blue, the scattering measurement in green and the image acquisition in red. 42
- 3.3. Stereo images of an exemplary deformed droplet and ice particle acquired during the IMPACTS campaign and their corresponding angular scattering functions as well as the calculated angular scattering function of a spherical particle ($D = 200 \mu\text{m}$) using Mie theory. The theoretical angular scattering function is scaled by a constant factor that accounts for the laser power and the conversion from counts to W of the MAPMT. 42
- 3.4. Schematic view of PHIPS' scattering setup (figure adapted from Stegmann et al. [2016]) 43
- 3.5. Sketch of the angular range of PHIPS' polar nephelometer channel, left: side view, right: top view (not to scale). 44
- 3.6. Calculated phase function p of a droplet with $D = 200 \mu\text{m}$ (blue) and the same differential scattering cross sections (ASF) integrated over the FoV of PHIPS' nephelometer channels (red). 45
- 3.7. Calculated Mie intensity for droplets of various size (left) and the same graph normalized by diameter squared (right). 45
- 3.8. Schematic view of PHIPS' imaging setup (figure adapted from Stegmann et al. [2016]). 46
- 3.9. a) Shape of the beam profile of PHIPS' scattering laser before the SOCRATES campaign. The yellow lines show the vertical and horizontal intensity distribution and the corresponding Gaussian fits are marked in green. The $1/e^2$ diameter is approximately 0.865 mm. b) Schematic visualization of the size and phase dependency of the sensitive area of PHIPS' trigger system. Due to the Gaussian shape of the laser beam profile, whether or not a particle at a given distance from the center of the laser beam is detected by the trigger sensor is dependent on their size and shape. 47
- 3.10. Sensitive area based on FRED simulations for ice (red) and droplets (grey). 48
- 3.11. Exemplary image during different stages of the image processing: original image (top left), removed BG (top right), final binarized image with all processing measures (bottom left) and the resulting chain vector (bottom right). 49
- 3.12. Uncorrected and corrected area equivalent diameter of CTA1 and CTA2 of the whole SOCRATES campaign. The 1:1 line is marked in white. 49
- 3.13. Relative difference between area equivalent diameter of CTA1 and CTA2 of the whole SOCRATES campaign, uncorrected (left) and corrected (right). The black markers show the mean per diameter bin. The red line shows the exponential fit through the bin means. 50
- 3.14. Illustration of the image post-processing. The upper panel shows 3 exemplary images throughout different stages of the image post-processing: a) original, b) enhanced, c) enhanced + BG correction and d) enhanced + BG correction + BG equalization. The lower panel shows the corresponding intensity histograms (0 corresponds to black pixels, 100% means white). More information is given in the text. 51
- 3.15. Parts of an image before and after background subtraction. The red arrow points to an artifact (likely a dust particle on the camera lens) that is removed via this method. 53

3.16. Examples of (1) columnar particles and (2) plates with different degrees of riming depending on the surface riming degree (SRD): unrimed (a, SRD=0%), slightly rimed (b, 0% < SRD < 25%), moderately rimed (c, 25 ≤ SRD ≤ 50%), heavily rimed (d, 50% < SRD ≤ 100%) and graupel particle (e, SRD ≫ 100%).	55
3.17. Overview of the flight tracks of all flights of the ACLOUD (purple), SOCRATES (blue) and IMPACTS (red) field campaign.	55
3.18. Overview of the flight tracks of all flights of the ACLOUD campaign.	56
3.19. Overview of the flight tracks of all flights of the SOCRATES campaign.	57
3.20. Overview of the flight tracks of all flights of the IMPACTS campaign.	58
3.21. Overview of the mean area equivalent diameter all sampled particles during ACLOUD, SOCRATES and IMPACTS.	59
3.22. Overview of the habit of the manual classified particles of ACLOUD in different temperature regimes.	60
3.23. Overview of the habit of the manual classified particles of SOCRATES in different temperature regimes.	60
4.1. Visualization of the four classification features: f_1 = Mie comparison (shaded area between curves and Mie calculation), f_2 = down slope, f_3 = up slope before the rainbow feature and f_4 = ratio around the minimum at 90°. The green line shows the calculated ASF for a theoretical spherical particle. The blue and red lines show the measured ASF of an exemplary droplet ($D = 119.6\mu\text{m}$) and ice particle ($D = 165.8\mu\text{m}$) from the SOCRATES campaign.	63
4.2. Schematics showing the basic working principle of the phase discrimination algorithm.	64
4.3. Determination of the feature parameter f_1 of two exemplary droplets: Droplet d1 (blue) is the same particle as in Fig. 2.21. Droplet d2 (red) is a theoretical Mie-sphere with $D = 200\mu\text{m}$. The plots show the particles' ASF (a), q and \bar{q} (b) and q' (c). The resulting f_1 is then calculated as the integral over all channels (i.e. area between each curve and $y=0$). The resulting values are $f_1 = 3.7$ for d1 and $f_1 = 2.2$ for d2.	65
4.4. Distribution of the feature parameter for the down slope after rainbow peak, based on the manually classified images from the SOCRATES campaign.	67
4.5. Normalized histograms of the discrimination features, f_i , evaluated for theoretical ASFs. Simulated ASFs were calculated using Mie theory in case of droplets (blue) and by selecting typical ice particle habits (red) from the light scattering databases by Baum et al. [2011] and Yang et al. [2013]. Normal distribution fits to the data are depicted by solid lines in the graphs. Note that the simulations provide orientation-averaged ASF whereas the observed particles by PHIPS have random but fixed orientation.	68
4.6. Left: normalized histograms of the discrimination features, f_1 , f_2 , f_3 and f_4 , of all manually classified particles (blue: droplets, red: ice) from the ACLOUD campaign that were used for the calibration of the discrimination algorithm. The histograms can be nicely fitted by normal distributions (solid lines). Right: corresponding probability for a given particle with a given feature parameter value to be classified as ice or droplet, including sigmoidal fits. The fit parameters are shown in Appendix A.4.	70

- 4.7. a) Correlation of the classification probability of feature parameters f_3 alone and the combination of all four features. The dashed lines mark the confidence limits. $P(f) > 66\%$ corresponds to particles that are classified correctly with high confidence, $33 < P(f) \leq 66\%$ means the classification is uncertain and particles with $P(f) \leq 33\%$ are classified falsely as droplets with high confidence. b) shows the corresponding statistics of the plot in a confusion matrix. The squares correspond to the dashed lines in a). 73
- 4.8. Confusion matrices that visualize the classification accuracy of the ice discrimination algorithm. The discrimination algorithm was applied to all manually classified particles from both the ACLOUD (left) and SOCRATES (right) data sets. In both cases the combined probability P_{combined} from the ACLOUD calibration was used to calculate the classification probability of each individual particle. 74
- 4.9. a) Discrimination confidence of all correctly classified (left) and misclassified particles (right). b) Correlation of misclassification rate (= 100% - discrimination accuracy) and particle size. The size binning is the same as used previously. 74
- 4.10. Example of a typical elongated droplet, stereo images (left: CTA1, middle: CTA2) and the corresponding ASF (right) including the theoretical Mie ASF of a spherical particle ($D = 200\mu\text{m}$) for comparison. 75
- 4.11. Example of a typical misclassified large drizzle droplet with multiple saturated channels. 76
- 4.12. Example of a particle that is clearly a pristine ice particle that is misclassified because the ASF resembles all typical features of a droplet's. 77
- 5.1. Calibration of the PHIPS integrated light scattering intensity measurement, expressed by the partial scattering cross section $\sigma_{\text{scatt}}^{\text{partial}}$, against the geometric diameter D_{geom} deduced from the concurrent stereo micrographs. Stereo micrographs from the SOCRATES data set were manually classified for droplets (left) and ice particles (right). 80
- 5.2. Comparison of PSDs based on D_{scatt} calculated from the single particle ASFs using the calibration defined in Eq. (5.3) (dotted line) and PSDs based on D_{geom} derived from stereo micrographs (average of CTA1 and CTA2, solid line) for droplets (blue) and ice particles (red). The data are from all flights recorded during SOCRATES. Only particles with stereo micrographs that showed only one, completely imaged particle were taken into account. The same particles were used for both PSDs. 81
- 5.3. Example of a shattering event during the transit leg of SOCRATES RF06. The images (left CTA1, right CTA2) show one representative shattering event during this time period. 82
- 5.4. Example of a shattering event (left CTA1, right CTA2) during another segment of RF06, indicating the breaking up of aggregates. 82
- 5.5. Histogram of interarrival times of ice particles (left) and droplets (right) measured during SOCRATES flights RF02 and RF03. Comparison of the interarrival times of all particles (blue) and only particles whose images were manually classified as shattering events (red). The red vertical line marks the $\tau \leq 0.5$ ms threshold. The lowest measured interarrival time is limited by the dead time of $t = 12 \mu\text{s} = 0.012$ ms after each trigger event. 83

- 5.6. a) Comparison of the total number concentrations of 2D-S and PHIPS. Each point is averaged over 30 s. The colour-code is based on the ratio of large 2D-S particles with $D_{max} \geq 800 \mu\text{m}$. The thick black line marks the 1:1 line, the dashed and dotted lines factor 2 and 10. b) Correlation of the ratio of number concentrations of PHIPS and 2D-S and the presence of large 2D-S particles. The horizontal line marks the 10% threshold. The colour-code is the same as in a). 84
- 5.7. Example of PHIPS data acquired in a low-level supercooled liquid cloud over the Southern Ocean during the SOCRATES campaign (research flight RF04). a) overview of meteorological parameters, CDP, 2D-S and PHIPS number concentrations (based on the ASF data) as well as HCR radar data. b) the comparison of the PSDs measured by CDP, 2D-S and PHIPS including statistical uncertainty bars $n^{-0.5}$ as discussed in Section 5.3. c) representative stereo micrographs of particles during that segment measured by PHIPS. 86
- 5.8. Same as in Fig. 5.7 but for a low-level droplet-dominated MPC during a transit leg of SOCRATES research flight RF07. All supercooled droplets (c) were sampled between 04:16:40 - 04:19:30, whereas the ice particles (d) were sampled between 04:19:30-04:21:00. 87
- 5.9. Same as in Fig. 5.7 and Fig. 5.8 but for a low-level MPC of SOCRATES research flight RF08. 88
- 6.1. Histograms of concentration (1) and water content (2) of droplets (blue) and ice (red) measured by the CDP (a), PHIPS (b) and 2D-S (c) during SOCRATES. 93
- 6.2. Histograms of concentration (1) and water content (2) of droplets (blue) and ice (red) measured by the SID-3 (a), PHIPS (b) and CIP (c) during ACLOUD, analogously to Fig. 6.1 for SOCRATES. 93
- 6.3. Frequency of occurrence of phase-fraction coefficient μ of cloud segments sampled during SOCRATES (a) and ACLOUD (b). The dashed vertical lines mark the $\mu_{liq} = 0.1$ and $\mu_{ice} = 0.9$ thresholds. The color-code corresponds to different temperature regions (note the logarithmic y-scale and the different temperature binning for SOCRATES and ACLOUD). 94
- 6.4. CPC for SOCRATES (a) and ACLOUD (b). The upper x-axis indicates the number of sampled cloud segments per temperature bin. The lowest temperature bin $-20 \leq T < -15^\circ\text{C}$ of ACLOUD has a low number of samples ($n = 85$) and is thus shown with faded colors. 95
- 6.5. (a) Relative frequency distribution of CPCs during SOCRATES taken from D'Alessandro et al. [2021]. The black line shows the number of cloud samples. (b) Relative CPCs based on LWC and IWC measured by the Nevzerov hot-wire probe during 5 in situ aircraft field campaigns over Canada, taken from Korolev et al. [2017]. 96
- 6.6. CPC of cloud segments of SOCRATES (a) and ACLOUD (b). The faded lines correspond to the linear fits through the data points from $-20 \leq T < +5^\circ\text{C}$. Fit parameters are shown in Table 6.1. Again, for ACLOUD, the lowest temperature bin is excluded due to the low number of measured cloud segments in this temperature regime. The dashed lines correspond to the parameterization from Mazin [2006]. 97
- 6.7. CPC for SOCRATES (a) and ACLOUD (b) identical to Fig. 6.4 (narrow solid bars) as well as the same analysis without taking PHIPS data into account (faded bars). 98

- 7.1. Histograms showing the absolute number of classified unrimed (blue) and rimed (red) particles during ACLOUD and SOCRATES as well as the riming fraction (relative percentage $n_{\text{rimed}}/n_{\text{all}}$, black, right axis) in correlation with different ambient parameters: Temperature (a), area-eq. diameter of the underlying ice particle measured by PHIPS (b), CDP LWC (c) and vertical HCR Doppler velocity (d). The red dotted line shows a fit to the riming fraction (see text). The corresponding fit parameters for all histograms are shown in Table 7.1. The statistical uncertainty bars correspond to the number of particles per bin ($n^{-1/2}$). Only bins with $n \geq 20$ are considered for the fit. Correlation plots with further parameters (CDP mean droplet diameter, ambient vertical velocity, relative cloud height, supersaturation with respect to ice), which show only a weak dependency are shown in Fig. A.3 in the Appendix. 102
- 7.2. Stereo image of one of the smallest particles that is conclusively classified as riming and showed no indication of shattering had an area equivalent diameter of $D_{\text{im,A}} = 116.1 \mu\text{m}$ and maximum dimension of $D_{\text{im,max}} = 193.7 \mu\text{m}$ (SOCRATES, RF12, #217). 103
- 7.3. Exemplary rimed particles showing the size of rimed droplets on the surface (a, b) and drizzle rimed ice (ice lollies, c, d). 103
- 7.4. Three exemplary one-sided rimed particles shown from different perspectives by the two camera telescope assemblies (CTA1 and CTA2). Note that the particle orientation in the stereo image does not reflect the orientation within the cloud. 104
- 7.5. Examples of (1) columnar particles and (2) plates with different degrees of riming depending on the SRD (unrimed (a, SRD = 0%), slightly rimed (b, $0\% < \text{SRD} < 25\%$), moderately rimed (c, $25\% \leq \text{SRD} \leq 50\%$), heavily rimed (d, $50\% < \text{SRD} \leq 100\%$) and graupel particle (e, $\text{SRD} \gg 100\%$). 105
- 7.6. The relative occurrence of particles of different SRD as defined in Fig. 7.5: slight (purple), moderate (yellow) and heavy riming (red) as well as graupel (blue) in correlation with ambient temperature (a), ice particle size (b), and HCR Doppler velocity (c) similar to Fig. 7.1a-c. The values on the upper x-axis correspond to the total number of particles per bin. 105
- 7.7. Exemplary rimed ice particles sampled during the IMPACTS campaign: "normally rimed" column (a), column with both normal and epitaxial riming (b), heavily epitaxially rimed columns (c, d) and a epitaxially rimed plate (e). 106
- 7.8. Absolute number of analyzed particles for normal (blue) and epitaxial (red) riming and fraction of epitaxially rimed particles as a function of ambient temperature (a), ice particle size (b) and HCR Doppler velocity (c). 107
- 7.9. Example of PHIPS data acquired in an MPC near the US east coast sampled during the IMPACTS campaign on February 1st, 2020. Left: overview of meteorological parameters, CDP LWC, 2D-S TWC, CDP and 2D-S number-weighted mean particle diameter and number of PHIPS images and total triggers. Right: representative PHIPS images of particles during the segment marked by the dashed black lines. The green shaded area marks a 45 s segment during which the four particles shown in Fig. 7.10 were acquired. 108
- 7.10. Schematic sketch of an epitaxially rimed column during different stages of the ageing process: unrimed (a), normally rimed (b), mixed (c), and epitaxially rimed column (d). The lower panel shows corresponding exemplary PHIPS images (#1309, #1325, #1320, and #1368) acquired within a 45 s segment in the presented case-study (shaded green area in Fig. 7.9). 109

7.11. Median ASF normalized by particle area (based on the image) of unrimed (blue), normally rimed (red) and epitaxially rimed (green) columns (a) and needles (b). The lower panel shows similar plots for unrimed (blue), slightly rimed (red), moderately rimed (green) and heavily rimed (purple) columns (c) and needles (d).	110
A.1. Average crosstalk intensity to neighbouring channels measured between the SOCRATES and IMPACTS campaign. The dashed black line marks 3%.	117
A.2. Comparison of 1a) an empty image (SOCRATES, RF04, #0003, CTA1) and 1b) the averaged intensity over images #1 to #999 of the same flight. 1c) shows the difference between 1a) and 1b). The lower panel (2a, 2b, 2c) shows the corresponding intensity histograms.	118
A.3. Histograms showing the absolute number of classified unrimed (blue) and rimed (red) particles during ACLOUD and SOCRATES as well as the relative percentage ($n_{\text{rimed}}/n_{\text{all}}$, black, right axis) in correlation with different ambient parameters: Temperature (a), area-eq. diameter of the underlying ice particle measured by PHIPS (b), CDP LWC (c), vertical HCR Doppler velocity (d), relative cloud height (e), and supersaturation with respect to ice (f), CDP mean droplet diameter (g), ambient vertical velocity (h). The red dotted line shows a fit to the percentage values. The statistical uncertainty bars correspond to the number of particles per bin ($n^{-1/2}$). Only bins with $n \geq 20$ are considered for the fits.	121
A.4. Correlation of surface riming degree with ambient parameters similar to Fig. A.3.	121
A.5. Correlation of the fraction of normally and epitactically rimed particles with ambient parameters similar to Fig. A.3.	121
A.6. Correlation of the fraction of one-sided rimed particles with ambient parameters similar to Fig. A.3.	122

List of Tables

2.1. Physical properties of water in different states at standard ambient conditions ($p_0 = 1,013.25$ hPa and $T = 0$ °C) [Feistel and Wagner, 2006; Hale and Query, 1973; Warren and Brandt, 2008].	7
4.1. Discrimination accuracy for different particle habits for the SOCRATES data set.	75
4.2. Classification accuracies for different ML approaches and different input information.	77
5.1. Averaging time that is needed until $n = 100$ particles are sampled as well as the total number of particles sampled during an averaging time of 30 s, calculated for the size bin of $20 \leq D < 200$ μm and exemplary particle concentrations.	85
6.1. Linear fit parameters for the CPC parameterization shown in Fig. 6.6 based on SOCRATES and ACLOUD as well as the parameterization from Mazin [2006].	97
7.1. Fit parameters to the riming percentage histograms shown in Fig. 7.1. . . .	103
7.2. Fit parameters to the riming percentage histograms shown in Fig. 7.8. . . .	107
A.1. Fit parameters of the Gaussian fits for the distribution of the feature parameters n_i	120
A.2. Fit parameters of the sigmoid fit for the discrimination probabilities P_i . . .	120

Publications in Peer Reviewed Journals

First author publications

1. **Waitz, F.**, Schnaiter, M., Leisner, T., and Järvinen, E.: PHIPS-HALO: the airborne Particle Habit Imaging and Polar Scattering probe – Part 3: Single-particle phase discrimination and particle size distribution based on the angular-scattering function, *Atmos. Meas. Tech.*, 14, 3049–3070, <https://doi.org/10.5194/amt-14-3049-2021>, 2021.
2. **Waitz, F.**, Schnaiter, M., Leisner, T., and Järvinen, E.: In-situ Observation of Riming in Mixed-Phase Clouds using the PHIPS probe, *Journal of the Atmospheric Sciences, in review*, 2021

Co-author publications

1. Finlon, J. A., Rauber, R. M., Wu, W., Zaremba, T. J., McFarquhar, G. M., Nesbitt, S. W., Schnaiter, M., Järvinen, E., **Waitz, F.**, Hill, T. C. J., DeMott, P. J.: Structure of an atmospheric river over Australia and the Southern Ocean: II. Microphysical evolution. *Journal of Geophysical Research: Atmospheres*, 125, e2020JD032514. <https://doi.org/10.1029/2020JD032514>, 2020.
2. Wang, Y., McFarquhar, G. M., Rauber, R. M., Zhao, C., Wu, W., Finlon, J. A., Stechman, D. M., Stith, J., Jensen, J. J., Schnaiter, M., Järvinen, E., **Waitz, F.**, Vivekanandan, J., Dixon, M., Rainwater, B., Toohey, D. W.: Microphysical properties of generating cells over the Southern Ocean: Results from SOCRATES. *Journal of Geophysical Research: Atmospheres*, 125, e2019JD032237. <https://doi.org/10.1029/2019JD032237>, 2020.
3. Järvinen, E., McCluskey, C. S., **Waitz, F.**, Schnaiter, M., Bansemer, A., Bardeen, C. G., Gettelman, A., Heymsfield, A., Stith, J., Wu, W., D'Allesandro, J. J., McFarquhar, G.G., Finlon, J. A., Hill, T. C. J., Levin, E. J. T., Moore, K., A., DeMott, P. J.: Evidence for Secondary Ice Production in Southern Ocean Maritime Boundary Layer Clouds, *Journal of Geophysical Research: Atmospheres, in review*, 2021
4. Lasher-Trapp, S., Scott, E. L., Schnaiter, M., Järvinen, E., **Waitz, F.**, DeMott, P. J., McCluskey, C. S., Hill, T. C. J.: Observations and Modeling of Rime-Splintering 1 in Southern Ocean Cumuli, *Journal of Geophysical Research: Atmospheres, in review*, 2021.
5. Järvinen, E., Van Dierenhoven, B., Magee, N., Neshyba, S., Schnaiter, M., Delene, D., Xu, G., **Waitz, F.**, Jourdan, S., Lolli, S., Kato, S.: Ice Crystal Complexity and Link to Cirrus Cloud Radiative Effect, *Journal of Geophysical Research: Atmospheres, in review*, 2021.

Bibliography

- A. Abdelmonem, E. Järvinen, D. Duft, E. Hirst, S. Vogt, T. Leisner, and M. Schnaiter. Phips–halo: the airborne particle habit imaging and polar scattering probe – part 1: Design and operation. *Atmospheric Measurement Techniques*, 9(7):3131–3144, 2016. doi: 10.5194/amt-9-3131-2016. URL <https://www.atmos-meas-tech.net/9/3131/2016/>.
- O. A. Alduchov and R. E. Eskridge. Improved magnus’ form approximation of saturation vapor pressure. 11 1997. doi: 10.2172/548871. URL <https://www.osti.gov/biblio/548871>.
- A. Ansmann, K. Ohneiser, R.-E. Mamouri, D. A. Knopf, I. Veselovskii, H. Baars, R. Engelmann, A. Foth, C. Jimenez, P. Seifert, and B. Barja. Tropospheric and stratospheric wildfire smoke profiling with lidar: mass, surface area, ccn, and inp retrieval. *Atmospheric Chemistry and Physics*, 21(12):9779–9807, 2021. doi: 10.5194/acp-21-9779-2021. URL <https://acp.copernicus.org/articles/21/9779/2021/>.
- R. Atlas, J. Mohrmann, J. Finlon, J. Lu, I. Hsiao, R. Wood, and M. Diao. The university of washington ice-liquid discriminator (uwild) improves single particle phase classifications of hydrometeors within southern ocean clouds using machine learning. *Atmospheric Measurement Techniques Discussions*, 2021:1–41, 2021. doi: 10.5194/amt-2021-123. URL <https://amt.copernicus.org/preprints/amt-2021-123/>.
- M. P. Bailey and J. Hallett. A comprehensive habit diagram for atmospheric ice crystals: Confirmation from the laboratory, airs ii, and other field studies. *Journal of the Atmospheric Sciences*, 66(9):2888 – 2899, 2009. doi: 10.1175/2009JAS2883.1. URL <https://journals.ametsoc.org/view/journals/atsc/66/9/2009jas2883.1.xml>.
- U. Baltensperger, M. Schwikowski, D. Jost, S. Nyeki, H. Gäggeler, and O. Poulida. Scavenging of atmospheric constituents in mixed phase clouds at the high-alpine site jungfraujoch part i: Basic concept and aerosol scavenging by clouds. *Atmospheric Environment*, 32(23): 3975–3983, 1998. ISSN 1352-2310. doi: [https://doi.org/10.1016/S1352-2310\(98\)00051-X](https://doi.org/10.1016/S1352-2310(98)00051-X). URL <https://www.sciencedirect.com/science/article/pii/S135223109800051X>.
- J. T. Bartlett. The growth of cloud droplets by coalescence. *Quarterly Journal of the Royal Meteorological Society*, 92(391):93–104, 1966. doi: <https://doi.org/10.1002/qj.49709239108>. URL <https://rmets.onlinelibrary.wiley.com/doi/abs/10.1002/qj.49709239108>.
- B. A. Baum, P. Yang, A. J. Heymsfield, C. G. Schmitt, Y. Xie, A. Bansemer, Y.-X. Hu, and Z. Zhang. Improvements in shortwave bulk scattering and absorption models for the remote sensing of ice clouds. *Journal of Applied Meteorology and Climatology*, 50(5): 1037–1056, 2011. doi: 10.1175/2010JAMC2608.1. URL <https://doi.org/10.1175/2010JAMC2608.1>.
- L. Bi, W. Lin, D. Liu, and K. Zhang. Assessing the depolarization capabilities of nonspherical particles in a super-ellipsoidal shape space. *Opt. Express*, 26(2):1726–1742, Jan 2018. doi: 10.1364/OE.26.001726. URL <http://www.opticsexpress.org/abstract.cfm?URI=oe-26-2-1726>.

- E. K. Bigg. Ice nucleus concentrations in remote areas. *J. Atmos. Sci.*, 30:1153–1157, 1973.
- N. Bjerrum. Structure and properties of ice. *Science*, 115(2989):385–390, 1952. ISSN 0036-8075. doi: 10.1126/science.115.2989.385. URL <https://science.sciencemag.org/content/115/2989/385>.
- U. Blahak and A. Seifert. Cosmo / clm / art training course, langen, march 2015, 2015. URL https://www.hzg.de/imperia/md/assets/clm/neu5_t13.pdf.
- C. F. Bohren and D. R. Huffman. *Appendix A: Homogeneous Sphere*, pages 477–482. John Wiley & Sons, Ltd, 1998. ISBN 9783527618156. doi: <https://doi.org/10.1002/9783527618156.app2>. URL <https://onlinelibrary.wiley.com/doi/abs/10.1002/9783527618156.app2>.
- R. T. Bruintjes, A. J. Heymsfield, and T. W. Krauss. An examination of double-plate ice crystals and the initiation of precipitation in continental cumulus clouds. *Journal of Atmospheric Sciences*, 44(9):1331 – 1350, 1987. doi: 10.1175/1520-0469(1987)044<1331:AEODPI>2.0.CO;2. URL https://journals.ametsoc.org/view/journals/atsc/44/9/1520-0469_1987_044_1331_aeodpi_2_0_co_2.xml.
- G. Bryant, J. Hallett, and B. Mason. The epitaxial growth of ice on single-crystalline substrates. *Journal of Physics and Chemistry of Solids*, 12(2):189–IN18, 1960. ISSN 0022-3697. doi: [https://doi.org/10.1016/0022-3697\(60\)90036-6](https://doi.org/10.1016/0022-3697(60)90036-6). URL <https://www.sciencedirect.com/science/article/pii/S0022369760900366>.
- S. M. Burrows, C. Hoose, U. Pöschl, and M. G. Lawrence. Ice nuclei in marine air: Biogenic particles or dust? *Atmos. Chem. Phys.*, 13:245–267, 2013.
- T. Choullarton, J. Latham, and B. Mason. A possible mechanism of ice splinter production during riming. *Nature: international weekly journal of science*, 274(5673):791–792, 1978. ISSN 0028-0836. doi: 10.1038/274791a0.
- S. Cober and G. Isaac. Aircraft icing environments observed in mixed-phase clouds. 01 2002. doi: 10.2514/6.2002-675.
- S. G. Cober, G. A. Isaac, A. V. Korolev, and J. W. Strapp. Assessing cloud-phase conditions. *Journal of Applied Meteorology*, 40(11):1967–1983, 2001. doi: 10.1175/1520-0450(2001)040<1967:ACPC>2.0.CO;2. URL [https://doi.org/10.1175/1520-0450\(2001\)040<1967:ACPC>2.0.CO;2](https://doi.org/10.1175/1520-0450(2001)040<1967:ACPC>2.0.CO;2).
- J. J. D’Alessandro, G. M. McFarquhar, W. Wu, J. L. Stith, J. B. Jensen, and R. M. Rauber. Characterizing the occurrence and spatial heterogeneity of liquid, ice, and mixed phase low-level clouds over the southern ocean using in situ observations acquired during socrates. *Journal of Geophysical Research: Atmospheres*, 126(11):e2020JD034482, 2021. doi: <https://doi.org/10.1029/2020JD034482>. URL <https://agupubs.onlinelibrary.wiley.com/doi/abs/10.1029/2020JD034482>. e2020JD034482 2020JD034482.
- B. Davies. What is the global volume of land ice and how is it changing?, 2020. URL <http://www.antarcticglaciers.org/glaciers-and-climate/what-is-the-global-volume-of-land-ice-and-how-is-it-changing/>.
- A. Ehrlich, M. Wendisch, C. Lüpkes, M. Buschmann, H. Bozem, D. Chechin, H.-C. Clemen, R. Dupuy, O. Eppers, J. Hartmann, A. Herber, E. Jäkel, E. Järvinen, O. Jourdan, U. Kästner, L.-L. Kliesch, F. Köllner, M. Mech, S. Mertes, R. Neuber, E. Ruiz-Donoso, M. Schnaiter, J. Schneider, J. Stapf, and M. Zanatta. Collection of data sources for the Arctic CLOUD Observations Using airborne measurements during polar Day (ACLOUD) campaign, North-West of Svalbard between 23 May - 26 June 2017, 2019. URL <https://doi.org/10.1594/PANGAEA.902603>.

- EOL. Socrates: Southern ocean clouds radiation aerosol transport experimental study., 2018a. URL <https://data.eol.ucar.edu/project/SOCRATES>.
- U. EOL. Ncar hcr radar and hsrl lidar moments data. version 1.0. ucar/ncar - earth observing laboratory, 2018b. URL <https://doi.org/10.5065/D64J0CZS>.
- J. Fan, S. Ghan, M. Ovchinnikov, X. Liu, P. J. Rasch, and A. Korolev. Representation of arctic mixed-phase clouds and the wegener-bergeron-findeisen process in climate models: Perspectives from a cloud-resolving study. *Journal of Geophysical Research: Atmospheres*, 116(D1), 2011a. doi: 10.1029/2010JD015375. URL <https://agupubs.onlinelibrary.wiley.com/doi/abs/10.1029/2010JD015375>.
- J. Fan, S. Ghan, M. Ovchinnikov, X. Liu, P. J. Rasch, and A. Korolev. Representation of arctic mixed-phase clouds and the wegener-bergeron-findeisen process in climate models: Perspectives from a cloud-resolving study. *Journal of Geophysical Research: Atmospheres*, 116(D1), 2011b. doi: <https://doi.org/10.1029/2010JD015375>. URL <https://agupubs.onlinelibrary.wiley.com/doi/abs/10.1029/2010JD015375>.
- T. Fawcett. An introduction to roc analysis. *Pattern Recognition Letters*, 27(8):861 – 874, 2006. ISSN 0167-8655. doi: <https://doi.org/10.1016/j.patrec.2005.10.010>. URL <http://www.sciencedirect.com/science/article/pii/S016786550500303X>. ROC Analysis in Pattern Recognition.
- R. Feistel and W. Wagner. A new equation of state for h2o ice ih. *Journal of Physical and Chemical Reference Data*, 35(2):1021–1047, 2006. doi: 10.1063/1.2183324. URL <https://doi.org/10.1063/1.2183324>.
- P. R. Field, R. Wood, P. R. A. Brown, P. H. Kaye, E. Hirst, R. Greenaway, and J. A. Smith. Ice particle interarrival times measured with a fast fssp. *Journal of Atmospheric and Oceanic Technology*, 20(2):249–261, 2003. doi: 10.1175/1520-0426(2003)020<0249:IPITMW>2.0.CO;2. URL [https://doi.org/10.1175/1520-0426\(2003\)020<0249:IPITMW>2.0.CO;2](https://doi.org/10.1175/1520-0426(2003)020<0249:IPITMW>2.0.CO;2).
- P. R. Field, R. J. Hogan, P. R. A. Brown, A. J. Illingworth, T. W. Chouarton, P. H. Kaye, E. Hirst, and R. Greenaway. Simultaneous radar and aircraft observations of mixed-phase cloud at the 100 m scale. *Quarterly Journal of the Royal Meteorological Society*, 130(600):1877–1904, 2004. doi: 10.1256/qj.03.102. URL <https://rmets.onlinelibrary.wiley.com/doi/abs/10.1256/qj.03.102>.
- P. R. Field, R. P. Lawson, P. R. A. Brown, G. Lloyd, C. Westbrook, D. Moisseev, A. Miltenberger, A. Nenes, A. Blyth, T. Chouarton, P. Connolly, J. Buehl, J. Crosier, Z. Cui, C. Dearden, P. DeMott, A. Flossmann, A. Heymsfield, Y. Huang, H. Kalesse, Z. A. Kanji, A. Korolev, A. Kirchgaessner, S. Lasher-Trapp, T. Leisner, G. McFarquhar, V. Phillips, J. Stith, and S. Sullivan. *Secondary Ice Production - current state of the science and recommendations for the future*, volume 58 of *Meteorological Monographs*, pages 7.1–7.20. American Meteorological Society, Boston (MA), 2017. doi: 10.1175/AMSMONOGRAPHS-D-16-0014.1.12.01.01; LK 01.
- W. Findeisen. Results of cloud and precipitation observations in weather reconnaissance flights over sea. *Forsch. Erfahr. Reichsamt Wetterdienst*, 8B:1–12, 1942.
- T. J. Garrett and S. E. Yuter. Observed influence of riming, temperature, and turbulence on the fallspeed of solid precipitation. *Geophysical Research Letters*, 41(18):6515–6522, 2014. doi: <https://doi.org/10.1002/2014GL061016>. URL <https://agupubs.onlinelibrary.wiley.com/doi/abs/10.1002/2014GL061016>.
- J.-F. Gayet, O. Crépel, J. Fournol, and S. Oshchepkov. A new airborne polar nephelometer for the measurements of optical and microphysical cloud properties. part i: Theoretical design. *Ann. Geophys.*, 15, 04 1997. doi: 10.1007/s00585-997-0451-1.

- A. Glen and S. D. Brooks. A new method for measuring optical scattering properties of atmospherically relevant dusts using the cloud and aerosol spectrometer with polarization (caspol). *Atmospheric Chemistry and Physics*, 13(3):1345–1356, 2013. doi: 10.5194/acp-13-1345-2013. URL <https://www.atmos-chem-phys.net/13/1345/2013/>.
- B. Guenther. *Modern Optics*. Oxford University Press, USA, 2 edition, 2015. ISBN 0198738773,9780198738770. URL <http://gen.lib.rus.ec/book/index.php?md5=079AC599D5C0803BA6C935DFEA93D728>.
- M. Haarig, A. Walser, A. Ansmann, M. Dollner, D. Althausen, D. Sauer, D. Farrell, and B. Weinzierl. Ccn concentration and inp-relevant aerosol profiles in the saharan air layer over barbados from polarization lidar and airborne in situ measurements. *Atmospheric Chemistry and Physics*, pages 1–24, 2019.
- G. M. Hale and M. R. Query. Optical constants of water in the 200-nm to 200- μ m wavelength region. *Appl. Opt.*, 12(3):555–563, 3 1973. doi: 10.1364/AO.12.000555. URL <http://ao.osa.org/abstract.cfm?URI=ao-12-3-555>.
- J. Hallet and S. C. Mossop. Production of secondary ice particles during the riming process. *Nature*, 249(5452):26–28, 1974. doi: <https://doi.org/10.1038/249026a0>. URL <https://rmets.onlinelibrary.wiley.com/doi/abs/10.1002/qj.49710042514>.
- J. Hallett and G. Isaac. *Aircraft icing in glaciated and mixed phase clouds*. 2002. doi: 10.2514/6.2002-677. URL <https://arc.aiaa.org/doi/abs/10.2514/6.2002-677>.
- J. Hallett and G. A. Isaac. Aircraft icing in glaciated and mixed phase clouds. *Journal of Aircraft*, 45(6):2120–2130, 2008. doi: 10.2514/1.37596. URL <https://doi.org/10.2514/1.37596>.
- S.-H. Ham, S. Kato, and F. G. Rose. Examining impacts of mass-diameter (m-d) and area-diameter (a-d) relationships of ice particles on retrievals of effective radius and ice water content from radar and lidar measurements. *Journal of Geophysical Research: Atmospheres*, 122(6):3396–3420, 2017. doi: <https://doi.org/10.1002/2016JD025672>. URL <https://agupubs.onlinelibrary.wiley.com/doi/abs/10.1002/2016JD025672>.
- J. Hansen, M. Sato, and R. Ruedy. Radiative forcing and climate response. *Journal of Geophysical Research: Atmospheres*, 102(D6):6831–6864, 1997. doi: <https://doi.org/10.1029/96JD03436>. URL <https://agupubs.onlinelibrary.wiley.com/doi/abs/10.1029/96JD03436>.
- T. Harimaya. The riming properties of snow crystals. *Journal of the Meteorological Society of Japan. Ser. II*, 53(6):384–392, 1975. doi: 10.2151/jmsj1965.53.6_384.
- D. A. Hegg, A. D. Clarke, S. J. Doherty, and J. Ström. Measurements of black carbon aerosol washout ratio on svalbard. *Tellus B*, 63(5):891–900, 2011. doi: <https://doi.org/10.1111/j.1600-0889.2011.00577.x>. URL <https://onlinelibrary.wiley.com/doi/abs/10.1111/j.1600-0889.2011.00577.x>.
- P. H. Herzegh and P. V. Hobbs. The mesoscale and microscale structure and organization of clouds and precipitation in midlatitude cyclones. ii: Warm-frontal clouds. *Journal of Atmospheric Sciences*, 37(3):597 – 611, 1980. doi: 10.1175/1520-0469(1980)037<0597:TMAMSA>2.0.CO;2. URL https://journals.ametsoc.org/view/journals/atsc/37/3/1520-0469_1980_037_0597_tmamsa_2_0_co_2.xml.
- E. Hirst and P. Kaye. Experimental and theoretical light scattering profiles from spherical and nonspherical particles. *Journal of Geophysical Research*, 101:19231–19236, 08 1996. doi: 10.1029/95JD02343.

- A. F. Holleman and N. Wiberg. *Lehrbuch der Anorganischen Chemie*. de Gruyter, 102 edition, 2007.
- E. Holroyd. Some techniques and uses of 2d-c habit classification software for snow particles. *Journal of Atmospheric and Oceanic Technology*, 4:498–511, 1987.
- C. Hoose and O. Möhler. Heterogeneous ice nucleation on atmospheric aerosols: a review of results from laboratory experiments. *Atmospheric Chemistry and Physics*, 12(20): 9817–9854, 2012. doi: 10.5194/acp-12-9817-2012. URL <https://acp.copernicus.org/articles/12/9817/2012/>.
- Y. Huang, T. Chubb, D. Baumgardner, M. deHoog, S. T. Siems, and M. J. Manton. Evidence for secondary ice production in southern ocean open cellular convection. *Quarterly Journal of the Royal Meteorological Society*, 143(704):1685–1703, 2017. doi: <https://doi.org/10.1002/qj.3041>. URL <https://rmets.onlinelibrary.wiley.com/doi/abs/10.1002/qj.3041>.
- D. M. Hueholt, S. E. Yuter, and M. A. Miller. Revisiting diagrams of ice growth environments. *Submitted to the Bulletin of the American Meteorological Society*, 2020. URL http://www.environmentanalytics.com/pdfs/20201102_Hueholtetal_BAMS_submitted_forweb.pdf.
- IPCC. Climate change 2021: The physical science basis. contribution of working group i to the sixth assessment report of the intergovernmental panel on climate change. 2021. doi: 10.1126/science.aaf7271. In Press.
- E. Järvinen, O. Jourdan, D. Neubauer, B. Yao, C. Liu, M. O. Andreae, U. Lohmann, M. Wendisch, G. M. McFarquhar, T. Leisner, and M. Schnaiter. Additional global climate cooling by clouds due to ice crystal complexity. *Atmospheric Chemistry and Physics*, 18(21):15767–15781, 2018. doi: 10.5194/acp-18-15767-2018. URL <https://www.atmos-chem-phys.net/18/15767/2018/>.
- O. Jourdan, S. Oshchepkov, J.-F. Gayet, V. Shcherbakov, and H. Isaka. Statistical analysis of cloud light scattering and microphysical properties obtained from airborne measurements. *Journal of Geophysical Research*, 108(D5), 2003. doi: 10.1029/2002jd002723. URL <https://hal.archives-ouvertes.fr/hal-01982541>.
- E. Järvinen, M. Schnaiter, G. Mioche, O. Jourdan, V. N. Shcherbakov, A. Costa, A. Afchine, M. Krämer, F. Heidelberg, T. Jurkat, C. Voigt, H. Schlager, L. Nichman, M. Gallagher, E. Hirst, C. Schmitt, A. Bansemer, A. Heymsfield, P. Lawson, U. Tricoli, K. Pfeilsticker, P. Vochezer, O. Möhler, and T. Leisner. Quasi-spherical ice in convective clouds. *Journal of the Atmospheric Sciences*, 73(10):3885–3910, 2016. doi: 10.1175/JAS-D-15-0365.1. URL <https://doi.org/10.1175/JAS-D-15-0365.1>.
- E. Järvinen, C. S. McCluskey, F. Waitz, M. Schnaiter, A. Bansemer, C. G. Bardeen, A. Gettelman, A. Heymsfield, J. Stith, W. Wu, J. J. D’Allesandro, G. McFarquhar, J. A. Finlon, T. C. J. Hill, E. J. T. Levin, K. Moore, A., and P. J. DeMott. Evidence for secondary ice production in southern ocean maritime boundary layer clouds. *Journal of the Atmospheric Sciences*, 2021a. in review.
- E. Järvinen, B. Van Dierenhoven, N. Magee, S. Neshyba, M. Schnaiter, D. Delene, G. Xu, F. Waitz, S. Jourdan, S. Lolli, and S. Kato. Ice crystal complexity and link to cirrus cloud radiative effect. *Journal of Geophysical Research: Atmospheres*, 2021, 2021b. in review.
- P. H. Kaye, E. Hirst, R. S. Greenaway, Z. Ulanowski, E. Hesse, P. J. DeMott, C. Saunders, and P. Connolly. Classifying atmospheric ice crystals by spatial light scattering. *Opt. Lett.*, 33(13):1545–1547, 7 2008. doi: 10.1364/OL.33.001545. URL <http://ol.osa.org/abstract.cfm?URI=ol-33-13-1545>.

- A. Keinert, D. Spannagel, T. Leisner, and A. Kiselev. Secondary ice production upon freezing of freely falling drizzle droplets. *Journal of the Atmospheric Sciences*, 77(8):2959 – 2967, 2020. doi: 10.1175/JAS-D-20-0081.1. URL <https://journals.ametsoc.org/view/journals/atsc/77/8/jasD200081.xml>.
- S. C. Keppas, J. Crosier, T. W. Choulaton, and K. N. Bower. Ice lollies: An ice particle generated in supercooled conveyor belts. *Geophysical Research Letters*, 44(10):5222–5230, 2017. doi: <https://doi.org/10.1002/2017GL073441>. URL <https://agupubs.onlinelibrary.wiley.com/doi/abs/10.1002/2017GL073441>.
- K. Kikuchi and H. Uyeda. Cloud droplets and rain drops collected and frozen on natural snow crystals. *Journal of the Meteorological Society of Japan. Ser. II*, 57(3):273–281, 1979. doi: 10.2151/jmsj1965.57.3_273.
- W. D. King, D. A. Parkin, and R. J. Handsworth. A hot-wire liquid water device having fully calculable response characteristics. *Journal of Applied Meteorology and Climatology*, 17(12):1809 – 1813, 1978. doi: 10.1175/1520-0450(1978)017<1809:AHWLWD>2.0.CO;2. URL https://journals.ametsoc.org/view/journals/apme/17/12/1520-0450_1978_017_1809_ahwld_2_0_co_2.xml.
- A. Kiselev, F. Bachmann, P. Pedevilla, S. J. Cox, A. Michaelides, D. Gerthsen, and T. Leisner. Active sites in heterogeneous ice nucleation—the example of k-rich feldspars. *Science*, 2016. ISSN 0036-8075. doi: 10.1126/science.aai8034. URL <https://science.sciencemag.org/content/early/2016/12/07/science.aai8034>.
- S. Kneifel and D. Moisseev. Long-term statistics of riming in nonconvective clouds derived from ground-based doppler cloud radar observations. *Journal of the Atmospheric Sciences*, 77(10):3495 – 3508, 2020. doi: 10.1175/JAS-D-20-0007.1. URL <https://journals.ametsoc.org/view/journals/atsc/77/10/jasD200007.xml>.
- E. M. Knudsen, B. Heinold, S. Dahlke, H. Bozem, S. Crewell, I. V. Gorodetskaya, G. Heygster, D. Kunkel, M. Maturilli, M. Mech, C. Viceto, A. Rinke, H. Schmithüsen, A. Ehrlich, A. Macke, C. Lüpkes, and M. Wendisch. Meteorological conditions during the acloud/pascal field campaign near svalbard in early summer 2017. *Atmospheric Chemistry and Physics*, 18(24):17995–18022, 2018. doi: 10.5194/acp-18-17995-2018. URL <https://www.atmos-chem-phys.net/18/17995/2018/>.
- H. König. Eine kubische eismodifikation. 105(1-6):279–286, 1943. doi: doi:10.1524/zkri.1943.105.1.279. URL <https://doi.org/10.1524/zkri.1943.105.1.279>.
- T. Koop and B. J. Murray. A physically constrained classical description of the homogeneous nucleation of ice in water. *The Journal of Chemical Physics*, 145(21):211915, 2016. doi: 10.1063/1.4962355. URL <https://doi.org/10.1063/1.4962355>.
- A. Korolev. Limitations of the wegener–bergeron–findeisen mechanism in the evolution of mixed-phase clouds. *Journal of the Atmospheric Sciences*, 64(9):3372 – 3375, 2007a. doi: 10.1175/JAS4035.1. URL <https://journals.ametsoc.org/view/journals/atsc/64/9/jas4035.1.xml>.
- A. Korolev. Reconstruction of the sizes of spherical particles from their shadow images. part i: Theoretical considerations. *Journal of Atmospheric and Oceanic Technology - J ATMOS OCEAN TECHNOL*, 24, 03 2007b. doi: 10.1175/JTECH1980.1.
- A. Korolev and G. Isaac. Phase transformation of mixed-phase clouds. *Quarterly Journal of the Royal Meteorological Society*, 129(587):19–38, 2003. doi: <https://doi.org/10.1256/qj.01.203>. URL <https://rmets.onlinelibrary.wiley.com/doi/abs/10.1256/qj.01.203>.
- A. Korolev, G. McFarquhar, P. R. Field, C. Franklin, P. Lawson, Z. Wang, E. Williams, S. J. Abel, D. Axisa, S. Borrmann, J. Crosier, J. Fugal, M. Krämer, U. Lohmann, O. Schlenczek,

- M. Schnaiter, and M. Wendisch. Mixed-phase clouds: Progress and challenges. *Meteorological Monographs*, 58:5.1–5.50, 2017. doi: 10.1175/AMSMONOGRAPHIS-D-17-0001.1. URL <https://doi.org/10.1175/AMSMONOGRAPHIS-D-17-0001.1>.
- A. Korolev, I. Heckman, M. Wolde, A. S. Ackerman, A. M. Fridlind, L. A. Ladino, R. P. Lawson, J. Milbrandt, and E. Williams. A new look at the environmental conditions favorable to secondary ice production. *Atmospheric Chemistry and Physics*, 20(3):1391–1429, 2020. doi: 10.5194/acp-20-1391-2020. URL <https://acp.copernicus.org/articles/20/1391/2020/>.
- A. V. Korolev, J. W. Strapp, G. A. Isaac, and A. N. Nevzorov. The nevezorov airborne hot-wire lwc–twc probe: Principle of operation and performance characteristics. *Journal of Atmospheric and Oceanic Technology*, 15(6):1495 – 1510, 1998. doi: 10.1175/1520-0426(1998)015<1495:TNAHWL>2.0.CO;2. URL https://journals.ametsoc.org/view/journals/atot/15/6/1520-0426_1998_015_1495_tnahwl_2_0_co_2.xml.
- A. V. Korolev, G. A. Isaac, S. G. Cober, J. W. Strapp, and J. Hallett. Microphysical characterization of mixed-phase clouds. *Quarterly Journal of the Royal Meteorological Society*, 129(587):39–65, 2003. doi: <https://doi.org/10.1256/qj.01.204>. URL <https://rmets.onlinelibrary.wiley.com/doi/abs/10.1256/qj.01.204>.
- R. Kumari and S. Srivastava. Machine learning: A review on binary classification. *International Journal of Computer Applications*, 160:11–15, 02 2017. doi: 10.5120/ijca2017913083.
- C. Kwak and A. Clayton-Matthews. Multinomial logistic regression. *Nursing Research*, 51(6), 2002. ISSN 0029-6562. URL https://journals.lww.com/nursingresearchonline/Fulltext/2002/11000/Multinomial_Logistic_Regression.9.aspx.
- A. Lauber, A. Kiselev, T. Pander, P. Handmann, and T. Leisner. Secondary ice formation during freezing of levitated droplets. *Journal of the Atmospheric Sciences*, 75(8):2815–2826, 2018. doi: 10.1175/JAS-D-18-0052.1. URL <https://doi.org/10.1175/JAS-D-18-0052.1>.
- R. P. Lawson, B. A. Baker, C. G. Schmitt, and T. L. Jensen. An overview of microphysical properties of arctic clouds observed in may and july 1998 during fire ace. *Journal of Geophysical Research: Atmospheres*, 106(D14):14989–15014, 2001. doi: <https://doi.org/10.1029/2000JD900789>. URL <https://agupubs.onlinelibrary.wiley.com/doi/abs/10.1029/2000JD900789>.
- R. P. Lawson, D. O’Connor, P. Zmarzly, K. Weaver, B. Baker, Q. Mo, and H. Jonsson. The 2d-s (stereo) probe: Design and preliminary tests of a new airborne, high-speed, high-resolution particle imaging probe. *Journal of Atmospheric and Oceanic Technology*, 23(11):1462 – 1477, 2006. doi: 10.1175/JTECH1927.1. URL https://journals.ametsoc.org/view/journals/atot/23/11/jtech1927_1.xml.
- R. P. Lawson, S. Woods, E. Jensen, E. Erfani, C. Gurganus, M. Gallagher, P. Connolly, J. Whiteway, A. J. Baran, P. May, A. Heymsfield, C. G. Schmitt, G. McFarquhar, J. Um, A. Protat, M. Bailey, S. Lance, A. Muehlbauer, J. Stith, A. Korolev, O. B. Toon, and M. Krämer. A review of ice particle shapes in cirrus formed in situ and in anvils. *Journal of Geophysical Research: Atmospheres*, 124(17-18):10049–10090, 2019. doi: <https://doi.org/10.1029/2018JD030122>. URL <https://agupubs.onlinelibrary.wiley.com/doi/abs/10.1029/2018JD030122>.
- J. Leinonen and W. Szyrmer. Radar signatures of snowflake riming: A modeling study. *Earth and Space Science*, 2(8):346–358, 2015. doi: <https://doi.org/10.1002/2015EA000102>. URL <https://agupubs.onlinelibrary.wiley.com/doi/abs/10.1002/2015EA000102>.

- J. Leinonen, M. D. Lebsock, S. Tanelli, O. O. Sy, B. Dolan, R. J. Chase, J. A. Finlon, A. von Lerber, and D. Moisseev. Retrieval of snowflake microphysical properties from multifrequency radar observations. *Atmospheric Measurement Techniques*, 11(10): 5471–5488, 2018. doi: 10.5194/amt-11-5471-2018. URL <https://amt.copernicus.org/articles/11/5471/2018/>.
- K. Libbrecht. *Ken Libbrecht's Field Guide to Snowflakes*. Voyageur Press, 2016. ISBN 9781616739478. URL <https://books.google.de/books?id=e0v83aUg0vwC>.
- K. Libbrecht, C. Miller, R. Potter, N. Budaeva, C. Lemon, and S. Thomas. Toward a comprehensive model of snow crystal growth: 4. measurements of diffusion-limited growth at -15 c. 12 2015.
- K. G. Libbrecht. The physics of snow crystals. *Reports on Progress in Physics*, 68(4): 855–895, 3 2005. doi: 10.1088/0034-4885/68/4/r03. URL <https://doi.org/10.1088/0034-4885/68/4/r03>.
- Y. Lin, L. Donner, and B. Colle. Parameterization of riming intensity and its impact on ice fall speed using arm data. *Monthly Weather Review - MON WEATHER REV*, 139: 1036–1047, 03 2011. doi: 10.1175/2010MWR3299.1.
- H. Lindqvist, K. Muinonen, T. Nousiainen, J. Um, G. Mcfarquhar, P. Haapanala, R. Makkonen, and H. Laakso. Ice-cloud particle habit classification using principal components. *Journal of Geophysical Research*, 117, 08 2012. doi: 10.1029/2012JD017573.
- K.-n. Liou and H. Lahore. Laser sensing of cloud composition: A backscattered depolarization technique. *Journal of Applied Meteorology and Climatology*, 13 (2):257 – 263, 1974. doi: 10.1175/1520-0450(1974)013<0257:LSOCCA>2.0.CO;2. URL https://journals.ametsoc.org/view/journals/apme/13/2/1520-0450_1974_013_0257_lsocca_2_0_co_2.xml.
- K.-N. Liou and R. M. Schotland. Multiple backscattering and depolarization from water clouds for a pulsed lidar system. *J. Atmos. Sci.*, 28:772–784, 1971. doi: 10.1175/1520-0469(1971)028%3C0772%3AMBADFW%3E2.0.CO;2.
- J. D. Locatelli and P. V. Hobbs. Fall speeds and masses of solid precipitation particles. *Journal of Geophysical Research (1896-1977)*, 79(15):2185–2197, 1974. doi: <https://doi.org/10.1029/JC079i015p02185>. URL <https://agupubs.onlinelibrary.wiley.com/doi/abs/10.1029/JC079i015p02185>.
- U. Lohmann and C. Hoose. Sensitivity studies of different aerosol indirect effects in mixed-phase clouds. *Atmospheric Chemistry and Physics*, 9(22):8917–8934, 2009. doi: 10.5194/acp-9-8917-2009. URL <https://www.atmos-chem-phys.net/9/8917/2009/>.
- A. Macke, J. Mueller, and E. Raschke. Single scattering properties of atmospheric ice crystals. *Journal of Atmospheric Sciences*, 53(19):2813 – 2825, 1996a. doi: 10.1175/1520-0469(1996)053<2813:SSPOAI>2.0.CO;2. URL https://journals.ametsoc.org/view/journals/atsc/53/19/1520-0469_1996_053_2813_sspoi_2_0_co_2.xml.
- A. Macke, J. Mueller, and E. Raschke. Single scattering properties of atmospheric ice crystals. *Journal of Atmospheric Sciences*, 53(19):2813 – 2825, 1996b. doi: 10.1175/1520-0469(1996)053<2813:SSPOAI>2.0.CO;2. URL https://journals.ametsoc.org/view/journals/atsc/53/19/1520-0469_1996_053_2813_sspoi_2_0_co_2.xml.
- C. Magono and H. Aburakawa. Experimental studies on snow crystals of plane type with spatial branches. *Journal of the Faculty of Science, Hokkaido University. Series 7, Geophysics*, 3(2):85–97, 3 1969. URL <http://hdl.handle.net/2115/8680>.

- C. Magono and C. W. Lee. Meteorological classification of natural snow crystals. *Journal of the Faculty of Science, Hokkaido University. Series 7, Geophysics*, 2(4):321–335, nov 1966. URL <http://hdl.handle.net/2115/8672>.
- F. Mahrt, J. Wieder, R. Dietlicher, H. R. Smith, C. Stopford, and Z. A. Kanji. A high-speed particle phase discriminator (ppd-hs) for the classification of airborne particles, as tested in a continuous flow diffusion chamber. *Atmospheric Measurement Techniques*, 12(6):3183–3208, 2019. doi: 10.5194/amt-12-3183-2019. URL <https://www.atmos-meas-tech.net/12/3183/2019/>.
- S. L. Mason, C. J. Chiu, R. J. Hogan, D. Moisseev, and S. Kneifel. Retrievals of riming and snow density from vertically pointing doppler radars. *Journal of Geophysical Research: Atmospheres*, 123(24):13,807–13,834, 2018. doi: <https://doi.org/10.1029/2018JD028603>. URL <https://agupubs.onlinelibrary.wiley.com/doi/abs/10.1029/2018JD028603>.
- A. V. Matus and T. S. L'Ecuyer. The role of cloud phase in earth's radiation budget. *Journal of Geophysical Research: Atmospheres*, 122(5):2559–2578, 2017. doi: <https://doi.org/10.1002/2016JD025951>. URL <https://agupubs.onlinelibrary.wiley.com/doi/abs/10.1002/2016JD025951>.
- J. C. Maxwell. Viii. a dynamical theory of the electromagnetic field. *Philosophical Transactions of the Royal Society of London*, 155:459–512, 1865. doi: 10.1098/rstl.1865.0008. URL <https://royalsocietypublishing.org/doi/abs/10.1098/rstl.1865.0008>.
- I. P. Mazin. Cloud phase structure: Experimental data analysis and parameterization. *Journal of the Atmospheric Sciences*, 63(2):667 – 681, 2006. doi: 10.1175/JAS3660.1. URL <https://journals.ametsoc.org/view/journals/atsc/63/2/jas3660.1.xml>.
- I. P. Mazin, A. V. Korolev, A. Heymsfield, G. A. Isaac, and S. G. Cober. Thermodynamics of icing cylinder for measurements of liquid water content in supercooled clouds. *Journal of Atmospheric and Oceanic Technology*, 18(4):543 – 558, 2001. doi: 10.1175/1520-0426(2001)018<0543:TOICFM>2.0.CO;2. URL https://journals.ametsoc.org/view/journals/atot/18/4/1520-0426_2001_018_0543_toicfm_2_0_co_2.xml.
- D. T. McCoy, I. Tan, D. L. Hartmann, M. D. Zelinka, and T. Storelvmo. On the relationships among cloud cover, mixed-phase partitioning, and planetary albedo in gcms. *Journal of Advances in Modeling Earth Systems*, 8(2):650–668, 2016. doi: 10.1002/2015MS000589. URL <https://agupubs.onlinelibrary.wiley.com/doi/abs/10.1002/2015MS000589>.
- G. M. McFarquhar, J. Um, and R. Jackson. Small cloud particle shapes in mixed-phase clouds. *Journal of Applied Meteorology and Climatology*, 52(5):1277–1293, 2013. doi: 10.1175/JAMC-D-12-0114.1. URL <https://doi.org/10.1175/JAMC-D-12-0114.1>.
- G. M. McFarquhar, J. A. Finlon, D. M. Stechman, W. Wu, R. C. Jackson, and M. Freer. University of Illinois/Oklahoma Optical Array Probe (OAP) Processing Software, June 2018. URL <https://doi.org/10.5281/zenodo.1285969>.
- G. M. McFarquhar, C. Bretherton, R. Marchand, P. J. DeMott, A. Protat, S. P. Alexander, S. R. Rintoul, G. Roberts, C. H. Twohy, D. W. Toohey, S. Siems, Y. Huang, R. Wood, R. M. Rauber, S. Lasher-Trapp, J. Jensen, J. L. Stith, J. Mace, J. UM, E. Järvinen, M. Schnaiter, A. Gettelman, K. J. Sanchez, C. McClusky, I. L. McCoy, K. A. Moore, T. C. J. Hill, and B. Rainwater. Airborne, ship-, and ground-based observations of clouds, aerosols, and precipitation from recent field projects over the southern ocean. *99th annual meeting, American Meteorological Society*, 2019. URL <https://ams.confex.com/ams/2019Annual/meetingapp.cgi/Paper/350863>.

- G. M. McFarquhar, C. S. Bretherton, R. Marchand, A. Protat, P. J. DeMott, S. P. Alexander, G. C. Roberts, C. H. Twohy, D. Toohey, S. Siems, Y. Huang, R. Wood, R. M. Rauber, S. Lasher-Trapp, J. Jensen, J. L. Stith, J. Mace, J. Um, E. Järvinen, M. Schnaiter, A. Gettelman, K. J. Sanchez, C. S. McCluskey, L. M. Russell, I. L. McCoy, R. L. Atlas, C. G. Bardeen, K. A. Moore, T. C. J. Hill, R. S. Humphries, M. D. Keywood, Z. Ristovski, L. Cravigan, R. Schofield, C. Fairall, M. D. Mallet, S. M. Kreidenweis, B. Rainwater, J. D'Alessandro, Y. Wang, W. Wu, G. Saliba, E. J. T. Levin, S. Ding, F. Lang, S. C. H. Truong, C. Wolff, J. Haggerty, M. J. Harvey, A. R. Klekociuk, and A. McDonald. Observations of clouds, aerosols, precipitation, and surface radiation over the southern ocean: An overview of capricorn, marcus, micre, and socrates. *Bulletin of the American Meteorological Society*, 2021(102(4)):E894–E928, 2021. doi: 10.1175/BAMS-D-20-0132.1. URL <https://journals.ametsoc.org/view/journals/bams/102/4/BAMS-D-20-0132.1.xml>.
- L. McMurdie, G. Heymsfield, J. Yorks, and S. Braun. Investigation of microphysics and precipitation for atlantic coast-threatening snowstorms (impacts) collection., 2019. URL <http://dx.doi.org/10.5067/IMPACTS/DATA101>.
- Michell Instruments Ltd. Humidity calculatr v1.08, 2015. URL <http://www.michell.com/de/calculator/>.
- Y. Mizuno. Epitaxial freezing of supercooled droplets on ice surfaces. *Contributions from the Institute of Low Temperature Science*, A33:1–27, mar 1984. URL <http://hdl.handle.net/2115/20248>.
- Y. Mizuno and G. Wakahama. Structure and orientation of frozen droplets on ice surfaces. *The Journal of Physical Chemistry*, 87(21):4161–4167, 1983. doi: 10.1021/j100244a037. URL <https://doi.org/10.1021/j100244a037>.
- D. Moisseev, A. von Lerber, and J. Tiira. Quantifying the effect of riming on snowfall using ground-based observations. *Journal of Geophysical Research: Atmospheres*, 122(7): 4019–4037, 2017. doi: <https://doi.org/10.1002/2016JD026272>. URL <https://agupubs.onlinelibrary.wiley.com/doi/abs/10.1002/2016JD026272>.
- A. Morbidelli, J. Chambers, J. I. Lunine, J. M. Petit, F. Robert, G. B. Valsecchi, and K. E. Cyr. Source regions and timescales for the delivery of water to the earth. *Meteoritics & Planetary Science*, 35(6):1309–1320, 2000. doi: <https://doi.org/10.1111/j.1945-5100.2000.tb01518.x>. URL <https://onlinelibrary.wiley.com/doi/abs/10.1111/j.1945-5100.2000.tb01518.x>.
- L. Mosimann. An improved method for determining the degree of snow crystal riming by vertical doppler radar. *Atmospheric Research*, 37(4):305–323, 1995. ISSN 0169-8095. doi: [https://doi.org/10.1016/0169-8095\(94\)00050-N](https://doi.org/10.1016/0169-8095(94)00050-N). URL <https://www.sciencedirect.com/science/article/pii/016980959400050N>.
- L. Mosimann, M. Steiner, J. Collett, and et al. Ice crystal observations and the degree of riming in winter precipitation. *Water Air Soil Pollution*, 68:29–42, 1993. doi: <https://doi.org/10.1007/BF00479391>.
- L. Mosimann, E. Weingartner, and A. Waldvogel. An analysis of accreted drop sizes and mass on rimed snow crystals. *Journal of Atmospheric Sciences*, 51(11):1548 – 1558, 1994. doi: 10.1175/1520-0469(1994)051<1548:AAOADS>2.0.CO;2. URL https://journals.ametsoc.org/view/journals/atsc/51/11/1520-0469_1994_051_1548_aoads_2_0_co_2.xml.
- S. C. Mossop. The mechanism of ice splinter production during riming. *Geophysical Research Letters*, 7(2):167–169, 1980. doi: <https://doi.org/10.1029/GL007i002p00167>. URL <https://agupubs.onlinelibrary.wiley.com/doi/abs/10.1029/GL007i002p00167>.

- D. M. Murphy and T. Koop. Review of the vapour pressures of ice and supercooled water for atmospheric applications. *Quarterly Journal of the Royal Meteorological Society*, 131(608):1539–1565, 2005. doi: <https://doi.org/10.1256/qj.04.94>. URL <https://rmets.onlinelibrary.wiley.com/doi/abs/10.1256/qj.04.94>.
- B. J. Murray. Enhanced formation of cubic ice in aqueous organic acid droplets. *Environmental Research Letters*, 3(2):025008, 4 2008. doi: [10.1088/1748-9326/3/2/025008](https://doi.org/10.1088/1748-9326/3/2/025008). URL <https://doi.org/10.1088/1748-9326/3/2/025008>.
- O. Möhler, A. Nink, H. Saathoff, S. Schaefers, M. Schnaiter, W. Schöck, and U. Schurath. The Karlsruhe aerosol chamber facility AIDA: technical description and first results of homogeneous and heterogeneous ice nucleation experiments. 2001. doi: [10.5170/CERN-2001-007.163](https://doi.org/10.5170/CERN-2001-007.163). URL <http://cds.cern.ch/record/557580>.
- L. Nichman, C. Fuchs, E. Järvinen, K. Ignatius, N. F. Höppel, A. Dias, M. Heinritzi, M. Simon, J. Tröstl, A. C. Wagner, R. Wagner, C. Williamson, C. Yan, P. J. Connolly, J. R. Dorsey, J. Duplissy, S. Ehrhart, C. Frege, H. Gordon, C. R. Hoyle, T. B. Kristensen, G. Steiner, N. McPherson, Donahue, R. Flagan, M. W. Gallagher, J. Kirkby, O. Möhler, H. Saathoff, M. Schnaiter, F. Stratmann, and A. Tomé. Phase transition observations and discrimination of small cloud particles by light polarization in expansion chamber experiments. *Atmospheric Chemistry and Physics*, 16(5):3651–3664, 2016. doi: [10.5194/acp-16-3651-2016](https://doi.org/10.5194/acp-16-3651-2016). URL <https://www.atmos-chem-phys.net/16/3651/2016/>.
- NOAA. Extreme weather events on climate.gov, 2021. URL <https://www.climate.gov/news-features/category/extreme-events>.
- A. Ono. The shape and riming properties of ice crystals in natural clouds. *Journal of Atmospheric Sciences*, 26(1):138 – 147, 1969. doi: [10.1175/1520-0469\(1969\)026<0138:TSARPO>2.0.CO;2](https://doi.org/10.1175/1520-0469(1969)026<0138:TSARPO>2.0.CO;2). URL https://journals.ametsoc.org/view/journals/atsc/26/1/1520-0469_1969_026_0138_tsarpo_2_0_co_2.xml.
- M. Ovchinnikov, A. S. Ackerman, A. Avramov, A. Cheng, J. Fan, A. M. Fridlind, S. Ghan, J. Harrington, C. Hoose, A. Korolev, G. M. McFarquhar, H. Morrison, M. Paukert, J. Savre, B. J. Shipway, M. D. Shupe, A. Solomon, and K. Sulia. Intercomparison of large-eddy simulations of arctic mixed-phase clouds: Importance of ice size distribution assumptions. *Journal of Advances in Modeling Earth Systems*, 6(1):223–248, 2014. doi: <https://doi.org/10.1002/2013MS000282>. URL <https://agupubs.onlinelibrary.wiley.com/doi/abs/10.1002/2013MS000282>.
- D. Pashley. The study of epitaxy in thin surface films. *Advances in Physics*, 5(18):173–240, 1956. doi: [10.1080/00018735600101175](https://doi.org/10.1080/00018735600101175). URL <https://doi.org/10.1080/00018735600101175>.
- W. Peppler. Unterkühlte wasserwolken und eiswolken (supercooled water clouds and ice clouds), 1940.
- M. D. Petters, A. J. Prenni, S. M. Kreidenweis, and P. J. DeMott. On measuring the critical diameter of cloud condensation nuclei using mobility selected aerosol. *Aerosol Science and Technology*, 41(10):907–913, 2007. doi: [10.1080/02786820701557214](https://doi.org/10.1080/02786820701557214). URL <https://doi.org/10.1080/02786820701557214>.
- V. T. J. Phillips, S. Patade, J. Gutierrez, and A. Bansemer. Secondary ice production by fragmentation of freezing drops: Formulation and theory. *Journal of the Atmospheric Sciences*, 75(9):3031 – 3070, 2018. doi: [10.1175/JAS-D-17-0190.1](https://doi.org/10.1175/JAS-D-17-0190.1). URL <https://journals.ametsoc.org/view/journals/atsc/75/9/jas-d-17-0190.1.xml>.
- J. O. Pinto. Autumnal mixed-phase cloudy boundary layers in the arctic. *Journal of the Atmospheric Sciences*, 55(11):2016–2038, 1998. doi: [10.1175/1520-0469\(1998\)055<2016:](https://doi.org/10.1175/1520-0469(1998)055<2016:)

- AMPCBL>2.0.CO;2. URL [https://doi.org/10.1175/1520-0469\(1998\)055<2016:AMPCBL>2.0.CO;2](https://doi.org/10.1175/1520-0469(1998)055<2016:AMPCBL>2.0.CO;2).
- C. Praz, S. Ding, G. M. McFarquhar, and A. Berne. A versatile method for ice particle habit classification using airborne imaging probe data. *Journal of Geophysical Research: Atmospheres*, 123(23):13,472–13,495, 2018. doi: <https://doi.org/10.1029/2018JD029163>. URL <https://agupubs.onlinelibrary.wiley.com/doi/abs/10.1029/2018JD029163>.
- H. R. Pruppacher and J. D. Klett. *Microphysics of Clouds and Precipitation*, volume 18 of *Atmospheric and Oceanographic Sciences*. Springer Netherlands, 2 edition, 1997. doi: 10.1007/978-0-306-48100-0.
- A. Rango, J. Foster, E. G. Josberger, E. F. Erbe, W. P. Wergin, and C. Pooley. Rime and graupel: Description and characterization as revealed by low-temperature scanning electron microscopy. *Scanning*, 25(3):121–131, 2003. doi: <https://doi.org/10.1002/sca.4950250304>. URL <https://onlinelibrary.wiley.com/doi/abs/10.1002/sca.4950250304>.
- R. M. Rauber and A. Tokay. An explanation for the existence of supercooled water at the top of cold clouds. *Journal of the Atmospheric Sciences*, 48(8):1005–1023, 1991. doi: 10.1175/1520-0469(1991)048<1005:AEFTEO>2.0.CO;2. URL [https://doi.org/10.1175/1520-0469\(1991\)048<1005:AEFTEO>2.0.CO;2](https://doi.org/10.1175/1520-0469(1991)048<1005:AEFTEO>2.0.CO;2).
- J. B. Reece, L. A. Urry, M. L. Cain, S. A. Wasserman, P. V. Minorsky, and R. B. Jackson. *Campbell Biology*. Pearson, 2011. ISBN 9780321775658. URL <https://www.pearson.com/us/higher-education/product/Reece-Campbell-Biology-10th-Edition/9780321775658.html>.
- D. Rzesanke, J. Nadolny, D. Duft, R. Müller, A. Kiselev, and T. Leisner. On the role of surface charges for homogeneous freezing of supercooled water microdroplets. *Phys. Chem. Chem. Phys.*, 14:9359–9363, 2012. doi: 10.1039/C2CP23653B. URL <http://dx.doi.org/10.1039/C2CP23653B>.
- S. M. Saleeby and W. R. Cotton. A binned approach to cloud-droplet riming implemented in a bulk microphysics model. *Journal of Applied Meteorology and Climatology*, 47(2):694–703, 2008. doi: 10.1175/2007JAMC1664.1. URL <https://journals.ametsoc.org/view/journals/apme/47/2/2007jamc1664.1.xml>.
- K. Sassen. The polarization lidar technique for cloud research: A review and current assessment. *Bulletin of the American Meteorological Society*, 72(12):1848–1866, 1991. doi: 10.1175/1520-0477(1991)072<1848:TPLTFC>2.0.CO;2. URL [https://doi.org/10.1175/1520-0477\(1991\)072<1848:TPLTFC>2.0.CO;2](https://doi.org/10.1175/1520-0477(1991)072<1848:TPLTFC>2.0.CO;2).
- M. Schnaiter, E. Järvinen, P. Vochezer, A. Abdelmonem, R. Wagner, O. Jourdan, G. Mioche, V. N. Shcherbakov, C. G. Schmitt, U. Tricoli, Z. Ulanowski, and A. J. Heymsfield. Cloud chamber experiments on the origin of ice crystal complexity in cirrus clouds. *Atmospheric Chemistry and Physics*, 16(8):5091–5110, 2016. doi: 10.5194/acp-16-5091-2016. URL <https://acp.copernicus.org/articles/16/5091/2016/>.
- M. Schnaiter, E. Järvinen, A. Abdelmonem, and T. Leisner. Phips-halo: the airborne particle habit imaging and polar scattering probe – part 2: Characterization and first results. *Atmospheric Measurement Techniques*, 11(1):341–357, 2018. doi: 10.5194/amt-11-341-2018. URL <https://www.atmos-meas-tech.net/11/341/2018/>.
- R. Schön, M. Schnaiter, Z. Ulanowski, C. Schmitt, S. Benz, O. Möhler, S. Vogt, R. Wagner, and U. Schurath. Particle habit imaging using incoherent light: A first step toward a novel instrument for cloud microphysics. *Journal of Atmospheric and Oceanic Technology*, 28(4):493–512, 2011. doi: 10.1175/2011JTECHA1445.1. URL <https://doi.org/10.1175/2011JTECHA1445.1>.

- R. Schön. Development of an optical instrument which combines ice crystal imaging with simultaneous measurements of their scattering function at visible wavelengths. 2007.
- E. L. Scott. The influence of primary nucleation and rime splintering on ice number concentrations in southern ocean cumuli. *Master's thesis at the graduate college of the university of Illinois at Urbana-Champaign*, 2019. URL <https://www.ideals.illinois.edu/bitstream/handle/2142/105704/SCOTT-THESIS-2019.pdf?sequence=1&isAllowed=y/>.
- G. Sotiropoulou, E. Vignon, G. Young, H. Morrison, S. J. O'Shea, T. Lachlan-Cope, A. Berne, and A. Nenes. Secondary ice production in summer clouds over the antarctic coast: an underappreciated process in atmospheric models. *Atmospheric Chemistry and Physics*, 21(2):755–771, 2021. doi: 10.5194/acp-21-755-2021. URL <https://acp.copernicus.org/articles/21/755/2021/>.
- P. Stegmann, C. Tropea, E. Järvinen, and M. Schnaiter. Comparison of measured and computed phase functions of individual tropospheric ice crystals. *Journal of Quantitative Spectroscopy and Radiative Transfer*, 178, 01 2016. doi: 10.1016/j.jqsrt.2015.12.019.
- R. G. Stevens, K. Loewe, C. Dearden, A. Dimitrellos, A. Possner, G. K. Eirund, T. Raatikainen, A. A. Hill, B. J. Shipway, J. Wilkinson, S. Romakkaniemi, J. Tonttila, A. Laaksonen, H. Korhonen, P. Connolly, U. Lohmann, C. Hoose, A. M. L. Ekman, K. S. Carslaw, and P. R. Field. A model intercomparison of ccn-limited tenuous clouds in the high arctic. *Atmospheric Chemistry and Physics*, 18(15):11041–11071, 2018. doi: 10.5194/acp-18-11041-2018. URL <https://acp.copernicus.org/articles/18/11041/2018/>.
- P. Stott. How climate change affects extreme weather events. *Science*, 352(6293):1517–1518, 2016. ISSN 0036-8075. doi: 10.1126/science.aaf7271. URL <https://science.sciencemag.org/content/352/6293/1517>.
- Z. Sun and K. P. Shine. Studies of the radiative properties of ice and mixed-phase clouds. *Quarterly Journal of the Royal Meteorological Society*, 120(515):111–137, 1994. doi: 10.1002/qj.49712051508. URL <https://rmets.onlinelibrary.wiley.com/doi/abs/10.1002/qj.49712051508>.
- C. Takahashi. Formation of poly-crystalline snow crystals by riming process. *Journal of the Meteorological Society of Japan. Ser. II*, 57(5):458–464, 1979a. doi: 10.2151/jmsj1965.57.5_458.
- C. Takahashi. Formation of poly-crystalline snow crystals by riming process. *Journal of the Meteorological Society of Japan. Ser. II*, 57(5):458–464, 1979b. doi: 10.2151/jmsj1965.57.5_458.
- C. Teichert. Corrasion by wind-blown snow in polar regions. *American Journal of Science*, 237(2):146–148, 1939. ISSN 0002-9599. doi: 10.2475/ajs.237.2.146. URL <https://www.ajsonline.org/content/237/2/146>.
- G. Touloupas, A. Lauber, J. Henneberger, A. Beck, and A. Lucchi. A convolutional neural network for classifying cloud particles recorded by imaging probes. 13(5):2219 – 2239, 2020. ISSN 1867-1381. doi: 10.3929/ethz-b-000415087.
- J. Um and G. M. McFarquhar. Dependence of the single-scattering properties of small ice crystals on idealized shape models. *Atmospheric Chemistry and Physics*, 11(7):3159–3171, 2011. doi: 10.5194/acp-11-3159-2011. URL <https://acp.copernicus.org/articles/11/3159/2011/>.
- H. Uyeda and K. Kikuchi. Freezing experiment of supercooled water droplets frozen by using single crystal ice. *Journal of the Meteorological Society of Japan. Ser. II*, 56(1):43–51, 1978. doi: 10.2151/jmsj1965.56.1_43.

- H. Uyeda and K. Kikuchi. Measurements of the principal axis of frozen hemispheric water droplets. *Journal of the Meteorological Society of Japan. Ser. II*, 58(1):52–58, 1980. doi: 10.2151/jmsj1965.58.1_52.
- B. Van Dierenhoven. The prevalence of the 22° halo in cirrus clouds. *Journal of Quantitative Spectroscopy and Radiative Transfer*, 146, 2014. ISSN 00224073. doi: 10.1016/j.jqsrt.2014.01.012.
- B. van Dierenhoven, A. Ackerman, B. Cairns, and A. Fridlind. A flexible parameterization for shortwave optical properties of ice crystals. *J. Atmos. Sci.*, 71(5):1763–1782, 2014. ISSN 15200469 00224928. doi: 10.1175/JAS-D-13-0205.1.
- L. Vardiman. The generation of secondary ice particles in clouds by crystal–crystal collisions. *J. Atmos. Sci.*, 35:2168–2180, 1978.
- P. Vochezer, E. Järvinen, R. Wagner, P. Kupiszewski, T. Leisner, and M. Schnaiter. In situ characterization of mixed phase clouds using the small ice detector and the particle phase discriminator. *Atmospheric Measurement Techniques*, 9(1):159–177, 2016. doi: 10.5194/amt-9-159-2016. URL <https://www.atmos-meas-tech.net/9/159/2016/>.
- F. Waitz. Photoacoustic spectroscopy of carbonaceous particles in snow. *Master’s thesis at Karlsruhe Institute of Technology, Institute for Meteorology and Climate Research, Department Atmospheric Aerosol Research (IMK-AAF)*, 2017.
- F. Waitz, M. Schnaiter, T. Leisner, and E. Järvinen. Phips-halo: the airborne particle habit imaging and polar scattering probe – part 3: Single-particle phase discrimination and particle size distribution based on the angular-scattering function. *Atmospheric Measurement Techniques*, 14(4):3049–3070, 2021a. doi: 10.5194/amt-14-3049-2021. URL <https://amt.copernicus.org/articles/14/3049/2021/>.
- F. Waitz, M. Schnaiter, T. Leisner, and E. Järvinen. In-situ observation of riming in mixed-phase clouds using the phips probe. *Journal of Atmospheric Sciences*, 2021b. in review.
- P. K. Wang and W. Ji. Collision efficiencies of ice crystals at low–intermediate reynolds numbers colliding with supercooled cloud droplets: A numerical study. *Journal of the Atmospheric Sciences*, 57(8):1001 – 1009, 2000. doi: 10.1175/1520-0469(2000)057<1001:CEOICA>2.0.CO;2. URL https://journals.ametsoc.org/view/journals/atsc/57/8/1520-0469_2000_057_1001_ceoica_2.0.co_2.xml.
- S. G. Warren and R. E. Brandt. Optical constants of ice from the ultraviolet to the microwave: A revised compilation. *Journal of Geophysical Research: Atmospheres*, 113 (D14), 2008. doi: <https://doi.org/10.1029/2007JD009744>. URL <https://agupubs.onlinelibrary.wiley.com/doi/abs/10.1029/2007JD009744>.
- A. Wegener. *Thermodynamik der Atmosphäre*, page 331, 1911.
- H. Weingärtner, I. Teermann, U. Borchers, P. Balsaa, H. V. Lutze, T. C. Schmidt, E. U. Franck, G. Wiegand, N. Dahmen, G. Schwedt, F. H. Frimmel, and B. C. Gordalla. *Water, 1. Properties, Analysis, and Hydrological Cycle*, pages 1–40. American Cancer Society, 2016. ISBN 9783527306732. doi: https://doi.org/10.1002/14356007.a28_001.pub3. URL https://onlinelibrary.wiley.com/doi/abs/10.1002/14356007.a28_001.pub3.
- M. Wendisch, A. Macke, A. Ehrlich, C. Lüpkes, et al. The arctic cloud puzzle: Using acloud/pascal multiplatform observations to unravel the role of clouds and aerosol particles in arctic amplification. *Bulletin of the American Meteorological Society*, 100(5): 841–871, 2019. doi: 10.1175/BAMS-D-18-0072.1. URL <https://doi.org/10.1175/BAMS-D-18-0072.1>.

- M. Wild, D. Folini, C. Schär, N. Loeb, E. G. Dutton, and G. König-Langlo. The global energy balance from a surface perspective. *Climate Dynamics*, 40(11):3107–3134, Jun 2013. ISSN 1432-0894. doi: 10.1007/s00382-012-1569-8. URL <https://doi.org/10.1007/s00382-012-1569-8>.
- E. R. Williams, R. Zhang, and J. Rydock. Mixed-phase microphysics and cloud electrification. *Journal of Atmospheric Sciences*, 48(19):2195 – 2203, 1991. doi: 10.1175/1520-0469(1991)048<2195:MPMACE>2.0.CO;2. URL https://journals.ametsoc.org/view/journals/atsc/48/19/1520-0469_1991_048_2195_mpmace_2_0_co_2.xml.
- W. Wu and G. M. McFarquhar. On the Impacts of Different Definitions of Maximum Dimension for Nonspherical Particles Recorded by 2D Imaging Probes. *Journal of Atmospheric and Oceanic Technology*, 33(5):1057–1072, 05 2016. ISSN 0739-0572. doi: 10.1175/JTECH-D-15-0177.1. URL <https://doi.org/10.1175/JTECH-D-15-0177.1>.
- Z. Wu, S. Liu, D. Zhao, L. Yang, Z. Xu, Z. Yang, W. Zhou, H. He, M. Huang, D. Liu, R. Li, and D. Ding. Neural network classification of ice-crystal images observed by an airborne cloud imaging probe. *Atmosphere-Ocean*, 58(5):303–315, 2020. doi: 10.1080/07055900.2020.1843393. URL <https://doi.org/10.1080/07055900.2020.1843393>.
- H. Xiao, F. Zhang, Q. He, P. Liu, F. Yan, L. Miao, and Z. Yang. Classification of ice crystal habits observed from airborne cloud particle imager by deep transfer learning. *Earth and Space Science*, 6(10):1877–1886, 2019. doi: <https://doi.org/10.1029/2019EA000636>. URL <https://agupubs.onlinelibrary.wiley.com/doi/abs/10.1029/2019EA000636>.
- P. Yang, K. N. Liou, K. Wyser, and D. Mitchell. Parameterization of the scattering and absorption properties of individual ice crystals. *Journal of Geophysical Research: Atmospheres*, 105(D4):4699–4718, 2000. doi: <https://doi.org/10.1029/1999JD900755>. URL <https://agupubs.onlinelibrary.wiley.com/doi/abs/10.1029/1999JD900755>.
- P. Yang, L. Bi, B. A. Baum, K.-N. Liou, G. W. Kattawar, M. I. Mishchenko, and B. Cole. Spectrally consistent scattering, absorption, and polarization properties of atmospheric ice crystals at wavelengths from 0.2 to 100 μm . *Journal of the Atmospheric Sciences*, 70(1):330–347, 2013. doi: 10.1175/JAS-D-12-039.1. URL <https://doi.org/10.1175/JAS-D-12-039.1>.
- J.-I. Yano and V. T. J. Phillips. Ice–ice collisions: An ice multiplication process in atmospheric clouds. *J. Atmos. Sci.*, 68:322–333, 2011.
- M. Yasutomi. Thermodynamic mechanism of the density anomaly of liquid water. *Frontiers in Physics*, 3:8, 2015. ISSN 2296-424X. doi: 10.3389/fphy.2015.00008. URL <https://www.frontiersin.org/article/10.3389/fphy.2015.00008>.
- B. Yi, P. Yang, B. A. Baum, T. L’Ecuyer, L. Oreopoulos, E. J. Mlawer, A. J. Heymsfield, and K.-N. Liou. Influence of ice particle surface roughening on the global cloud radiative effect. *Journal of the Atmospheric Sciences*, 70(9):2794 – 2807, 2013. doi: 10.1175/JAS-D-13-020.1. URL <https://journals.ametsoc.org/view/journals/atsc/70/9/jas-d-13-020.1.xml>.
- T. J. Zaremba, R. M. Rauber, G. M. McFarquhar, P. J. DeMott, J. J. D’Alessandro, and W. Wu. Ice in southern ocean clouds with cloud top temperatures exceeding -5c . *Journal of Geophysical Research: Atmospheres*, 126(14):e2021JD034574, 2021. doi: <https://doi.org/10.1029/2021JD034574>. URL <https://agupubs.onlinelibrary.wiley.com/doi/abs/10.1029/2021JD034574>. e2021JD034574 2021JD034574.
- S. Zhu, X. Guo, G. Lu, and L. Guo. Ice crystal habits and growth processes in stratiform clouds with embedded convection examined through aircraft observation in northern china. *Journal of the Atmospheric Sciences*, 72(5):2011 – 2032, 2015. doi: 10.1175/

JAS-D-14-0194.1. URL <https://journals.ametsoc.org/view/journals/atsc/72/5/jas-d-14-0194.1.xml>.

E. E. Ávila, N. E. Castellano, C. P. R. Saunders, R. E. Bürgesser, and G. G. Aguirre Varela. Initial stages of the riming process on ice crystals. *Geophysical Research Letters*, 36(9), 2009. doi: <https://doi.org/10.1029/2009GL037723>. URL <https://agupubs.onlinelibrary.wiley.com/doi/abs/10.1029/2009GL037723>.

Acknowledgements

First and foremost, I want to thank my doctoral supervisor Prof. T. Leisner for giving me the opportunity to write my doctoral thesis at the IMK-AAF. I also want to express thanks to my co-referee, Prof. C. Hoose, who gave me the idea with the riming topic.

Next, I want to express my deep gratitude to Dr. Emma Järvinen and Dr. Martin Schnaiter, not only for the supervision during my PhD time, but for their continuous support throughout my whole academic career. Also, I want to thank my colleagues, especially Shawn Wagner, Sepehr Ariaei, Dr. Mario Nachbar, Dr. Magdalena Vallon, Franziska Vogel and Tobias Schorr, as well as the whole IMK-AAF staff, for the great time over the years.

I want to say thank you to all the amazing people that I had the pleasure to meet during the SOCRATES and IMPACTS field campaigns, especially my fellows Bryan Rainwater and Dr. Joe Finlon, as well as the NASA team, foremost Kelly Griffin and Rodney Turbak, and technical staff Mike, Mike, *Fat Mike* and Mike, and many others.

I want to thank all my dear friends, who were always there for me during the different stages of my studies, namely Dr. Tim Seifert, Dr. Jakob Schwichtenberg, Dr. Christian Schmitt, Marcel Köpke, Tobias Himmel, Timo + Roman Lehmann, Michael Daam, Fabian Tschunko, Greta Heine, Deniz Flaig, Dennis Normann and Max Stadelmaier, as well as the K.B.K., AC, Z10 and Hochschulsport-Crew.

Finally, I want to thank my family, especially my parents, who supported me during my studies and my whole life.